

TECHNISCHE UNIVERSITÄT MÜNCHEN

Lehrstuhl E23 für Technische Physik

Walther-Meißner-Institut für Tieftemperaturforschung
der Bayerischen Akademie der Wissenschaften

Josephson Junctions with Ferromagnetic Interlayer

Georg Hermann Wild

Vollständiger Abdruck der von der Fakultät für Physik der Technischen Universität München zur Erlangung des akademischen Grades eines

Doktors der Naturwissenschaften

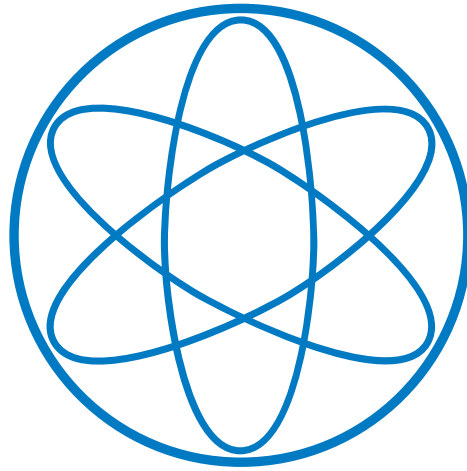
genehmigten Dissertation.

Vorsitzender: Univ.-Prof. Dr. M. Zacharias

Prüfer der Dissertation: 1. Univ.-Prof. Dr. R. Gross
2. Univ.-Prof. J. J. Finley, Ph.D.

Die Dissertation wurde am 16.06.2011 bei der Technischen Universität München eingereicht und durch die Fakultät für Physik am 27.02.2012 angenommen.

Physik-Department



Josephson Junctions with Ferromagnetic
Interlayer

Dissertation
von
Georg Wild



Technische Universität München

CONTENTS

<i>Contents</i>	v
<i>List of Figures</i>	ix
<i>List of Tables</i>	xiii
<i>Abstract</i>	xv
<i>Kurzzusammenfassung</i>	xvii
<i>Part I Introduction</i>	1
<i>1. Introduction</i>	3
1.1 Motivation	3
1.2 Josephson Junctions with a Ferromagnetic Interlayer	4
1.3 π Junctions as a New Building Element for Quantum Electronics	6
1.4 Probing the Josephson Dynamics by the Fiske Resonances and Microwave Irradiation	8
1.5 Experimentally Demonstrating Macroscopic Quantum Behavior	9
1.6 Thesis Overview	10
<i>Part II Theory</i>	13
<i>2. The Different Types of Josephson Junctions and their Application</i>	15
2.1 Classical Tunnel Junctions	15
2.2 Josephson Junctions with a Normal Conducting Interlayer	18
2.2.1 The Andreev Reflection	19
2.2.2 Transport via Andreev Bound States	20
2.2.3 Transport across a Diffusive Normal Metal Interlayer	23
2.3 Josephson Junctions with a Ferromagnetic Interlayer	27
2.3.1 Long Ballistic SFS Junctions	27
2.3.2 Diffusive SFS Junctions	28
2.3.3 Historical Review: The Fulde-Ferrel Larkin-Ovchinnikov State	30

2.4	Josephson Junctions, Quantum Electronics and Superconducting Qubits	32
3.	<i>The Dynamic Properties of Small Josephson Junctions</i>	35
3.1	The Resistively and Capacitively Shunted Junction Model	35
3.1.1	Overdamped and Underdamped Josephson Junctions	38
3.2	Josephson Junctions beyond the Lumped Element Limit	40
3.2.1	Josephson Junctions in an Applied Magnetic Field	40
3.2.2	The Time-Dependent Sine-Gordon Equation	43
3.2.3	The Fiske Resonances	44
3.2.4	The Quality of the Fiske Resonances	46
3.2.5	Effective Magnetic Thickness	49
3.2.6	Effective Swihart Velocity and Frequencies of Resonant Modes	51
4.	<i>The Escape of the Phase Particle from a Metastable State</i>	53
4.1	Thermally Activated Escape	53
4.1.1	The Transition-State Theory	54
4.1.2	Kramers' Theory	55
4.1.3	Kramers' Theory applied to Josephson Junctions	56
4.2	Macroscopic Quantum Tunneling	57
4.3	The Crossover between Thermally Activated Escape and Macroscopic Quantum Tunneling	58
4.4	The Irradiation of Josephson Junctions with Microwaves	59
4.4.1	The Quantum Mechanical Interpretation	60
4.4.2	The Semi-Classical Dynamics of a Strongly Microwave Driven Josephson Junction	61
<i>Part III Experiments</i>		65
5.	<i>Sample Preparation</i>	67
5.1	Introduction	67
5.2	The Self-Align Multilayer Process	68
5.3	Multilayer Deposition and Characterization	74
5.3.1	Sputtering and Oxidation	74
5.3.2	The Superconducting Niobium	77
5.3.3	The Magnetic Properties of PdNi	79
5.4	Etching and Insulating the Mesa	80
5.5	Concluding Remarks	82
6.	<i>0-π Crossover, Current-Voltage Characteristics and $I_c(H)$</i>	85
6.1	The 500 mK Measurement Setup	85
6.2	The Critical Current Dependence on the Ferromagnetic Interlayer Thickness	88

6.3	The Current-Voltage Characteristics	92
6.4	The Magnetic Field Dependence of the Critical Current	96
6.5	Concluding Remarks	97
7.	<i>The Fiske Resonances and their Quality</i>	99
7.1	Concluding Remarks	109
8.	<i>Switching Experiments and Macroscopic Quantum Tunneling</i>	113
8.1	The Experimental Setup	114
8.2	Switching Experiments	119
8.3	The Irradiation of a Josephson Junction with Microwaves	122
8.4	The Observation of Macroscopic Quantum Tunneling	128
8.5	Concluding Remarks	133
9.	<i>Excitations in the Ferromagnetic Interlayer</i>	135
 <i>Part IV Conclusion and Outlook</i>		143
10.	<i>Conclusion and Future Prospects</i>	145
10.1	Implications of This Work	145
10.2	Outlook	147
10.3	Conclusion	148
 <i>Part V Appendix</i>		149
A.	<i>Junction Growth Recipe</i>	151
B.	<i>The Semi-Classical Simulation of the Josephson Junction Dynamics</i>	153
B.1	The Time Evolution of the Phase Difference	153
C.	<i>Material Constants</i>	155
D.	<i>The Parameters of the Sample GInsitu-203b</i>	157
E.	<i>Nomenclature</i>	159
<i>Bibliography</i>		163
<i>List of Publications</i>		183
<i>Index</i>		187

LIST OF FIGURES

1.1	RSFQ cells realized by a dc SQUID with and without a π -junction . . .	6
2.1	Potential energy and magnitude of the wave function versus the position perpendicular to the barrier for a Josephson tunnel junction	16
2.2	Illustration of the specular and the Andreev reflection	20
2.3	Andreev bound states confined between SN interfaces	20
2.4	Bound states and transport in SNS junctions	21
2.5	Diffusion of a correlated electron-hole pair	24
2.6	The order parameter at an SN interface	25
2.7	Spectral supercurrent density for long, diffusive SNS and SFS junctions	26
2.8	Bound states and transport in SFS junctions	27
2.9	Influence of the phase difference on the level structure in SFS junctions	28
2.10	The order parameter at an SF interface	29
2.11	Schematic representation of a Cooper-pair with and without an applied magnetic field	31
2.12	The rf-SQUID as a qubit	33
2.13	An active and a passive π -junction incorporated into a persistent current qubit	34
3.1	The Stewart-McCumber model	35
3.2	The tilted washboard potential	37
3.3	Phase diagram of a Josephson junction	38
3.4	IVCs of an underdamped Josephson junction	39
3.5	Schematic drawing of an extended Josephson junction	41
3.6	Sketch of the SIFS junction geometry with an overhang region	44
3.7	Equivalent circuit of a long Josephson junction	45
3.8	Height of the n -th Fiske current step versus $Z_n F_n$	49
4.1	Potential with a metastable state	54
4.2	Equivalent circuit of a Josephson junction irradiated with microwaves	59
4.3	Discrete energy levels in a potential well	60
4.4	The bias current versus the equilibrium phase difference for a JJ irradiated with microwaves	62
5.1	Multilayer stack	68

5.2	A mesa structure with the shrunked resist stencil on top	69
5.3	Complete junction	69
5.4	Scanning electron micrograph of the SiO ₂ layer overgrowing the niobium mesa structure	70
5.5	Lithography mask	71
5.6	Photograph and SEM micrograph of a junction	72
5.7	Photograph of the UHV thin film cluster tool	73
5.8	In-situ, non-contact AFM micrograph	76
5.9	Current-voltage characteristics of an SIS Josephson tunnel junction . .	76
5.10	In-plane and out-of-plane magnetization of the PdNi interlayer versus the applied magnetic field and the magnetization of the ferromagnetic interlayer during the warm up	78
5.11	A typical resist profile after etching	81
6.1	500 mK setup sample holder	85
6.2	500 mK setup high field coil 2	86
6.3	Photograph of the 500 mK measurement setup	86
6.4	Photograph of the 500 mK dewar setup	87
6.5	Schematic diagram of slow-sweep measurements	89
6.6	Dependence of the $I_c R_n$ -product of SIFS junctions on the thickness of the ferromagnetic Pd _{0.82} Ni _{0.18} layer	90
6.7	IVCs and the magnetic field dependence of I_c obtained for a π -coupled SIFS junction with $A = 20 \times 20 \mu\text{m}^2$	93
6.8	IVCs and the magnetic field dependence of I_c obtained for a π -coupled SIFS junction with $A = 50 \times 50 \mu\text{m}^2$	94
6.9	Critical current dependence on the applied magnetic field for a junction with a magnetized ferromagnetic interlayer	98
7.1	IVCs of the 50 μm junction of GInsitu-203b measured in different applied magnetic fields	100
7.2	The differential resistance versus the applied voltage measured in-situ with the data in Fig. 7.1	102
7.3	IVCs and the differential resistance versus the applied voltage for the 20 μm junction of GInsitu-203b in different applied magnetic fields . .	103
7.4	Dependence of the critical current and the height of the Fiske steps on the applied magnetic field	105
7.5	Quality factors of the Fiske resonances	106
7.6	Detailed study of the height of the HF step	110
8.1	Photograph of the dilution refrigerator setup	114
8.2	Bonded sample	115
8.3	Schematic diagram of the dilution unit wiring	117
8.4	A superconducting coil mounted in the dilution unit dewar setup . . .	118

8.5	The sample holder of the dilution unit	118
8.6	The microwave coupling at different frequencies	119
8.7	Schematic diagram of a switching experiment	120
8.8	Typical standard deviation of the switching currents versus temperature	121
8.9	Standard deviation of the switching currents versus microwave frequency and mean switching current	123
8.10	Temperature dependence of the standard deviation of the switching currents versus the reduced attempt frequency for a JJ irradiated with microwaves of frequency 7580MHz	124
8.11	Semi-classical simulation of the switching current of a JJ under strong microwave irradiation	125
8.12	Switching current histograms versus microwave power for a JJ irradiated with microwaves of frequency 15295MHz	127
8.13	Switching current histograms versus microwave power for a JJ irradiated with microwaves of frequency 18380MHz measured at different bath temperatures	129
8.14	Switching current histograms acquired at different bath temperatures .	130
8.15	Standard deviation of the switching currents versus bath temperature .	132
9.1	Steps in the IVCs of SIFS π Josephson junctions with and without a magnetized ferromagnetic interlayer	136
9.2	Steps in the IVCs of a $5 \times 5 \mu\text{m}^2$ SIFS π Josephson junction for different applied magnetic fields	139
9.3	Shapiro steps in a $5 \times 5 \mu\text{m}^2$ SIFS π Josephson junction under microwave irradiation	140
9.4	Standard deviation of the switching currents versus bath temperature for a $5 \times 5 \mu\text{m}^2$ SIFS π Josephson junction	141

LIST OF TABLES

5.1	Etching parameters for the RIE process	70
5.2	Typical sputter parameters for a SIFS JJ	70
5.3	Surface roughness at different process stages of the SIFS growth process determined by non-contact AFM	77
6.1	Critical current and resistance values obtained from the IVCs of a $20 \times 20 \mu\text{m}^2$ and a $50 \times 50 \mu\text{m}^2$ SIFS π -junction	95
7.1	The voltage position and the step height of the n -th Fiske step obtained from the IVCs of a $50 \times 50 \mu\text{m}^2$ SIFS π -junction	101
D.1	Summary of the parameters determined for the sample GInsitu-203b .	158

ABSTRACT

We report on the fabrication of superconductor/insulator/ferromagnetic metal/superconductor (Nb/AlO_x/Pd_{0.82}Ni_{0.18}/Nb) Josephson junctions (SIFS JJs) with high critical current densities, large normal resistance times area products, and high quality factors. For these junctions, a transition from 0- to π -coupling is observed for a thickness $d_F = 6$ nm of the ferromagnetic Pd_{0.82}Ni_{0.18} interlayer. The magnetic field dependence of the critical current of the junctions demonstrates good spatial homogeneity of the tunneling barrier and ferromagnetic interlayer. Magnetic characterization shows that the Pd_{0.82}Ni_{0.18} has an out-of-plane anisotropy and large saturation magnetization indicating negligible dead layers at the interfaces. A careful analysis of Fiske modes up to about 400 GHz provides valuable information on the junction quality factor and the relevant damping mechanisms. Whereas losses due to quasiparticle tunneling dominate at low frequencies, at high frequencies the damping is explained by the finite surface resistance of the junction electrodes. High quality factors of up to 30 around 200 GHz have been achieved. They allow to study the junction dynamics, in particular the switching probability from the zero-voltage into the voltage state with and without microwave irradiation. The experiments with microwave irradiation are well explained within semi-classical models and numerical simulations. In contrast, at mK temperature the switching dynamics without applied microwaves clearly shows secondary quantum effects. Here, we could observe for the first time macroscopic quantum tunneling in Josephson junctions with a ferromagnetic interlayer. This observation excludes fluctuations of the critical current as a consequence of an unstable magnetic domain structure of the ferromagnetic interlayer and affirms the suitability of SIFS Josephson junctions for quantum information processing.

KURZZUSAMMENFASSUNG

Wir berichten über die Fabrikation von Supraleiter/Isolator/Ferromagnet/Supraleiter (SIFS) π -Josephson-Kontakten mit hohen kritischen Stromdichten, hohen Widerstands-Flächen-Produkten und hohen Gütefaktoren. Für diese Nb/AlO_x/Pd_{0.82}Ni_{0.18}/Nb Kontakte beobachten wir einen Übergang von einer 0- zu einer π -Kopplung für eine Dicke $d_F = 6$ nm der ferromagnetischen Pd_{0.82}Ni_{0.18}-Zwischenschicht. Die Abhängigkeit des kritischen Stroms vom angelegten Magnetfeld bestätigt eine gute Homogenität der Tunnelbarriere und der Zwischenschicht. Bei der magnetischen Charakterisierung zeigt sich, dass Pd_{0.82}Ni_{0.18} eine Anisotropie senkrecht zur Filmebene und eine hohe Sättigungsmagnetisierung aufweist, was auf vernachlässigbare Totzonen an den Grenzflächen hindeutet. Durch sorgfältige Analyse von Fiske-Resonanzen bis 400 GHz erhalten wir wertvolle Informationen über die Gütefaktoren und die relevanten Dämpfungsmechanismen. Während Verluste aufgrund von Quasiteilchen-Tunneln bei tiefen Frequenzen dominieren, wird die Dämpfung bei hohen Frequenzen durch den endlichen Oberflächenwiderstand an den Kontaktelektroden erklärt. Hohe Gütefaktoren von bis zu 30 wurden bei 200 GHz erreicht. Diese erlauben eine Untersuchung der dynamischen Eigenschaften der Kontakte, insbesondere des Schaltens aus dem Nullspannungs- in den Spannungszustand mit und ohne Einstrahlung von Mikrowellen. Die Experimente mit Mikrowelleneinstrahlung können gut im Rahmen semi-klassischer Modelle und Simulationsrechnungen beschrieben werden. Bei Temperaturen im mK-Bereich zeigt die Dynamik ohne Mikrowellen-Einstrahlung sekundäre Quanten-Effekte. Hier konnte zum ersten Mal makroskopisches Quantentunneln in Josephson-Kontakten mit ferromagnetischer Zwischenschicht beobachtet werden. Dieses Resultat schließt Fluktuationen des kritischen Stroms als Konsequenz einer instabilen magnetischen Domänen-Struktur der ferromagnetischen Zwischenschicht aus und bestätigt klar die Tauglichkeit von SIFS Josephson-Kontakten für die Quanten-Informationsverarbeitung.

Part I

INTRODUCTION

Chapter 1

INTRODUCTION

1.1 Motivation

We will certainly never be able to finally decide whether really the Chinese were the first that understood the properties of a lodestone and thus invented the magnetic compass.¹ However, it is clear that no other scientific finding has influenced navigation more up to the middle ages and hence fostered long-distance trade. But obviously the success story of magnetism continued and still continues. Here, one has to think of the giant magnetoresistive effect²⁻⁶ and the tunnel magnetoresistance⁷, which led to a revolution in the storage density of magnetic hard drives. And the first signs of the future direction are already visible: Magnetism influences the quantum properties of electrons. Here, not the magnetic field strength, but the magnetic vector potential plays the dominant role as Aharonov and Bohm confirmed in their famous electron interference experiment.^{8,9} Today, the most promising direction to find new applications of ferromagnetism is certainly towards mesoscopic systems and of course quantum electronics. The latter one uses the fluxoid quantization and the Josephson effect to define discrete states representing classical and quantum binary digits (bits) and quantum dynamics to process this information.

Quantum electronics uses Josephson junctions (JJs) as elementary building blocks, which are formed by two weakly coupled superconductors. In the superconducting tunnel junction, two superconducting electrodes are separated by a thin insulating barrier. Nonetheless, this structure is able to carry a dissipationless tunnel current $I = I_c \sin \varphi$, which is defined by the critical current I_c and the phase difference φ between the macroscopic wave functions describing the superconducting electrodes.¹⁰⁻¹² Moreover, it turned out that a supercurrent between two superconductors can also be carried across a normal metal¹³ or even a ferromagnetic metal¹⁴ by coherent electron-hole pairs. In the latter case, the quantum phases of the electrons and the holes are modified by the intrinsic magnetic field of the ferromagnetic layer analogously to the Aharonov-Bohm effect. This shifts the current-phase relation of a suitable superconductor/ferromagnetic metal/superconductor (SFS) Josephson junction by π to $I = |I_c| \sin(\varphi + \pi) = -|I_c| \sin \varphi$.¹⁵⁻¹⁷ These junctions are called π -junctions and define a new building element for quantum electronics. We note that π -coupling can also be realized by controlling the energy distribution of the current-carrying states

in the normal metal layer N of an SNS junction^{18, 19}, by a superconductor/quantum dot/superconductor junction²⁰, or by using the unusual pairing symmetry in *d*-wave superconductors^{21–30, 31}. However, these implementations have drawbacks: In the first two cases, one needs an additional external bias current or bias voltage, while the latter case suffers from technological difficulties. In contrast, SFS Josephson junctions can be grown in a multilayer process. Nevertheless, it is still unknown whether excitations in the ferromagnetic interlayer or critical current fluctuations³² are present in SFS Josephson junctions and make these devices unusable for applications in quantum information processing (QIP). Because of this, we examine critical current fluctuations and the dynamics of Josephson junctions with a ferromagnetic interlayer within this work.

We focus on superconductor/insulator/ferromagnetic metal/superconductor (SIFS) Josephson junctions. There, an additional ultrathin insulating barrier between the bottom electrode and the ferromagnetic layer reduces the quasiparticle current, which is responsible for the intrinsic damping.³³ This improves the coherence times of qubits with π -junctions³⁴ and allows to explore the dynamic properties of the junctions, especially at high frequencies. As we will see in section 1.5, the agreement between the dynamic properties and their theoretical prediction allows to exclude low-lying excitations due to spin-flip processes and to examine critical current fluctuations as a dynamic response to a fluctuating magnetic domain structure of the interlayer. We note that instead of the insulator/ferromagnet combination also a ferromagnetic insulator FI has been suggested, but the implementation of underdamped S-FI-S Josephson junctions is still beyond today's technology.^{35–39}

1.2 Josephson Junctions with a Ferromagnetic Interlayer

Historically, an important step for the understanding of the influence of an applied magnetic field to a macroscopic wave function was the prediction of an oscillating order parameter of a superconductor in a magnetic field by Fulde and Ferrell⁴⁰ and simultaneously by Larkin and Ovchinnikov⁴¹ in the 1960s (cf. section 2.3.3). It stimulated L. N. Bulaevskii and A. I. Buzdin to predict an oscillatory dependence of the critical current of an SFS Josephson junction on the F layer thickness as a consequence of the interference of the phases of the electrons of a Cooper-pair in 1982.^{15, 42–44} In detail, the oscillatory behavior is a direct consequence of the exchange splitting of the spin-up and spin-down subbands in the F layer, causing a finite momentum shift $q = \pm 2E_{\text{ex}}/v_F$ of the spin-up and spin-down electron of a Cooper-pair leaking into the F layer.^{16, 33, 42–44} Here, E_{ex} is the exchange energy and v_F the Fermi velocity in the F layer. Historically, the first indirect experimental evidences for this phenomenon were an oscillation of the critical temperature of superconductor/ferromagnetic metal (S/F) bilayers with increasing F layer thickness^{45, 46} and the variation of the critical temperature of FSF trilayers as a function of the relative magnetization direction of the F layers⁴⁷ and their thicknesses^{48–50}.^[A2] Finally, Ryazanov *et al.*^{14, 51–53} experimentally verified the critical

current oscillation nearly 20 years after Buzdin's prediction by observing a cusp in the temperature dependence of the critical current of an SFS junction. In this experiment, the use of the very weak diluted ferromagnet $\text{Cu}_{0.48}\text{Ni}_{0.52}$ reduces the exchange coupling E_{ex} between the intrinsic magnetic field and the spins of the electrons in the ferromagnetic layer to ~ 1 meV. This increases the oscillation length of the critical current with the F layer thickness d_{F} to ~ 27 nm, a value that could be realized that time. This achievement has further stimulated research on SFS junctions in the dirty limit^{53–63}, where the interlayer thickness d_{F} exceeds the mean free path ℓ , as well as later in the clean limit^{64–66}. Quite important was the direct proof of π -coupling by incorporating SFS junctions in dc SQUIDs. In general, direct current superconducting quantum interference devices (dc SQUIDs) consist of a superconducting ring which is interrupted by two JJs. Here, the phase differences across the JJs are coherently related by the fluxoid quantization condition, so that a maximum supercurrent across the two junctions only flows when an integer number of magnetic flux quanta Φ_0 is coupled into the superconducting loop.^{67–69} Incorporating a single π -junction shifts the magnetic field dependence by $\Phi_0/2$ which was detected.^{70, 71} Finally, a current-phase relation has been directly measured by embedding an SFS junction into a more advanced SQUID loop geometry.⁷²

Due to the high conductivity of the interlayer, SFS junctions are characterized by a tiny resistance-area product $R_{\text{n}} \cdot A < 0.1 \Omega \mu\text{m}^2$, so that the voltages across the junctions are only detectable by a sensitive SQUID voltage amplifier. Things changed when T. Kontos *et al.*⁵⁴ added a 50 nm partially oxidized aluminum interlayer in the stack which resulted in superconductor/normal conductor/insulator/ferromagnetic metal/superconductor Nb/Al/AIO_x/PdNi/Nb junctions with a huge normal resistance-area product $R_{\text{n}} \cdot A \approx 100 \text{k}\Omega \mu\text{m}^2$ and a tiny critical current density $j_{\text{c}} \approx 10 \text{mA}/\text{cm}^2$. These values were already sufficient to easily detect I_{c} and R_{n} and to observe an oscillatory behavior in the $I_{\text{c}}R_{\text{n}}(d_{\text{F}})$ dependence with an increasing ferromagnetic interlayer thickness d_{F} .

However, the plasma frequency $\omega_{\text{p}} \propto \sqrt{I_{\text{c}}}$ of Kontos' junctions and their critical current density j_{c} were too small for applications in QIP and to perform measurements to test the macroscopic quantum behavior (MQB). Therefore, by improving the fabrication technology and replacing the 50 nm oxidized aluminum layer by an ultrathin 4 nm barrier, this work reaches much higher $j_{\text{c}} \approx 30 \text{A}/\text{cm}^2$ at modest $R_{\text{n}} \cdot A \approx 130 \Omega \mu\text{m}^2$. Here, the resulting plasma frequency $\omega_{\text{p}}/2\pi \approx 20 \text{GHz}$ and reasonable intrinsic quality factors $Q_0 \gg 1$ already dominate thermal fluctuations when the junctions are cooled appropriately. Hence, the junctions grown within this work are already suitable for applications in QIP or for MQB experiments. We note that for a π -junction with a ferromagnetic NiCu interlayer and an ultrathin barrier the critical current density has been reported an order of magnitude lower than our value for the same $I_{\text{c}}R_{\text{n}}$ ^{73, 74}, which is most probable related to a reduced superconducting gap of the niobium electrodes due to fabrication details. In contrast, the critical current density can be further improved by utilizing the ferromagnet Ni₃Al, which allows to go beyond the dirty limit condition.⁶⁶ There, critical current densities are an order of magnitude larger than in the PdNi system

at similar junction resistances. Using Josephson junctions with a step-like F layer thickness, also junctions with a coupling changing between 0 and π along the junction have been realized.^{75–77}

1.3 π Junctions as a New Building Element for Quantum Electronics

Conventional electronics is based on the flow of electrons in electronic circuits. There, electronic transport takes place over macroscopic distances in normal metals, so that incoherent scattering processes allow to treat the circuits classically. In contrast, superconducting quantum electronics uses superconductors with a well defined macroscopic wave function. In this case, coherent effects play a role and allow to implement electronics based on the fluxoid quantization and the Josephson physics. Here, discrete building elements exist analogously to classical electronics, the Josephson junctions. For applications, there is a strong demand for the so-called π -junctions, across which the macroscopic quantum phase shifts by π .⁷⁸ These devices would simplify superconducting electronic circuits and promise quiet qubits²⁴ since they substitute a magnetic bias. We note that quiet qubits have also been suggested where a flux bias is provided by trapped flux quanta in a superconducting ring⁷⁹ or by magnetic dots⁸⁰. However, the phase bias realized by these implementations is in contrast to SFS junctions not well defined and badly reproducible.

Regarding the classical implementation of a digital computer⁸¹, we only shortly discuss the rapid single flux quantum (RSFQ) logic.^{82–90} It is based on shifting flux quanta in a superconducting circuit. Already today, clocked superconducting RSFQ circuits outrange our classical computer based on the complementary metal-oxide-semiconductor (CMOS) logic⁹¹ and are expected to exceed a clock frequency of 100GHz. Figure 1.1a shows the standard implementation of an RSFQ cell. Due to the fluxoid quantization, this circuit has two distinct states, one without a fluxon (no circulating current in the loop) and the other with a fluxon. These states represent a binary digit (bit). However, it is necessary for the information processing that the dynamics in the RSFQ cell is dominated by the Josephson physics rather than the electrostatics. This requires that the relevant current $\sim I_c$ across the JJs exceeds the current Φ_0/L generated by a magnetic flux quantum

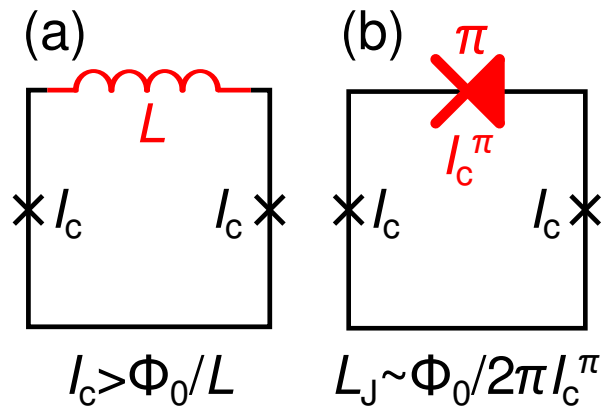


Fig. 1.1: RSFQ cells realized by a dc SQUID with a geometric inductance L (a) and with a π -junction (b)

generated by a magnetic flux quantum

Φ_0 penetrating the cell with the inductance L , which translates for the most common technology to a minimum conventional cell size of hundreds of micrometers. Using a large π -junction instead of the inductance L (see Fig. 1.1b) circumvents this drawback by replacing the geometric inductance L by the Josephson inductance $L_J \sim \Phi_0/2\pi I_c^\pi$. This allows to scale superconducting logic circuits down to submicron dimensions.^{92, 93} Moreover, π -junctions are necessary to implement the Josephson junction inverter as the superconducting analog of the complementary metal-oxide-semiconductor logic.^{94, 95} We note that the classical Josephson computing is not the main interest within this work; however, a detailed understanding of π -junction properties at high frequencies and an optimization for large critical current densities and large $I_c R_n$ products coincide with our goals.

Our primary concern is the application of SIFS π -junctions for quantum information processing. There, one uses the degeneracy of the ground state in appropriately flux biased superconducting loops to implement quantum bits, the elementary unit to store and process quantum information.^{96–103} These so-called persistent current or flux quantum bits (qubits) require an external flux bias $\Phi_{\text{ext}} = \Phi_0(n + \frac{1}{2})$ to operate them at the degeneracy point. Here, $\Phi_0 = h/2e$ is the magnetic flux quantum with the Planck constant $h = 2\pi\hbar$ and the elementary charge e , and n is an integer. This requirement makes flux qubits susceptible to flux noise, which may be introduced through the flux biasing circuitry. Furthermore, to operate a cluster of (coupled) flux qubits, which will inevitably have a spread in parameters, requires an individual and precise flux bias for each qubit. To circumvent this problem, the insertion of π -phase shifters into the flux qubit loop has been suggested.^{24, 37, 104–106} Here, suitable π -coupled Josephson junctions require high critical current densities j_c and high critical current times normal resistance products, $I_c R_n$. Only these devices do not deteriorate the coherence properties when used in superconducting quantum circuits. Potential sources of decoherence are furthermore spin-flip processes in the F layer, which couple excitations of the ferromagnet to the Josephson dynamics. Fluctuations in the magnetic domain structure of the interlayer, which influence I_c , are relevant for active π -junctions, that is when the dynamics of the phase difference across the π -junctions plays a role. Another serious difficulty comes from dissipation due to the excitation of quasiparticles. It has been recently shown that long decoherence times require junctions with both, a high j_c and large normal resistance times area products $R_n \cdot A$.³⁴ This is difficult to be achieved in SFS junctions due to the low resistivity of the metallic F layer. However, we have improved the situation as discussed above by inserting an additional insulating barrier, resulting in a SIFS stack. Here, much higher $R_n \cdot A$ values at modest j_c can be achieved. In particular, underdamped SIFS Josephson junctions can be realized allowing for the study of the dynamics of the junctions. Therefore, there has been strong interest in SIFS junctions.^{107–109,[A2]}

Up to now, the insertion of a SIFS π -junction in a superconducting flux qubit has not been realized, but Feofanov *et al.*⁹⁵ recently introduced a π -junction in a phase qubit. However, since this phase qubit¹¹⁰ exhibits a coherence time of only a few nanoseconds, this experiment solely allows to clarify that the π -junction does not influence the qubit

dynamics on this timescale. Because Feofanov's work only uses a large passive π -junction, which just provides a phase bias and does not influence the dynamics, critical current fluctuations cannot be excluded there. Hence, we analyze the dynamics of the phase difference across JJs with a ferromagnetic interlayer in this work and carefully examine MQB using switching current experiments to exclude low-lying excitations and critical current fluctuations in SIFS junctions.

1.4 Probing the Josephson Dynamics by the Fiske Resonances and Microwave Irradiation

The evolution of the phase difference across a Josephson junction in the zero-voltage state is well characterized by the plasma resonance, which can be illustrated as the resonance of the LC resonator formed by the capacitance C between the electrodes and the Josephson inductance L_J . The plasma resonance with the intrinsic resonance quality $Q_0 = \omega_p RC$ is found at the plasma frequency $\omega_p = \sqrt{2eI_c/\hbar C}$ with the elementary charge e , the reduced Planck constant $\hbar = h/2\pi$, and the junction parameters critical current I_c , junction capacitance C and junction resistance R .¹¹¹ Typically, the important parameter ω_p is determined by microwave spectroscopy or by an analysis of the frequencies of eigen oscillations; Q_0 follows for underdamped junctions from the hysteresis in the current-voltage characteristics (IVCs).

However, the plasma resonance does not necessarily determine the junction dynamics; especially, the dynamics of SIFS JJs may be influenced by excitations in the ferromagnetic interlayer.^{112, 113} Therefore, we examine the dynamics of SIFS junctions at high frequencies up to 400 GHz by a detailed study of the Fiske resonances in this work to fully understand these devices. The Fiske resonances originate from a nonlinear interaction of two intrinsic junction oscillations. We have, on the one hand, the cavity modes of the transmission line resonator formed by the junction geometry. On the other hand, the current across a Josephson junction oscillates with a frequency $\omega_J = 2\pi V/\Phi_0$ when a constant voltage V is applied across the junction (Josephson oscillation). As we will see in section 3.2.3, the nonlinear interaction between the cavity modes and the Josephson oscillation results in the resonant case in self-induced current steps in the IVCs. The resonance quality of the Fiske resonances can be extracted from the detailed shape of these steps, which we evaluate for different applied voltages and hence different resonance frequencies in this thesis. This allows to identify the dominating damping mechanisms: While at low frequencies resistive losses due to quasiparticle damping dominate, we observe surface impedance losses at high frequencies. Moreover, we conclude from the analysis above that the examined SIFS π -junction follows the same physics as classical Josephson tunnel junctions; however, we observe an increased surface impedance damping compared to tunnel junctions, which we attribute to an increased quasiparticle density in the superconducting electrodes due to the inverse proximity effect.

We further examine the dynamics of a SIFS π -junction in this work by irradiating it with microwaves of different frequencies $\omega_{\text{mw}}/2\pi$ and different powers P_{mw} . With these measurements, we undeniably affirm the parameters extracted from the IVCs. Clear resonances are detected. These resonances are reproduced in semi-classical simulations and hence validate today's literature^{114–118}, which suggests that the reported resonant excitation of quantum levels^{119–121} in Josephson junctions can also be understood by classical nonlinear dynamics. We note that today theory already explains a direct quantitative analogy between experimentally reported Rabi oscillations and classical nonlinear dynamics.^{116, 122}

1.5 Experimentally Demonstrating Macroscopic Quantum Behavior

Macroscopic quantum behavior (MQB) has been first addressed in classical Josephson junctions nearly 30 years ago to identify a tunneling process of a macroscopic object.^{123–126} Today, it is possible to directly demonstrate a superposition of macroscopic states^{127–129} and to observe coherent temporal oscillations of macroscopic quantum states in a Josephson junction¹³⁰ or superconducting circuits^{99, 131–133}. However, since these measurements require a cryogenic setup capable of time-resolved microwave spectroscopy and an on-chip circuitry, one still uses the observation of the transition from thermally activated (TA) escape to macroscopic quantum tunneling (MQT) to experimentally verify MQB in new material systems. Hence, MQT has been recently observed in 1d-superconductors (quantum phase slips)^{134–139}, a suspended nanowire forming a weak link between two superconductors¹⁴⁰, dc-SQUIDs representing a system with 2 degrees of freedom^{141, 142}, high- T_c superconductor $\text{Bi}_2\text{Sr}_2\text{Ca}_2\text{Cu}_2\text{O}_{8+\delta}$ junctions and stacks^{143–145}, and $\text{YBa}_2\text{Cu}_3\text{O}_{7-\delta}$ grain boundary junctions^{146–149}.

We come back to Josephson junctions with a ferromagnetic interlayer and mention that there MQB got a lot of attention when Pfeiffer *et al.*¹⁵⁰ and Madek *et al.*¹⁵¹ examined superconductor/insulator/normal metal/ferromagnetic metal/superconductor (SINFS) junctions with a NiCu interlayer and could not observe MQT. The measurements of Krasnov *et al.*¹⁵² and Petković *et al.*¹⁰⁸ did not reach the quantum limit due to a too high temperature. We note that the experiments reported above base on the statistical evaluation of the switching currents I_{sw} , at which a junction switches from the zero-voltage into the voltage state.¹⁵³ The first two experiments observe according to theory that at high temperatures the switching process is dominated by TA escape indicated by a steadily decreasing switching current histogram width with decreasing bath temperature. At low temperatures, they detect a saturation of the histogram width, that is the escape process is temperature independent. The crossover between these regimes is characterized by the crossover temperature T_{exp}^* , which theoretically calculates for the transition from TA escape to MQT in the absence of dissipation to $T_{\text{th}}^* = \hbar\omega_a/2\pi k_B$ ¹⁵⁴ with the Boltzmann constant k_B , the reduced bias current $i_b = I_b/I_c$,

and the attempt frequency $\omega_a = (1 - i_b^2)^{1/4} \omega_p$. However, the experimentally observed and the theoretically expected values T_{exp}^* and T_{th}^* did not agree suggesting that the experiments above do not observe MQT at low temperatures, and hence additional fluctuations play a role. We note that a reduction of the critical current by an applied magnetic field resulted in a decrease of the crossover temperature T_{exp}^* in these experiments. Although this is claimed to prove that the experiments are not limited by noise from the electrical setup, in our feeling this validity check is fault-prone: On the one hand, that is because one usually uses at a lower I_c different measurement parameters for technical reasons (e.g. another current range in the current source, another current ramp, ...) and hence changes the noise properties of the setup. On the other hand, the observation of a reduced T_{exp}^* is not able to assure a good thermalization of the junction, that is, due to the heat dissipated during the measurement, we cannot cool the junction to the bath temperature and extract the lowest junction temperature as the crossover temperature T_{exp}^* . In this case, the lower T_{exp}^* at a lower I_c is explained by less heat dissipation and hence by the lower junction temperature. Evidently, thermal aspects are especially important for ferromagnetic junctions since the critical current densities are there very low resulting in crossover temperatures at the leading edge of today's cooling technology.¹⁵⁵

Excited by these puzzling results, we perform analog experiments using our SIFS junctions. As suggested above, thermal heating and noise present in the measurement and detection setup, apparently originating from the detection electronics, complicated the measurements, possibly analogously to the references above. However, after a careful analysis of potential noise sources, we are able to experimentally demonstrate macroscopic quantum tunneling at the expected temperature by switching experiments within this work. This apparently clarifies, first, that there is no coupling between the Josephson dynamics and low-energy excitations of the ferromagnetic interlayer and, second, that there are no fluctuations of the critical current due to e.g. a dynamic reorientation of the magnetic domain structure of the interlayer. Hence, we doubtlessly prove MQB for SIFS Josephson junctions with a PdNi interlayer. From that we learn that our junctions are well suitable for quantum information processing, on the one hand, as passive π -shifters since no magnetic excitations couple to the junction dynamics. On the other hand, they are also useful as active π -junctions since critical current fluctuations do not play a role.

1.6 Thesis Overview

Before elaborating the important results of this thesis, we introduce the reader in chapter 2 into the elementary theory of weakly coupled superconductors and Josephson junctions. Chapter 3 extends this theory to dynamic properties in the framework of the Stewart-McCumber model and of the Sine-Gordon equation. This allows to understand secondary quantum effects in chapter 4 where macroscopic quantum phenomena are

explained.

In the experimental part, chapter 5 introduces the device fabrication developed within this work and characterizes the respective materials. The quality of the junctions is evaluated thereupon in chapter 6: The dependencies of the critical current on an applied in-plane magnetic field follow a Fraunhofer diffraction pattern, which nicely validates the homogeneity of the junction barriers and the ferromagnetic interlayers. Moreover, the intrinsic junction qualities are large enough for the application of the junctions in quantum information processing and to identify macroscopic quantum tunneling. A more detailed analysis of the intrinsic damping up to frequencies of 400 GHz follows in chapter 7 by a detailed study of the Fiske resonances. Here, the damping mechanisms are quasiparticle damping at low frequencies and surface impedance damping at high frequencies. Chapter 8 supports the parameters found in chapters 6 and 7 by a precise study of the dynamics of a SIFS Josephson junction under strong microwave driving. With these parameters, we calculate the crossover temperature T_{th}^* , below which a JJ is cooled into its quantum mechanical ground state. Experimentally, the corresponding value T_{exp}^* is extracted from switching experiments where one statistically evaluates the switching of a junction from the zero-voltage state into the voltage state at different temperatures (cf. section 8.2). In our case, we observe a perfect agreement between the theoretically expected and the experimentally observed crossover temperatures T_{th}^* and T_{exp}^* and hence demonstrate for the first time macroscopic quantum tunneling in Josephson junctions with a ferromagnetic interlayer. This proves that, on the one hand, a SIFS JJ can be cooled into its quantum mechanical ground state, which testifies that no low-lying excitations couple to the junction dynamics. In other words, the ferromagnetic layer of a SIFS π -junction does not induce noise in superconducting qubits. On the other hand, we prove that fluctuations in the ferromagnetic interlayer do not influence the critical current of a junction, which is a requirement for the application of a SIFS π -junction as an active π -shift element in quantum information processing³² or in RSFQ circuits.

Finally, chapter 9 discusses as an outlook resonances observed in the IVCs of SIFS π Josephson junctions possibly indicating a new type of interaction between the Josephson dynamics and a ferromagnetic excitation. Chapter 10 gives a short conclusion.

Part II

THEORY

Chapter 2

THE DIFFERENT TYPES OF JOSEPHSON JUNCTIONS AND THEIR APPLICATION

A lot of phenomena have been theoretically understood after the elaboration of the principles of quantum physics at the end of the last millennium. Here, one has to name the Bose-Einstein condensation of bosons and -closely related- the Fermi condensation of paired fermions at low temperatures. The latter allowed J. Bardeen, L. N. Cooper, and J. R. Schrieffer (BCS) to microscopically understand superconductors by the condensation of electrons to Cooper-pairs^{156, 157} nearly fifty years after the observation of superconductivity in mercury by H. Kammerlingh-Onnes in 1911¹⁵⁸⁻¹⁶⁰. Since the Cooper-pair condensate occupies a macroscopic ground state, it can be described by a single macroscopic wave function, which is proven by the observation of the fluxoid quantization in a superconducting ring.^{161, 162}

The existence of this macroscopic wave function, which is apart from a gauge transformation well-defined and unique, forms the foundation of superconducting quantum electronics. In contrast to the conventional electronics where charges flow due to applied voltages, the driving force in this type of circuits is the fulfillment of quantization conditions. Besides that, there exist discrete lumped element devices analogously to the resistor and the transistor in today's consumer electronics, which take advantage of this new degree of freedom. These devices are called Josephson junctions (JJs) and essentially weakly couple superconductors. In the classical Josephson tunnel junction treated in section 2.1, the weak coupling of two distinct superconductors is realized via an insulating barrier, but was later found also possible across a constriction or some normal conducting material as explained in section 2.2.¹⁶³ However, we mainly focus on the coupling across a ferromagnetic metal in this work and introduce in section 2.3 a π -coupled JJ with a ferromagnetic interlayer. For convenience, we discuss the possible applications of this device and generally JJs at the end of this chapter in section 2.4 when the reader is familiar to the underlying physics.

2.1 Classical Tunnel Junctions

Classical superconductor/insulator/superconductor (SIS) Josephson tunnel junctions weakly couple two superconductors S_1 and S_2 across an insulating barrier I of the

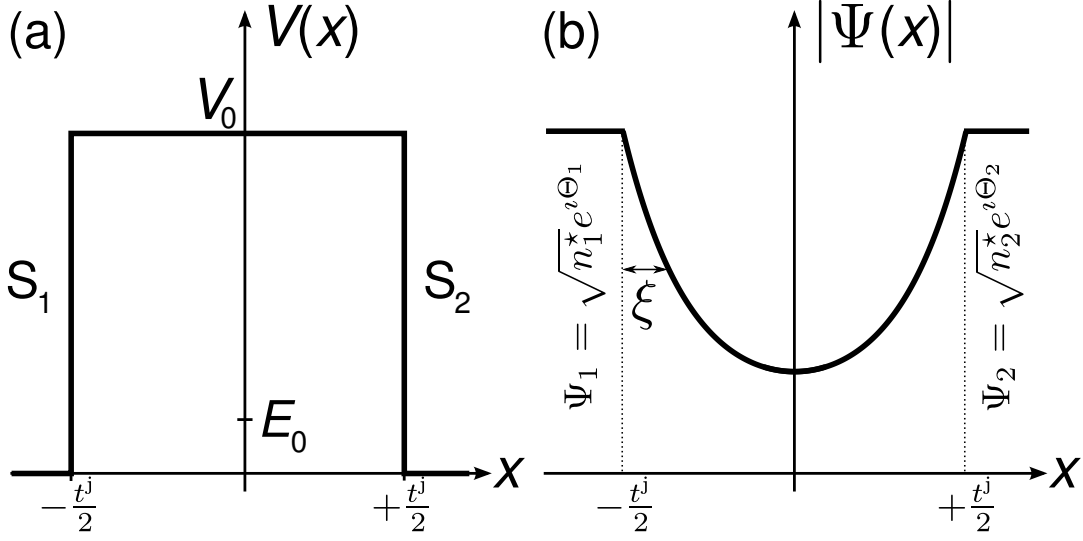


Fig. 2.1: (a) The potential energy $V(x)$ and (b) the magnitude of the wave function $|\Psi(x)|$ versus the position x perpendicular to the barrier for an SIS Josephson tunnel junction (cf. Fig. 3.5). The superconductors S_1 and S_2 are separated by an insulating barrier of the thickness t^j , which we model by a potential of the height V_0 higher than the kinetic energy E_0 of the superelectrons. The constant magnitude of the Cooper-pair wave function inside the superconductor decays exponentially into the insulating barrier. The characteristic decay length ξ is defined by the potential height V_0 and the mass m^* of the Cooper-pairs. (similar to Ref. [164])

thickness t^j . The latter one is modeled by the potential barrier of the height V_0 in Fig. 2.1a. The superconductors are represented by their macroscopic wave functions

$$\begin{aligned}\Psi_1(t) &= \sqrt{n_1^*} e^{i\Theta_1(t)} \quad \text{and} \\ \Psi_2(t) &= \sqrt{n_2^*} e^{i\Theta_2(t)}\end{aligned}\quad (2.1)$$

with n_1^* and n_2^* their Cooper-pair densities and $\Theta_1(t)$ and $\Theta_2(t)$ the phases of their macroscopic wave functions, respectively. These wave functions are coupled across the insulating region ($|x| \leq t^j/2$) of the tunnel junction. We first concentrate on junctions with a small bias current $I_b < I_c$, that is on junctions with a constant phase difference φ between the superconducting electrodes. In this case, we can describe the junction with a single wave function $\Psi(x)$. The absolute value of $\Psi(x)$ is shown in Fig. 2.1b for an SIS junction. Of course, $\Psi(x)$ equals the wave functions Ψ_1 and Ψ_2 in the superconducting electrodes, respectively. The coupling across the barrier region follows the Schrödinger equation

$$-\frac{\hbar^2}{2m^*} \nabla^2 \Psi(x) = (E_0 - V_0) \Psi(x) \quad (2.2)$$

with the kinetic energy E_0 of the superelectrons. $\hbar = h/2\pi$ denotes the reduced Planck constant, and the mass m^* of a Cooper-pair is twice the electron mass m_e . The solution

of Eq. (2.2) can be written as the sum of a growing and a decaying exponential inside the barrier region, or equivalently as¹⁶⁴

$$\Psi(x) = C_1 \cosh \frac{x}{\xi} + C_2 \sinh \frac{x}{\xi} \quad (2.3)$$

with the decay length

$$\xi = \sqrt{\frac{\hbar^2}{2m^*(V_0 - E_0)}}. \quad (2.4)$$

The continuity of the wave function at $x = \pm t^j/2$ determines C_1 and C_2 . Moreover, we identify the electric charge q^* of a Cooper-pair as minus twice the elementary charge e and arrive at the supercurrent density¹⁶⁴

$$j_s = \frac{\hbar q^*}{m^* \xi} \Im(C_1^* C_2) = j_c \sin(\Theta_1 - \Theta_2) \quad (2.5)$$

across the junction with C_1^* the complex conjugate of C_1 and the critical current density

$$j_c = \frac{e\hbar}{m_e \xi} \frac{\sqrt{n_1^* n_2^*}}{\sinh \frac{t^j}{\xi}}. \quad (2.6)$$

In this notation, $\Im(x)$ denotes the imaginary part of x . Here, Equation (2.5) is widely known as the dc or first Josephson equation. Hence, our calculation tells us that a Josephson junction is able to carry a finite supercurrent with a maximal current density j_c , and this current is proportional to the sine of the phase difference across the JJ. Since in typical experimental situations $t^j \gg \xi$, we can approximate $\sinh \frac{t^j}{\xi}$ by $\frac{1}{2} e^{t^j/\xi}$ and observe that the critical current across a superconducting tunnel junction decreases exponentially with the barrier thickness t^j as expected for a tunneling process.^{10–12, 165} To conclude, we have observed electronic transport across an SIS tunnel junction that directly depends on the details of the quantum mechanical wave function describing the superconductors S, that is, we obviously identify coherent transport. This evidently opens the possibility to implement electronics based on the quantum mechanics of electrons, which in our case condense into the macroscopic ground state as Cooper-pairs. We note that by applying a microscopic theory to a tunnel junction geometry, Ambegaokar and Baratoff found a more practical expression than Eq. (2.6).¹⁶⁶ Their equation

$$I_c R_n = \frac{\pi \Delta(T)}{2e} \tanh \left(\frac{\Delta(T)}{2k_B T} \right) \quad (2.7)$$

relates the critical current I_c of a tunnel junction at the temperature T with the gap $\Delta(T)$ of the superconductors and with the normal state resistance R_n of the JJ, which is experimentally well accessible.¹¹¹ k_B denotes the Boltzmann constant.

Exceeding the critical current density j_c , the zero-resistance transport across a JJ is not possible any more. In this case, we have to look at the evolution of the phase

difference across the junction. Here, we have to describe the time-dependent wave function $\Psi_1(t)$ of the superconducting electrode S_1 by the time-dependent Schrödinger equation

$$i\hbar \frac{\partial \Psi_1(t)}{\partial t} = E_1 \Psi_1(t) \quad (2.8)$$

with E_1 the potential energy of the Cooper-pairs in S_1 . Since $\Psi_1(t)$ is an eigenstate, its magnitude $|\Psi_1(t)|$ is time independent, and we can use $\frac{\partial \Psi_1(t)}{\partial t} = |\Psi_1(t)| e^{i\Theta_1(t)} i \frac{\partial \Theta_1(t)}{\partial t}$ to transform Eq. (2.8) to

$$-\hbar \frac{\partial \Theta_1(t)}{\partial t} = E_1, \quad (2.9)$$

which describes the time evolution of the phase for the superconductor S_1 . Subtracting the analog expression for the superconductor S_2 yields

$$-\hbar \frac{\partial (\Theta_1(t) - \Theta_2(t))}{\partial t} = E_1 - E_2. \quad (2.10)$$

Taking into account that the potential energy difference between the superconducting electrodes is given by $E_1 - E_2 = q^* V^\diamond = -2eV^\diamond$ with the voltage V^\diamond applied across the JJ, we arrive at the second or ac Josephson equation

$$2eV^\diamond = \hbar \frac{\partial \varphi(t)}{\partial t} \quad (2.11)$$

with the phase difference $\varphi(t) = \Theta_1(t) - \Theta_2(t)$ across the JJ. Hence, we found in the case of a constant voltage V^\diamond applied across a Josephson junction that the phase difference $\varphi(t)$ between the superconducting electrodes constantly advances at a rate $\frac{\partial \varphi(t)}{\partial t} = \frac{2e}{\hbar} V^\diamond = \frac{2\pi}{\Phi_0} V^\diamond$ with Φ_0 the magnetic flux quantum. Apart from the theoretical importance of the second Josephson equation (2.11), which we will understand later, already this result is very important for precision metrology. There, a microwave signal with the frequency f , which can be accurately generated with today's technology, is coupled into a JJ. Under certain conditions, it phase-locks with the Josephson oscillation, which results in an evolution of the phase difference across the JJ which is defined by the external microwave signal. This provides according to Eq. (2.11) a constant voltage $V(f) \approx 2.068 \mu\text{V}/\text{GHz} \cdot f$ across the JJ, which serves as the voltage standard.^{167–172} However, since not the volt, but the ampere is an SI base unit¹⁷³, a second quantity, e.g. the von-Klitzing constant R_K describing the quantum Hall effect^{174, 175}, is still necessary for the SI-definition.

2.2 Josephson Junctions with a Normal Conducting Interlayer

Despite the coupling of electrons to Cooper-pairs is absent in normal metals, it is known since H. Meissner's pioneer work that a thin ($\approx 1000 \text{ \AA}$) normal slab N separating

two superconductors S_1 and S_2 is able to carry a finite supercurrent from S_1 to S_2 .¹³ In those days, this proximity effect was explained by the leakage of Cooper-pairs into the normal conductor.¹⁷⁶ In detail, it was assumed that the potential between the electrons (of e.g. a Cooper-pair) may be of either sign in a normal metal in proximity to a superconductor depending on a delicate balance between the Coulomb repulsion and the phonon induced attraction.¹⁷⁷ Here, the attraction is defined by the Fröhlich interaction¹⁷⁸, which ties together the electrons to Cooper-pairs in superconductors. However, it was not possible to understand the processes involved in superconductor-normal metal-superconductor (SNS) transport in detail within this theory and to explain the peculiar resonances observed in the IVCs of SNS junctions.

A deeper understanding of the processes appearing in superconductors in the proximity of a normal metal came when A. F. Andreev introduced his theory about the electron reflection on superconductor-normal metal interfaces in 1964.¹⁷⁹ As explained in section 2.2.1, there exists an unusual scattering process on these interfaces, which converts an incident electron into a reflected hole.¹⁸⁰ We apply this mechanism in section 2.2.2 to explain the coherent, ballistic transport over long SNS structures following the theory of I. O. Kulik.¹⁸¹ There, we treat an SNS junction as a quantum well structure where the walls are formed by the energy gap Δ_0 of the superconductors. Here, long junctions represent the case with a few discrete energy levels inside the potential well. Section 2.2.3 expands this theory to the dirty limit where the mean free path of the electrons in the normal metal layer is much less than the thickness of the interlayer. We note that nowadays the Blonder-Tinkham-Klapwijk (BTK) theory^{182–187} is able to describe the whole crossover from high resistance junctions, where the tunneling of Cooper-pairs is responsible for transport (see section 2.1), to highly transparent junctions, which we model by Andreev bound states in this section.¹⁸⁸

2.2.1 The Andreev Reflection

An electron e^- reaching an insulator I from a normal metal N is specularly reflected as schematically illustrated in Fig. 2.2a. However, if we replace the insulator I by a superconductor S, the physics gets unusual. As realized in 1964 by A. F. Andreev¹⁷⁹, a hole h^+ may be reflected into the normal metal instead of the electron leaving behind an additional Cooper-pair inside the superconductor (cf. Fig. 2.2b). The reason for this phenomenon gets clear when one looks into the conserved quantities in the specular reflection on the one hand and in the Andreev reflection on the other hand. The Andreev reflection at an NS interface approximately preserves momentum, while the momentum perpendicular to the interface is inverted in a specular reflection. The explanation for this difference is obvious. While an insulator can exert a significant force on an incident electron, the energy gap Δ_0 of a superconductor is too small compared to the kinetic energy of the electron (approximately the Fermi energy E_F) to significantly change the velocity of the particle.¹⁸⁹ Faced with the challenge of having to reflect a particle without changing its momentum, the only chance for the superconductor is to reflect a

hole. In this case, the momenta of both particles cancel out each other.^{190–192}

We note, moreover, that the wave functions of the incident electron and the reflected hole are correlated. However, this is not strictly true for an electron with the kinetic energy ε above the Fermi energy E_F . There, we observe a reflected hole with the energy ε below the Fermi energy. This results in a transferred momentum $\delta k = k_F \frac{\varepsilon}{E_F}$ between the electron and the hole and hence in an increasing phase difference $\delta\Theta = d \cdot \delta k$ between the Andreev quasiparticles at a distance d from the interface. When the acquired phase difference is of the order of π , the Andreev electron-hole pair has lost its coherence. The coherent transport is not possible any more. We note that the Andreev reflection on a superconductor/ferromagnetic metal interface is qualitatively different from the non-ferromagnetic case because the Andreev reflection is modified by the exchange interaction in the ferromagnet.¹⁹³

Comparing the specular and the Andreev reflection in terms of the charge conservation, we notice that, in contrast to the specular reflection, the Andreev reflection does not conserve the charge. Here, a single correlated Andreev electron-hole pair transfers the charge $-2e$. We note that also the time reversed process, where an electron is reflected for a hole, is possible; it is called inverse Andreev reflection and correspondingly transfers the charge $2e$. Consequently, coherent electronic transport across a normal metal is possible by using the two SN interfaces of an SNS structure as explained in the next section 2.2.2.^{188, 190}

2.2.2 Transport via Andreev Bound States

We analyze the so-called Andreev bound states formed across the interlayer of an SNS junction in this section. As schematically sketched in Fig. 2.3, they are confined by the Andreev (A) and the inverse Andreev (\bar{A}) reflection within the N layer between the superconducting electrodes and this way remind us of the discrete states in a potential well. Hence the Andreev reflection A generates a Cooper-pair while the inverse Andreev reflection \bar{A} annihilates one, we understand the coherent transport of Cooper-pairs across a normal metal by the Andreev bound states.^{188, 190} To quantify this process, we follow below the analytic treatment of I. O. Kulik.¹⁸¹

In Fig. 2.4, we observe the superconducting order parameter in an SNS junction where a normal metal interlayer N is put between the two semi-infinite superconducting

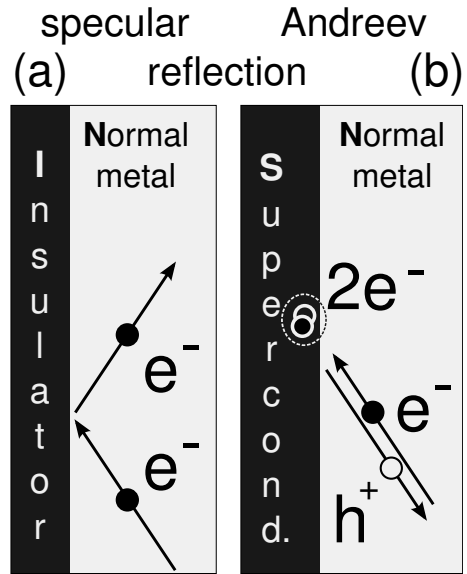


Fig. 2.2: Illustration of the specular (a) and the Andreev (b) reflection of an electron on an NI and an NS interface.

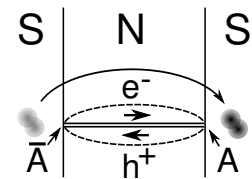


Fig. 2.3: Andreev bound states confined between the SN interfaces.

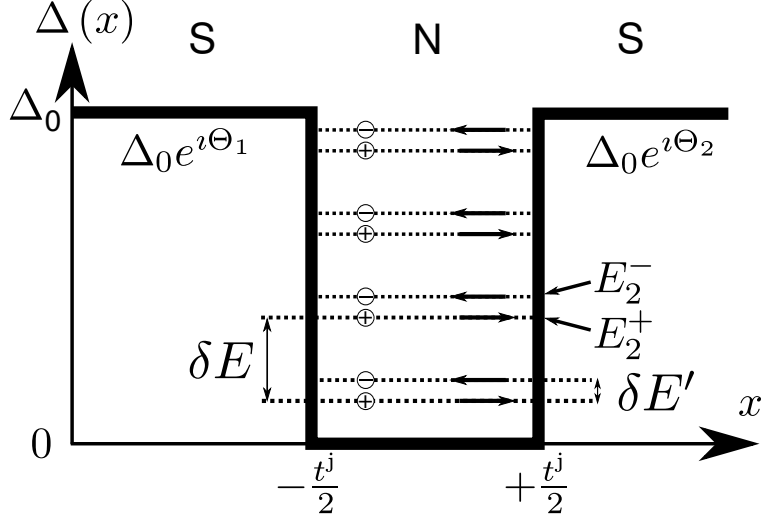


Fig. 2.4: The thick black line represents the superconducting gap $\Delta(x)$ versus the spatial coordinate x in a superconductor-normal metal-superconductor (SNS) structure. Since this setup reminds of a quantum well in the N layer, discrete energy levels appear below the gap energy Δ_0 of the superconductor (dotted lines). The distance between adjacent levels $\delta E = E_+^{n+1} - E_+^n = E_-^{n+1} - E_-^n \simeq \pi E_{\text{Th}}$ is given by the Thouless energy E_{Th} , while the phase difference $0 < \varphi = \Theta_1 - \Theta_2 < \pi/2$ between the phases Θ_1 and Θ_2 of the macroscopic wave functions of the superconductors S_1 and S_2 defines the minor splitting $\delta E' = E_-^n - E_+^n = \varphi E_{\text{Th}}$. The lower energy states (\oplus) are responsible for a current along the phase gradient, while the upper ones (\ominus) establish transport against it. In the special case of SNS junctions, a \oplus -channel is nearest to the Fermi energy, thus has the highest carrier density, and defines the current-phase relation $I = +|I_c| \sin \varphi$. Obviously, we get current transport along the phase gradient and hence a zero-coupled junction. (similar to Ref. [181])

electrodes S at $|x| > t^j/2$; the superconductors are characterized by their energy gap Δ_0 . Here, we concentrate on the ballistic transport across long structures. There, at least a few discrete energy levels are inside the potential well. To calculate the eigenenergies of these states, we start with the Bogoliubov-de Gennes equations^{177, 194}

$$H\vec{\Psi} = E\vec{\Psi}; \quad H = \begin{pmatrix} T & \Delta \\ \Delta^* & -T \end{pmatrix} \quad (2.12)$$

with the kinetic and potential energy operator T acting on the two-component wave function $\vec{\Psi} = \begin{pmatrix} \psi \\ \eta \end{pmatrix}$ describing electrons (ψ) and holes (η).¹⁹⁵ We note that here the off-diagonal terms Δ and Δ^* are related to spin-paired operators, whose non-vanishing expectation values originate from the non-number-conserving BCS variational wave function and related ensembles, and are referred as pair amplitudes.^{196, 197} They measure the strength of the Cooper-pairing and are hence well suited for the characterization of superconductivity. We assume below a pair potential $\Delta = 0$ for $|x| < t^j/2$ and $\Delta = \Delta_0$ for $|x| > t^j/2$ in the superconductors where the energy gap Δ_0 is a material-specific

quantity. The solutions of the Bogoliubov-de Gennes equations of our problem are for low-lying states¹⁸¹

$$\overrightarrow{\Psi}_+ = \left\{ \begin{array}{ll} A_+ e^{ik_0 x} \begin{pmatrix} 1 \\ 0 \end{pmatrix} + B_+ e^{ik_1 x} \begin{pmatrix} 0 \\ 1 \end{pmatrix} & \text{for } |x| < \frac{t^j}{2} \\ C_+ e^{i\lambda_+ (x - \frac{t^j}{2})} \begin{pmatrix} e^{i\Theta_2} \\ \gamma \end{pmatrix} & \text{for } x > \frac{t^j}{2} \\ D_+ e^{i\lambda_- (x + \frac{t^j}{2})} \begin{pmatrix} \gamma \\ e^{-i\Theta_1} \end{pmatrix} & \text{for } x < -\frac{t^j}{2} \end{array} \right\} \quad (2.13)$$

representing excitations moving from left to right ($k_x > 0$) and

$$\overrightarrow{\Psi}_- = \left\{ \begin{array}{ll} A_- e^{-ik_0 x} \begin{pmatrix} 1 \\ 0 \end{pmatrix} + B_- e^{-ik_1 x} \begin{pmatrix} 0 \\ 1 \end{pmatrix} & \text{for } |x| < \frac{t^j}{2} \\ C_- e^{-i\lambda_- (x - \frac{t^j}{2})} \begin{pmatrix} e^{i\Theta_2} \\ \gamma^* \end{pmatrix} & \text{for } x > \frac{t^j}{2} \\ D_- e^{-i\lambda_+ (x + \frac{t^j}{2})} \begin{pmatrix} \gamma^* \\ e^{-i\Theta_1} \end{pmatrix} & \text{for } x < -\frac{t^j}{2} \end{array} \right\} \quad (2.14)$$

for excitations propagating in the opposite direction ($k_x < 0$). Here, we have introduced the parameter $\gamma = \frac{\Delta_0}{E + i\sqrt{\Delta_0^2 - E^2}}$. Θ_1 and Θ_2 are the phases of the macroscopic wave functions describing the superconductors and A_\pm , B_\pm , C_\pm , and D_\pm arbitrary complex numbers.

$$\hbar^2 \lambda_\pm^2 = 2m \left(E_F \pm i\sqrt{\Delta_0^2 - E^2} \right) \quad (2.15)$$

describes the decay of the wave function for a Bogoliubov quasiparticle¹⁹⁸ with the mass m and the energy E in the superconductor with the gap Δ_0 . In contrast to Kulik's treatment, we neglect below the kinetic energy fraction parallel to the junction plane from the beginning. Thus, the wave vectors k_0 and k_1 represent the propagation of electrons and holes, respectively. The continuity of Eqs. (2.13) and (2.14) at $x = \pm t^j/2$ then requires

$$\gamma^2 e^{i(k_0 - k_1)t^j} e^{\pm i\varphi} = 1 \quad (2.16)$$

with $\varphi = \Theta_1 - \Theta_2$ for the energy levels E_n^\pm inside the potential well. Assuming low-lying energy levels ($E_n^\pm \ll \Delta_0$) and accordingly $\arccos \frac{E_n^\pm}{\Delta_0} \simeq \frac{\pi}{2}$ and equating the imaginary part of the exponential in Eq. (2.16) to an integer multiple n of 2π , we finally arrive at the discrete energy levels

$$E_n^\pm = E_{\text{Th}} \left(\pi \left(n + \frac{1}{2} \right) \mp \frac{\varphi}{2} \right) \quad (2.17)$$

with the Thouless energy

$$E_{\text{Th}} = \frac{\hbar v_F}{t^j} \quad (2.18)$$

for the ballistic transport and the Fermi velocity v_F in N.¹⁹⁹

We now calculate the supercurrent across an SNS structure using the energy states E_n^\pm . We do not plan to discuss Kulik's quite theoretical derivation based on Green's

functions^{181, 200}, but rather want to use the crude estimation of J. Bardeen and J. L. Johnson.^{201, 202} They derive the supercurrent flow by Galilean invariance arguments. In detail, they assume a current flow $n_e e v_s$ with the electron density n_e arising from a velocity displacement of the entire SNS system of electrons by v_s and superpose a contribution

$$\propto \sum_n \frac{1}{t^j} e v_F \cdot (f(E_n^+) - f(E_n^-)) \quad (2.19)$$

due to the quasiparticles with the equilibrium occupation $f(E_n^\pm) = (1 + e^{\beta E_n^\pm})^{-1}$ of the states n where $\beta = 1/k_B T$. Provided that the spacing between the energy levels is not much bigger than the thermal energy ($\pi E_{\text{Th}} \lesssim 5k_B T$), this leads for an SNS junction to a current-phase relation

$$j = j_c \sin \varphi \quad (2.20)$$

as for a tunnel junction with the critical current density

$$j_c = \frac{6n_e \hbar e}{m_e t^j} e^{-\frac{2t^j}{\xi_0} \frac{k_B T}{\Delta_0}} \quad (2.21)$$

and the coherence distance ξ_0 of the superconductors. This formula is (apart from the fact that we neglect the penetration of the wave functions into the electrodes) the same as in Kulik's calculation, which uses Green's functions. Hence, Eq. (2.21) predicts an exponential decrease of the critical current I_c of an SNS junction with the interlayer thickness t^j at finite temperatures. Since the junction resistance R_n increases only linearly with t^j , the $I_c R_n$ -product is in contrast to the tunnel junction case not a constant, but decreases nearly exponentially with the barrier thickness t^j .¹¹¹ We note that the occupation of the quasiparticle states rapidly decreases with their energy in the summation Eq. (2.19). Hence, the dominant supercurrent direction is defined by the energetically lowest Andreev bound state, which in our case carries a current along the phase gradient. Consequently, SNS junctions are 0-coupled.

The quality of surfaces plays a major role in SNS junctions. Hence a clean SN interface is difficult to grow in reality, the structures have been between a classical Josephson tunnel junction defined by resistive interfaces and the desired weak link in the early days of SNS junction fabrication. The understanding of the transition between these limits came up in 1982 when T. M. Klapwijk, G. E. Blonder and M. Tinkham published their famous theory about the subharmonic gap structure in superconducting contacts.^{182–187} Since the junctions discussed within this work use an interlayer best described within a dirty limit theory, we give an introduction into diffusive transport in section 2.2.3.

2.2.3 Transport across a Diffusive Normal Metal Interlayer

We have up to now only investigated the ballistic transport across SNS junctions. However, in most N interlayers the electronic transport is best described in the dirty limit where the mean free path ℓ is less than the interlayer thickness t^j . Hence, we

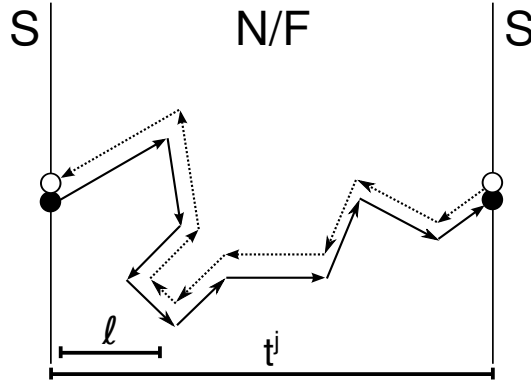


Fig. 2.5: Diffusion of a correlated Andreev electron-hole pair between the two superconducting electrodes of an SNS or an SFS junction. When the mean free path ℓ of the Andreev quasiparticles decreases below the thickness t^j of the normal conducting interlayer, the transport mechanism across the junction is diffusion. The main parameter describing the dynamics is the diffusion constant $D = v_F \ell / 3$ depending on the Fermi velocity v_F and the mean free path ℓ in the interlayer.^{203, 204} We note that the Andreev quasiparticles elastically scatter on impurities, which preserves the phase. This allows for the coherence of an Andreev electron-hole pair since the hole travels back the time-reversed electron path.

want to fathom in this section how the electronic transport in the diffusive regime takes place. Here, the current carrying quasiparticles get multiply elastically scattered as illustrated in Fig. 2.5. These processes preserve the phase, which allows to define coherent Andreev electron-hole pairs where each electron traveling through the normal metal interlayer has its hole counterpart exactly tracing back the time-reversed electron path. Due to this, each correlated electron-hole pair may be formally seen as a Cooper-pair which loses its coherence on its way through the normal metal due to the effects introduced in section 2.2.1. Here, a measure for the remaining correlation is the pair potential.^{205, 206} Unfortunately, the theoretical treatment of this order parameter is quite complicated in diffusive SNS junctions.^{207, 208} Here, one has to use Green's functions, which are generally defined by the Nambu-Gorkov equations.^{195, 209} In contrast to the clean limit where we find a highly anisotropic Fermi surface, electron scattering tends to average out the underlying electronic anisotropy here in the dirty limit situation. This permits the construction of an universal description based on spherical harmonics¹⁹⁶ and is outlined by the Usadel equation²¹⁰. In our case, this equation predicts an order parameter which exponentially decays from the superconductor into the normal metal with the characteristic length scale²⁰⁶

$$\xi_N = \sqrt{\frac{\hbar D}{2\pi k_B T}}. \quad (2.22)$$

This interpretation is illustrated in Fig. 2.6 for an SN interface. Hence, the critical

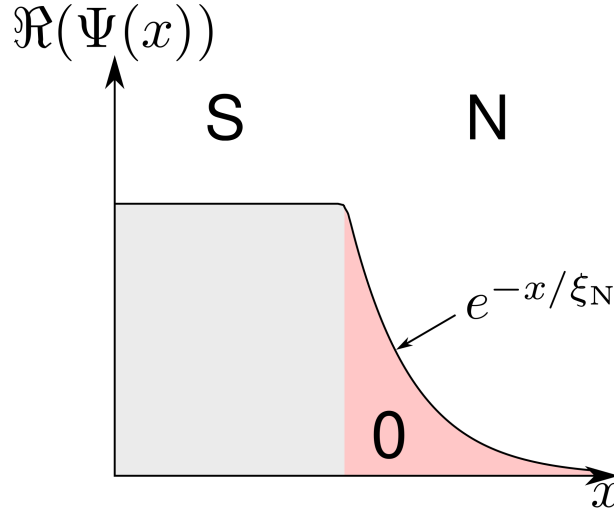


Fig. 2.6: The real part of the order parameter $\Psi(x)$ at an SN interface. While the real part of the order parameter is constant within the superconductor S, it decays exponentially within the normal metal N. The characteristic length scale ξ_N is given by Eq. (2.22). We note that the order parameter never changes sign, so that an SNS junction is always 0-coupled.

current

$$I_c \propto \frac{t^j}{\xi_N} e^{-t^j/\xi_N} \quad (2.23)$$

across an SNS junction reflects the fact that the weakest part of the structure, i.e. the overlap region in the middle, defines the bottleneck for the supercurrent.²¹¹ We note that, in general, the transport across diffusive SNS junctions may also be described by thermally excited bound states. However, since our diffusive regime wipes out the discrete states seen in the clean regime, we have to work with a continuous energy spectrum and a supercurrent density $N_J(\varepsilon)$ for the transport channels. The thermal occupation $h(\varepsilon) = \tanh \frac{\varepsilon}{2k_B T}$ takes into account the transport in electron and hole states with the energy ε above and below the Fermi energy E_F , respectively.^{55, 212, 213} In this formalism, the supercurrent⁵⁵

$$I_s = \frac{1}{eR_n} \int_0^\infty N_J(\varepsilon) h(\varepsilon) d\varepsilon \quad (2.24)$$

across an SNS junction can be calculated by integrating $N_J(\varepsilon)$ weighted with $h(\varepsilon)$. To illustrate this theory, we plot the spectral supercurrent density $N_J(\varepsilon)$ for an SNS junction in red in Fig. 2.7. It is calculated using the Usadel equations²¹⁰ as in Ref. [55] for an applied phase difference of $\pi/2$ across the JJ. Here, the relevant energy scale is again the Thouless energy $E_{Th} = \hbar/\tau$. However, the mean scattering time $\tau = t^j/v_F$ has to be replaced with the diffusion expression $\tau = t^{j^2}/D$ here in the dirty limit. This leads

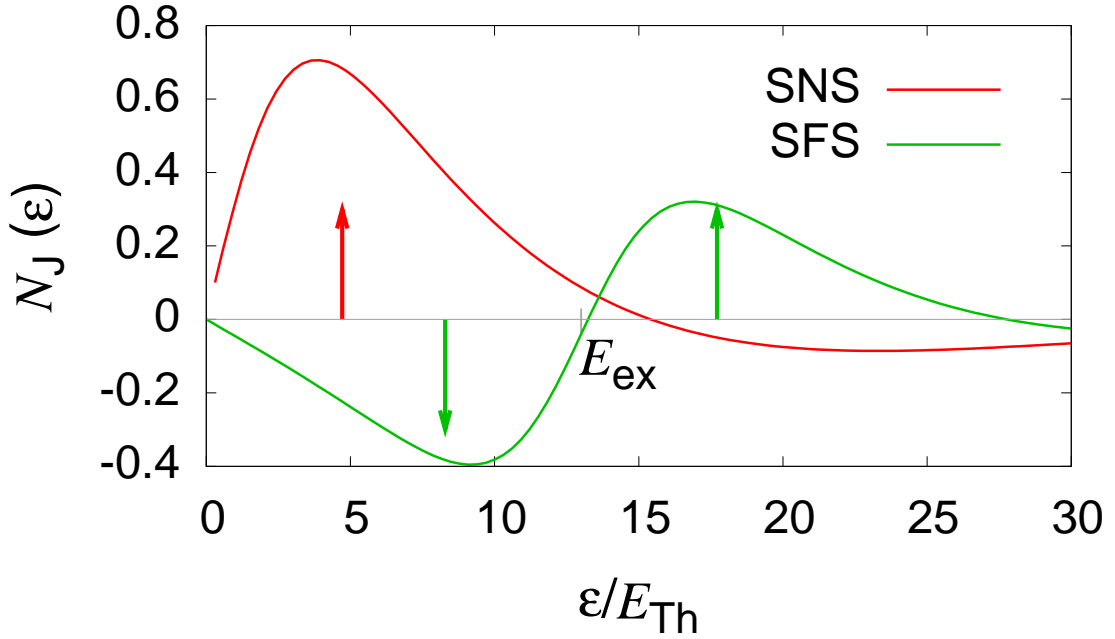


Fig. 2.7: The spectral supercurrent density $N_J(\varepsilon)$ versus the energy ε for long, diffusive SNS and SFS junctions calculated using the formulas in Ref. [55] for an applied phase difference $\varphi = \pi/2$. Following Ref. [55], we take for the SFS case $E_{\text{ex}} = 13 E_{\text{Th}}$ and assume the energy gap Δ_0 much bigger than the Thouless energy E_{Th} . As explained in the text, the discrete energy levels in a clean limit SNS or SFS Josephson junction, which we indicate as arrows, smear out when the interlayer gets into the dirty limit. There, we observe instead of the discrete levels a continuous supercurrent density (solid lines), which can be used to calculate the supercurrent across the JJ by integrating $N_J(\varepsilon)$ weighted by the occupation of the energy levels (see Eq. (2.24)). Hence the electronic transport takes place just above the Fermi level, the negative supercurrent density in the SFS junction for $\varepsilon < E_{\text{ex}}$ leads to a negative Josephson coupling. This results in a Josephson junction with a negative critical current I_c or with a current-phase relation shifted by π . This junction is called π -junction.

to the Thouless energy⁵⁵

$$E_{\text{Th}} = \frac{\hbar D}{t^2} \quad (2.25)$$

in the dirty limit as known from the Anderson localization theory.^{214–216} The red arrow indicates in Fig. 2.7 where the clean limit theory predicts a discrete state by this energy scale. Evidently, this position quite well coincides with the maximum of the supercurrent density illustrating the clear analogy between the clean and the dirty limit theory. Moreover, we observe a decay of the supercurrent with increasing energy due to the loss of the phase coherence in the Andreev pairs as explained in section 2.2.1.

2.3 Josephson Junctions with a Ferromagnetic Interlayer

In this section, we discuss the electronic transport across SFS Josephson junctions with a ferromagnetic metal interlayer F. To do so, we generalize the treatment of the SNS case in section 2.2 and introduce an exchange coupling E_{ex} between the magnetic field of the ferromagnet and the electrons in the interlayer. Analogously to the previous treatment, we first look into long, ballistic Josephson junctions in section 2.3.1 and go over to the diffusive case in section 2.3.2. Finally, we embed the system under discussion in its historical background in section 2.3.3.

2.3.1 Long Ballistic SFS Junctions

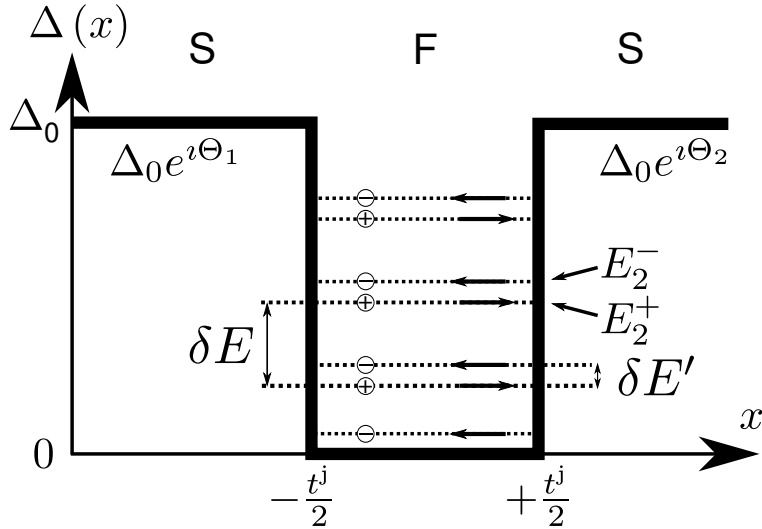


Fig. 2.8: The thick black line represents the superconducting gap $\Delta(x)$ versus the spatial coordinate x in a superconductor-ferromagnetic metal-superconductor (SFS) structure with the exchange energy $E_{\text{ex}} = \frac{\pi}{2}E_{\text{Th}}$ of the ferromagnet and a phase difference $0 < \varphi < \frac{\pi}{2}$ between the superconducting electrodes. Compared to SNS junctions (cf. Fig. 2.4), the discrete energy levels in the interlayer (black dotted lines) are shifted by half the level splitting $\delta E = \pi E_{\text{Th}}$. Since the electronic transport across this structure is dominated by the lowest bound state, which carries a current against the phase gradient between the superconductors (\ominus), this junction is π -coupled.

We have examined Andreev bound states within the normal conducting region of an SNS junction in section 2.2. Here, we extend this theory to the case where this region is ferromagnetic resulting in a level splitting between the spin-up and spin-down subbands. For simplicity, we consider the particular value $E_{\text{ex}} = \frac{\pi}{2}E_{\text{Th}}$ for the exchange coupling, which increases the difference of the wave vectors $k_0 - k_1$ in Eq. (2.16) by $\pm\pi$ shifting

the discrete energy levels in Eq. (2.17) to

$$E_n^\pm = E_{\text{Th}} \left(\pi n \mp \frac{\varphi}{2} \right). \quad (2.26)$$

This situation is illustrated in Fig. 2.8.

With these discrete energy levels in mind, we examine the transport properties of our particular SFS junction. We compare the available transport channels for the two distinct phase differences $\varphi = 0$ and $0 < \varphi < \pi/2$ across our JJ in Fig. 2.9. As expected, we observe a symmetry between currents flowing with (\oplus) and against (\ominus) the phase gradient and hence no net current in the first case. We note, moreover, that the lowest Andreev bound state lies directly on the Fermi level. However, when we now apply a phase difference $0 < \varphi < \pi/2$ across the JJ, the physics gets quite interesting: The bound states responsible for the positive and the negative currents shift downwards and upwards, respectively, analogously to the SNS case. However, here the lowest bound state relocates below the Fermi energy and in this special case does not take part in the electronic transport. Hence, the lowest state just above the Fermi energy carries a current against the phase gradient as shown in Fig. 2.9. Since this transport channel defines the current direction of the whole junction, the current-phase relation of the junction becomes

$$I = -|I_c| \sin \varphi = |I_c| \sin(\varphi + \pi). \quad (2.27)$$

We observe a negative or π Josephson coupling.⁵⁵ We note that by further increasing the exchange coupling, we alternately reach zero- and π -coupled situations. In detail, a zero-coupled junction is formed when the level structure is shifted by an integer multiple n of the level distance πE_{Th} , that is when $E_{\text{ex}} = n\pi E_{\text{Th}}$; π -coupling occurs when $E_{\text{ex}} = (n + 1/2)\pi E_{\text{Th}}$. Because $E_{\text{Th}} \propto 1/t^j$, an oscillating behavior between positive and negative critical currents also occurs with the ferromagnetic layer thickness t^j . This oscillatory behavior can be also identified in the critical current dependence on the ferromagnetic interlayer thickness. However, the coupling type (0 or π) of SFS junctions can only be determined free of doubt in experiments with the junction under test embedded in a superconducting loop.⁷⁰⁻⁷²

2.3.2 Diffusive SFS Junctions

The transition from ballistic to diffusive SFS Josephson junctions can be performed analogously to the SNS case. Here, we have to again take into account the exchange

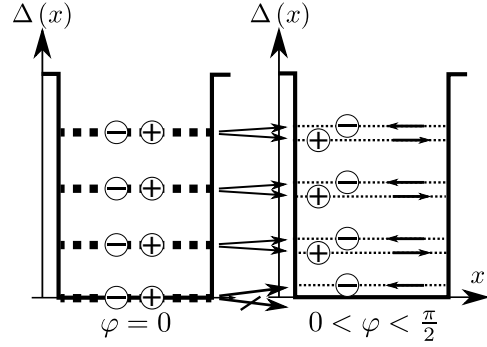


Fig. 2.9: Influence of the phase difference φ on the level structure in an SFS junction as described in the text. (similar to Ref. [55])

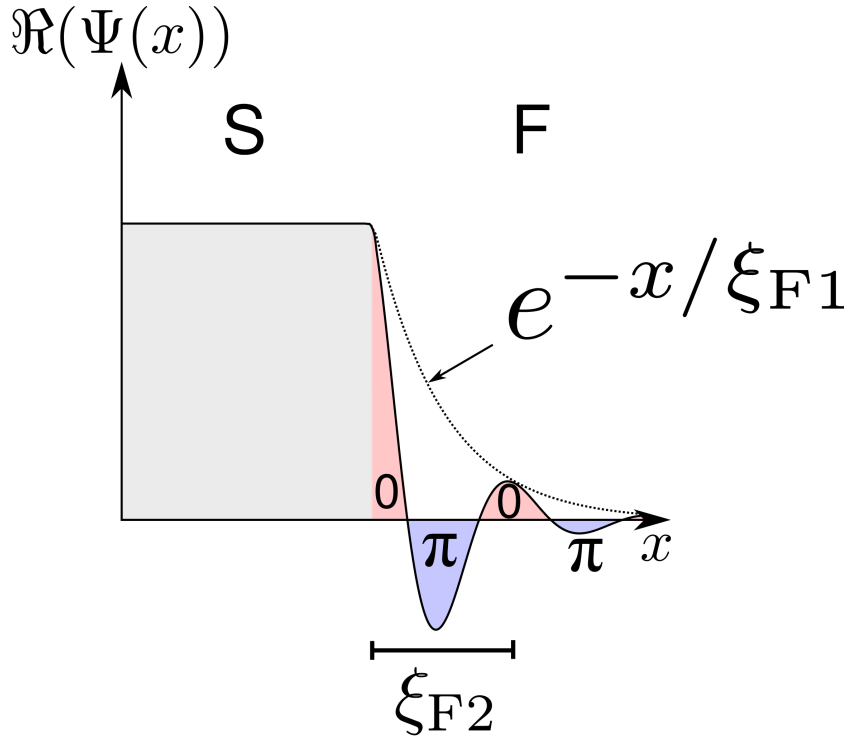


Fig. 2.10: The real part of the order parameter $\Psi(x)$ at an SF interface. We identify a constant order parameter within the superconductor S as in the SN case (cf. Fig. 2.6). However, we do not only observe an exponential decay with the characteristic length scale ξ_N in the F layer as in the SN case, but Eq. (2.28) also predicts in the SF case an additional oscillation with the characteristic length scale $2\pi\xi_{F2}$. This oscillation can particularly change the sign of the order parameter resulting in π -coupling across SFS junctions.

splitting of the spin-up and spin-down subbands in the ferromagnetic interlayer in the Usadel equation (see also the historical review in section 2.3.3). It turns out that this replaces the decay length ξ_N present in SNS junctions (see Eq. (2.22)) with the complex decay constant^{14, 52}

$$\xi_F = (\xi_{F1}^{-1} + i\xi_{F2}^{-1})^{-1} = \sqrt{\frac{\hbar D}{2(\pi k_B T + iE_{ex})}}. \quad (2.28)$$

This decreases the exponential decay length ξ_N (see Eq. (2.22)) to

$$\xi_{F1} = \sqrt{\frac{\hbar D}{\sqrt{E_{ex}^2 + (\pi k_B T)^2} + \pi k_B T}}, \quad (2.29)$$

but first of all introduces an additional oscillation of the order parameter with a period $2\pi\xi_{F2}$ where

$$\xi_{F2} = \sqrt{\frac{\hbar D}{\sqrt{E_{\text{ex}}^2 + (\pi k_B T)^2} - \pi k_B T}}. \quad (2.30)$$

Hence, the order parameter

$$\Psi(x) \propto e^{-x/\xi_F} \propto e^{-x/\xi_{F1}} \cdot e^{-ix/\xi_{F2}} \quad (2.31)$$

at an SF interface can apparently evince a negative real part. This particularly applies for the blue shaded regions in Fig. 2.10, where we illustrate the exponential decay of the order parameter superposed by an additional oscillation at an SF interface. Obviously, when placing a second superconductor in this π -region, one is able to probe the coupling with the resulting SFS junction, and evidently, it will be negative, that is, we observe π -coupling. Within this picture, we easily understand the multiple transitions from zero- to π -coupling and vice versa in SFS junctions with the ferromagnetic interlayer thickness d_F . These transitions are particularly useful to experimentally characterize the coupling by analyzing $I_c(d_F)$ for a series of junctions. Moreover, we point out that for $E_{\text{ex}} \gg k_B T$ the constants ξ_{F1} and ξ_{F2} are equal. However, this is different at elevated temperatures $E_{\text{ex}} \approx k_B T$: Here, the decay length ξ_{F1} increases with decreasing temperature whereas the oscillation period ξ_{F2} decreases. This results in a transition between 0- and π -coupling with the temperature T for a junction with an appropriate d_F .^{14, 51–53}

Of course, we can again analyze the spectral supercurrent density using the Usadel equation⁵⁵, which obviously depends on the exchange energy E_{ex} of the ferromagnet. As an example, we discuss in Fig. 2.7 $N_J(\varepsilon)$ for the value $E_{\text{ex}} = 13 E_{\text{Th}}$. This allows again to compare the supercurrent density calculated for the dirty limit (green line) with the discrete transport channels from the clean limit theory (green arrows) after using the appropriate scattering time, which we have introduced in section 2.2.3. This way, we again clearly understand the diffusive limit of our junctions as the clean limit with wiped out discrete transport channels; especially, we observe a negative Josephson coupling at low energies analogously to the lowest transport channel in the clean case. Since these states are most occupied, they dominate the electronic transport, which exposes the π -coupling of our particular system.

2.3.3 Historical Review: The Fulde-Ferrel Larkin-Ovchinnikov State

We elucidate the historical background of the present work in this section. Josephson junctions with a ferromagnetic interlayer are similar to the Fulde-Ferrel Larkin-Ovchinnikov (FFLO) state.^{16, 40, 41} This state got a lot of attention since it extends the high field limit of superconductivity $B_P = \frac{\Delta_0}{\mu_B \sqrt{2}} \approx 0.71 \frac{\Delta_0}{\mu_B}$ for a superconductor with the gap Δ_0 and the Bohr magneton μ_B discussed by Chandrasekhar and Clogston.^{217, 218}

Here, the applied field B_P destroys the ground state of a superconductor by the paramagnetic or Pauli mechanism.^{219, 220} In the FFLO phase, however, the superconductor lowers its free energy by allowing a spatially inhomogeneous superconducting phase in a magnetic field H . This state corresponds to Cooper-pairs with a finite center of mass momentum in the BCS picture as explained in Fig. 2.11. This momentum causes a periodically modulated order parameter analogously to the one in the ferromagnetic interlayer of an SFS junction.^{52, 221, 222} Inspired by this oscillation effect, the possibility of π -coupling across SFS junctions has been predicted by L. N. Bulaevskii and A. I. Buzdin^{15, 42–44, 223, 224} already more than 25 year ago, but it was only recently when the experience in thin film growth technique as well as material knowledge allowed layers thin enough to experimentally realize a π -coupled SFS Josephson junction. The first observation was achieved in a NiCu material system^{14, 51, 52}; the π -coupling in PdNi junctions, in which the ferromagnetic properties are believed to be more homogeneous as discussed in section 5.3.3, was discovered shortly after that.⁵⁴

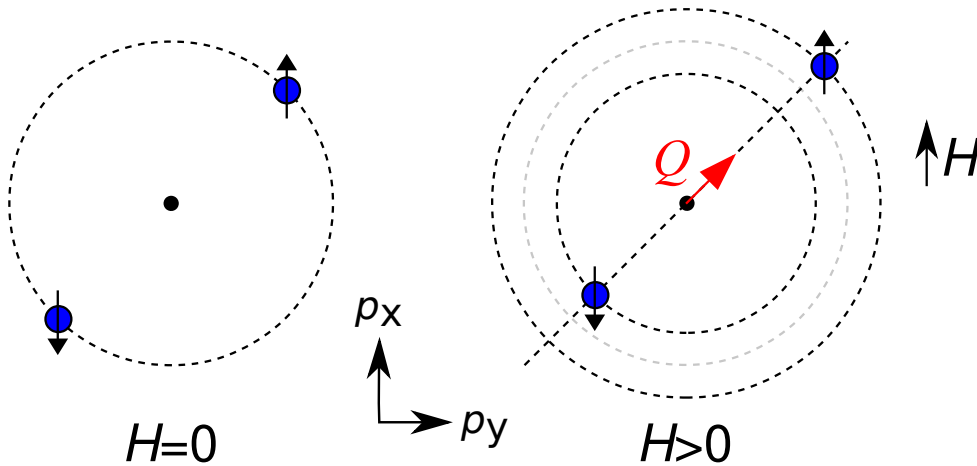


Fig. 2.11: Schematic representation of a Cooper-pair²²⁵ with and without an applied magnetic field in momentum space. The BCS theory describes the formation of Cooper-pairs as an essential ingredient of superconductivity. They are formed at low temperatures when their condensation energy is dominant compared to the thermal energy and condense in a single macroscopic ground state. In the absence of a magnetic field, a Cooper-pair consists of two electrons with opposite spins and opposite momenta. However, if a magnetic field H is applied to Cooper-pairs, the energy of one electron is increased while the energy of the other one is decreased due to the Zeeman coupling²²⁶. The same occurs for the momenta. Hence, summing up the momenta of the electrons leads to a finite center of mass momentum Q of the Cooper-pairs and consequently to a modulation of the wave function of a superconductor in a magnetic field.

2.4 Josephson Junctions, Quantum Electronics and Superconducting Qubits*

It is well known since the famous discovery of the fluxoid quantization in superconducting rings that the wave function describing the Cooper-pair condensate in superconducting loops is well defined.^{161, 162} Already in the 1960s, the idea was born based on this breakthrough to establish conventional computing based on superconducting circuits and Josephson junction devices. Nowadays, this technology uses generation, storage, and transmission of identical single-magnetic-flux-quantum pulses at rates approaching 1 THz. Small asynchronous circuits have already been demonstrated at 770 GHz, and clocked rapid single flux quantum (RSFQ) circuits are expected to exceed 100 GHz.^{82–90} Unfortunately, bias currents are usually necessary for these circuits, but can be superseded by using π -coupled JJs.^{93, 95, 228} In this case, π -junctions without critical current fluctuations are necessary to securely define an RSFQ state. As we see in chapter 8, this work clarifies for our SIFS π -junctions that the thermal and quantum fluctuations of the critical current exceed the ones possibly caused as a dynamic response to instabilities of the magnetic domain structure of the ferromagnetic interlayer at all temperatures. This validates SIFS Josephson junctions as ideal building blocks for RSFQ circuits. However, although RSFQ computing has always promised to be the next generation technology since its development, its computation speed advantage did never compete with the semiconductor CMOS technology⁹¹ because of the necessary cryogenic equipment. Moreover, quantum effects limit the predicted exponential growth over time of the computing power for both technologies, RSFQ and CMOS, in near future.²²⁹ Since these limits are more of a fundamental nature than technological, one needs rather a new concept than a technology improvement.

Scientists believe that this new concept must be based on quantum mechanics. Here, the elementary unit of information is the quantum bit (qubit)^{96, 97}, which physically consists of a quantum two level system with a long coherence time. The basis states of such a system can be denoted as $|0\rangle$ and $|1\rangle$. In contrast to the classical case, the value of a qubit must be denoted as a wave function

$$|\Psi(t)\rangle = a(t) |0\rangle + b(t) |1\rangle$$

with the normalized probabilities $a(t)$ and $b(t)$ of the qubit for being in the state $|0\rangle$ and $|1\rangle$, respectively. The advantage of quantum systems stems from entanglement, which allows for superdense coding and quantum computing.^{227, 230–232} To understand these features, let us compare a system of two classical bits with one of two quantum bits: Two classical bits can only be defined separately, each 0 or 1. In contrast to this, a quantum system shows entanglement. This means the basis states of a two qubit system are $|00\rangle$, $|01\rangle$, $|10\rangle$, and $|11\rangle$. These four states can be occupied separately. Hence, the information stored in n classical bits scales with n while in qubits it scales

* This chapter is partially based on my work Ref. [227].

with 2^n . In addition to the enormous increase of the data storage density compared to classical computers, we can process a superposition of states in quantum gates and hence parallelize computation.²³³ This can be used e.g. in P. Shor's quantum algorithm to factorize numbers²³⁴, whose calculation time scales polynomially with the length of the numbers whereas the best classical algorithm shows an exponential scaling, or in L. Grover's search algorithm, which provides a quadratic speed-up for searching databases.²³⁵

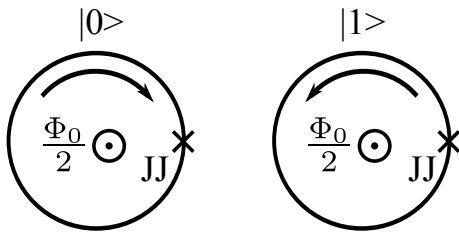


Fig. 2.12: A shielding current running either clockwise or counter-clockwise in an rf-SQUID biased with half a magnetic flux quantum $\Phi_0/2$ serves to represent the states $|0\rangle$ and $|1\rangle$ of a qubit.

However, the question today is which quantum two level system with a long enough coherence time we can use to represent a qubit. Although the factorization of 15 via the Shor algorithm has been demonstrated via a nuclear magnetic resonance experiment on molecules²³⁶, this way seems not feasible for a large scale integration. Looking at this aspect, solid state systems are very promising due to their well-established fabrication technique; especially superconducting systems raise expectations of long coherence times due to their energy gap. Today, one uses there the flux degree of freedom to get immune of the offset charges originating from the substrate. To introduce the basic concept, let us discuss the rf-SQUIDs shown in Fig. 2.12. When one supplies a bias of half a magnetic flux quantum Φ_0 into the SQUID loop, the ground state of this system degenerates due to the fluxoid quantization condition; obviously, it is equivalent from symmetry to fulfill the fluxoid quantization condition by a shielding current running clockwise and one running counter-clockwise. These two states may serve to represent a qubit.^{237–241}

However, it is necessary for the representation of a qubit by a persistent current in an rf-SQUID that the Josephson effect dominates over the electrostatics. Therefore, the geometrical inductance of the SQUID loop and hence the loop area has to be large. Unfortunately, this results in rf-SQUID qubits which are well susceptible to flux noise from stray fields²³⁷ (see also section 1.3). Hence, one uses more elaborate designs today, e.g. persistent current qubits. Here, the single JJ of the rf-SQUID is substituted by three Josephson junctions, two of them with the critical current I_c and a third one with αI_c . Here, the parameter $\alpha \approx 0.8$ allows to fine tune the potential barrier between the qubit states.^{98, 131} But it is even here necessary to supply a bias of half a magnetic flux quantum with a stability better than 10^{-6} into the superconducting loop, which is difficult to be supplied stably and homogeneously enough for a large cluster of qubits.¹⁰⁴ Hence, it would be convenient to circumvent this problem by a π -shift element incorporated into the superconducting ring. These π -shift elements

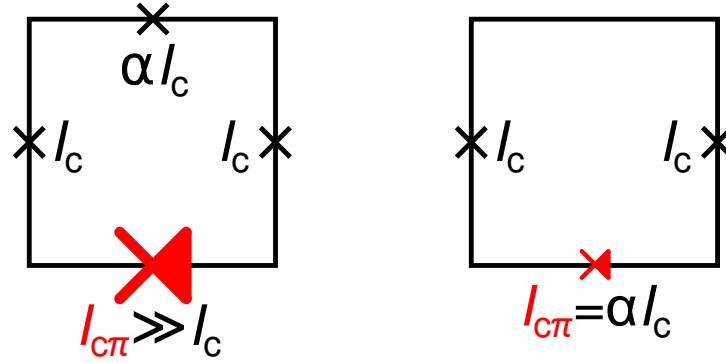


Fig. 2.13: A passive (left) and an active (right) π -junction incorporated into a persistent current qubit allows to shift the working point of this qubit to zero applied flux. In the passive implementation, a large π -junction supplies a constant phase bias of π . Although in this case the qubit does not need an external flux bias and we speak of a “quiet qubit”, in actual experiments the π -junction itself may cause severe decoherence of the qubit.³⁴ In contrast, if the π -junction is introduced as an active Josephson element, it can substitute the small Josephson junction. There, no additional decoherence is introduced by the π -junction.

may be implemented by SIFS Josephson π -junctions. By providing a static phase shift of π , they would allow to operate persistent current qubits in a magnetic field free environment and hence make them immune to flux noise introduced by an external magnetic field bias. Figure 2.13 shows two possible ways of implementation: First, using a single, large, passive π -junction, whose only task is to provide a phase difference of π , and second, replacing the small junction with an active π -junction with similar parameters.

Both, the active and the passive implementation of quiet qubits with π -junctions, can be evaluated in terms of the decoherence the π -shift element introduces into a qubit. The passive implementation was intensively discussed by Kato *et al.*³⁴ It turns out that in this case the relaxation by far dominates the dephasing. While the relaxation time increases with both, the subgap resistance and the critical current of the junction, it is with the present SIFS junctions limited to below 1 μ s. Therefore, it is more promising to use an active π -junction.^{105, 106} Although there should be no additional decoherence introduced by the π -junction in this case, it is technologically more complicated to grow two different types of JJs with defined parameters. We point out that the use of an active Josephson element requires a well-defined critical current.³² Albeit it was speculated that there are critical current fluctuations in SIFS Josephson junctions due to the magnetic properties of the interlayer¹⁵⁰, it is the merit of this work to experimentally verify that no critical current fluctuations influence the dynamics of Josephson junctions with a ferromagnetic interlayer down to the quantum limit of escape. Moreover, this work excludes low-lying excitations in SIFS π -junctions by observing macroscopic quantum behavior. This is important since these excitations would diminish the coherence times in π -biased qubits.

Chapter 3

THE DYNAMIC PROPERTIES OF SMALL JOSEPHSON JUNCTIONS IN AN APPLIED MAGNETIC FIELD

3.1 The Resistively and Capacitively Shunted Junction Model*

A model capable of describing real Josephson junctions should take into account the capacitance C between the two superconducting electrodes. Additionally, thermally excited quasiparticles in the electrodes can propagate across the barrier introducing a quasiparticle resistance R . To describe these effects, W. C. Stewart and D. E. McCumber developed the resistively and capacitively shunted junction (RCSJ) model in 1965.^{242, 243} It models a real Josephson junction by an ideal Josephson element with a critical current I_c in parallel with a capacitance C and a voltage independent normal resistance R as schematically depicted in Fig. 3.1. This leads to a total bias current¹¹¹

$$I_b = I_c \sin \varphi + \frac{V}{R} + C\dot{V} \quad (3.1)$$

across the structure. By substituting the voltage V across the junction via the second Josephson equation (2.11), Eq. (3.1) yields

$$I_b = I_c \sin \varphi + \frac{1}{R} \left(\frac{\Phi_0}{2\pi} \right) \frac{\partial \varphi}{\partial t} + C \left(\frac{\Phi_0}{2\pi} \right) \frac{\partial^2 \varphi}{\partial t^2} \quad (3.2)$$

where Φ_0 denotes the magnetic flux quantum. Equation (3.2) may be illustrated by introducing the “tilted washboard potential”

$$U(\varphi, i_b) = -\frac{\Phi_0}{2\pi} (I_b \varphi + I_c \cos \varphi) = -E_J (i_b \varphi + \cos \varphi) \quad (3.3)$$

with the Josephson energy

$$E_J = \frac{\Phi_0}{2\pi} I_c \quad (3.4)$$

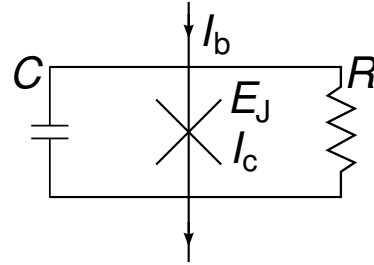


Fig. 3.1: RCSJ model. A Josephson junction is modeled as an ideal Josephson element in parallel to a capacitor C formed by the electrodes and a resistor R describing the quasiparticle tunneling.

* This section is partially based on my work Ref. [227].

and $i_b = I_b/I_c$. Using this potential, Eq. (3.2) reads

$$C \left(\frac{\Phi_0}{2\pi} \right)^2 \frac{\partial^2 \varphi}{\partial t^2} + \frac{1}{R} \left(\frac{\Phi_0}{2\pi} \right)^2 \frac{\partial \varphi}{\partial t} + \frac{d}{d\varphi} U(\varphi, i_b) = 0 \quad (3.5)$$

with the potential $U(\varphi, i_b)$ shown in Fig. 3.2 for a 0-coupled JJ ($I_c > 0$) and a π -coupled JJ ($I_c < 0$). Hence, the dynamics of the phase difference φ across a JJ is in the RCSJ model similar to the one of a phase particle with the mass $m = C(\Phi_0/2\pi)^2$ proportional to the junction capacitance C which moves under the ohmic dissipation $\gamma = (\Phi_0/2\pi)^2/R$ indirectly proportional to the junction resistance R in a tilted washboard potential.

The transition from zero- to π -coupling may be illustrated in the following manor: We look at the cosine potential ($i_b=0$) for a 0-junction in Fig. 3.2 where the phase particle finds its ground state at $\varphi = 2\pi n$ with n an arbitrary integer. There, we continuously reduce the critical current I_c , that is the cosine amplitude, until it gets negative. In this case, the potential minima are found at $\varphi = (2n+1)\pi$, that is, compared to zero-coupled junctions with $I_c > 0$, the potential is shifted by π in the φ -direction. The shift along the y -axis, that is the addition of a constant to the potential, is physically negligible. Tilting the potential is in the π -case analogous to the zero-case. Hence, the dynamics of the phase difference across π -coupled Josephson junctions follows the same physics as across 0-coupled junctions as long as no phase defining condition is given, that is as long as the junction electrodes are not connected to superconductors with a defined phase difference. This is obviously true for the Fiske analysis in chapter 7 and the junction dynamics under microwave irradiation as well as for the quantum properties in chapter 8. Because of this, we will base our argumentation there on zero-coupled junctions. In contrast, the dynamics of superconducting loops containing a π -junction is obviously strongly different from those containing only 0-coupled junctions. This difference sets the main application of π -junctions as π -shift elements in superconducting circuits.

In summary, Eq. (3.5) and the potential in Fig. 3.2 state that the dynamics of the phase difference across 0-coupled as well as π -coupled Josephson junctions follows the same physics apart from a phase shift of π . Both cases can be modeled by a phase particle in a tilted washboard potential. We note that introducing the plasma frequency

$$\omega_p = \sqrt{\frac{2eI_c}{\hbar C}} = \sqrt{\frac{2\pi I_c}{\Phi_0 C}}, \quad (3.6)$$

which is the eigenfrequency of a small amplitude oscillation in a potential minimum of the washboard potential in the absence of a bias current, and the reduced time

$$\tau = \omega_p t \quad (3.7)$$

allows to transform Eq. (3.5) to its dimensionless form¹¹

$$\frac{d^2 \varphi}{d\tau^2} + Q_0^{-1} \frac{d\varphi}{d\tau} + \sin \varphi = i_b. \quad (3.8)$$

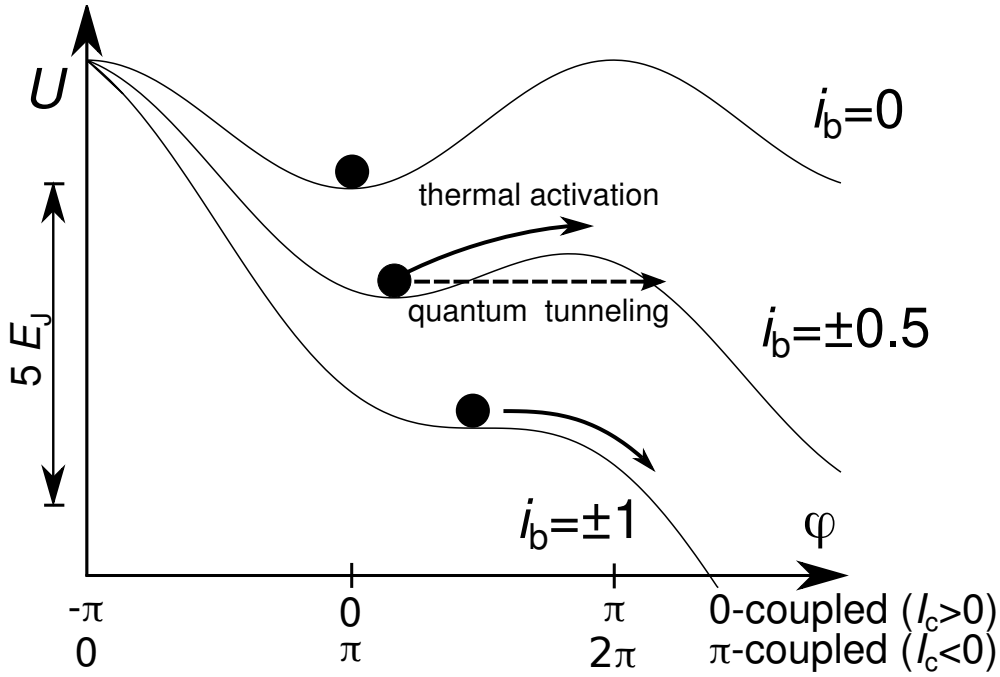


Fig. 3.2: The tilted washboard potential $U(\varphi, i_b)$ versus the phase difference φ for the reduced bias currents $i_b = \pm 0$, $i_b = \pm 0.5$, and $i_b = \pm 1$. Here, the plus-minus sign takes into account that a positive bias current $I_b > 0$ in a π -junction with $I_c < 0$ results in $i_b < 0$. A Josephson junction in the zero-voltage state corresponds to the phase particle trapped in a potential well, while a running particle represents due to the second Josephson equation (2.11) a Josephson junction in the voltage state. The switching from the zero-voltage state into the voltage state can occur due to thermal activation over the barrier (cf. section 4.1) or quantum tunneling through the barrier (cf. section 4.2). Since we later analyze π -junctions, we plot the potential for both configurations—for a classical zero-coupled JJ ($I_c > 0$) and for a π -coupled JJ ($I_c < 0$).

Here, $Q_0 = \omega_p RC$ denotes the plasma resonance quality factor for a bias current free junction. As we will see in section 3.1.1, a hysteresis in the current-voltage characteristics of a junction emerges for high Q_0 values. Also widely used is the Stewart-McCumber parameter $\beta_c = Q_0^2$.¹¹¹ We note that we use the index 0 in Q_0 to clarify that we look at small oscillations in a potential well of the washboard potential with zero tilt (in a bias current free junction). When we later concentrate on oscillations in a junction with the bias current I_b comparable to the critical current I_c in Sections 4 and 8, this restriction gets important. There, we use the values ω_p and Q_0 for the plasma frequency and the resonance quality in junctions without a bias current and ω_a and Q for the corresponding quantities in junctions where a bias current decreases these values.

We note that adding a fluctuating current $I_F(t)$, whose source can be thermal noise

in dissipative elements and other external perturbations, to Eq. (3.2)

$$I_b + I_F(t) = I_c \sin \varphi + \frac{1}{R} \left(\frac{\Phi_0}{2\pi} \right) \frac{\partial \varphi}{\partial t} + C \left(\frac{\Phi_0}{2\pi} \right) \frac{\partial^2 \varphi}{\partial t^2} \quad (3.9)$$

results in an additional wobbling of the tilted washboard potential

$$U(\varphi, i_b) = -E_J \left(\left(i_b + \frac{I_F(t)}{I_c} \right) \varphi + \cos \varphi \right). \quad (3.10)$$

Hence, fluctuations strongly influence the dynamics of Josephson junctions.

3.1.1 Overdamped and Underdamped Josephson Junctions*

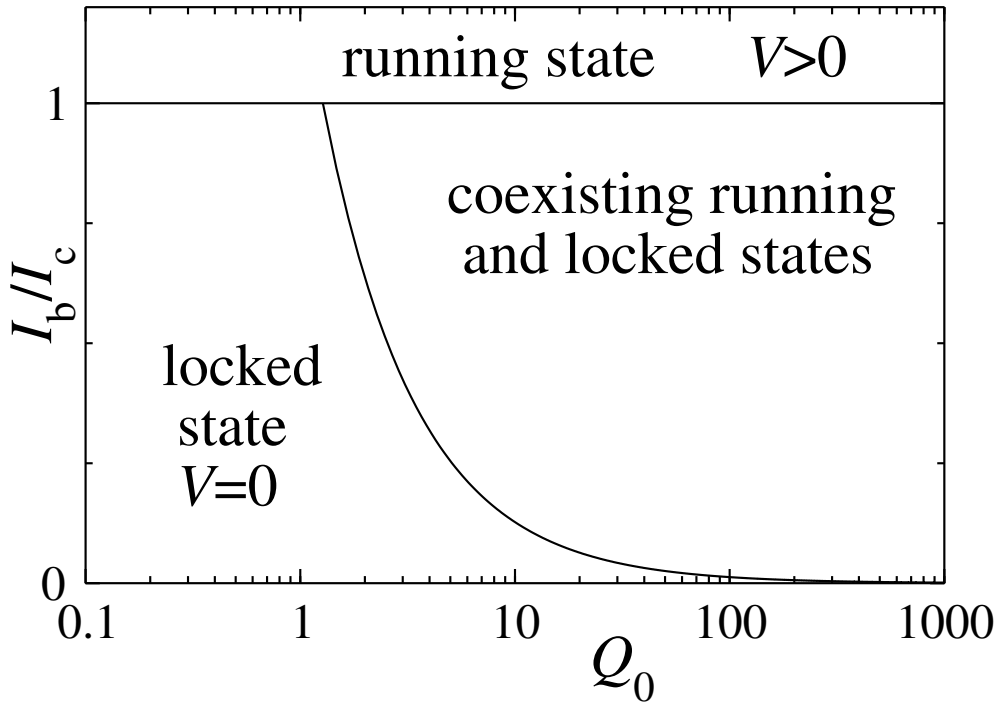


Fig. 3.3: The phase diagram of a Josephson junction described within the RCSJ model. Depending on its reduced bias current $i_b = I_b/I_c$ and its quality factor Q_0 , a Josephson junction is either in the running state or in the locked state. A running particle results in a finite voltage V across the junction which is absent for a locked particle ($V = 0$). There exists a hysteretic region for underdamped junctions ($Q_0 \gg 1$) where their state is determined from history (cf. Eq. (3.11)). (similar to Ref. [227])

We have already seen in section 3.1 that the dynamics of the phase difference across a Josephson junction can be modeled by a phase particle moving in a tilted washboard potential where metastable states exist as depicted in Fig. 3.2. Depending on the intrinsic quality factor Q_0 of the junction and the bias current I_b , the phase particle can be either trapped in a potential well or has enough kinetic energy to overcome the

barriers, respectively. This equals for a JJ either being in the voltage state or in the superconducting state. Figure 3.3 shows which states are possible for a JJ depending on the bias current I_b and the quality factor Q_0 . Evidently, if the bias current across a JJ exceeds the critical one, no metastable states exist, and the JJ is in the running state. The phase continually advances ($d\phi/dt > 0$) inducing a voltage across the junction due to the second Josephson equation (2.11). On the other hand, if no bias current is applied, the potential is not tilted, and there are only stable states. In this case, the phase remains constant ($\phi \simeq \arcsin \frac{I_b}{I_c}$) and no voltage drops across the junction. Finite bias currents below the critical current are more complicated to treat. However, in the case of overdamped junctions ($Q_0 \ll 1$) the viscous damping of the phase particle dominates the inertia. Therefore, no hysteresis exists in these junctions, and we observe a non-hysteretic switching between the running and the locked state at $I_b = I_c$.

Underdamped Josephson junctions strongly differ from the overdamped ones because they exhibit a hysteresis between the critical current I_c , where the junction switches from the zero-voltage into the voltage state, and the retrapping current I_r , where it switches back. A typical IVCs of an underdamped Josephson junction predicted by the RCSJ model is given in Fig. 3.4. Following the Stewart-McCumber model, it is easily understood by the inertia of the phase particle. At the critical current I_c , where the potential wells vanish from the tilted washboard potential, the phase particle escapes from a metastable state. The phase particle acquires enough kinetic energy to overcome even the following barriers, that is the JJ switches into the voltage state. To retrap the particle, one has to reduce the current to the retrapping current^{111, 242}

$$I_r \approx \frac{4I_c}{\pi Q_0} \quad (3.11)$$

to compensate for the inertia. In this case, the JJ switches back to the superconducting state at $I_r < I_c$.

Because of the hysteresis, underdamped Josephson junctions are sensitive to noise originating from the junction wiring. Equation (3.10) shows that these fluctuations wobble the tilted washboard potential. This results in premature switching from the zero-voltage into the voltage state for currents below the critical current I_c and retrapping at currents above the retrapping current I_r , respectively. In detail, the histogram of the switching currents shifts to lower currents and becomes broader.

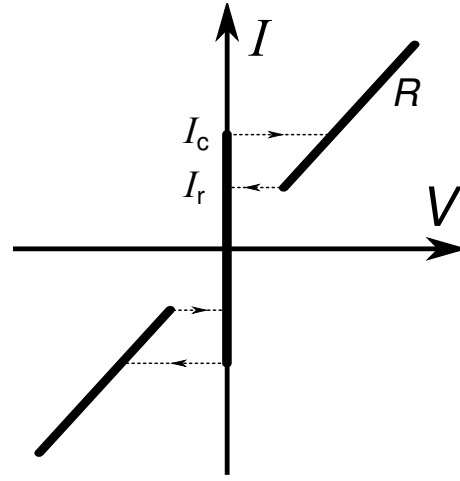


Fig. 3.4: IVCs of an underdamped Josephson junction predicted by the RCSJ model. The junction switches from the superconducting into the voltage state at the critical current I_c and switches back at the retrapping current I_r . In the voltage state, we observe the ohmic resistance R .

3.2 Josephson Junctions beyond the Lumped Element Limit

Josephson junctions can be seen as lumped elements as long as the applied magnetic field is small enough not to spatially modulate the current distribution as explained in section 3.2.1 and their spatial extension is much less than the Josephson penetration depth²³³

$$\lambda_J = \sqrt{\frac{\Phi_0}{2\pi\mu_0 t_B j_c}} \quad (3.12)$$

This value depends on the natural constants magnetic flux quantum Φ_0 and vacuum permeability μ_0 , on the magnetic thickness $t_B = 2\lambda_L + \mu t^j$ of the junction with the relative permeability μ of its barrier and the London penetration depth λ_L of the superconductors, and on the critical current density j_c of the junction. Beyond the lumped element limit, the dynamics of JJs can be described via the Sine-Gordon equation (3.26), which we introduce in section 3.2.2. This equation allows for the detailed understanding of the Fiske resonances, which we introduce in section 3.2.3, and to determine the qualities of the Fiske resonances in section 3.2.4. Sections 3.2.5 and 3.2.6 evaluate corrections to the theory of the Fiske resonances originating from a finite electrode thickness and an overhang region between the bottom electrode and the wiring layer.

3.2.1 Josephson Junctions in an Applied Magnetic Field

The critical current across a (small) Josephson junction of the length L^j and the width W^j depends characteristically on an applied in-plane magnetic field. As we see below, this effect allows to explore the homogeneity of the critical current density across a JJ and hence to evaluate the quality of the junction barrier. To explain the influence of an applied magnetic field, we follow the geometry of Fig. 3.5 below and apply an in-plane magnetic field H_y in the y -direction. This way, we observe a modulation of the gauge invariant phase difference $\varphi(z)$ across the junction in the z -direction.

Because superconductors can be described by a single macroscopic wave function, the accumulated phase Θ along every closed loop inside a superconductor is an integer multiple n of 2π . This also holds true for the yellow loop Υ with the infinitesimal width Δz in Fig. 3.5:²³³

$$\oint_{\Upsilon} \nabla\Theta \cdot d\vec{r} = (\Theta_B - \Theta_A) + (\Theta_C - \Theta_B) + (\Theta_D - \Theta_C) + (\Theta_A - \Theta_D) = 2\pi n \quad (3.13)$$

Here, Θ_x denotes the phase of the superconductor at the point x . By enlarging the integration paths $B \rightarrow C$ and $D \rightarrow A$ deep inside the superconductors, one can neglect the first term in the London equation²⁴⁴

$$\nabla\Theta = \frac{2\pi}{\Phi_0} \left(\Lambda \vec{j}_s + \vec{A} \right) \quad (3.14)$$

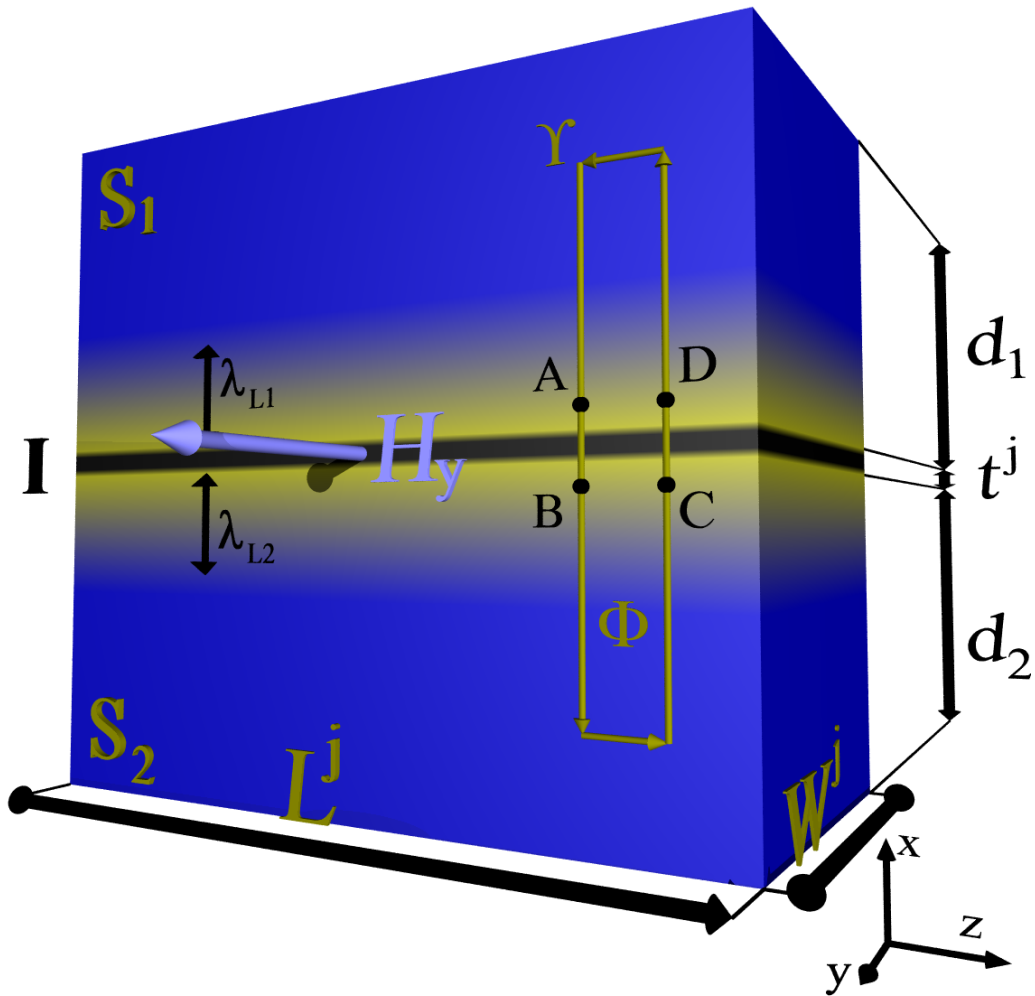


Fig. 3.5: Schematic drawing of an extended Josephson junction with the length L^j and the width W^j . Here, the two superconducting electrodes S_1 and S_2 with the thicknesses d_1 and d_2 are separated by an insulating barrier I with the thickness t^j . Magnetic fields penetrate into the two electrodes S_1 and S_2 up to the London penetration depths λ_{L1} and λ_{L2} . A magnetic field H_y , applied in the y -direction results in the magnetic flux Φ coupled into the area enclosed by the loop Γ .

with the London coefficient Λ , the supercurrent \vec{j}_s , and the vector potential \vec{A} . The phase differences between the points A and B and between C and D are given by the z -dependent gauge invariant phase differences $\varphi(z_{AB})$ and $\varphi(z_{CD})$ at the appropriate intersections z_{AB} and z_{CD} between the barrier and the loop. Summing up all contributions of Eq. (3.13) using Eq. (3.14), one arrives at terms originating from $\varphi(z)$ at the positions z and $z + \Delta z$ and the term $\frac{2\pi}{\Phi_0} \oint_{\Upsilon} \vec{A} \cdot d\vec{r} = \frac{2\pi}{\Phi_0} \Phi(\Delta z)$ coming from the magnetic flux $\Phi(\Delta z)$ coupled into the area enclosed by the contour Υ . Thus, Eq. (3.13) reads²³³

$$\varphi(z + \Delta z) - \varphi(z) = 2\pi n + 2\pi \frac{\Phi(\Delta z)}{\Phi_0}. \quad (3.15)$$

Below, we assume no vortices trapped in the junction ($n = 0$). Hence, the flux inside the area of the size Δz in the z -direction times the magnetic thickness $t_B = \mu t^j + \lambda_{L1} + \lambda_{L2}$ of the junction in the x -direction calculates to

$$\Phi(\Delta z) = \mu_0 H_y \left(\mu t^j + \lambda_{L1} + \lambda_{L2} \right) \Delta z \quad (3.16)$$

with λ_{Ln} the London penetration depth of the superconductor n and H_y the magnetic field applied in the y -direction. Since the magnetic field in a magnetically active barrier with the thickness t^j is enlarged by its relative permeability μ , this region has a major influence on the enclosed flux as taken into account by the first term in the brackets of Eq. (3.16). Here, we have assumed small junctions ($L^j, W^j \ll \lambda_J$), that is, the junction does not shield the magnetic field itself. Finally, substituting Eq. (3.16) into Eq. (3.15) yields²³³

$$\frac{\partial \varphi}{\partial z} = \frac{2\pi}{\Phi_0} \mu_0 H_y \left(\mu t^j + \lambda_{L1} + \lambda_{L2} \right) \equiv k \quad (3.17)$$

in the limit $\Delta z \rightarrow 0$. With this linear increase of the phase difference across the JJ along the z -direction in mind, we integrate the supercurrent²³³

$$\begin{aligned} I_s(\Phi, \varphi_0) &= \int_0^{W^j} dy \int_0^{L^j} dz j_c(z) \sin(kz + \varphi_0) \\ &= W^j \Im \left(e^{i\varphi_0} \int_{-\infty}^{\infty} j_c(z) e^{ikz} dz \right) \end{aligned}$$

with an arbitrary phase φ_0 and a to $\pm\infty$ enlarged integration range in the second line with $j_c(z) = 0$ outside of the junction. Obviously, the maximum supercurrent²³³

$$I_s^m(\Phi) = W^j \left| \int_{-\infty}^{\infty} j_c(z) e^{ikz} dz \right| \quad (3.18)$$

across the junction equals the modulus of the Fourier transform of its critical current density. By putting in the values for our small rectangular Josephson junction with the

length L^j , one ends analogously to the double-slit experiment in optics in the Fraunhofer diffraction pattern^{233, 245}

$$I_s^m(\Phi) = I_c \left| \frac{\sin \frac{kL^j}{2}}{\frac{kL^j}{2}} \right| = I_c \left| \frac{\sin \frac{\pi\Phi}{\Phi_0}}{\frac{\pi\Phi}{\Phi_0}} \right|. \quad (3.19)$$

Here, of course, the total magnetic flux Φ threading a junction with a ferromagnetic barrier is composed of the flux Φ_H due to the applied external magnetic field and the flux Φ_M due to the magnetization of the ferromagnetic layer.

3.2.2 The Time-Dependent Sine-Gordon Equation

The time t evolution of the phase difference $\varphi(z, t)$ across an extended Josephson junction can be described via the Sine-Gordon equation. We consider for its derivation the magnetic field \vec{H} in the junction barrier, which is according to Ampere's law²⁴⁶

$$\nabla \times \vec{H} = \vec{j} + \frac{\partial \vec{D}}{\partial t} \quad (3.20)$$

generated by the supercurrent \vec{j} across the junction and by a time-dependent electric field \vec{D} . Since we are here in the limit where the external magnetic field in the JJ by orders of magnitude exceeds the magnetization of the ferromagnetic interlayer, we use the magnetic field $\vec{H} = \vec{B}/\mu_0$ and the electric field $\vec{D} = \epsilon_r \epsilon_0 \vec{E}$ with the electric and magnetic constants ϵ_0 and μ_0 and the relative permittivity ϵ_r . For simplicity, we assume the transverse magnetic (TM) wave ansatz with $\vec{j}, \vec{D} \parallel x$ and $\vec{H} \parallel y$. This allows to reduce Eq. (3.20) to

$$-\frac{\partial H_y}{\partial z} = j_x + \epsilon_r \epsilon_0 \frac{\partial E_x}{\partial t}. \quad (3.21)$$

By substituting the magnetic field H_y via Eq. (3.17), $E_x = -V_x/t^j$ with V_x the voltage across the barrier, and j_x using the Josephson equations (2.5) and (2.11), we arrive at the condition

$$\frac{\partial^2 \varphi(z, t)}{\partial z^2} - \frac{2\pi}{\Phi_0} t_B \mu_0 \left(j_c \sin \varphi(z, t) + \frac{\epsilon_r \epsilon_0 \Phi_0}{t^j} \frac{\partial \varphi(z, t)}{\partial t} \right) = 0 \quad (3.22)$$

for the gauge invariant phase difference $\varphi(z, t)$. Hence, introducing the Swihart velocity

$$\bar{c} = \sqrt{\frac{t^j}{\mu_0 \epsilon_r \epsilon_0 t_B}} \quad (3.23)$$

and the Josephson penetration depth

$$\lambda_J = \sqrt{\frac{\Phi_0}{2\pi \mu_0 t_B j_c}} \quad (3.24)$$

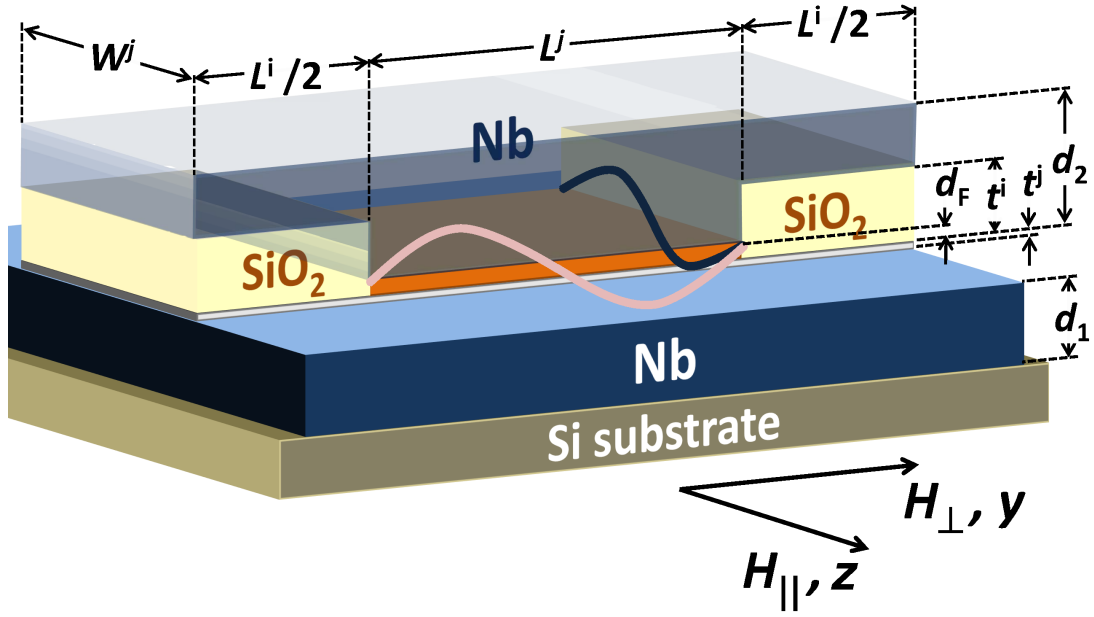


Fig. 3.6: Sketch of the SIFS junction geometry. The junction of the length L^j and the width W^j is formed by the junction electrodes of the thicknesses d_1 and d_2 , which are separated by the tunneling barrier with the thickness t^j and the dielectric constant ϵ^j and the ferromagnetic layer with the thickness d_F . Next to the junction area, there is an overlap of the Nb wiring layer and the base electrode, forming the so-called idle region of the length $L^i/2$ at each side ($L^i =$ a few $10\ \mu\text{m}$ and $W^i \simeq 0$ in our junctions). Both layers are separated by the SiO_2 wiring insulation of the thickness t^i with the dielectric constant ϵ^i . (similar to Ref. [A2])

simplifies Eq. (3.22) to the Sine-Gordon equation²³³

$$\frac{\partial^2 \varphi(z,t)}{\partial z^2} - \frac{1}{c^2} \frac{\partial^2 \varphi(z,t)}{\partial t^2} - \frac{1}{\lambda_J^2} \sin \varphi(z,t) = 0. \quad (3.25)$$

Equation (3.25) can be extended to

$$\frac{\partial^2 \varphi(z,t)}{\partial z^2} - \frac{1}{c^2} \left(\frac{\partial^2 \varphi(z,t)}{\partial t^2} + \frac{1}{R_{\text{sg}} C} \frac{\partial \varphi(z,t)}{\partial t} \right) - \frac{1}{\lambda_J^2} \sin \varphi(z,t) = 0 \quad (3.26)$$

with the junction capacitance $C = \epsilon_r \epsilon_0 A / t^j$ and the junction area A to allow for an additional leakage current $I_q = V_x / R_{\text{sg}}$ in j_x , which damps the junction dynamics.²⁴⁷

3.2.3 The Fiske Resonances

According to the Josephson equations, the supercurrent across a Josephson junction oscillates at a constant frequency $\omega_J = 2\pi V / \Phi_0$ when a constant voltage V is applied

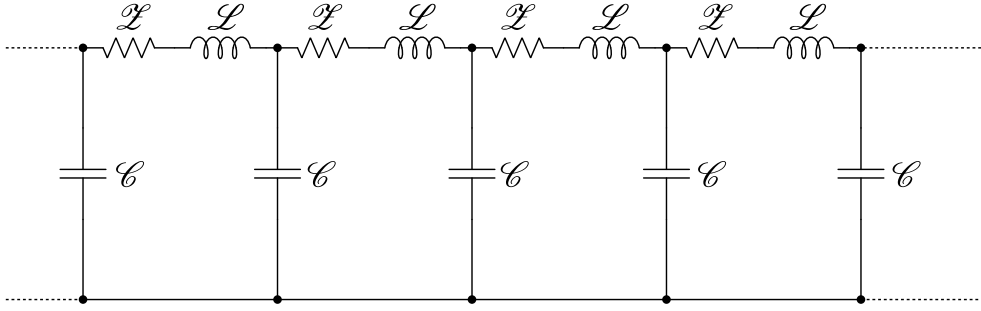


Fig. 3.7: Equivalent circuit of a long Josephson junction. A long Josephson junction may be modeled as an $\mathcal{L}\mathcal{C}$ transmission line with the junction natural capacitance per length \mathcal{C} and the kinetic inductance per length \mathcal{L} . The impedance per length \mathcal{Z} mimics damping.

across the junction.^{10–12} This oscillation can excite the transmission line resonator²⁴⁸ of the length L^j formed by the junction geometry (cf. Fig. 3.6). This resonator can be identified within the lumped element model developed by Eck *et al.*²⁴⁹, which describes the Fiske resonances within the $\mathcal{L}\mathcal{C}$ -resonator model sketched in Fig. 3.7. While the capacitance per length

$$\mathcal{C} = \epsilon_0 \epsilon_r \frac{W^j}{t_j} \quad (3.27)$$

is naturally given by the junction geometry, the kinetic inductance per length \mathcal{L} is not obvious. For its derivation, we use Faraday's law of induction

$$\frac{\partial E_x}{\partial z} \cdot t^j = -\mu_0 \frac{\partial H_y}{\partial t} \cdot t_B \quad (3.28)$$

averaged over the loop Υ in Fig. 3.5. Here, we consider a transverse magnetic (TM) wave ansatz with the electric field \vec{E} across the barrier in the x -direction and the magnetic field \vec{H} in the y -direction perpendicular to the wave propagation along the z -axis. On the other hand, Ampere's law $\nabla \times \vec{H} = \vec{j} + \vec{D}$ relates the magnetic field

$$H_y = I/W^j \quad (3.29)$$

with the current I in the junction. By substituting Eq. (3.29) into Eq. (3.28), we end in the inductance per length

$$\mathcal{L} = \mu_0 \frac{t_B}{W^j}. \quad (3.30)$$

The impedance per length \mathcal{Z} is here only introduced for completeness; however, it is very useful for the understanding of the damping due to the surface resistance.²⁵⁰ Within the lumped element model, the phase velocity of the electromagnetic modes inside our extended Josephson junction calculates to the Swihart velocity²⁵¹

$$\bar{c} = \frac{1}{\sqrt{\mathcal{L}\mathcal{C}}} = c \sqrt{\frac{t^j}{\epsilon_r t_B}} \quad (3.31)$$

with $c = 1/\sqrt{\mu_0\epsilon_0}$ the speed of light in vacuum in agreement with Eq. (3.23). Compared to electromagnetic waves (EMWs) in free space, we observe for our modes the expected slow-downs $\propto 1/\sqrt{\epsilon_r}$ known for EMWs in matter and $\propto \sqrt{t^j/t_B}$ since the magnetic field penetrates the superconducting electrodes while the electric field concentrates across the insulating barrier. Another important quantity our model unveils is the characteristic wave impedance^{247, 251}

$$Z = \sqrt{\frac{\mathcal{L}}{\mathcal{C}}} = Z_0 \sqrt{\frac{1}{\epsilon_r} \frac{\sqrt{t_B t^j}}{W^j}} \quad (3.32)$$

of our Josephson transmission line. Here, $Z_0 = \sqrt{\mu_0/\epsilon_0} \approx 377 \Omega$ is the characteristic wave impedance of free space, the second term gives a small correction due to the dielectric properties of the interlayer, and the most important third term depends on the junction dimensions. Since the magnetic thickness t_B or the barrier thickness t^j are typically three orders of magnitude smaller than the junction diameter, one gets a huge impedance mismatch between the Josephson transmission line and the free space. This results in a nearly perfect reflection of excitations in the JJ transmission line at both junction edges, which defines a cavity with the n -th resonance frequencies²⁵⁰

$$\frac{\omega_n}{2\pi} = n \frac{\bar{c}}{2L^j}. \quad (3.33)$$

At an applied junction voltage

$$V_n = \frac{\omega_n \Phi_0}{2\pi} = n \frac{\Phi_0 \bar{c}}{2L^j} \quad (3.34)$$

the oscillation frequency of the Josephson current matches the n -th harmonic of the junction cavity mode resulting in the excitation of this mode. The excitation of the cavity resonances is most effective if the spatial period of the Josephson current distribution along the junction is about matching the spatial period of the n -th resonant electromagnetic mode of the junction. Since for short junctions the Josephson current density is spatially uniform at zero magnetic field, there is no excitation of the resonant modes. However, a spatial modulation can be easily achieved by applying a magnetic field. The resonance is a highly nonlinear process, which results in self-induced current steps at V_n in the IVCs denoted as Fiske steps.^{247, 252–255,[A2]} A quantitative description of the position and the shape of these resonances in terms of the quality factors Q_n of the n -th harmonic of the Fiske resonance was given by Kulik for classical Josephson tunnel junctions.²⁵⁶ We discuss this theory below in section 3.2.4.

3.2.4 The Quality of the Fiske Resonances

The theoretical treatment of the quality of the Fiske resonances goes back to I. O. Kulik. He first treated the case of resonant modes for low Q junctions characterized by $Q_1 \ll 4\pi^2 \lambda_j^2 / L^j{}^2$ with Q_1 the quality factor of the first Fiske resonance²⁵⁶ and later

extended this theory to arbitrary high Q junctions.²⁵⁷ His treatment for low Q junctions is based on the extended Sine-Gordon equation (3.26).²⁴⁷ He identifies the phase difference

$$\varphi(z, t) = \omega t - kz + \varphi_1(z, t) \quad (3.35)$$

across a Josephson junction as a running wave pattern $\omega t - kz$ with the wave vector $k = \frac{2\pi}{\Phi_0} t_B \mu_0 H_y$ introduced in Eq. (3.17), which is slightly influenced by the Fiske resonances via the term $\varphi_1(z, t)$. The frequency ω is defined via the applied voltage and the second Josephson equation (2.11). This allows to reduce Eq. (3.26) to

$$\frac{\partial^2 \varphi_1(z, t)}{\partial z^2} - \frac{1}{c^2} \left(\frac{\partial^2 \varphi_1(z, t)}{\partial t^2} + \frac{1}{R_{sg} C} \frac{\partial \varphi_1(z, t)}{\partial t} \right) = \frac{1}{\lambda_J^2} \sin(\omega t - kz), \quad (3.36)$$

which can be solved by expanding²⁴⁷

$$\varphi_1(z, t) = \Im \left(\sum_{n=0}^{\infty} g_n e^{i\omega_n t} \cos\left(\frac{n\pi z}{L_j}\right) \right) \quad (3.37)$$

to the junction normal modes ω_n . Here, the complex weight²⁴⁷

$$g_n = \frac{c^2}{\omega^2 \lambda_J^2} \frac{1 - \left(\frac{\omega_n}{\omega}\right)^2 + \frac{i}{Q_n}}{\left(1 - \left(\frac{\omega_n}{\omega}\right)^2\right)^2 + \frac{1}{Q_n^2}} (B_n(k) - iC_n(k)) \quad (3.38)$$

with the functions

$$B_n(k) = \frac{2}{L_j} \int_0^{L_j} dz \cos\left(\frac{n\pi z}{L_j}\right) \cos(kz), \quad (3.39)$$

$$C_n(k) = \frac{2}{L_j} \int_0^{L_j} dz \cos\left(\frac{n\pi z}{L_j}\right) \sin(kz) \quad \text{and} \quad (3.40)$$

$$Q_n = \omega_n R_{sg} C \quad (3.41)$$

of each mode n is evaluated by substituting Eq. (3.37) into the extended Sine-Gordon equation (3.26). This allows to estimate the time averaged supercurrent

$$\begin{aligned} \Delta I(V_0, H_y) &= \lim_{T \rightarrow \infty} \frac{1}{T} \int_0^T dt \frac{1}{L_j} \int_0^{L_j} I_c \sin(\omega t - kz + \varphi_1(z, t)) dz \\ &\simeq \lim_{T \rightarrow \infty} \frac{1}{T} \int_0^T dt \frac{1}{L_j} \int_0^{L_j} I_c \cos(\omega t - kz) \varphi_1(z, t) dz \end{aligned}$$

generated by the Fiske resonances in the low quality limit ($\sin \varphi_1 \simeq \varphi_1$). The result²⁴⁷

$$\Delta I(V_0, \phi) = I_c \left(\frac{L_j}{\lambda_J}\right)^2 \frac{1}{4\pi^2 n^2} \sum_{n=0}^{\infty} \frac{Q_n^{-1}}{\left(1 - \left(\frac{V_n}{V}\right)^2\right)^2 + \frac{1}{Q_n^2}} F_n^2(\phi) \quad (3.42)$$

with $\phi = \frac{\Phi}{\Phi_0}$ and

$$F_n^2(\phi) = \left(\frac{2\phi \sin\left(\pi\phi - \frac{n\pi}{2}\right)}{\phi + \frac{n}{2} \pi\phi - \frac{n\pi}{2}} \right)^2 \quad (3.43)$$

describes the magnetic field dependence of the current step height of the n -th resonance and the maximum current step height

$$\Delta I_n(\phi_n^{\max}) = I_c \left(\frac{L^j}{\lambda_J} \right)^2 \frac{Q_n}{4\pi^2 n^2} F_n^2(\phi_n^{\max}). \quad (3.44)$$

At higher Q_n values ($Q_1 \sim 4\pi^2 \lambda_J^2 / L^j^2$), the approximation $\sin \phi_1 \approx \phi_1$ is not valid any more. Here, the maximum current generated by the Fiske resonances is limited by nonlinear effects.¹⁶³ However, no analytic formula is known for the current step height dependence in this limit. Despite that, the quality factor Q_n of the n -th resonance can be calculated by the following procedure:²⁵⁷ The Fiske oscillation amplitude a is defined via the implicit equation²⁴⁷

$$\Delta I_n(\phi) = I_c J_0 \left(\frac{a}{2} \right) J_1 \left(\frac{a}{2} \right) F_n(\phi) \quad (3.45)$$

with J_m the Bessel function of the first kind and order m . The quality factor Q_n can then be extracted from²⁵⁸

$$J_0^2 \left(\frac{a}{2} \right) = \frac{a}{Z_n F_n} \quad \text{and} \quad Z_n = \left(\frac{L^j}{\lambda_J} \right)^2 \frac{Q_n}{n^2 \pi^2} \quad (3.46)$$

A numerical evaluation of the dependence of $\Delta I_n(\phi) / I_c F_n(\phi)$ on $Z_n F_n(\phi)$ is given in Fig. 3.8.

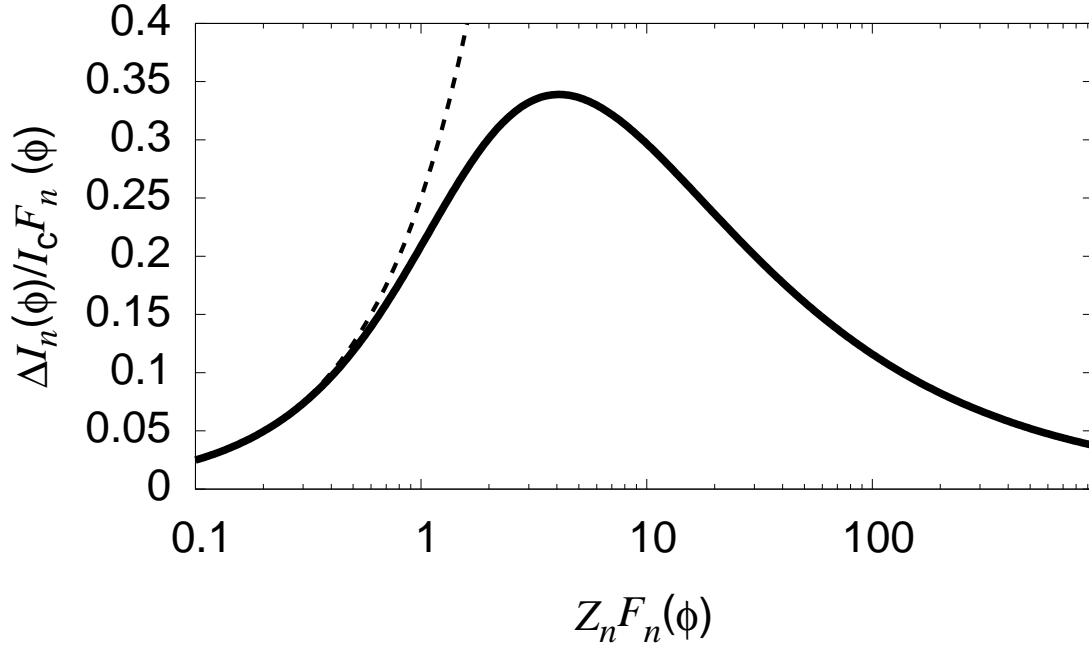


Fig. 3.8: The height $\Delta I_n(\phi)$ of the n -th Fiske current step normalized to $I_c F_n(\phi)$ versus $Z_n F_n(\phi)$. The solid line represents the step height calculated by the algorithm introduced by Eqs. (3.45) and (3.46), while the dashed line is analytically calculated for low Q resonances. (similar to Refs. [163] and [258])

3.2.5 Effective Magnetic Thickness[†]

In our experiments, we use Josephson junctions with an electrode thickness of the order of the London penetration depth λ_L . This results in a modification of the junction properties in an applied magnetic field and of the junction eigen resonances, which we discuss within this section.

It is well known that a magnetic field applied parallel to the surface of a bulk superconductor decays exponentially inside the superconductor due to the Meißner effect.¹¹¹ The characteristic screening length is the London penetration depth λ_L , which is about 90 nm for sputtered niobium thin films.²⁵⁹ However, we are using a bottom niobium electrode of the thickness $d_{1,\text{Nb}} = 85$ nm in our junctions as we discuss in chapter 5. In such a thin film superconductor, the magnetic field perpendicular to the film (x -direction) is obtained to

$$H(x) = \frac{H_{\text{ext},1} + H_{\text{ext},2}}{2} \frac{\cosh(x/\lambda_L)}{\cosh(d/2\lambda_L)} - \frac{H_{\text{ext},1} - H_{\text{ext},2}}{2} \frac{\sinh(x/\lambda_L)}{\sinh(d/2\lambda_L)} \quad (3.47)$$

[†] This chapter is based on the publication Ref. [A2].

by solving the London equations.¹¹¹ Here, the film is assumed to extend from $-d/2$ to $+d/2$, and $H_{\text{ext},1}$ and $H_{\text{ext},2}$ are the external magnetic fields applied parallel to the film at both sides. The boundary conditions and the resulting current distributions are different for different physical situations. We have to distinguish for our Josephson junctions between two cases: On the one hand, we look on the critical current in an externally applied magnetic field; in this case, the magnetic field is applied on both sides of the electrodes. On the other hand, the magnetic field generated by internal junction resonances (cf. sections 3.2.2, 3.2.3 and 3.2.4) penetrates the electrodes only from one side.

We first discuss the case where internal junction resonances generate the field between the superconducting electrodes; here, we assume $H_{\text{ext},1} = H_0$ and $H_{\text{ext},2} = 0$ for both electrodes. At an electrode thickness $d < \lambda_L$, screening currents are confined to a length scale smaller than λ_L , resulting in an enhanced kinetic inductance $L_s = \mu_0 \lambda_L \coth(d/\lambda_L)$ as compared to a bulk superconductor with $L_s = \mu_0 \lambda_L$. That is, the thin film superconductor behaves equivalent to the bulk one with an effective screening length $\lambda_L \coth(d/\lambda_L)$. Then, the magnetic penetration in the barrier layer and the junction electrodes can be described by the effective magnetic thickness

$$t_B^j = t^j + \mu d_F + \lambda_{L1} \coth \frac{d_1}{\lambda_{L1}} + \lambda_{L2} \coth \frac{d_2}{\lambda_{L2}}. \quad (3.48)$$

Compared to section 3.2, we already distinguish here between the thickness t^j of the oxide barrier and the thickness d_F of the F layer; d_1 and d_2 are the thicknesses of the Nb junction electrodes and λ_{L1} and λ_{L2} the corresponding penetration depths. For our junctions, we have $t^j = 4$ nm (we assume for simplicity that the oxide thickness is equal to the thickness of the Al layer), $d_1 = 85$ nm, $d_2 = 250$ nm, $\lambda_{L1} = \lambda_{L2} = \lambda_{\text{Nb}} = 90$ nm²⁵⁹, $d_F = 8.4$ nm and $\mu = 1.8$ resulting in $t_B \simeq 230$ nm. We note that Swihart has addressed the same situation by solving Maxwell's equations for the same geometry.²⁵⁰ In contrast to the treatment above, this ansatz is quite formal; however, it points out that Eq. (3.48) assumes a very thin barrier.

The other interesting situation is the junction embedded in a homogeneous magnetic field. Here, $H_{\text{ext},1} = H_{\text{ext},2} = H_0$ and hence $H(x) = H_0 \cosh(x/\lambda_L) / \cosh(d/2\lambda_L)$. This case particularly applies when we are measuring the dependence of the junction critical current on a magnetic field applied parallel to the junction electrodes. Since the junction (we are considering only short junctions here) cannot screen the applied field from the region between the junction electrodes, the same field is present at both surfaces of the junction electrodes. To derive an effective magnetic thickness for this situation, we consider the total flux threading the junction. The latter is obtained by integrating Eq. (3.47) along the x -direction. Whereas $\int H(x) dx = 2H_0 \lambda_L$ for bulk electrodes ($d \gg \lambda_L$), for thin film electrodes we obtain $\int H(x) dx = 2H_0 \lambda_L \tanh(d/2\lambda_L)$. That is, regarding the flux the thin film superconductor behaves equivalently to the bulk one with an effective screening length $\lambda_L \tanh(d/2\lambda_L)$. Then, we can use the effective

magnetic thickness²⁶⁰

$$\tilde{t}_B^j = t^j + \mu d_F + \lambda_{L1} \tanh \frac{d_1}{2\lambda_{L1}} + \lambda_{L2} \tanh \frac{d_2}{2\lambda_{L2}} \quad (3.49)$$

for the description of the total flux threading the junction.

3.2.6 Effective Swihart Velocity and Frequencies of Resonant Modes[‡]

We discuss the so-called idle region of a Josephson junction in this section, that is the region where the wiring layer overlaps the base electrode due to fabrication details (cf. Fig. 3.6). This region influences the dynamic properties of the junction. The reason is that the idle region acts as a dispersive transmission line in parallel with the junction or loads the Josephson transmission line at its ends. Hence, the resonance frequencies and corresponding voltages are shifted for a junction with an idle region. We evaluate this shift below.

We first discuss the effect of a lateral idle region extending parallel to the resonant mode. In this case, we have to consider the junction transmission line in parallel with the two transmission lines of the idle regions at both sides of the junction where we from now on use t^i and t_B^i for the appropriate thicknesses to distinguish from the respective quantities t^j and t_B^j in the junction. As derived in section 3.2.3, we can assign the inductance $\mathcal{L}^{i,j} = \mu_0 t_B^{i,j} / W^{i,j}$ and capacitance $\mathcal{C}^{i,j} = \epsilon_0 \epsilon^{i,j} W^{i,j} / t^{i,j}$ each per unit length to both isolated transmission lines where the indices i and j refer to the idle and junction region. The corresponding phase velocities are $v_{\text{ph}}^{i,j} = \sqrt{\mathcal{L}^{i,j} \mathcal{C}^{i,j}}$ with $v_{\text{ph}}^j = \bar{c}$. The phase velocity of the combined transmission lines is given by $v_{\text{ph}} = 1 / \sqrt{\mathcal{L} \mathcal{C}}$ with $\mathcal{L}^{-1} = (\mathcal{L}^i)^{-1} + (\mathcal{L}^j)^{-1}$ and $\mathcal{C} = \mathcal{C}^i + \mathcal{C}^j$. Evidently, the idle region increases the capacitance and decreases the inductance per unit length. However, the inductance effect is dominant since usually $t_B^j / t_B^i \gg t^j / t^i$. This is true also for our samples. Therefore, the phase velocity is increased by the idle region. A more detailed analysis yields^{261–263}

$$v_{\text{ph}} = \bar{c} \sqrt{\frac{1 + \frac{t_B^j}{t_B^i} \frac{W^i}{W^j}}{1 + \frac{j \epsilon^i}{i \epsilon^j} \frac{W^i}{W^j}}}. \quad (3.50)$$

We next discuss the effect of a longitudinal idle region extending perpendicular to the resonant mode. In this situation, the idle region can be considered as a lumped capacitance loading the junction at its ends since the wave length usually is much larger than the dimension of the idle region. For short junctions ($L^j, W^j \ll \lambda_j$) detailed calculations yield²⁶³

$$v_{\text{ph}} = \bar{c} \frac{1}{1 + 4 \left(\sqrt{\frac{C_1}{C_0} + 1} - 1 \right)}. \quad (3.51)$$

[‡] This chapter is based on the publication Ref. [A2].

Here, C_1 is the lumped load capacitance and C_0 the total junction capacitance. We see that the effect of C_1 is to decrease the phase velocity. However, since usually $t^i/\epsilon^i \gg t^j/\epsilon^j$ we have $C_1 \ll C_0$, that is, the effect is quite small even if the idle region has a similar area as the junction. With $t^i = 50$ nm, $\epsilon^i \simeq 3.9$, $t^j = 2$ nm, $\epsilon^j \simeq 9.1$, $t_B^j \simeq 230$ nm, $t_B^i \simeq 260$ nm, and $W^i/W^j = 0.8$ (typical for a $50 \times 50 \mu\text{m}^2$ junction) we estimate $v_{\text{ph}} \simeq 1.22 \bar{c}$ for the lateral and $v_{\text{ph}} \simeq 0.95 \bar{c}$ for the longitudinal mode.

Chapter 4

THE ESCAPE OF THE PHASE PARTICLE FROM A METASTABLE STATE IN THE TILTED WASHBOARD POTENTIAL*

The dynamics of lumped element Josephson junctions can be modeled by a phase particle in a tilted washboard potential as explained in section 3.1. There exist metastable states in this potential where the phase particle may be trapped; a trapped particle equals a JJ in the zero voltage state. The phase particle can escape from a metastable state by thermal activation (TA) at high temperatures or by macroscopic quantum tunneling (MQT) at low temperatures. Here, the escape of the phase particle equals the switching of the JJ from the zero-voltage into the voltage state. In the following sections 4.1 and 4.2, we theoretically analyze both processes, TA and MQT, following Ref. [227] and calculate in section 4.3 the theoretically expected crossover temperature T^* , below which quantum tunneling dominates thermal escape. We note that the crossover temperature T^* of a JJ is mainly defined by the plasma frequency ω_p , which can be experimentally determined from an analysis of the Fiske resonances or from microwave spectroscopy experiments as we discuss in section 4.4.

We point out that although for Josephson tunnel junctions the transition from TA to MQT has been observed more than twenty years ago^{123, 124, 153}, it is nevertheless important to verify the quantum behavior of π -coupled Josephson junctions with a ferromagnetic interlayer. This allows to exclude low-lying resonances destroying the coherence in quantum circuits based on SIFS π JJs and to examine critical current fluctuations due to a fluctuating magnetic domain structure of the interlayer.^{264, 265} We note that it was recently claimed that the quantum limit in JJs containing a NiCu interlayer can not be reached.^{150, 151}

4.1 *Thermally Activated Escape**

A metastable state is defined by a local minimum in a potential landscape, which is separated from a lower energy state by a potential barrier. A necessary condition for its temporary stability is that this barrier is large compared to the thermal energy. In this

* This chapter is partially based on my work Ref. [227].

section we clarify what happens if this limit is not strictly valid. To do so, we give a short introduction to the intuitive transition-state theory (TST) in section 4.1.1. This theory describes the escape of a particle out of a metastable state without dissipation. To evaluate the escape with ohmic damping, we go over to Kramers' theory in section 4.1.2. Section 4.1.3 applies Kramers' theory to underdamped Josephson junctions.

4.1.1 The Transition-State Theory*

Before using Kramers' theory to analyze the escape out of a metastable state, let us first use the less complex transition-state ansatz.²⁶⁶ We assume a particle with the mass m in the cubic potential with a metastable state at $x = a$ shown in Fig. 4.1. The bottleneck for the particle leaving the metastable state is immediately observable at the top of the barrier of the height W at $x = b$.

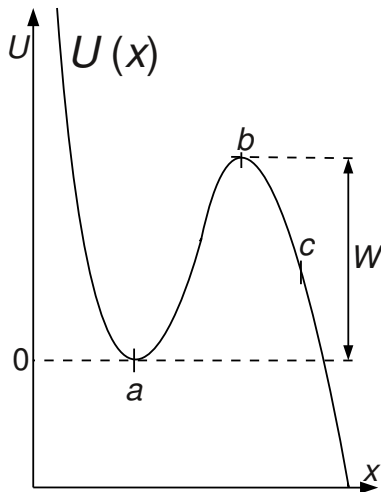


Fig. 4.1: Potential with a metastable state at $x = a$ (similar to Ref. [267])

The transition-state ansatz uses two key assumptions, namely the strong-coupling assumption and the point of no return c . The strong-coupling assumption requires a system in thermal equilibrium or, equivalently speaking, the timescale for the particle to escape out of the metastable state must be much longer than the time necessary to thermalize. The point of no return assumption states that any orbit crossing a certain point c on the outer side of the barrier will not recross it. This means that a particle that has overcome the point c will not move back into the metastable state. Below, we use these assumptions to introduce the canonical transition-state theory (TST), which uses the Boltzmann weighting function at a given temperature T to calculate the escape rate from the metastable state. This theory always overestimates the escape rate, so that the real escape rate Γ is always smaller than the calculated rate Γ_{TST} . In our case, the Boltzmann factor helps to minimize the phase space at the top of the barrier. Thus, statistics predicts a very small probability to find the particle at $x = b$. Hence, we assume that any particle that has overcome the barrier at $x = b$ will not move back into the metastable state and define the point of no return at $c = b$. To analyze this case, let us use the “flux-over-population” method and look for a stationary solution assuming that particles are injected by a source into the metastable region of attraction and removed by a sink on the other side of the barrier. This way, one can apply a stationary probability distribution function for the position of the particle. Particles overcoming the barrier are removed such that this function is zero for $x > b$.^{227, 266}

One calculates with these assumptions the probability²⁶⁸

$$\begin{aligned} P_{\text{out}}(\Delta t) &= \int_0^\infty dv \int_{b-v\Delta t}^b dx \frac{e^{-\frac{mv^2}{2k_B T}}}{\int_{-\infty}^\infty dv' e^{-\frac{mv'^2}{2k_B T}}} \frac{e^{-\frac{U(b)}{k_B T}}}{\int_{-\infty}^\infty dx' e^{-\frac{U(x')}{k_B T}}} \\ &= \Delta t \sqrt{\frac{k_B T}{2\pi m}} \left(\int_{-\infty}^b dx e^{-\frac{U(x)-U(a)}{k_B T}} \right)^{-1} e^{-\frac{W}{k_B T}} \end{aligned} \quad (4.1)$$

that a particle leaves the metastable state in the time interval Δt where k_B denotes the Boltzmann constant. For the following calculation, we use the harmonic approximation

$$\tilde{U}(x) = U(a) + \frac{1}{2} m \omega_a^2 (x - a)^2$$

for the potential around $x = a$ where the attempt frequency ω_a denotes the frequency of small oscillations around the potential minimum. In this case, expanding the integration limits in Eq. (4.1) to $\pm\infty$ results in the transition-state escape rate

$$\Gamma_{\text{TST}} = \frac{\omega_a}{2\pi} e^{-\frac{W}{k_B T}}. \quad (4.2)$$

This result may be illustrated as follows: A particle is oscillating with the frequency ω_a in a harmonic potential. Thus the ‘‘hit’’ or ‘‘attempt frequency’’ on the wall is $\omega_a/2\pi$. Every time the particle hits the wall, it has the probability $e^{-W/k_B T}$ to cross the wall.²⁶⁷

4.1.2 Kramers' Theory*

Kramers' theory describes a classical particle of the mass m moving in a one-dimensional asymmetric double-well potential $U(x)$ with dissipation. At the temperature T , the particle feels a thermal fluctuating force $\xi(t)$ which obeys²⁶⁶

$$\begin{aligned} \langle \xi(t) \rangle &= 0 & \text{and} \\ \langle \xi(t) \xi(s) \rangle &= 2m\gamma k_B T \delta(t - s) \end{aligned}$$

with the Dirac delta function $\delta(x)$; a linear damping force $-m\gamma\dot{x}$ is introduced where γ denotes the damping relaxation constant. Hence, the equation of motion takes the form of the Langevin-equation²⁶⁶

$$m\ddot{x} = -\frac{\partial U(x)}{\partial x} - \gamma m\dot{x} + \xi(t). \quad (4.3)$$

The dynamics in this two-dimensional system can be described with the variables position x and velocity $v = \dot{x}$ by the Klein-Kramers equation²⁶⁶

$$\frac{\partial p(x, v, t)}{\partial t} = \left(-\frac{\partial}{\partial x} v + \frac{\partial}{\partial v} \frac{U'(x) + m\gamma v}{m} + \frac{\gamma k_B T}{m} \frac{\partial^2}{\partial v^2} \right) p(x, v, t) \quad (4.4)$$

where $U'(x)$ denotes the spatial derivative of $U(x)$.^{266, 269} Since we treat the escape of a particle from a metastable state over a potential barrier in this section, we do not have a double-well potential. However, our case can be simply deduced from Kramers' problem by only allowing transitions out of the metastable state. Because we assume only weak friction, the particle follows an unperturbed, conservative equation of motion.²⁶⁶ Hence, the energy, or equivalently speaking, the action $I(E)$ can be used to describe the dynamics of the particle. Kramers found the escape rate²⁶⁹

$$\Gamma_t = \frac{\gamma I(W)}{k_B T} \frac{\omega_a}{2\pi} \exp\left(-\frac{W}{k_B T}\right) \quad (4.5)$$

in this limit. Compared to the TST, which we have introduced in section 4.1.1, this result does take the damping into account. In this case, we have to replace the Boltzmann distribution from the TST by a non-equilibrium probability distribution. We note that in the limit of very weak damping M. Büttiker *et al.*²⁷⁰ improved Eq. (4.5) to

$$\Gamma_t = \frac{\sqrt{1 + \frac{4k_B T}{\gamma I(W)} - 1}}{\sqrt{1 + \frac{4k_B T}{\gamma I(W)} + 1}} \frac{\gamma I(W)}{k_B T} \frac{\omega_a}{2\pi} \exp\left(-\frac{W}{k_B T}\right) \quad (4.6)$$

by taking into account phase space corrections at the top of the barrier.

4.1.3 The Application of Kramers' Theory to Underdamped Josephson Junctions*

We have analyzed the Stewart-McCumber model and the Josephson dynamics using a tilted washboard potential (TWP) in section 3.1. There, we have identified a sequence of metastable states for a finite potential tilt. These are relevant for underdamped Josephson junctions biased with a current $I_r < I_b < I_c$. In this case, two voltages V are possible across a JJ at a given bias current I_b , which relate to a trapped ($V = 0$) and a running ($|V| > 0$) phase particle. We examine below the escape dynamics of the phase particle and thereby the switching of the JJ from the zero-voltage into the voltage state by thermal activation. We mention the early works of Ivanchenko and Zil'berman²⁷¹ and Ambegaokar and Halperin²⁷² since they first addressed the problem of the thermally induced escape in Josephson junctions, but base our analysis on Kramers' theory as explained above. Here, we use for technical reasons a cubic approximation of the TWP near a metastable state. It is defined by the barrier height^{121, 273}

$$W = 2E_J \left(\sqrt{1 - i_b^2} - i_b \arccos i_b \right) \quad (\text{for } i_b < 1) \quad (4.7)$$

$$\approx \frac{4\sqrt{2}}{3} E_J (1 - i_b)^{3/2} \quad (\text{for } i_b \sim 1) \quad (4.8)$$

and the attempt frequency

$$\omega_a = \alpha \omega_p = (1 - i_b^2)^{1/4} \omega_p \quad (4.9)$$

of small oscillations around the potential minimum where $i_b = I_b/I_c$ denotes the normalized bias current and $\alpha = (1 - i_b^2)^{1/4}$ the normalized attempt frequency. With these values, Eq. (4.6) allows to calculate the switching rate¹²¹

$$\Gamma_t = a_t \frac{\omega_a}{2\pi} \exp\left(-\frac{W}{k_B T}\right) \quad (4.10)$$

from the zero-voltage into the voltage state with the quantum prefactor

$$a_t \approx \frac{4}{\left(\sqrt{1 + \frac{Qk_B T}{1.8W}} + 1\right)^2} \quad (4.11)$$

for a JJ at a given temperature T .

4.2 Macroscopic Quantum Tunneling*

In this section, we analyze quantum tunneling through a potential barrier with a particular focus on the escape of a phase particle out of a metastable state in the tilted washboard potential. Quantum tunneling first got attention by G. Gamow²⁷⁴ and, independently, by R. Gurney and E. Condon^{275, 276}, who examined the alpha decay of a nucleus via quantum tunneling.^{277, 278} Here, we apply the same theory to model the escape of the phase particle out of a metastable state in a tilted washboard potential by quantum tunneling or, equivalently, to describe the switching of a Josephson junction from the zero-voltage state into the voltage state. We use the cubic approximation of the potential well as we have done in section 4.1.3 and apply the quasi-classical Wenzel-Kramers-Willouin (WKB) method^{277, 279–283}. This results in the quantum tunneling escape rate²⁶⁶

$$\Gamma = \frac{\omega_a}{2\pi} \exp\left(-\frac{36}{5} \frac{W}{\hbar \omega_a}\right) \quad (4.12)$$

of a particle out of the metastable state in the cubic potential defined by the attempt frequency ω_a and the barrier height W . However, in the case of Josephson junctions and particularly of SIFS junctions with a moderate quality factor $Q < 10$, we have to take dissipation into account. This situation has been theoretically evaluated in the zero temperature limit by A. O. Caldera and A. J. Leggett.^{284–288} In this case, Eq. (4.12) is replaced by^{121, 125, 266}

$$\Gamma_q = a_q \left(\frac{\omega_a}{2\pi}\right) \exp\left(-\frac{36}{5} \frac{W}{\hbar \omega_a} \left(1 + 1.74 \frac{1}{2Q}\right) + \dots\right) \quad (4.13)$$

for a JJ with a quality factor Q where we have introduced the quantum prefactor

$$a_q = \sqrt{120\pi \left(\frac{7.2W}{\hbar\omega_a} \right)} \quad (4.14)$$

based on the detailed calculation of S. Coleman.^{289, 290}

We note that in the 1980s macroscopic quantum tunneling in Josephson junctions was actively discussed since it involves the collective behavior of many electrons and macroscopic dissipation plays a role.^{123, 124}

4.3 The Crossover between Thermally Activated Escape and Macroscopic Quantum Tunneling*

The escape out of a metastable state has been discussed with a particular focus on the escape of the phase difference across a JJ in the preceding sections 4.1 and 4.2. We have observed in the thermal limit the escape rate Eq. (4.10) and Eq. (4.13) for the escape induced by quantum tunneling. For a better comparison of these values, we follow Martinis *et al.*¹²¹ and introduce the escape temperature T_{esc} by the implicit definition

$$\Gamma = \frac{\omega_a}{2\pi} e^{-\frac{W}{k_B T_{\text{esc}}}}. \quad (4.15)$$

Hence, the thermal and the quantum escape (Eqs. (4.10) and (4.13)) are characterized by the escape temperatures

$$T_{\text{esc}}^t = \frac{T}{1 - p_t} \quad \text{and} \quad T_{\text{esc}}^q = \frac{\hbar\omega_a}{7.2k_B} \frac{1}{1 + \frac{0.87}{Q}} \frac{1}{1 - p_q}$$

with the parameters

$$p_t = \frac{\ln a_t}{W/k_B T} \quad \text{and} \quad p_q = \frac{\ln a_q}{7.2W/\hbar\omega_a \left(1 + \frac{0.87}{Q}\right)},$$

respectively. Since the thermal prefactor a_t and the quantum prefactor a_q are of the order of one in the experimentally relevant situations, the parameters p_t and p_q are negligible and we end in the escape temperatures

$$T_{\text{esc}}^t = T \quad \text{and} \quad T_{\text{esc}}^q = \frac{\hbar\omega_a}{7.2k_B \left(1 + \frac{0.87}{Q}\right)}.$$

We realize that the escape temperature simply equals the temperature necessary to explain a given escape behavior by a thermal escape. We note that a higher escape temperature identifies a higher escape rate. Because of this, at a high temperature

$T = T_{\text{esc}}^t > T_{\text{esc}}^q$ thermally activated escape dominates over quantum tunneling, which one observes below the temperature T_{esc}^q .

Although the analysis above is a good starting point to determine the crossover temperature T^* between thermally activated escape and quantum tunneling by estimating $T_{\text{esc}}^t = T_{\text{esc}}^q$, the exact determination of T^* is better executed by means of a functional-integral approach.¹⁵⁴ We calculate with this ansatz the crossover temperature

$$T^* = \frac{\hbar\omega_a}{2\pi k_B} \left(\sqrt{1 + \left(\frac{1}{2Q}\right)^2} - \frac{1}{2Q} \right) \quad (4.16)$$

in the presence of dissipation.^{291, 292}

4.4 The Irradiation of Josephson Junctions with Microwaves

In the preceding sections, we have analyzed the escape of the phase particle out of a potential well when the particle was either in thermal equilibrium with a heat bath or cooled into its quantum mechanical ground state. In this section, we add an external driving to the phase particle, which is realized by irradiating the JJ with microwaves of the frequency $\omega_{\text{mw}}/2\pi$ and the power P_{mw} . This results in an additional current $I_{\text{mw}} \cos(\omega_{\text{mw}}t)$ across the JJ. As sketched in Fig. 4.2, it can be superimposed to the dc bias current and hence results in an additional wobbling of the tilted washboard potential (cf. section 3.1). Below, we examine how this additional wobbling influences the escape of the phase particle out of a metastable well. It is analyzed in literature in two different ways: The quantum mechanical interpretation assumes thermally occupied discrete energy levels inside a potential well where higher energy levels can be excited by the resonant absorption of photons.^{41, 120, 121, 293–296} On the other hand, our experimental results, which we report in section 8.3, must be interpreted by a classically driven phase particle in a nonlinear potential.^{114, 115, 115–117} We discuss both interpretations below.

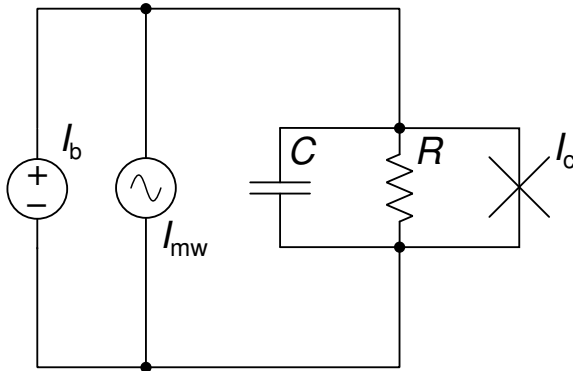


Fig. 4.2: Equivalent circuit of a Josephson junction irradiated with microwaves. The junction is modeled via an ideal Josephson element with the critical current I_c in parallel with a resistance R and a capacitance C . A bias current I_b is supplied via an external current source. The microwaves induce an ac current $I_{\text{mw}} \cos(\omega_{\text{mw}}t)$ parallel to I_b .

4.4.1 The Quantum Mechanical Interpretation*

A metastable state in the tilted washboard potential can be treated quantum mechanically. We locally confine the phase particle in the potential well, which leads to energy level quantization. The potential around a metastable state can be well approximated harmonically for small oscillations as indicated in Fig. 4.3¹¹⁹, so that we observe $N \simeq W/\hbar\omega_a$ discrete energy levels at the discrete energies²⁹⁷

$$E_n = \hbar\omega_a \left(n + \frac{1}{2} \right) \quad (4.17)$$

where n is an integer enumerating the ground state $n = 0$ and the excited states $n = 1 \dots N$ and W is the barrier height defined in section 4.1.3.

We examine the quantized level structure in this section by spectroscopy where we excite analogously to the spectroscopy on atoms higher energy levels by the irradiation with electromagnetic waves; the excitations are detected by an increased switching probability of the junction. However, albeit in atoms the transitions are in the optical regime, here we have to apply microwaves. Unfortunately, these microwaves induce an additional ac current $I_{mw} \cos(\omega_{mw}t)$ across the junction as explained above, which wobbles the tilted washboard potential (cf. Eq. (3.10)). Because of this, the observation of the excitation of higher levels in a JJ requires at most a weak microwave signal, which leaves the potential untouched. Moreover, the fluctuation-induced escape of the Josephson phase from excited levels has to be large according to Fistul *et al.*¹¹⁴, i.e. the exponent in Eq. (4.13) has to be of the order of unity. Together with the resonance condition

$$\omega_{mw} = \omega_p(1 - i_b^2)^{1/4} \quad (4.18)$$

this demands¹¹⁴

$$\left(\frac{\omega_{mw}}{\omega_p} \right)^5 \lesssim \frac{\hbar\omega_p}{E_J}. \quad (4.19)$$

Typical values for the junctions grown within this work are $\omega_p/2\pi = 20\text{GHz}$ and $E_J = 0.2\text{eV}$. Hence, Eq. (4.19) requires for the quantum mechanical interpretation of the dynamics of our junctions under microwave driving $\omega_{mw} \lesssim 0.2 \omega_p$. However, for these values excitations are expected at $i_b \gtrsim 0.998$ according to Eq. (4.18). Since the junction has already switched into the voltage state there, this range is experimentally not accessible. Because of that, we do not want to go here more into detail and discuss

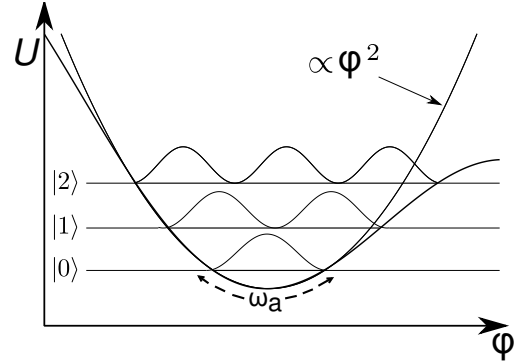


Fig. 4.3:

A potential well with discrete energy levels and the absolute square of the respective wave functions. (similar to Ref. [291])

in section 4.4.2 the strong driving case.

4.4.2 The Semi-Classical Dynamics of a Strongly Microwave Driven Josephson Junction

Although we have started to look into the dynamics of Josephson junctions under microwave irradiation by means of the excitation of quantum levels in a metastable potential minimum in section 4.4.1, historically the Josephson dynamics has been examined with a particular focus on the study of nonlinear phenomena. Here, the scientific interest was to understand the chaos in Josephson junctions.^{298, 299} We expand below these theories³⁰⁰ and unite the works of Fistul *et al.*^{114, 301, 302}, which use a harmonic balance method to explain harmonic excitations, and of Grønbech-Jensen *et al.*^{115–117}, which discuss the nonlinear potential landscape. We start by adding a microwave current $I_{\text{mw}} \cos(\omega_{\text{mw}}t)$ to Eq. (3.5), which results in

$$C \left(\frac{\Phi_0}{2\pi} \right)^2 \frac{\partial^2 \varphi}{\partial t^2} + \frac{1}{R} \left(\frac{\Phi_0}{2\pi} \right)^2 \frac{\partial \varphi}{\partial t} + E_J \sin \varphi = E_J (i_b + i_{\text{mw}} \cos(\omega_{\text{mw}}t)) \quad (4.20)$$

with $i_b = I_b/I_c$ and $i_{\text{mw}} = I_{\text{mw}}/I_c$. Here, we can separate the phase difference

$$\varphi = \varphi_0 + \kappa \cos(\omega_{\text{mw}}t + \Theta) + \delta\varphi \quad (4.21)$$

across the JJ into a constant term φ_0 , a quickly oscillating term $\kappa \cos(\omega_{\text{mw}}t + \Theta)$ and an additional small term $\delta\varphi \ll 1$. In this case, the first terms reflect the dynamics due to microwave irradiation while the latter term describes the motion of the phase particle in the potential well of the tilted washboard potential. Substituting Eq. (4.21) into Eq. (4.20) yields³⁰⁰

$$\begin{aligned} \delta\ddot{\varphi} + \frac{\omega_p}{Q_0} \delta\dot{\varphi} + \omega_p^2 \cos(\varphi_0 + \kappa \cos(\omega_{\text{mw}}t + \Theta)) \delta\varphi = \\ \omega_p^2 i_b + \omega_p^2 i_{\text{mw}} \cos(\omega_{\text{mw}}t) + \kappa \omega_{\text{mw}}^2 \cos(\omega_{\text{mw}}t + \Theta) + \\ \kappa \omega_{\text{mw}} \frac{\omega_p}{Q_0} \sin(\omega_{\text{mw}}t + \Theta) - \omega_p^2 \sin(\varphi_0 + \kappa \cos(\omega_{\text{mw}}t + \Theta)) \end{aligned} \quad (4.22)$$

where the last term can be expanded by a Fourier-Bessel transform. Defining the special values³⁰⁰

$$i_b = \sin \varphi_0 J_0(\kappa), \quad (4.23)$$

$$i_{\text{mw}} = \kappa \sqrt{\left(\frac{2J_1(\kappa)}{\kappa} \cos \varphi_0 - f_{\text{mw}}^2 \right)^2 + \left(\frac{f_{\text{mw}}}{Q_0} \right)^2}, \quad \text{and} \quad (4.24)$$

$$\tan \Theta = \frac{f_{\text{mw}}/Q_0}{f_{\text{mw}}^2 - 2 \cos \varphi_0 J_1(\kappa)/\kappa} \quad (4.25)$$

with J_m the Bessel function of the first kind and order m and $f_{\text{mw}} = \omega_{\text{mw}}/\omega_p$ will secure that the right side of Eq. (4.22) has neither time independent nor ω_{mw} -harmonic terms

of the first order; in detail, Eq. (4.22) reduces to³⁰⁰

$$\begin{aligned} \delta\ddot{\varphi} + \frac{\omega_p}{Q_0} \delta\dot{\varphi} + \omega_p^2 \cos(\varphi_0 + \kappa \cos(\omega_{mw}t + \Theta)) \delta\varphi = \\ \omega_p^2 (2 \tan \varphi_0 J_2(\kappa) \cos(2(\omega_{mw}t + \Theta)) + 2J_3(\kappa) \cos(3(\omega_{mw}t + \Theta)) + \dots). \end{aligned} \quad (4.26)$$

Equation (4.26) clarifies that the small term $\delta\varphi$ supports oscillations with the frequency $\approx \omega_p (\cos \varphi_0)^{1/4}$ and its harmonics. We note that it can be shown by Fourier-Bessel expanding the last term on the left side of Eq. (4.26) that it also supports half-harmonic oscillations.³⁰⁰

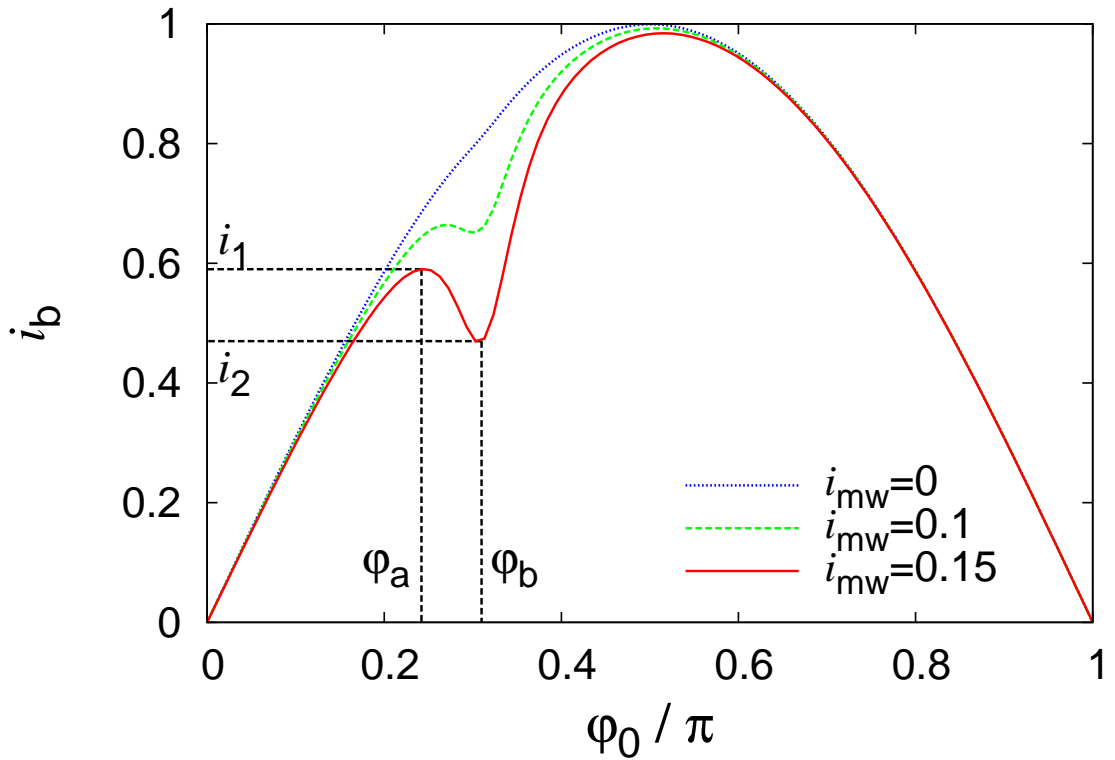


Fig. 4.4: The reduced bias current i_b versus the equilibrium phase difference φ_0 for a JJ under microwave irradiation with the current amplitudes $i_{mw} = 0, 0.1,$ and 0.15 . It is calculated with Eq. (4.27) for the parameters $f_{mw} = 0.75$ and $Q_0 = 7$, which are typical values for the experiments in section 8.3. For zero applied microwave power, one observes for a particular bias current two possible equilibrium phase positions φ_0 where the one with $0 < \varphi_0 < \pi/2$ is stable. Under microwave driving one identifies four ones, e.g. for $i_{mw} = 0.15$ in the bias current range $0.47 < i_b < 0.59$. There, the solutions $\varphi_0 < \varphi_a$ and $\varphi_b < \varphi_0 < \pi/2$ are stable.

We next discuss the results of the calculation above. We have analyzed a Josephson junction under microwave irradiation. We found out that in this case the phase difference across the junction potentially supports stable oscillations around an equilibrium phase

φ_0 , which depends on the bias current

$$i_b = \sin \varphi_0 J_0 \left(\frac{i_{\text{mw}}}{\sqrt{(\cos \varphi_0 - f_{\text{mw}}^2)^2 + \left(\frac{f_{\text{mw}}}{Q_0}\right)^2}} \right) \quad (4.27)$$

across the junction. This current calculates from Eq. (4.23) where we put in κ from Eq. (4.24) and for algebraic reasons assume a small oscillation amplitude κ to get rid of the Bessel function $J_1(\kappa) \simeq \kappa/2 - o(\kappa^3)$. Figure 4.4 plots i_b versus the equilibrium phase φ_0 , that is a “current-equilibrium phase”-relation, for the parameters $f_{\text{mw}} = 0.75$ and $Q_0 = 7$, which are typical values for the experiments in section 8.3, and different microwave driving strengths i_{mw} . There, we observe in the absence of microwave driving ($i_{\text{mw}} = 0$) a sinusoidal current-phase relation with two possible equilibrium phase positions with $0 < \varphi_0 < \pi$. Here, the smaller φ_0 value corresponds to the phase particle trapped in the potential well where it can freely oscillate (libration state), while the other one relates to the barrier maximum, which is unstable. However, two new equilibrium phase positions emerge under microwave driving in a particular bias current region $i_2(\varphi_b) < i_b < i_1(\varphi_a)$ where the one with $\pi/2 > \varphi_0 > \varphi_b$ corresponds to an additional stable oscillation (libration state). Hence, for the equilibrium phase positions between φ_a and φ_b no stable oscillation exists. On the other hand, stable oscillations are possible for two different bias currents in certain bias current ranges due to the nonlinear nature of our potential. This results at a characteristic microwave driving in two possible switching currents corresponding to the two libration oscillations.

In summary, we extract three important results from the treatment above: First, microwave irradiation suppresses the critical current

$$I_c \sin \varphi_0 \left(1 - \frac{i_{\text{mw}}^2/2}{(\cos \varphi_0 - f_{\text{mw}}^2)^2 + \left(\frac{f_{\text{mw}}}{Q_0}\right)^2} \right) \quad (4.28)$$

of a Josephson junction (according to Eq. (4.27) with the approximation $J_0(x) \simeq 1 - x^2/2$); this effect is particularly strong in the resonant case. This result agrees with the derivation of Fistul *et al.*³⁰¹ based on a harmonic balance method. We annotate that we have seen above that a JJ also supports sub- and superharmonic frequencies via the additional oscillation term $\delta\varphi$. These modes are responsible for a suppression of the critical current at small integer fractions and multiples of the resonance frequency, which has been observed by Grønbech-Jensen *et al.*^{115–117} Second, the Josephson dynamics is not unique under microwave driving, so that we observe for some microwave driving powers stable oscillations for two different bias currents with different φ_0 and different oscillation amplitudes κ , which experimentally results in two different possible switching currents of a JJ under microwave driving (see also Ref. [114]). We note that the observation of two distinct switching currents has been originally interpreted as the

escape from different discrete quantum levels as introduced in section 4.4.1, but as we have seen can also be explained classically. Third, the resonance frequency

$$\omega_r = \sqrt{\frac{2J_1(\kappa)}{\kappa}} \sqrt{1 - \left(\frac{i_b}{J_0(\kappa)}\right)^2} \quad (4.29)$$

can be extracted from Eq. (4.24). It corrects Eq. (4.9) for nonlinear effects.

Part III

EXPERIMENTS

Chapter 5

SAMPLE PREPARATION*

5.1 Introduction

The growth of high quality Josephson junctions (JJs) demands for a sophisticated technology with a particular focus on material aspects. Today, aluminum and niobium are widely used for the superconducting electrodes, and insulating barriers are implemented via oxidizing an aluminum layer. While the superconducting properties of aluminum are rather poor ($T_c \approx 1$ K), it oxidizes into a stable oxide allowing for the in-situ growth of reproducible tunnel barriers. Hence, the Al/Al₂O₃ material system is heavily used in the nano-fabrication of Josephson junctions where shadow mask evaporation techniques allow for the junction growth using a single lithography step.^{303–305} In contrast, growing a tunnel barrier between two superconducting niobium electrodes is more difficult. In the 1980s there have been numerous experiments in forming tunnel barriers by oxidizing the niobium itself, but the formation of different niobium sub-oxides always resulted in a poor junction quality.³⁰⁶ Hence, the development of the niobium technology only started when Gurvitch *et al.*^{307, 308} deposited an ultrathin aluminum layer, which was partially oxidized, as the tunnel barrier between the niobium electrodes. Here, favorable surface properties induced a complete wetting of the aluminum on the top of the niobium layer, which resulted after partial oxidation in a homogeneous insulating barrier. This process allows for the growth of excellent JJs with a high critical temperature ($T_c \approx 9$ K), high critical current densities up to $j_c = 10$ kA/cm², and tiny leakage currents.

In this work, we discuss junctions containing ferromagnetic and superconducting layers. Since ferromagnetism tends to align the electrons of the Cooper-pairs in a superconductor, which suppresses superconductivity³⁰⁹, we decide to use niobium as the electrode material and an oxidized ultrathin aluminum layer as the tunneling barrier. As we have seen in section 2.3.2, the growth of SFS π -junctions requires very thin ferromagnetic interlayers, which are difficult to prepare. The required thickness increases with a decreasing exchange energy E_{ex} according to Eq. (2.30), so that for technological reasons a very weak ferromagnet is advantageous. Hence, we use the diluted ferromagnet Pd_{0.82}Ni_{0.18} for our superconductor/insulator/ferromagnetic metal/superconductor (SIFS) Josephson junctions, which consist of a Nb/AlO_x/Pd_{0.82}Ni_{0.18}/Nb layer stack.

* This chapter is based on the publication Ref. [A2].

This chapter is organized as follows: In section 5.2 we give an overview of the junction growth process. Then, section 5.3 discusses the multilayer deposition in detail, which includes the analysis of the superconducting properties of the niobium and the magnetic properties of the $\text{Pd}_{0.82}\text{Ni}_{0.18}$. Section 5.4 develops the etch process, and section 5.5 gives a short summary.

5.2 The Self-Align Multilayer Process*

In this work, the fabrication of SIFS Josephson junctions with controllable and reproducible properties is realized by the deposition of $\text{Nb}/\text{AlO}_x/\text{Pd}_{0.82}\text{Ni}_{0.18}/\text{Nb}$ multilayers by UHV dc magnetron sputtering and subsequent patterning of this multilayer stack using optical lithography, a lift-off process, as well as reactive ion etching (RIE).[†] Thermally oxidized silicon wafers (~ 50 nm oxide thickness) are used as substrates. The optical lithography is performed by a Karl Süss MJB 3 mask aligner where for each process step a chromium on glass mask serves to pattern each photoresist stencil. The four masks are shown in Fig. 5.5 in different colors. The yellow mask, which was originally designed for the patterning of gold bonding pads before the multilayer growth, was left out for process simplicity as explained in the caption of Fig. 5.6.

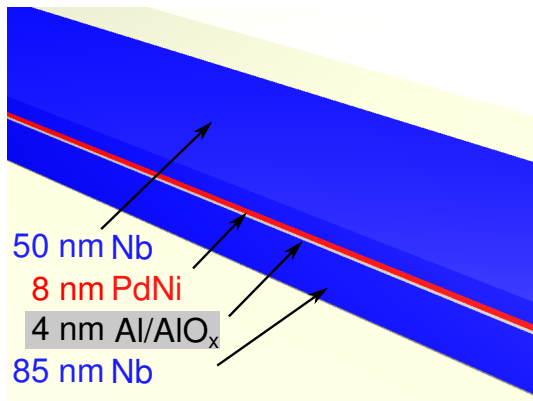


Fig. 5.1: Multilayer stack

In a first deposition step the whole $\text{Nb}/\text{AlO}_x/\text{Pd}_{0.82}\text{Ni}_{0.18}/\text{Nb}$ SIFS multilayer stack shown in Fig. 5.1 was sputtered in-situ. The multilayer stack consists of a niobium base electrode with the thickness $d_{1,\text{Nb}} = 85$ nm, an oxidized aluminum layer of the thickness $d_{\text{Al}} = 4$ nm, a ferromagnetic $\text{Pd}_{0.82}\text{Ni}_{0.18}$ (PdNi) interlayer with the thickness d_{F} ranging from 4 to 15 nm, and finally a niobium top electrode with the thickness $d_{2,\text{Nb}} = 50$ nm. The reproducible fabrication of ferromagnetic SIFS Josephson junctions requires the precise control of the thickness of the PdNi layer and the minimization of the roughness of the involved interfaces. Therefore, we carefully optimize the parameters of the sputtering process for the Nb and the PdNi layers in section 5.3.1 to obtain films with very smooth surfaces. We characterize the niobium and the magnetic properties of the PdNi in sections 5.3.2 and 5.3.3.

After the controlled in-situ deposition of the $\text{Nb}/\text{AlO}_x/\text{Pd}_{0.82}\text{Ni}_{0.18}/\text{Nb}$ multilayer stack, in the next step the SIFS Josephson junctions are fabricated by a suitable patterning process. We use a three-stage self-align process based on optical lithography, a lift-off process and reactive ion etching (RIE) with SF_6 .³¹⁰ In the first step, the base electrode is defined by patterning a long strip into the whole multilayer stack via the

After the controlled in-situ deposition of the $\text{Nb}/\text{AlO}_x/\text{Pd}_{0.82}\text{Ni}_{0.18}/\text{Nb}$ multilayer stack, in the next step the SIFS Josephson junctions are fabricated by a suitable patterning process. We use a three-stage self-align process based on optical lithography, a lift-off process and reactive ion etching (RIE) with SF_6 .³¹⁰ In the first step, the base electrode is defined by patterning a long strip into the whole multilayer stack via the

[†] A detailed growth recipe is given in Appendix A.

red mask in Fig. 5.5. This is achieved by placing a suitable photoresist stencil on the Si substrate and using a lift-off process after the deposition of the SIFS multilayer stack.

Next, the junction area is patterned by etching a mesa structure into the SIFS stack. This is achieved by placing a photoresist stencil on top of the SIFS stack. This resist stencil serves as the etching mask in an RIE patterning process thereby defining the shape and the size of the junction area (for the process parameters see Table 5.1). Junction areas between $2.5 \times 2.5 \mu\text{m}^2$ and $50 \times 50 \mu\text{m}^2$ have been realized. Note that the RIE process selectively patterns the Nb top electrode because the PdNi and the AlO_x layers act as effective stopping layers. The resist stencil defining the junction area is used for the lift-off process in the subsequent deposition of the SiO_2 wiring insulation (self-align process). To avoid electrical shorts between the wiring layer and the base electrode, the lateral dimensions of the resist mask were reduced by about 150 nm using an oxygen plasma process in the RIE system immediately after the mesa patterning (cf. section 5.4). Fig. 5.2 shows the SIFS multilayer after this step.

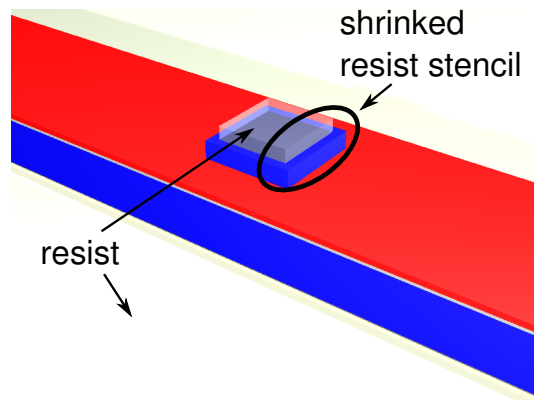


Fig. 5.2:

A mesa structure with the shrunk resist stencil on top

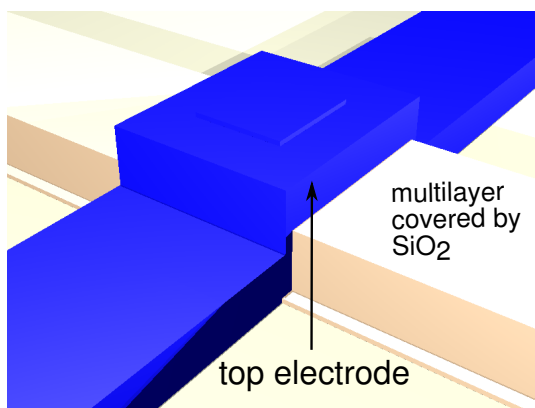


Fig. 5.3: Complete junction

In this way, the SiO_2 wiring insulation also covers the junction edges preventing electrical shorts as proven by the SEM micrograph Fig. 5.4. The 50 nm thick SiO_2 wiring insulation is deposited by rf magnetron sputtering in a 75% Ar/25% O_2 atmosphere since films sputtered in argon-only gases suffer from a porous film structure with many microvoids and oxygen deficient composition.³¹¹ In a last step, the 200 nm thick niobium wiring layer is deposited. The Nb deposition was done by dc magnetron sputtering, and the patterning

was realized by optical lithography and a subsequent lift-off process. To obtain a good superconducting contact between the Nb wiring layer and the Nb top electrode, the surface of the top electrode has been cleaned in-situ prior to the deposition of the wiring layer using an Ar ion gun (time: 1 min, voltage: 1 kV, current: 30 mA). Figures 5.3 and 5.6 show the completed junction. Of course, the junction fabrication process allows for the fabrication of several junctions with different junction areas on the same wafer. In this way, the reproducibility of the process can be checked by measuring the on-chip parameter spread and the scaling behavior of junction properties.

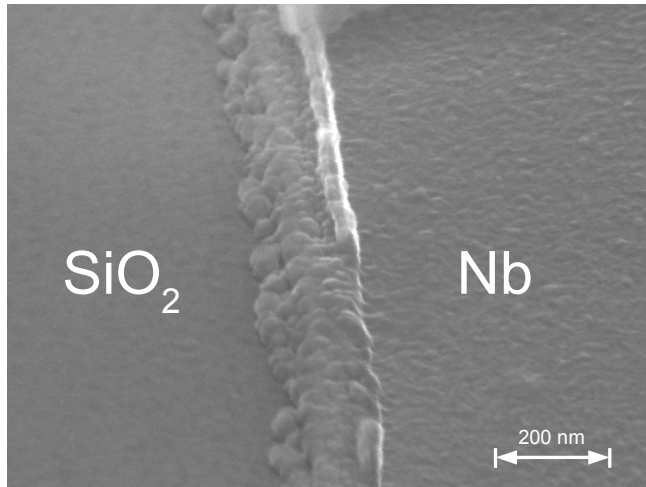


Fig. 5.4: Scanning electron micrograph of the SiO₂ layer overgrowing the niobium mesa structure.

gas flow (sccm/min)	pressure (mtorr)	RIE power (W)	ICP power (W)	voltage (V)	time (s)
10 Ar + 20 SF ₆	15	100	50	320	70
50 Ar	60	200	0	450	240
50 O ₂	30	0	300	0	180
50 O ₂	30-60	100	0	330	60

Tab. 5.1: Etching parameters for the RIE process. The first process step serves for removing the top niobium electrode around the mesa structure. The succeeding optional process step removes the Al/PdNi layers in a physical etch process. The last ashing step shrinks the resist. We note that the two ashing steps at the end remove contaminants from the substrate.

material	sputter pressure (μ bar)	power (W)	time (s)	growth rate ($\text{\AA}/\text{s}$)	thickness (nm)	
bottom niobium	2.7	200	dc	120	7	85
aluminum	2.7	40	dc	20	2	4
Pd _{0.82} Ni _{0.18}	20	40	dc	10-40	3.8	4-15
(oxidation in O ₂)	107			1-4 h		
top niobium	2.7	200	dc	70	7	50
SiO ₂	1 (75% Ar/25% O ₂)	70	ac	380	1.3	50
wiring niobium	2.7	200	dc	300	7	200

Tab. 5.2: Typical sputter and oxidation parameters for a SIFS JJ.

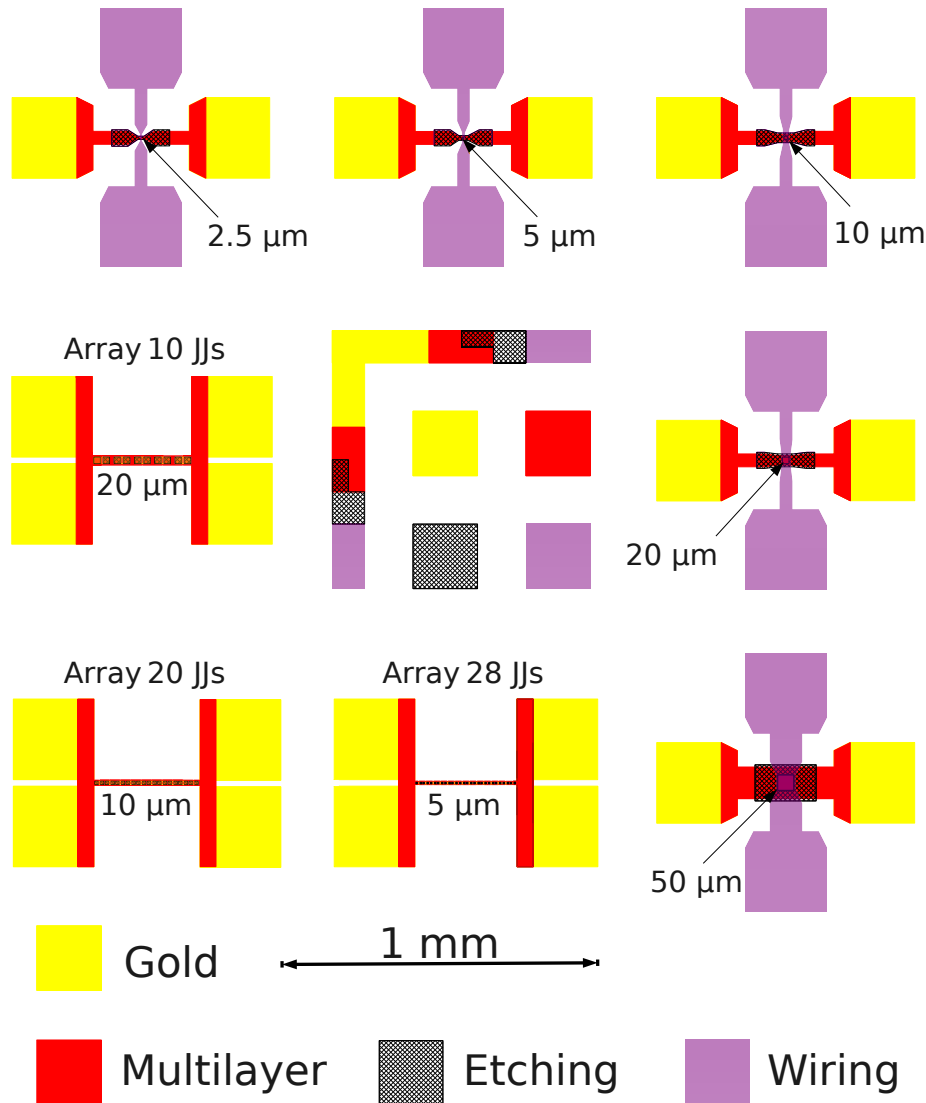


Fig. 5.5: Schematic drawing of the lithography masks containing 5 square Josephson junctions with a side-length of 2.5, 5, 10, 20, and 50 μm and 3 arrays with 28, 20, and 10 square Josephson junctions with a side-length of 5, 10, and 20 μm , respectively. Here, each color denotes one process mask. The yellow bonding pads have only been used at the beginning of this work, while in the later stage the bonding has been realized directly on the multilayer (red color) as discussed in Fig. 5.6. The hatched etching layer defines the junction geometry, while the magenta wiring layer connects the top electrode. The arrows indicate the positions of the Josephson junctions.

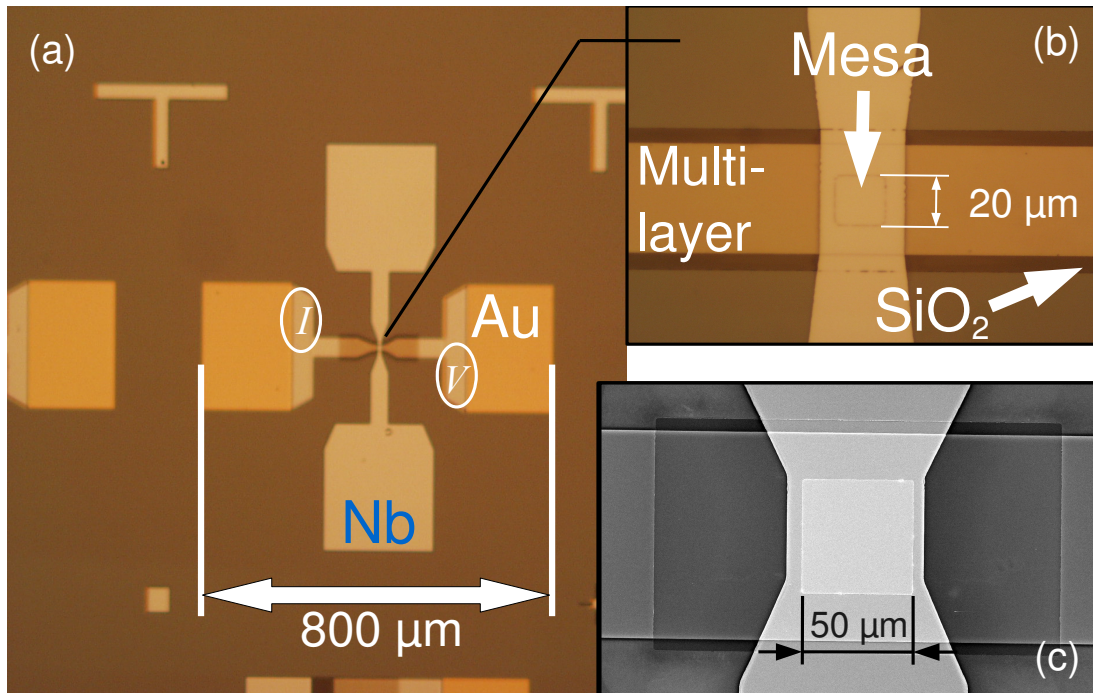


Fig. 5.6: Photograph of a junction in the standard design (a) and zoom into a mesa region (b) and SEM micrograph of the mesa region of a 50 μm JJ.

All transport measurements are based on a four-probe geometry in this work. During the development of the fabrication process, the bottom niobium electrode was directly contacted via gold bonding pads processed before the multilayer growth. However, the preparation of the gold wiring layer requires a lift-off process before the multilayer deposition leaving behind some precipitates on the substrate. Because of this, the Au layer growth was omitted in the experiments discussed within this work, and the base electrode was contacted via bonds at the points marked *V* and *I* in (a). This eventually results in the transport measurements in an additional lead resistance, which is negligible due to the four-probe measurement technique. We note that in the switching current measurements the bonding area, which is large compared to the JJ size, provides a JJ in the zero-voltage state, so that no additional heat is dissipated at this point.

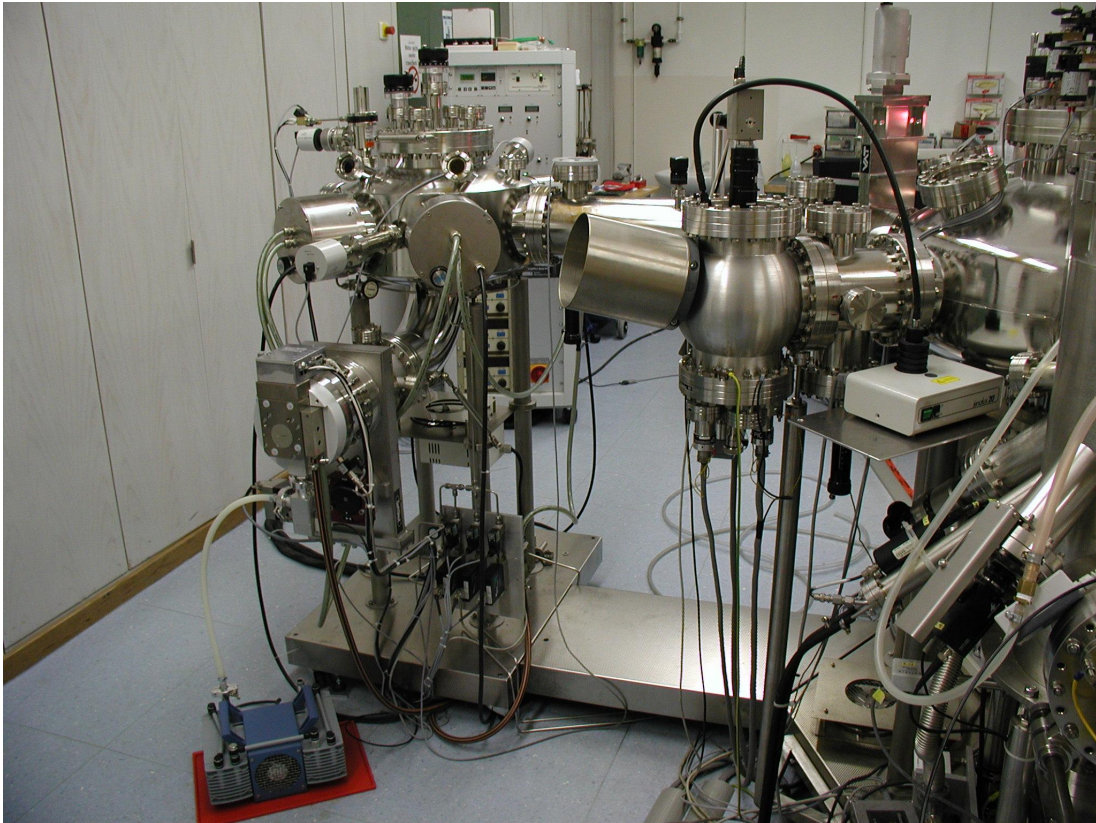


Fig. 5.7: Photograph of the UHV sputtering system and of the Omicron in-situ scanning probe microscope (SPM). On the left hand side, one observes the sputtering system including the Nb and PdNi magnetrons, which is connected via a UHV transport channel to the main system. This allows to transfer the grown layers in-situ into the UHV SPM for their characterization.

5.3 Multilayer Deposition and Characterization*

Since the multilayer contains the complete JJ and thus all relevant interfaces, its growth is a crucial step in the process development. The definition of the geometry of the multilayer is possible via a lift-off or an etching technique. Although the latter one might have been recommendable since impurities desorbed from a resist stencil may accumulate in the niobium layers during their deposition, a lift-off technique has been chosen in favor of minor process complexity. We note that in a lift-off process side wall coverage on the resist stencil plays a major role, which we suppress in our case by an undercut in the resist stencil. The undercut has been realized with the image reversal resist AZ 5214E.³¹² Nevertheless, the undercut height limits the thickness of the multilayer and hence of the bottom niobium electrode to about 90 nm, which is the London penetration depth λ_L of sputtered niobium thin films.²⁵⁹ As we have seen in section 3.2.5, so thin electrodes influence the magnetic field dependence of the critical current and the frequencies of eigen resonances in Josephson junctions.

We grow the SIFS multilayer in the sputtering system shown in Fig. 5.7. Since niobium easily getters impurities present in this system, the reduction of the background pressure is quite important. We achieved typical pressures of around 10^{-9} mbar after a back-out of the UHV system at 150 K for 3 days. Another source of impurities is the argon sputtering gas, which was in our case certified to have less impurity than 1 ppm. The sputtering system is equipped with three 2" Gencoa SW50UHV circular magnetrons dc driven by three Advanced Energy MDX-1K magnetron power supplies for the sputter deposition of Nb, Pd_{0.82}Ni_{0.18} and Al. Additionally, an Ar ion beam gun model "Vacuum Engineering IG35 IONEC" serves for surface cleaning.³¹³ In a sputtering process, gas flow-controllers provide a constant flow of an ultra-pure gas (argon or oxygen), while the chamber pressure is regulated via active feedback using an Intellisys adaptive pressure controller. Here, Pfeiffer capacitive pressure gauge sensors CMR273 (and CMR275) regulate a flow impedance before the Pfeiffer TMU 621 turbo pump. Our sputtering chamber is attached to a UHV cluster tool, which allows for combining sputtering of metallic multilayers with e.g. in-situ surface characterization by AFM/STM. This allows to evaluate the surface roughness of the Nb and PdNi layers to obtain films with very smooth surfaces in section 5.3.1, which is necessary for the precise control of the PdNi layer thickness. The properties of the niobium and the ferromagnetic interlayer will be analyzed in sections 5.3.2 and 5.3.3.

5.3.1 Sputtering and Oxidation*

The properties of Josephson junctions are characterized by their insulating barrier or their normal conducting interlayer. Since we grow in our process a very thin ferromagnetic interlayer with a well defined thickness (< 10 nm) into the structure, a very low surface roughness is essential. In our case, the rms roughness is defined by the substrate and increases during the layer growth.³¹⁴ Hence, it is important to

optimize for smooth surfaces below the ferromagnetic layer, which means at the bottom niobium and the Al layer. In a sputtering process growth kinetics is heavily influenced by the reduced growth temperature (the temperature compared to the melting point of the material) and the process pressure.³¹⁵ Since we cannot heat the sample in our system and are thus in the low temperature regime (the melting point of niobium is 2468 K³¹⁶), the only relevant parameter influencing the surface roughness was found to be the process pressure. In agreement with Thornton's zone diagram, a lower pressure slightly increases the surface smoothness.³¹⁷ Another point is the incorporation of argon into the niobium, which heavily influences the internal stress and thus the properties of the formed JJs.^{318, 319} Taking into account all these facts and the minor influence of the sputter gas impurities at a lower pressure on the one hand and the instability of the sputtering process at a low pressure on the other hand, we determine the optimal sputter pressure in our system to $2.7 \cdot 10^{-3}$ mbar Ar for the Nb/Al bilayer. We sputter niobium at 200 W and aluminum at 40 W resulting in the deposition rates 0.7 nm/s and 0.2 nm/s, respectively. In contrast, we use for PdNi $2 \cdot 10^{-2}$ mbar Ar pressure at 40 W for the rate 0.4 nm/s due to plasma stability problems for low pressures.³¹³ The sputter rates have been calculated by dividing the deposited layer thickness of test samples determined by small angle X-ray scattering by the sputtering time. The sputtering system is equipped with shutters at all magnetrons to allow pre-sputtering for target cleaning, which is typically done for 1 min. For the sputtering of the bottom Nb/Al-bilayer, the appropriate magnetrons are simultaneously started enabling us to change between niobium and aluminum deposition in typically 20 s to prevent the oxidation of the bottom niobium layer. All sputter parameters are given in Table 5.2.

The tunneling barrier is realized by a partial thermal oxidation of the 4 nm thick Al layer inside the sputtering chamber. The thickness of the AlO_x tunneling barrier was adjusted by varying the oxygen partial pressure and the duration of the thermal oxidation process. The oxidation time was varied between 60 and 240 min in a pure oxygen atmosphere of 0.1 mbar. We note that the thickness of the AlO_x tunneling barrier determines the $R_n \cdot A$ values of the junctions because the tunneling resistance is much larger than the resistance of the $\text{Pd}_{0.82}\text{Ni}_{0.18}$ layer.

The surface roughness of all interfaces in the multilayer has been examined by non-contact AFM. Therefore, test samples have been grown with the respective layers. These samples were transferred in-situ into the AFM and evaluated there. The growth parameters and the resulting surface roughnesses are tabulated in Table 5.3. Figure 5.8a shows an AFM measurement of the surface of an 85 nm Nb/4 nm Al/ AlO_x bilayer, while Figure 5.8b plots the height distribution of this surface before and after the deposition of 6 nm PdNi. We learn from these data that the rms surface roughness steadily increases during the growth process. We observe for the rms roughness of the substrate ≈ 0.3 nm, which increases to ≈ 0.9 nm above the ferromagnetic interlayer.

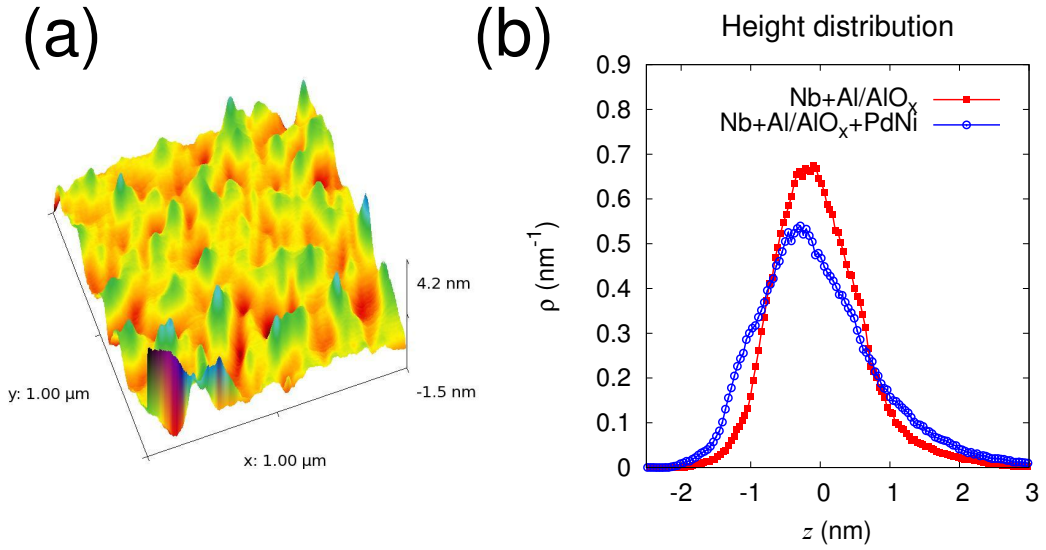


Fig. 5.8: In-situ, non-contact AFM micrograph of the surface of a 85 nm Nb/4 nm Al/AIO_x bilayer (a) and the height distribution on this bilayer before and after the deposition of 6 nm PdNi (for the preparation details see Table 5.3).

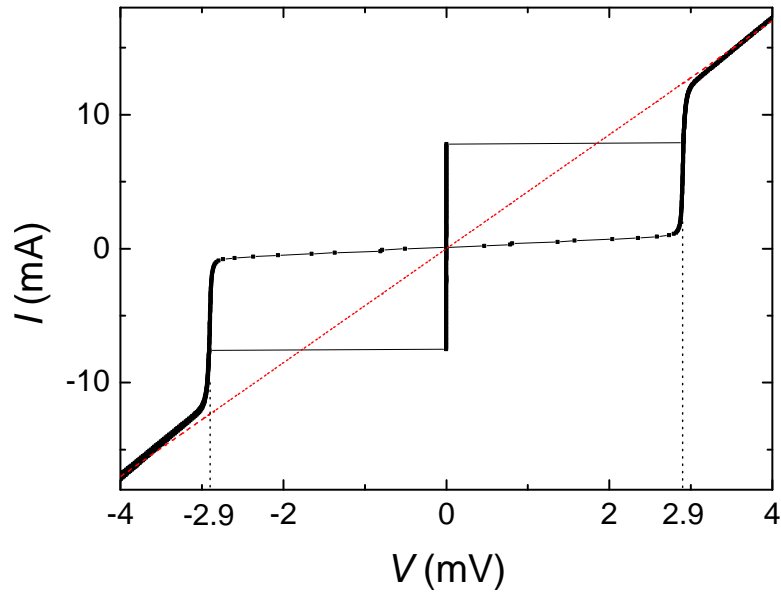


Fig. 5.9: Current-voltage characteristics of a $20 \times 20 \mu\text{m}^2$ SIS Josephson tunnel junction (grown analogously to SIFS junctions, but without a ferromagnetic layer; oxidation time: 90 min) measured at 2 K. The dashed black lines emphasize the gap sum voltage $V_g = 2\Delta_{\text{Nb}}/e = 2.9 \text{ mV}$. One observes a critical current $I_c = 7.7 \text{ mA}$ at a normal resistance $R_n = 235 \text{ m}\Omega$ (dashed red line).

sputter pressure	layer structure				roughness (\AA_{RMS})
	power	time	thickness		
	standard substrate Si 50 nm oxidized				2.6
3 μbar	200 W	120 s	85 nm	Nb	4.3
3 μbar	200 W	120 s	85 nm	Nb	5.0
3 μbar	40 W	20 s	4 nm	Al	
3 μbar	200 W	120 s	85 nm	Nb	6.0
3 μbar	40 W	20 s	4 nm	Al	
0.107 mbar		60 min		oxid.	
3 μbar	200 W	120 s	85 nm	Nb	8.7
3 μbar	40 W	20 s	4 nm	Al	
0.107 mbar		60 min		oxid.	
20 μbar	40 W	15 s	6 nm	PdNi	

Tab. 5.3: The surface roughness at the different SIFS growth process stages. Test samples have been grown, which represent the layer structure at the different stages of the SIFS growth process. They are transferred in-situ into the SPM for surface characterization, and their surface roughness is determined by in-situ, non-contact AFM. The growth parameters and the appropriate surface roughnesses are given in the table.

5.3.2 The Superconducting Niobium

An important material property of thin niobium films with the critical temperature $T_c \approx 9$ K is their energy gap. Therefore, we evaluate in Fig. 5.9 the current-voltage characteristics of a classical $20 \times 20 \mu\text{m}^2$ Nb/ AlO_x /Nb SIS Josephson tunnel junction, which is fabricated with the process introduced in section 5.2. The black dashed lines emphasize the gap sum voltage $V_g = 2\Delta_{\text{Nb}}/e = 2.9$ mV, from which the energy gap

$$\Delta_{\text{Nb}} = 1.45 \text{ meV} \quad (5.1)$$

of our niobium can be extracted^{299, 320}. This value agrees very well with literature.³²¹ Moreover, one observes a critical current $I_c = 7.7$ mA at a normal resistance $R_n = 235$ m Ω resulting in $I_c R_n = 1.81$ mV. The theoretically expected value is given by the Ambegaokar-Baratoff relation Eq. (2.7)

$$I_c R_n = \frac{\pi \Delta_{\text{Nb}}}{2e} \tanh\left(\frac{\Delta_{\text{Nb}}}{2k_B T}\right) \approx 2.27 \text{ mV}.^{166} \quad (5.2)$$

The overestimation can be explained by the premature switching from the zero-voltage into the voltage state due to noise. From the values above one calculates a critical current density $j_c \simeq 1.9$ kA/cm² and $R_n \cdot A \simeq 94$ $\Omega \mu\text{m}^2$.

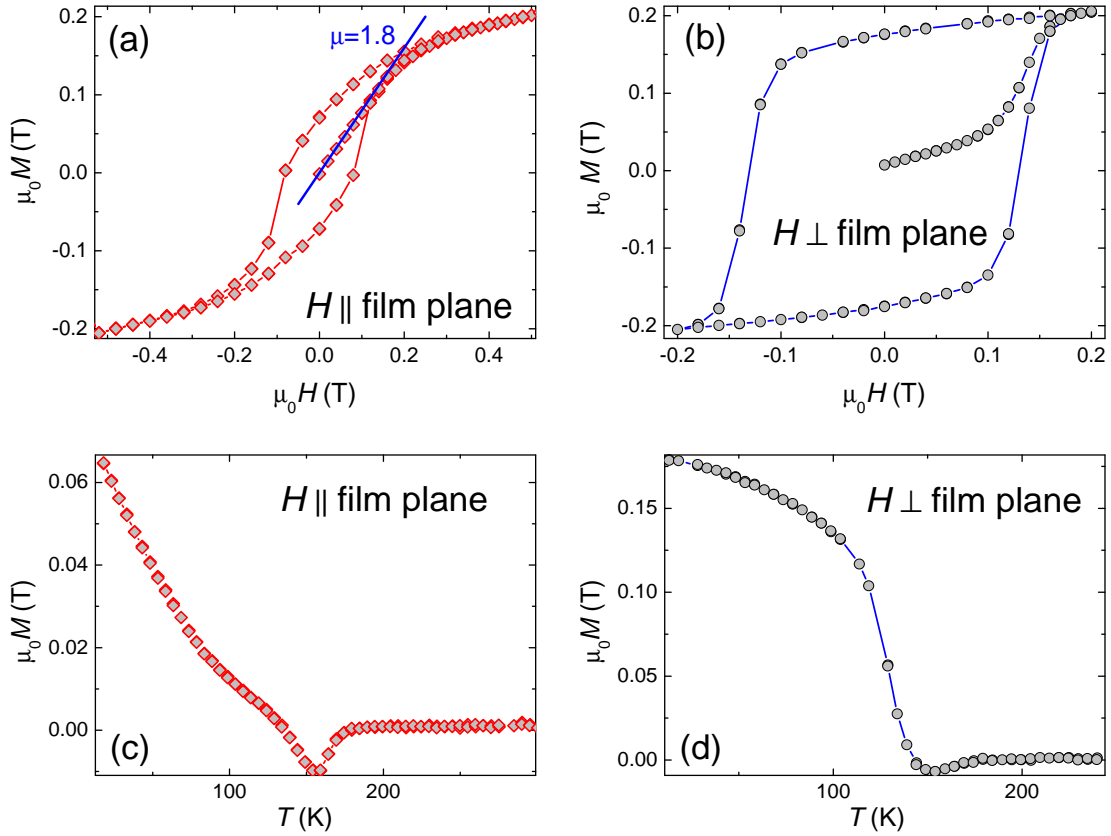


Fig. 5.10: Magnetization versus applied magnetic field curves of an 8.4 nm thick $\text{Pd}_{0.82}\text{Ni}_{0.18}$ layer sandwiched in a $\text{Nb}/\text{AlO}_x/\text{PdNi}/\text{Nb}$ multilayer stack for the magnetic field applied parallel (a) and perpendicular (b) to the film plane and the magnetization M versus the temperature T during the warm up (c) and (d). The $M(H)$ -curves were measured at 11 K, that is just above the critical temperature of the Nb films. The magnetization data have been corrected by subtracting the diamagnetic background due to the metallic layers and the substrate. This contribution is determined from the slope of the $M(H)$ -curves at high fields above 1 T where the magnetization of the ferromagnetic layer is fully saturated. The blue line in (a) is a linear approximation of the virgin curve for $\mu = 1.8$ around zero applied field. The measurements (c) and (d) show the magnetization of the ferromagnetic interlayer during the warm up in zero field directly after the measurements in (a) and (b). There, one estimates the Curie temperature $T_C \approx 150$ K.

5.3.3 The Magnetic Properties of PdNi*

π -coupling across a Josephson junction can be realized by including a ferromagnetic metal layer with a thickness of a few nanometers into the junction. We note that the growth of such thin layers with a well defined thickness d_F has only recently been achieved with the progress in UHV deposition technology. Additionally, the use of diluted ferromagnets results in a low exchange energy E_{ex} in the F layer and hence enlarges according to Eq. (2.30) the d_F required for the growth of π -coupled junctions.^{14, 54} Today, the most widely examined diluted ferromagnets are NiCu and PdNi. In the first system the ferromagnetism originates from clusters of at least 8 Ni atoms due to statistical concentration fluctuations³²², while in the latter material the ferromagnetism is not only caused by the diluted Nickel atoms, but also originates from the paramagnetic Pd matrix. This leads to a homogeneous ferromagnetic material rather than a matrix with ferromagnetic clusters.³²³ Because of the higher values of the interface transparency of PdNi in combination with niobium compared to NiCu^{324, 325}, we concentrate on this material system and use Pd_{0.82}Ni_{0.18}, whose composition we prove by energy dispersive X-ray spectroscopy (EDX).

For thin ferromagnetic films, the easy axis of the magnetization is usually parallel to the film plane to minimize the free energy contribution due to the shape anisotropy. However, in very thin films the magnetic surface energy may be dominant resulting in an easy axis perpendicular to the film plane.^{326, 327} To get information on the direction of the easy axis, we have recorded the magnetization versus applied magnetic field curves of the thin Pd_{0.82}Ni_{0.18} layer within a Nb/AlO_x/Pd_{0.82}Ni_{0.18}/Nb multilayer stack with the magnetic field applied in- and out-of-plane using a Quantum Design SQUID magnetometer. The result is shown in Figures 5.10 a and b. Qualitatively, an almost rectangularly shaped $M(H)$ -curve is expected for the field applied along the easy axis because the magnetization tries to stay along this preferred direction as long as possible and then abruptly switches to the opposite direction at the coercive field. In contrast, for the field applied along the hard axis the magnetization is expected to be gradually rotated out of the easy axis direction into the hard axis direction on increasing the applied magnetic field, resulting in a gradually increasing and decreasing magnetization when sweeping the field.^{328–330} As demonstrated by Figures 5.10 a and b, the measured $M(H)$ -curve is much more rounded and has a smaller remanent magnetization when the field is applied in-plane, whereas it has an almost rectangular shape when the field is applied out-of-plane. This is clear evidence for an out-of-plane anisotropy of the PdNi film. That is, the out-of-plane (in-plane) direction is the magnetic easy (hard) axis in agreement with literature.⁶³ An out-of-plane anisotropy has been observed also for NiCu.³³¹ A more detailed analysis of the magnetic anisotropy of the PdNi films would require additional experiments such as ferromagnetic resonance and methods providing information on the domain structure. However, it is difficult to perform such experiments with ferromagnetic layers enclosed by two metallic Nb layers.

The saturation magnetization M_s of the Pd_{0.82}Ni_{0.18} layer is about $\mu_0 M_s \simeq 0.2$ T in good agreement with literature values.⁶³ This magnetization corresponds to a magnetic

moment of slightly above $1 \mu_B$ per Ni atom if one assumes that there is negligible contribution of Pd. This is close to the values in polycrystalline bulk samples, for which $\mu_{\text{Ni}} \simeq 1.1 \mu_B$ and $\mu_{\text{Pd}} \simeq 0.1 \mu_B$ has been reported by Cable and Child³³² and $\mu_{\text{Ni}} \simeq 0.8 \mu_B$ and $\mu_{\text{Pd}} \simeq 0.1 \mu_B$ by K. Ikeda³³³. This suggests that there are no significant magnetic dead layers. Since M_s was measured with an only 8 nm thick PdNi film, even very thin dead layers at the interfaces would result in a significant reduction of M_s . In the measurement of the magnetic field dependence of the critical current of the SIFS junctions, only an in-plane magnetic field of the order of a few mT is applied. In this small field range only the virgin $M(H)$ -curve is relevant, which is about linear and almost non-hysteretic. From the experimental data taken at 11 K, the slope of the $M(H)$ -curve is determined to $\mu = dB/dH = 1.8$.

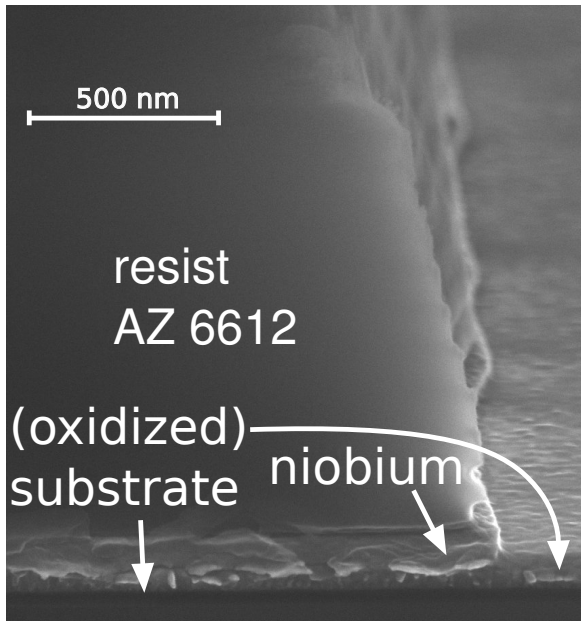
Figures 5.10 c and d determine the Curie temperature of the $\text{Pd}_{0.82}\text{Ni}_{0.18}$ layer to about 150 K by measuring the magnetization versus temperature dependence. These measurements have been taken directly after the magnetization curves during the warm up at zero applied external field. An astonishing feature is the observation of a magnetization opposite to the originally applied field. This phenomenon can be explained by the change of the preferential directions with temperature due to the magnetostriction.

5.4 Etching and Insulating the Mesa

Mesa structures are usually etched by chemical wet or physical dry etching. However, it is for our material system more advantageous to combine these two methods and to apply reactive ion etching (RIE) with SF_6 , that is to use fluorine ions, which chemically react with niobium.³³⁴ Due to the different chemical properties of niobium, on the one hand, and of aluminum or PdNi, on the other hand, there exists a huge difference between the etching rates for the first and the latter materials in a RIE fluorine process. This allows to selectively remove the top niobium layer of a Nb/ AlO_x /PdNi/Nb structure using the first process in Table 5.1 (in an Oxford Instruments Plasma Technology RIE system Plasmalab 80 Plus with an ICP plasma source). In this case, the aluminum or PdNi layers act as effective stop layers.^{310, 334–338} After the niobium etch process, these layers may be also removed by a dry etch process (the second process in Table 5.1). Thus, we can selectively remove all layers in a SIFS multilayer stack.

With this experience, we define a SIFS Josephson junction in a multilayer stack. As we have seen in section 5.2, this is done by placing a suitable resist stencil on the top of the SIFS multilayer and succeedingly etching the top niobium and the Al/PdNi layers. We note that the latter layers are only removed for the samples with an order number higher than GInsitu-200 in this work. Of course, after the mesa patterning and etching the insulation of the mesa edges is particularly important. We realize it in this work by a self-align deposition of a SiO_2 dielectric layer.

To develop the self-align dielectric deposition, we first evaluate a resist profile

**Fig. 5.11:**

A typical resist profile after etching with SF_6 . A resist layer is spin coated on a niobium layer sputtered onto a 50 nm thermally oxidized silicon substrate and patterned by optical lithography. After a typical etching process (the first step in Table 5.1), the substrate is cleaved and the SEM picture of the resist profile is taken by tilting the sample.

after an etching process. To do so, we sputter a niobium layer on an oxidized silicon substrate. Then, we deposit a photoresist stencil on this sample and pattern it by optical lithography (analogously to the mesa definition). In a last step, an SF_6 etch process (the first process in Table 5.1) mimics mesa etching. This allows, after cleaving the sample, to acquire the SEM micrograph Fig. 5.11 of the resist profile after a niobium etching process. Here, one observes on the left hand side the $\sim 1 \mu\text{m}$ high resist structure on the niobium layer and the silicon substrate. We realize that the resist edge is approximately in line with the niobium edge.

We now transfer our knowledge of the resist profile on the SIFS junction etch process. There, we remove the top niobium layer beside the mesa (using the first process in Table 5.1) and refill the resulting empty space in a self-align process. In detail, we sputter the dielectric SiO_2 and use the etch resist stencil for a lift-off process. Since the resist stencil and the niobium edge are next to the junction approximately in line as we conclude from the analysis above, we do certainly not grow a perfect, gapless connection between the SiO_2 and the top niobium layer, that is, there are some deep valleys between the top niobium layer and the SiO_2 layer extending down to the junction barrier. In these valleys, the succeeding in-situ cleaning of the top niobium electrode with an Ar ion gun removes the PdNi and AlO_x layers, that is, the bottom electrode is partially unprotected prior to the wiring layer deposition. This results for the completed junction in short circuits at the junction edges. Hence, a Josephson junction grown by simply using the etch stencil for the self-align SiO_2 insulation suffers from short circuits between the superconducting electrodes, which destroy the Fraunhofer diffraction pattern like magnetic field dependence of the critical current.

Therefore, we implement an anisotropic resist ashing step before the SiO_2 deposition in our process (the last step in Table 5.1). We observe in Fig. 5.11 a shallow resist

sidewall, so that anisotropic ashing shrinks the resist stencil predominantly at the mesa edges. This way, a lift-off process after the sputter deposition of SiO_2 creates a perfect mesa insulation with a dielectric overgrowing the mesa edges by approximately 150 nm (cf. Fig. 5.4). This securely excludes short circuits at the junction edges. Of course, the ashing step additionally removes contaminants present on the substrate, for which also the third step in Table 5.1 was implemented.

We note that etching the mesa structure out of the multilayer strip requires to protect the substrate beside the strip by photoresist. Of course, to assure that the top niobium layer is completely removed on the multilayer strip, it is necessary to define the resist window slightly larger than the geometry of the multilayer. This naturally results in etching into the substrate near to the multilayer strip edges. However, the etched groove is filled again during the SiO_2 deposition, so that it does not prevent the film growth of the wiring layer, which would result in no electric connection.

5.5 Concluding Remarks

When this work was started, the first evidence of π -coupling across Josephson junctions with a ferromagnetic interlayer has just been found.^{14, 54} The fabrication of the devices was still focused on the growth and the patterning of junctions to examine π -coupling, that is, one looked at the critical current dependence on the ferromagnetic interlayer thickness to identify a transition from zero- to π -coupling; on the other hand, superconducting loops containing zero- and π -junctions were studied to directly prove π -coupling⁵⁵. For this type of studies, one needs only a moderate quality of the interfaces between the different layers of the junctions, that is ex-situ processing of the junctions was possible.

In contrast, we focus in the present work on the dynamics of π -junctions and discuss their application in superconducting quantum electronics. In this case, we need well reproducible Josephson junctions with high critical current densities and $I_c R_n$ products, which requires an in-situ process, that is a process which does not break the vacuum during the junction growth for patterning. Presently, only very few of such processes are available world-wide for the growth of π -junctions with a ferromagnetic interlayer. Here, one has to mention the process of M. Weides, which uses a ferromagnetic NiCu interlayer⁷⁴, and the process introduced within this work. The insulation of the mesa structure is realized by an anodic oxidation step in the first process, that is by an electrolytic process which forms Nb_2O_5 at the edges of the junctions.^{73, 74} We note that the anodization changes the material composition, which may induce strain in the junction. This influences the junction properties and limits the miniaturization for later applications.³³⁹ Because of this, we have implemented a self-align deposition technique to grow a thick dielectric layer within this work. Here, the mesa insulation is realized by a SiO_2 layer, which does not induce strain into the junctions and hence promises better scalability for future applications. Of course, using sputter deposition instead of

anodic oxidation also simplifies the growth process.

The most important parameters for the application of π -junctions in superconducting electronics are the critical current density and the $I_c R_n$ product. Here, the first junctions have been grown with a ferromagnetic interlayer and an additional insulating barrier by T. Kontos *et al.*⁵⁴ with $I_c R_n$ products comparable to our junctions before starting this work; however, these junctions were only based on an ex-situ fabrication process resulting in small critical current densities. Hence, the plasma frequency $\omega_p/2\pi \propto \sqrt{j_c}$ of these junctions was too small for experiments to test macroscopic quantum behavior, and the small critical current densities were insufficient to implement quiet qubits based on these junctions. This situation improved when M. Weides fabricated SIFS junctions based on a ferromagnetic NiCu interlayer with the critical current density $j_c \sim 1 \text{ A/cm}^2$.^{73, 74} However, the plasma frequency $\omega_p/2\pi \sim 10 \text{ GHz}$ was still too small to observe MQT.¹⁵¹ This problem was solved during this work. We reach much higher $j_c \approx 30 \text{ A/cm}^2$ at modest $R_n \cdot A \approx 130 \Omega \mu\text{m}^2$. As we will see in chapter 7, this results in a plasma frequency $\omega_p/2\pi \approx 20 \text{ GHz}$ and in a quality factor $Q_0 \gg 1$, which allows in section 8.4 to cool a junction down into its quantum mechanical ground state. This proves for the first time macroscopic quantum behavior in Josephson junctions with a ferromagnetic interlayer.

We note that nowadays Born *et al.*⁶⁶ further improved the situation by using a ferromagnetic Ni₃Al layer, which allows to go beyond the dirty limit condition. In this case, the decay length ξ_{F1} introduced in section 2.3.2 is completely independent from the oscillation period $2\pi\xi_{F2}$, that is the suppression of the critical current of a junction with the F layer thickness may be much slower than the critical current oscillation due to the exchange coupling. This allows to implement π -junctions with critical current densities an order of magnitude larger than in a PdNi junction where the transport is best described within a dirty limit theory. Naturally, this results in higher plasma frequencies and further improves noise aspects. However, in these junctions neither the dynamic properties nor the macroscopic quantum behavior has been examined.

Chapter 6

THE CROSSOVER BETWEEN 0- AND π -COUPLING, THE CURRENT-VOLTAGE CHARACTERISTICS AND THE MAGNETIC FIELD DEPENDENCE OF THE CRITICAL CURRENT*

In this chapter, we pre-characterize SIFS Josephson junctions fabricated with the process introduced in chapter 5. For these junctions, we first observe a transition from 0- to π -coupling for a thickness $d_F \simeq 6$ nm of the ferromagnetic $\text{Pd}_{0.82}\text{Ni}_{0.18}$ interlayer in section 6.2. Then, we concentrate on the sample GInsitu-203b (oxidation time: 4 h, $d_F = 8.4$ nm), which contains π -coupled junctions. There, we analyze the IVCs of the $20 \times 20 \mu\text{m}^2$ and the $50 \times 50 \mu\text{m}^2$ junction in section 6.3 and demonstrate the good spatial homogeneity of the tunneling barrier and the ferromagnetic interlayer in section 6.4 by studying the magnetic field dependence of the critical current. We start in section 6.1 with the introduction of the 500 mK pumping cryostat measurement setup.

6.1 The 500 mK Measurement Setup

The characterization of the SIFS junctions has been performed in the 500 mK measurement setup shown in Fig. 6.3. The cryogenic part of this setup consists of the gas handling system, which is composed of a ^3He vessel, a cold-trap for gas cleaning and a ^3He pump, and the cryo insert. The latter one is mainly formed by three metal pots, which are concentrically fit into each other. In Fig. 6.3 the cryo insert is directly immersed into a helium storage dewar.



Fig. 6.1: 500 mK setup sample holder with a JJ mounted and bonded on a chip carrier printed circuit board (PCB). One observes the Helmholtz coil surrounding the PCB and the bonded sample. In the measurements a cryoperm or a brass pot protects the wiring and shields the sample.

The setup works in the following manor: A vacuum between the outer and the middle pot of the cryo insert thermally decouples the two inner pots from the liquid

* This chapter is based on the publication Ref. [A2].

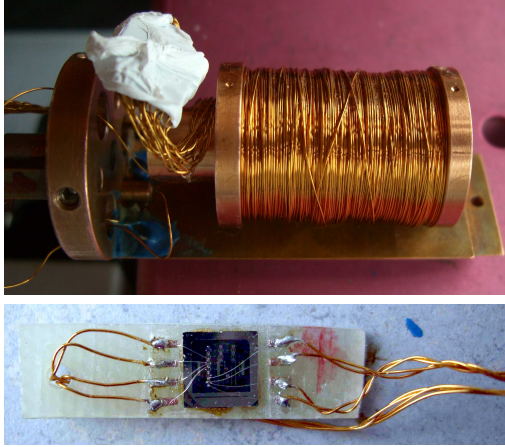


Fig. 6.2: The 500 mK setup high field coil 2 (top) and a sample mounted and bonded on an appropriate chip carrier PCB (bottom). With the Helmholtz coil in Fig. 6.1, only small magnetic fields $\ll 100$ mT may be applied. Therefore, a high field setup (top) was designed for the analysis in Fig. 6.9 to provide > 100 mT. Here, a copper wire is used in contrast to the Helmholtz coil setup. This allows to cool a junction down in an applied magnetic field. We note that this would be impossible with a superconducting wire due to its high normal conducting resistance. The sample is mounted on a PCB (bottom), which is fed into the 10 mm bore of the coil.

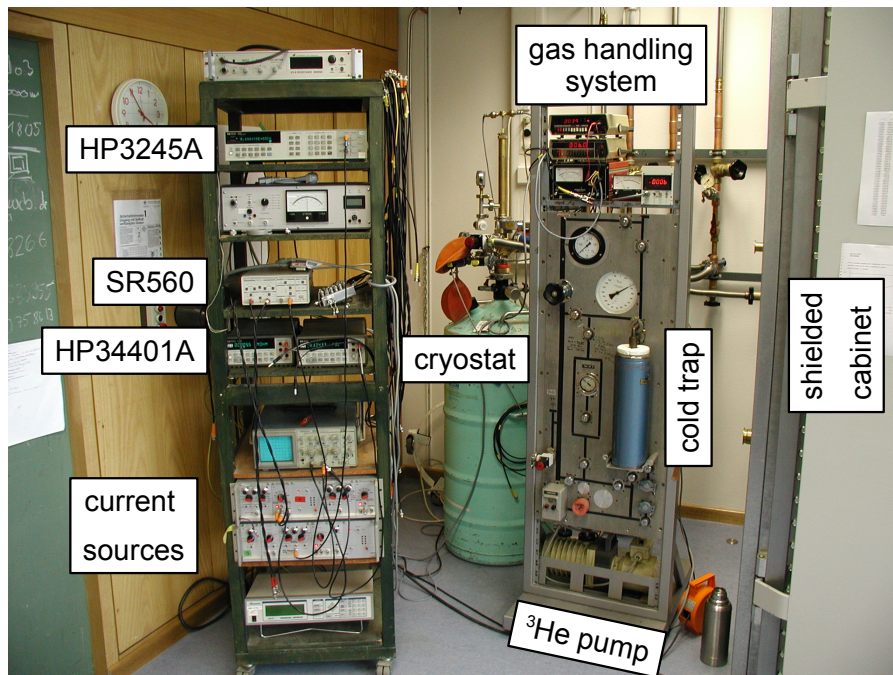


Fig. 6.3: Photograph of the 500 mK measurement setup. Shown is one of the first experiments in a helium storage dewar, while the actual experiments have been taken with the dip-stick inside the shielded cabinet in a glass fiber reinforced cryostat (cf. Fig. 6.4).

^4He reservoir. During operation, the space between the middle and the inner pot is permanently pumped by a vacuum pump, which allows to expand ^4He via an impedance from the helium reservoir into this volume. Obviously, this cools the sample insert by the Joule-Thompson effect down to about 1.5 K. At this temperature, ^3He gas from the gas handling system may be liquefied into the inner pot containing the sample holder.³⁴⁰ Evaporating this ^3He liquid by pumping on the inner volume results during the experiments in a typical ^3He liquid temperature of around 500 mK in the sample pot.³⁴¹ In the actual measurements, the copper sample holder shown in Fig. 6.1, which was developed within this work to mount the sample parallel to the cryo insert, is partially immersed into this liquid. The thermal coupling of the sample to the sample holder is realized in multiple ways:

First, the wiring lines are thermally anchored to the sample holder[†]; second, the silicon substrate containing the JJ is glued on a printed circuit board (PCB), which is thermally connected via vacuum grease to the sample holder; third, a finite amount of ^3He gas is available for the thermal transport. On the sample holder, a superconducting Helmholtz coil is mounted to apply small magnetic fields aligned parallel to the junction barrier. For the measurements where higher magnetic fields are needed (e.g. for magnetizing the F layer in the analysis shown in Fig. 6.9), a sample holder with a normal conducting coil (cf. Fig. 6.2) was implemented, too.

During the present work, the cryogenic part of the setup has been extensively expanded. It is now permanently mounted in a dewar setup in a shielded cabinet (cf. Fig. 6.4).

Since it is not possible to exchange the samples inside the shielded room for space reasons, the mechanical mounting containing the dewar and the cryo insert is movable to outside of the cabinet on a mechanical rail system. There, the dewar position may be lowered to the laboratory floor via an elevation mechanism, which enables the user to easily exchange samples and to refill the dewar. The setup uses a glass fiber reinforced dewar, which is mechanically clamped onto the mounting. It is magnetically shielded by three concentric mumetal³⁴² pots. To preserve the hermetic rf sealing of the shielded cabinet, the gas supply lines and the electrical connections are established through the

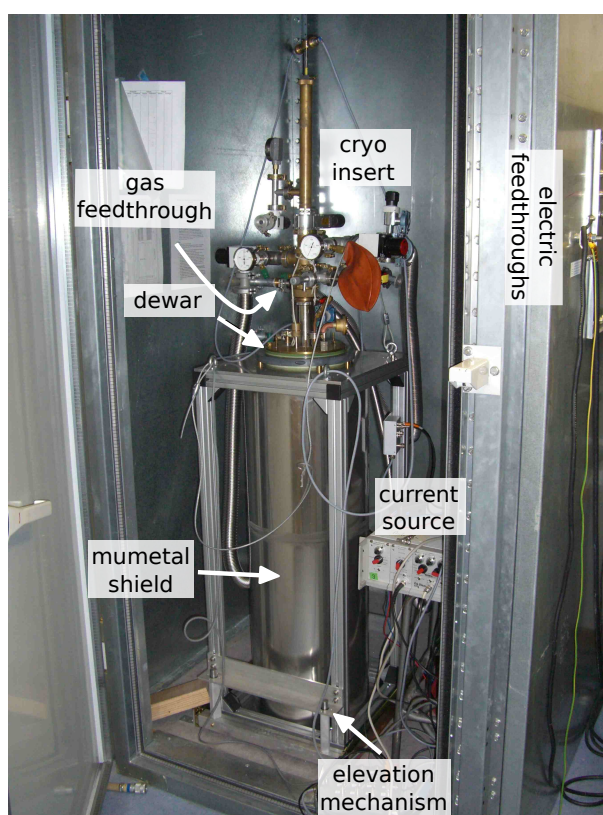


Fig. 6.4: Photograph of the 500 mK dewar setup.

[†] The lines are glued in ceramic tubes mounted in the sample holder.

cabinet wall via commercially available feedthroughs, so that the ^3He supply can be provided from outside of the shielded room.

The electronic setup has also been completely reworked during this thesis. The electrical transport measurements are performed in a four-probe configuration as discussed in Fig. 5.6. A schematic diagram of the wiring is given in Fig. 6.5. Here, one observes that the voltage across the device under test is amplified by a Stanford Research low-noise voltage preamplifier SR 560. The current across the junction is provided by a home made, battery powered current source. Both are placed inside the shielded room and electrically connected via the electrical feedthroughs through the cabinet wall. The current source is externally controlled from outside of the shielded room by the voltage source V_{in} (during the process development by an HP 3245A universal source, later on by an Agilent 33250A arbitrary waveform generator); the preamplifier output is digitalized via a digital multimeter HP 34401A on V_{out} . Derivatives of the IVCs have been taken using a lock-in technique utilizing a Stanford Research SR 530 lock-in amplifier. The whole measurement process was automated via different LabView³⁴³ programs within this work. They allow among other things to acquire IVCs and $dV/dI(V)$ dependencies whereby the applied magnetic field may be computer-controlled. This was essential to acquire the data for Figs. 7.1 and 7.2, which required a measurement time of more than one day.

6.2 The Critical Current Dependence on the Ferromagnetic Interlayer Thickness*

We next discuss the dependence of the characteristic junction voltage $V_c = I_c R_n$ on the thickness d_F of the ferromagnetic interlayer. The V_c values of about 40 junctions with different d_F and junction areas A ranging from $5 \times 5 \mu\text{m}^2$ to $50 \times 50 \mu\text{m}^2$ are plotted in Fig. 6.6 versus the thickness d_F of the F layer. To achieve these data, a series of junctions with different d_F was fabricated with otherwise identical parameters. In particular, all junctions have AlO_x barriers obtained by a 90 min long thermal oxidation process, resulting in $R_n \cdot A \simeq 40 \Omega \mu\text{m}^2$. This series clearly shows a change of sign in the slope of the $I_c R_n(d_F)$ dependence at a $\text{Pd}_{0.82}\text{Ni}_{0.18}$ layer thickness of $d_F \simeq 6 \text{ nm}$. At this d_F value I_c approaches zero. This feature is a clear signature of the crossover from 0 - to π -coupling on increasing d_F , corresponding to a change of sign of I_c . Obviously, in the experiment we can only measure the modulus of I_c .

In order to theoretically describe the behavior shown in Fig. 6.6, one has to distinguish different regimes defined by three energy scales.⁴³ These scales are the exchange energy E_{ex} in the ferromagnet, the energy gap Δ of the superconductor, and \hbar/τ where τ is the elastic scattering time in the ferromagnet. In our samples $E_{\text{ex}} \gg \Delta$ ($\Delta_{\text{Nb}} = 1.45 \text{ meV}$) as in the overwhelming part of other reports on SFS or SIFS junctions. However, there is a significant variation in \hbar/τ relative to the other two energy scales. The true clean-limit holds for $E_{\text{ex}}, \Delta \gg \hbar/\tau$. In this case, the mean free path $\ell = v_F \tau$

* This section is based on the publication Ref. [A2].

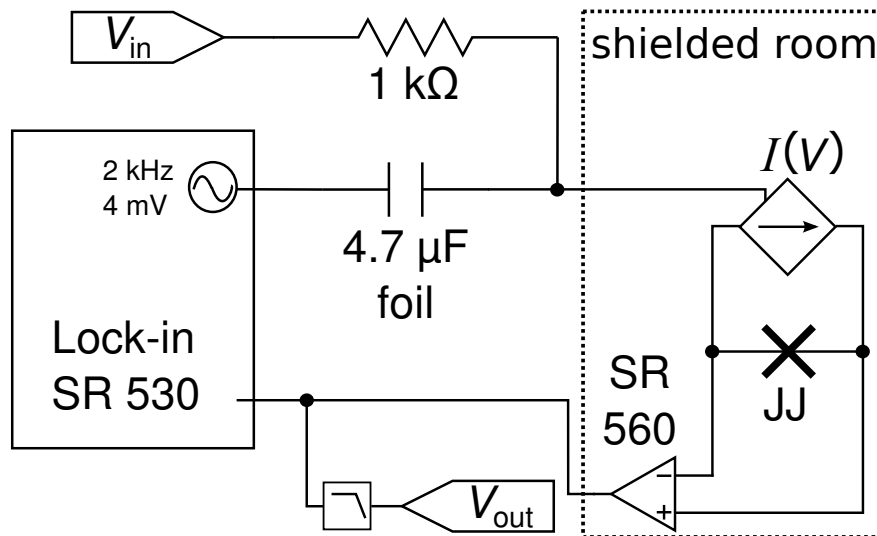


Fig. 6.5: Schematic diagram of slow-sweep measurements. The IVCs and the dependence of the differential resistance on the applied bias voltage have been simultaneously acquired within this work. Therefore, in slow-sweep measurements a tiny ac current was superimposed to the dc bias current. This was realized by adding the oscillator voltage of an SR 530 lock-in amplifier to the computer-controlled dc voltage V_{in} where $|V_{in}| < 10\text{ V}$. This voltage is fed into the voltage-controlled current source $I(V)$, which provides the bias current across the JJ. The voltage across the JJ is amplified by an SR 560 low-noise voltage preamplifier and fed into the lock-in amplifier and after low-pass filtering into a digital multimeter (V_{out}).

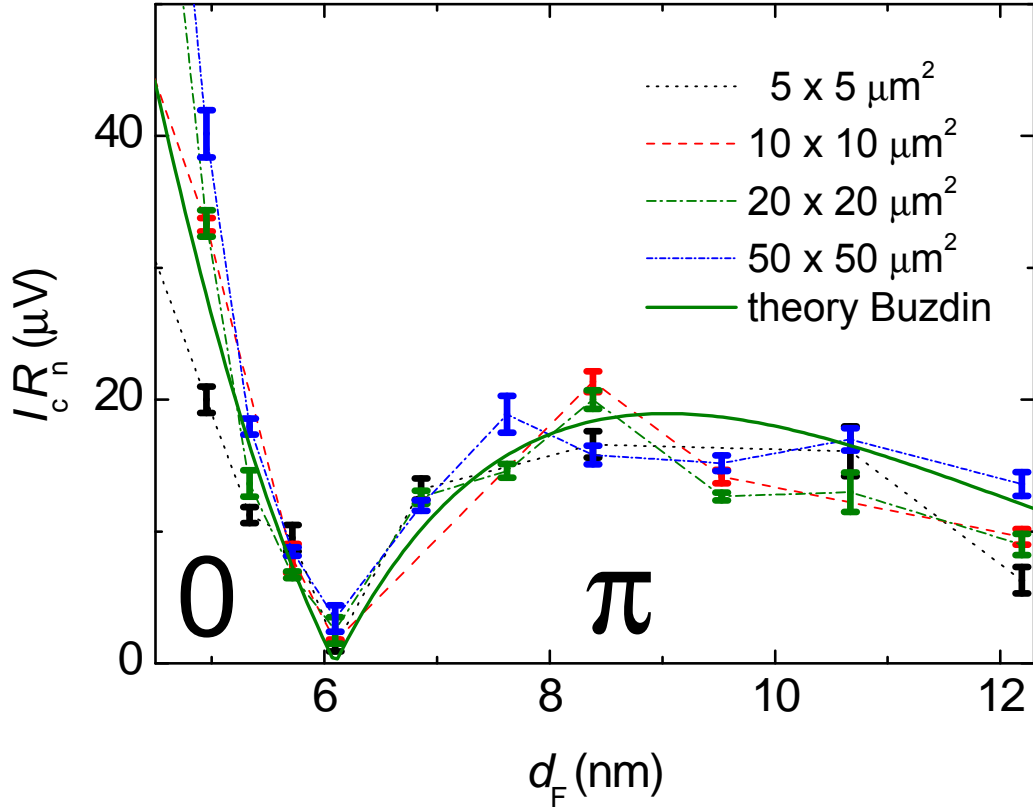


Fig. 6.6: Dependence of the $I_c R_n$ -product of SIFS junctions on the thickness d_F of the ferromagnetic $\text{Pd}_{0.82}\text{Ni}_{0.18}$ layer for samples with different junction areas. The broken lines are guides to the eye. The olive line is a fit of the data to the theory of Buzdin *et al.*³³ using $\xi_F = 3.88$ nm and $\pi\Delta_1\Delta_2/ek_B T_c = 280$ μV .

is large compared to the clean-limit superconducting coherence length $\tilde{\xi}_s = \hbar v_F / \pi\Delta$ and exchange length $\tilde{\xi}_F = \hbar v_F / 2E_{\text{ex}}$. Here, v_F is the Fermi velocity in the respective material. The true dirty limit holds for $E_{\text{ex}}, \Delta \ll \hbar/\tau$. In this case, the mean free path $\ell = v_F \tau$ is the smallest length scale and the dirty-limit superconducting coherence length $\xi_s \simeq \sqrt{\tilde{\xi}_s \ell} \simeq \sqrt{\hbar D / \pi\Delta}$ and exchange length $\xi_F \simeq \sqrt{\tilde{\xi}_F \ell} \simeq \sqrt{\hbar D / E_{\text{ex}}}$ are given by the geometric mean. Here, D is the diffusion coefficient in the respective material. There is also an intermediate regime, where $E_{\text{ex}} > \hbar/\tau$ and $\Delta < \hbar/\tau$, which is the most complicated situation. This regime may particularly apply for a ferromagnet with large E_{ex} .

Due to the small mean free path in the PdNi alloy and Nb films, for our samples the simple dirty limit holds. Several theoretical models have been proposed for this limit.^{16, 33, 43, 54, 344–346} For weak ferromagnets such as PdNi the spin-up and spin-down subbands can be treated identically (same Fermi velocity and mean free path) resulting

in a single characteristic length scale

$$\xi_F = \sqrt{\frac{\hbar D}{E_{\text{ex}}}} \quad (6.1)$$

for the decay and oscillation of the critical current as a function of d_F . We note, however, that in the presence of spin-flip or spin-orbit scattering the decay and oscillation of I_c is governed by two different length scales.^{16, 344–346}

The solid olive line in Fig. 6.6 is obtained by fitting the data using the simple dirty limit expression

$$I_c R_n = \frac{\pi \Delta_1 \Delta_2}{ek_B T_c} \left| \frac{\cos(x) \cosh(x)}{\cos(2x) + \cosh(2x)} \right| \quad (6.2)$$

with $x = d/\xi_F$ of Buzdin *et al.*³³ Here, $T_c = 9.2$ K is the critical temperature of the niobium layers, e the elementary charge, and Δ_1 and Δ_2 are the superconducting order parameters just at the boundary with the ferromagnetic layer. They are certainly much smaller than the superconducting gap in bulk niobium but difficult to be determined in the geometry of our experiment. The fit yields $\xi_F = 3.88$ nm and $\frac{\pi \Delta_1 \Delta_2}{ek_B T_c} = 280 \mu\text{V}$. The value $\xi_F = 3.88$ nm found for our SIFS junctions agrees very well with literature values.^{33, 54, 347} The value of $280 \mu\text{V}$ found for $\frac{\pi \Delta_1 \Delta_2}{ek_B T_c}$ for our SIFS junctions is larger than the value of $110 \mu\text{V}$ obtained by Kontos and coworkers.^{33, 54} Unfortunately, the detailed comparison of different experiments is difficult because the authors often do not state whether they are plotting $I_c R_n(d_F)$ or $I_c R_{\text{sg}}(d_F)$. If we use the much higher subgap resistance R_{sg} , the corresponding value derived for $\frac{\pi \Delta_1 \Delta_2}{ek_B T_c}$ would be about ten times larger. We finally note that the measured $I_c(d_F)$ dependence can be well explained by dirty limit theory with a single length scale ξ_F , suggesting that spin-flip or spin-orbit scattering do not play a dominant role.

Beyond the parameter ξ_F describing the characteristic length of superconducting correlations in the F layer, the dimensionless parameter

$$\gamma_B = \frac{\rho_B \sigma_F}{\xi_F} \quad (6.3)$$

is used to describe ferromagnetic Josephson junctions. It characterizes the transparency of the F/S interfaces with ρ_B the interface resistance times area and σ_F the conductivity of the F layer. In general, two γ_B values for the two F/S interfaces have to be used. In our experiment the presence of the additional AlO_x barrier at one F/S boundary can be modeled by a very low transparency interface ($\gamma_{B1} \gg 1$), while the other boundary has high transparency ($\gamma_{B2} \ll 1$) for the in-situ fabricated stacks, i.e. $\gamma_B \simeq \gamma_{B1}$. We further note that in general the measured total $R_n \cdot A$ product can be expressed as

$$R_n \cdot A = \rho_{\text{tun}} + \rho_{\text{int}} + \frac{d_F}{\sigma_F} . \quad (6.4)$$

Here, ρ_{tun} and ρ_{int} are the resistance times area values due to the tunneling barrier and the PdNi/Nb interfaces. For our junctions, $\rho_{\text{tun}} \gg \rho_{\text{int}}$ and, moreover, $\rho_{\text{tun}} \gg d_F/\sigma_F$.

With $\sigma_{\text{PdNi}} \simeq 10^7 \Omega^{-1} \text{m}^{-1}$, we estimate $d_{\text{F}}/\sigma_{\text{F}} \simeq 10^{-3} \Omega \mu \text{m}^2$ which is by about five orders of magnitude smaller than the measured $R_{\text{n}} \cdot A$ values. That is, the contribution of the F layer to $R_{\text{n}} \cdot A$ is negligible. Hence, $R_{\text{n}} \cdot A \simeq \rho_{\text{tun}}$, meaning that the measured $R_{\text{n}} \cdot A$ values are dominated by the AlO_x tunneling barrier as expected. In this case, we can write $\gamma_{\text{B}} \simeq R_{\text{n}} A \sigma_{\text{F}}/\xi_{\text{F}}$. With $\sigma_{\text{PdNi}} \simeq 10^7 \Omega^{-1} \text{m}^{-1}$, $\xi_{\text{F}} = 3.88 \text{ nm}$ and the measured $R_{\text{n}} \cdot A$ value of about $40 \Omega \mu \text{m}^2$ for this junction series, we estimate $\gamma_{\text{B}} \simeq 10^5$. This high value is not surprising due to the additional tunneling barrier in our junctions.

The derived ξ_{F} values can be used to estimate the exchange energy in PdNi. Using a Fermi velocity $v_{\text{F}} \simeq 5 \times 10^5 \text{ m/s}$ ³⁴⁸ and the fact that the mean free path ℓ for the very thin PdNi layers is about given by the film thickness d_{F} , we obtain $D \simeq v_{\text{F}} \ell \simeq v_{\text{F}} d_{\text{F}} = 5 \times 10^{-3} \text{ m}^2/\text{s}$ for $d_{\text{F}} = 10 \text{ nm}$. With this value we derive $E_{\text{ex}} \simeq \hbar D/\xi_{\text{F}}^2 \simeq 20 \text{ meV}$ using $\xi_{\text{F}} = 3.88 \text{ nm}$. This value is in good agreement with values between about 10 and 50 meV quoted in previous work.^{54, 63, 349, 350} With the same numbers we obtain $\hbar/\tau \simeq \hbar v_{\text{F}}/d_{\text{F}} \simeq 30 \text{ meV}$. This shows that the SIFS junctions with a PdNi interlayer are close to the intermediate regime since $E_{\text{ex}} \sim \hbar/\tau$.

6.3 The Current-Voltage Characteristics*

Figures 6.7a and 6.8a show the IVCs of two π -coupled SIFS junctions with the junction areas $A = 20 \times 20 \mu \text{m}^2$ and $50 \times 50 \mu \text{m}^2$ (GInsitu-203b; $d_{\text{F}} = 8.4 \text{ nm}$; oxidation time: 4 h). From the IVCs we can determine several relevant junction parameters. First, the current value for the switching from the zero to the finite voltage state and vice versa gives the critical current I_{c} and the so-called retrapping current I_{r} (see the insets of Figs. 6.7a and 6.8a). The corresponding current densities j_{c} and j_{r} are obtained by dividing by the junction area A . From j_{c} together with the effective magnetic thickness t_{B}^{j} of the junction (cf. Eq. (3.48)) the Josephson penetration depth $\lambda_{\text{J}} = \sqrt{\hbar/2e\mu_0 t_{\text{B}}^{\text{j}} j_{\text{c}}}$ is derived. At $T = 2 \text{ K}$ we obtain $\lambda_{\text{J}} \simeq 70 \mu \text{m}$. Since this value is larger than the lateral junction dimensions, we are in the small Josephson junction limit. Using the simple resistively and capacitively shunted junction (RCSJ) model introduced in section 3.1, we can further derive the junction quality factor $Q_{\text{IVC}} = \sqrt{\beta_{\text{C}}} = \omega_{\text{p}}/\omega_{\text{RC}} = 4I_{\text{c}}/\pi I_{\text{r}}$. Here, β_{C} is the Stewart-McCumber parameter, ω_{p} the junction plasma frequency, and $1/\omega_{\text{RC}}$ the RC time constant of the junction. Second, from the asymptotic behavior at voltages large compared to the gap sum voltage the normal resistance R_{n} and the normal resistance times area product $R_{\text{n}} \cdot A$ are obtained, which are about temperature independent. The R_{n} value has to be distinguished from the temperature dependent subgap resistance R_{sg} obtained from the slope of the IVCs at voltages well below the gap sum voltage. For SIFS junctions, R_{sg} is expected to increase with decreasing temperature in agreement with the experimental data. At 2 K, for our SIFS junctions R_{sg} is almost an order of magnitude larger than R_{n} .

We note that the values of I_{c} and I_{r} may be reduced and enhanced, respectively, by premature switching due to thermal activation or external high-frequency noise.

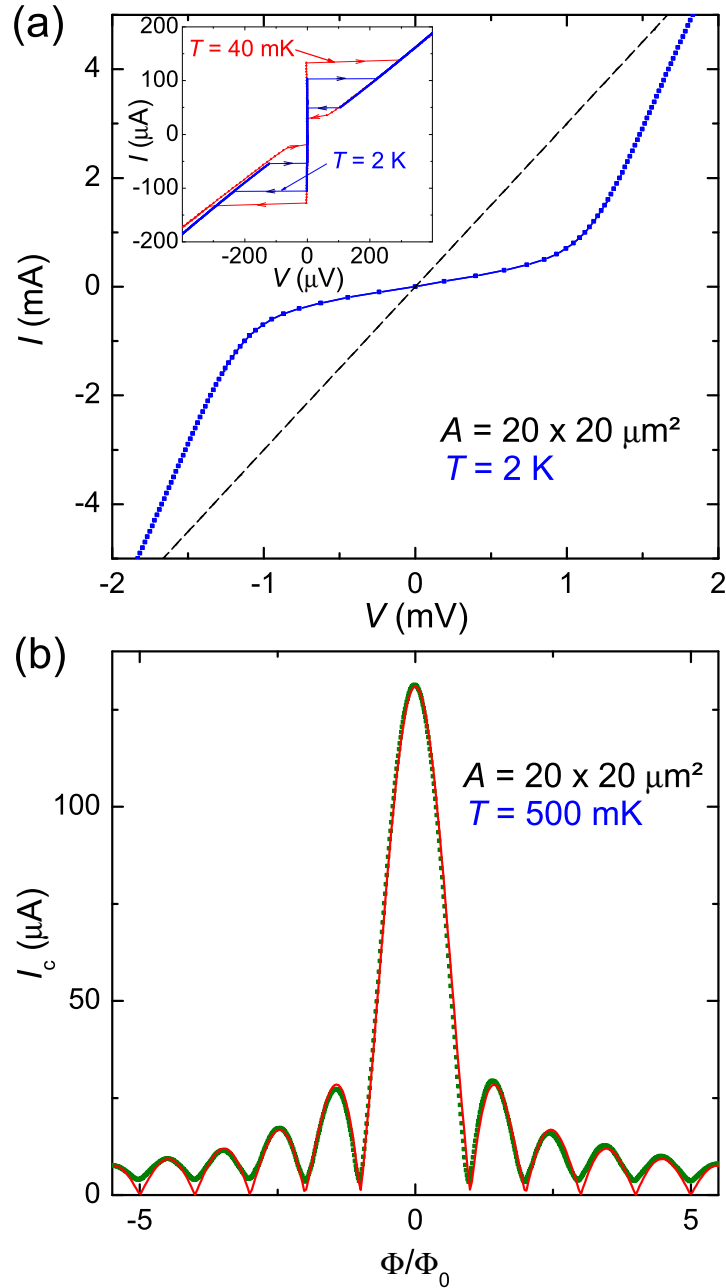


Fig. 6.7: The IVCs (a) and the magnetic field dependence of the critical current I_c (b) obtained for the π -coupled SIFS junction with $A = 20 \times 20 \mu\text{m}^2$ of the sample GInsitu-203b. The IVCs (a) is measured at 2 K. The dashed line indicates the ohmic behavior $V = IR_n$ approached at large voltages. The inset shows an enlarged view of the IVCs around zero voltage measured at 2 K (blue line) and 40 mK (red line). The $I_c(\Phi)$ dependency (b) is taken at 500 mK in a magnetic field applied parallel to the junction barrier (green squares) and fit to a Fraunhofer pattern (red line). The total magnetic flux $\Phi = \Phi_H + \Phi_M$ threading the junction originates from the applied magnetic field (Φ_H) and the magnetization of the F interlayer (Φ_M).

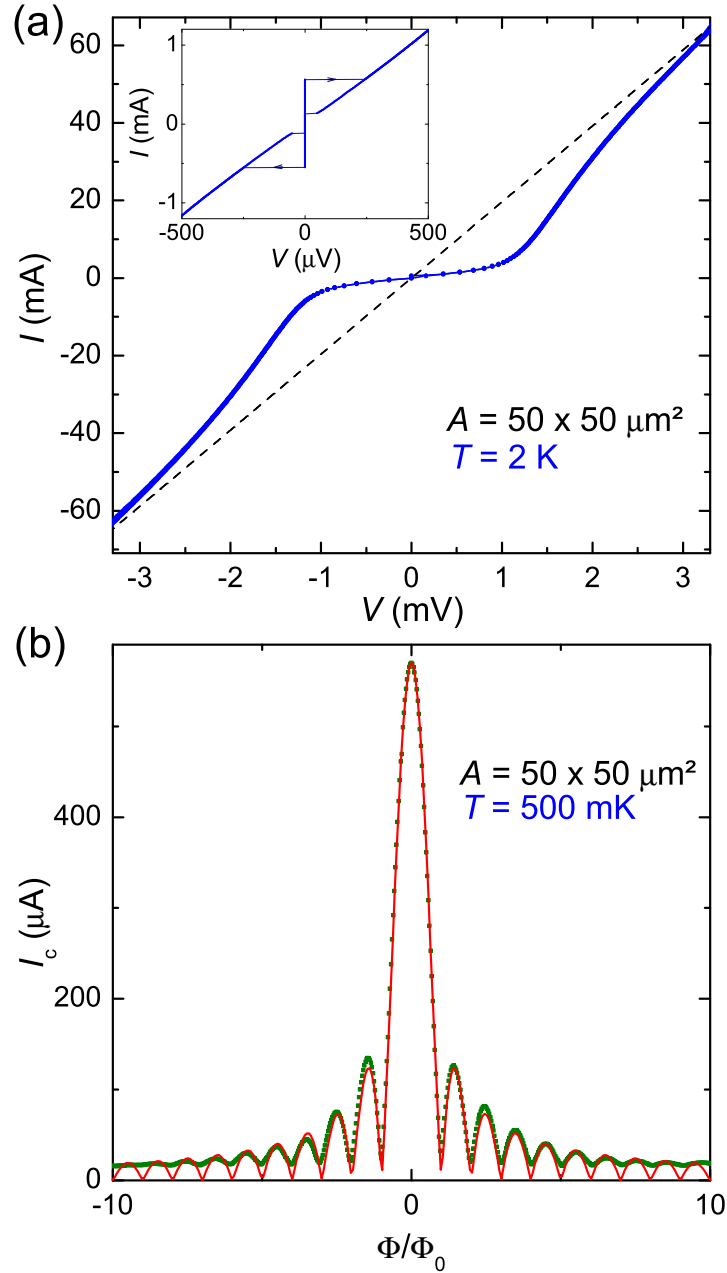


Fig. 6.8: The IVCs (a) and the magnetic field dependence of the critical current I_c (b) obtained for the π -coupled SIFS junction with $A = 50 \times 50 \mu\text{m}^2$ of the sample GInsitu-203b. The IVCs (a) is measured at 2K. The dashed line indicates the ohmic behavior $V = IR_n$ approached at large voltages. The inset shows an enlarged view of the IVCs around zero voltage. The $I_c(\Phi)$ dependency (b) is taken at 500 mK in a magnetic field applied parallel to the junction barrier (green squares) and fit to a Fraunhofer pattern (red line). The total magnetic flux $\Phi = \Phi_H + \Phi_M$ threading the junction originates from the applied magnetic field (Φ_H) and the magnetization of the F interlayer (Φ_M).

Tab. 6.1: Critical current and resistance values obtained from the IVCs of the SIFS junctions of the sample GInsitu-203b ($d_F = 8.4$ nm; oxidation time: 4 h) shown in Figs. 6.7a and 6.8a and parameters derived from them. The quantities are listed for the $50 \times 50 \mu\text{m}^2$ and $20 \times 20 \mu\text{m}^2$ junction at 2 K and 40 mK, respectively.

A (μm^2)	20×20	50×50
T (K)	40 mK	2 K
I_c (μA)	131	555
j_c (A/cm^2)	33	22
I_T (μA)	27	125
R_n (Ω)	0.33	0.051
$R_n \cdot A$ ($\Omega\mu\text{m}^2$)	133	128
R_{sg} (Ω)	2.14	0.44
$I_c R_n$ (μV)	44	28.3
$I_c R_{sg}$ (μV)	280	244
λ_J (μm)	59	71
Q_{IVC}	6.2	5.7

This is particularly true for small area junctions with small absolute values of I_c and I_T . In turn, this results in reduced values of the quality factor. This effect is shown in the inset of Fig. 6.7a where IVCs of a $20 \times 20 \mu\text{m}^2$ junction are shown for $T = 2$ K and 40 mK. The 40 mK data were taken in a well shielded dilution refrigerator using various filters at different temperature stages in the current and voltage lines, including stainless steel powder filters.^{351, 352} Clearly, at 40 mK significantly larger I_c and smaller I_T values are observed resulting in an about three times larger quality factor $Q_{IVC} = 6.2$. These enhanced/reduced values are only partly caused by lowering the temperature but mostly by the reduced thermal and external noise. For large area junctions this effect is negligible. Here, I_c and I_T are large, making the relative effect of the equivalent noise current very small. For example, at $T = 2$ K $Q_{IVC} = 5.7$ is obtained for the $50 \times 50 \mu\text{m}^2$ junction, whereas $Q_{IVC} < 2$ for the $20 \times 20 \mu\text{m}^2$ junction fabricated on the same chip. This small quality factor is related to the smaller I_c and I_T values of the small area junction, making it more susceptible to thermal and external noise. In Table 6.1 we have tabulated the junction parameters derived from the IVCs of the $50 \times 50 \mu\text{m}^2$ and $20 \times 20 \mu\text{m}^2$ junction at 2 K and 40 mK, respectively.

6.4 The Magnetic Field Dependence of the Critical Current*

Figures 6.7b and 6.8b show the magnetic field dependence of the critical current of the SIFS Josephson junctions from section 6.3 measured at 500 mK (green squares). The dependencies are close to a Fraunhofer diffraction pattern (red line)

$$I_c(H) = I_c(0) \left| \frac{\sin(\pi\Phi/\Phi_0)}{\pi\Phi/\Phi_0} \right| \quad (6.5)$$

expected for an ideal short Josephson junction with a spatially uniform j_c . This demonstrates that our SIFS junctions have good uniformity of j_c across the junction area, that is a spatially homogeneous tunneling barrier and ferromagnetic interlayer. In particular, there are no short circuits at the junction edges or the surrounding SiO₂ wiring insulation. Of course, direct information on junction inhomogeneities on smaller length scales can be obtained by Low Temperature Scanning Electron Microscopy.^{353–356}

We note that the total magnetic flux Φ threading the junction is composed of the flux Φ_H due to the applied external magnetic field and the flux Φ_M due to the magnetization of the ferromagnetic layer. The two components are given by

$$\Phi_H = \tilde{t}_B^j L^j \mu_0 H, \quad (6.6)$$

$$\Phi_M = d_F L^j \mu_0 M. \quad (6.7)$$

Here, L^j is the lateral dimension of the rectangular junction perpendicular to the field direction, d_F the thickness of the F interlayer, and \tilde{t}_B^j the effective magnetic thickness of the junction given by Eq. (3.49). Since the applied magnetic field $H_{\Phi_0} = \Phi_0/\mu_0 L^j \tilde{t}_B^j$ required for the generation of a single flux quantum in the junction is less than about 1 mT for $10 \mu\text{m} \leq L^j \leq 50 \mu\text{m}$, the typical field range used in the measurement of the $I_c(\Phi/\Phi_0)$ curves of Figs. 6.7b and 6.8b is restricted to less than about 10 mT. For such small in-plane magnetic fields the $M(H)$ -curve of the ferromagnetic PdNi layer (cf. Fig. 5.10a) can be well approximated by a linear dependence $M \simeq (\mu - 1)H$ with $\mu = 1.8$. With this approximation the total magnetic flux threading the junction can be expressed as

$$\begin{aligned} \Phi &= \mu_0 H L^j (\tilde{t}_B^j - d_F) + \mu_0 \mu H L^j d_F \\ &= \mu_0 H L^j \tilde{t}_B^j \left(1 + (\mu - 1) \frac{d_F}{\tilde{t}_B^j} \right). \end{aligned} \quad (6.8)$$

Here, M is the magnetization component parallel to the applied magnetic field. If there is a significant in-plane magnetic anisotropy of the ferromagnetic material, this component may be much smaller than the absolute value of the magnetization. Furthermore, there can be a complicated domain structure. In this case, M is the average magnetization

parallel to the field direction; we note that in the latter case also the domain wall structure may play a role.^{357, 358}

We can use Eq. (6.8) to estimate the magnitude of the additional magnetic flux Φ_M due to the F layer. For the junctions of Figs. 6.7 and 6.8, $d_F = 8.4$ nm and hence $d_F/\tilde{t}_B^j \simeq 0.05$. Therefore, for $\mu = 1.8$ the second summand in the brackets of Eq. (6.8) amounts to only about 0.04. That is, compared to a junction without an F interlayer the total flux is enhanced only by about 4%. Due to the uncertainties in λ_L and the geometrical dimensions of the junctions, this small effect is difficult to prove. Furthermore, since the virgin part of the hard axis $M(H)$ -curve of the PdNi layer is about linear at small fields with negligible hysteresis, the $I_c(\Phi/\Phi_0)$ curves are expected to show negligible hysteresis on sweeping back and forth the applied magnetic field. This is in agreement with our data and measurements on SIFS junctions with ferromagnetic NiCu interlayers.³⁵⁹ We note, however, that Φ_M strongly depends on the magnetic history when magnetic fields $\mu_0 H > 50$ mT are applied. This can be seen in the measurement shown in Fig. 6.9 where we magnetize a $50 \times 50 \mu\text{m}^2$ SIFS Josephson junction in different in-plane magnetic fields and acquire $I_c(H)$ after cycling the sample above the critical temperature T_c of niobium. There, we observe for not too large magnetization a simple shift of the Fraunhofer pattern. In contrast, at high magnetization, which we technically realize by cooling the JJ down in a magnetic field, we do not observe a Fraunhofer pattern (see the inset of Fig. 6.9). Here, most likely heating the JJ above T_c is not enough to get rid of Abrikosov vortices trapped in the Nb junction electrodes.³⁶⁰

6.5 Concluding Remarks

In the preceding sections, we have analyzed SIFS Josephson junctions grown with the process introduced in chapter 5. For these junctions, we identify a transition from 0- to π -coupling for a thickness $d_F \simeq 6$ nm of the Pd_{0.82}Ni_{0.18} layer, which can be well explained by the dirty limit theory of Buzdin *et al.*³³ with the single length scale $\xi_F = 3.88$ nm. With this knowledge, we concentrate on a single sample containing π -coupled junctions and analyze in detail the current-voltage characteristics of a $20 \times 20 \mu\text{m}^2$ and a $50 \times 50 \mu\text{m}^2$ SIFS π -junction. Here, we extract a high critical current density $j_c \approx 30$ A/cm² at modest $R_n \cdot A \approx 130 \Omega \mu\text{m}^2$ and an intrinsic quality factor $Q_0 \sim 6$. These parameters compete very well with junctions reported in literature^{54, 73, 74} and are already sufficient for the application of the junctions in quantum information processing and to test their macroscopic quantum behavior. Finally, we prove the homogeneity of the junction barrier and the ferromagnetic interlayer by observing a Fraunhofer diffraction pattern for the critical current dependence on the applied magnetic field. This qualifies the junctions for further experiments related to standing electromagnetic waves across the junction barrier and especially for a careful analysis of the Fiske resonances in chapter 7.

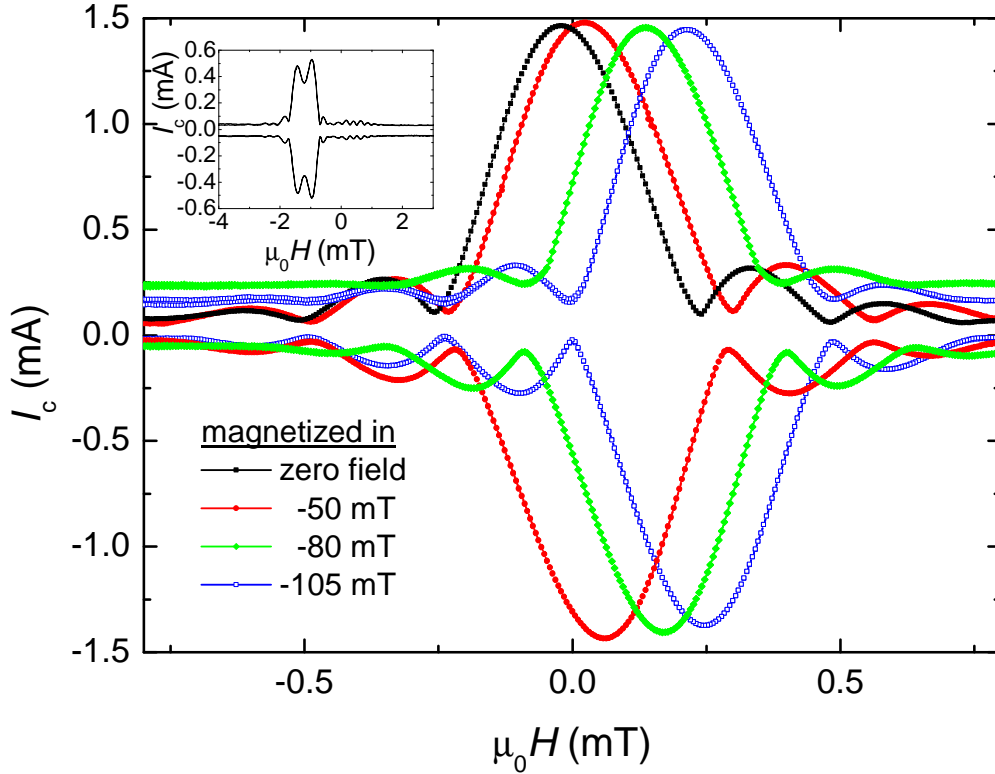


Fig. 6.9: Dependence of the critical current I_c on the applied in-plane magnetic field H for a $50 \times 50 \mu\text{m}^2$ SIFS Josephson junction (GInsitu-186; $d_F = 8.4 \text{ nm}$; oxidation time: 2 h) with the ferromagnetic interlayer magnetized in different in-plane magnetic fields measured at 2 K. The black line represents the positive critical current I_c versus the applied in-plane magnetic field H after the junction was thermally cycled to $\sim 170 \text{ K}$. This is well above the critical temperature $T_{c,\text{Nb}}$ of niobium and slightly above the Curie temperature $T_{c,\text{PdNi}}$ of $\text{Pd}_{0.82}\text{Ni}_{0.18}$. We note that we, nevertheless, observe a tiny remanent magnetization due to an insufficient magnetization relaxation of the preceding experiment. After this measurement, we apply three different in-plane magnetic fields decreasing from -50 mT to -80 mT and -105 mT , thermally cycle each time the junction above $T_{c,\text{Nb}}$ to remove Abrikosov vortices, and acquire $I_c(H)$. In this case, we observe an increasing shift of the Fraunhofer pattern to higher magnetic fields. This clearly identifies a negative magnetization of the interlayer. We note that for a visible effect a field of 50 mT is necessary, which is far above the fields we apply to examine $I_c(H)$. The inset shows the $I_c(H)$ dependence for the JJ field-cooled in $+20 \text{ mT}$ and thermally cycled above $T_{c,\text{Nb}}$. Here, the resulting high magnetization most probably traps Abrikosov vortices in the junction electrodes. The characteristic double-peaked $I_c(H)$ dependence reminds to the one observed in $0-\pi$ Josephson junctions.¹⁰⁷

Chapter 7

THE FISKE RESONANCES AND THEIR QUALITY*

In this chapter, we examine the Fiske resonances in the $20 \times 20 \mu\text{m}^2$ and the $50 \times 50 \mu\text{m}^2$ junction of the sample GInsitu-203b, which we have already pre-characterized in chapter 6. The Fiske steps are clearly visible in the IVCs shown in Fig. 7.1 and the derivatives dV/dI plotted in Fig. 7.2. These data are recorded for the junction with area $A = 50 \times 50 \mu\text{m}^2$ at different magnetic fields applied parallel (z -direction) and perpendicular (y -direction) to the bottom electrode. The dV/dI versus V curves are measured by a lock-in technique. In the case of negligible damping, the resonances are very sharp at almost constant voltages. However, in reality the resonances are damped due to different loss mechanisms. For planar type SIFS junctions as studied in our work, the junction damping due to radiation losses is small due to the large electromagnetic impedance mismatch at the junction boundaries (cf. Eq. (3.32)). Then, the quality factors Q_n of the Fiske resonances are given mainly by the internal losses, most likely due to quasiparticle tunneling and the finite surface resistance. In general, the detailed analysis of the Fiske resonances can provide information on the damping mechanisms in Josephson junctions at very high frequencies.

When analyzing the voltage position of the Fiske resonances in detail, we have to take into account the idle region next to the junction area (cf. Fig. 3.6). As discussed in section 3.2.6, this idle region results in an increase or decrease of the phase velocity v_{ph} compared to the Swihart velocity \bar{c} of an ideal junction without any idle region, depending on whether the idle region is lateral or longitudinal, respectively. In turn, this causes an increase or decrease of the characteristic voltages $V_n = n \frac{\Phi_0 v_{\text{ph}}}{2L_j}$. For $H \parallel y$, the resonant modes are extending in z -direction, that is, parallel to the idle region (lateral mode). In this case, the effect on the phase velocity is described by Eq. (3.50), and we expect a slight increase of v_{ph} and V_n . Analogously, for $H \parallel z$ the resonant modes are extending in y -direction, that is, perpendicular to the idle region (longitudinal mode). In this case, the effect on the phase velocity is described by Eq. (3.51), and we expect a slight decrease of v_{ph} and V_n . This is in good qualitative agreement with our experimental observation. For $H \parallel z$, resonant modes are found at $167 \mu\text{V}$, $322 \mu\text{V}$, $475 \mu\text{V}$, $630 \mu\text{V}$ and $772 \mu\text{V}$, whereas for $H \parallel y$ the resonant modes appear at slightly larger voltages $181 \mu\text{V}$, $336 \mu\text{V}$, $483 \mu\text{V}$, $636 \mu\text{V}$ and $780 \mu\text{V}$. We note that the correction factors estimated from Eq. (3.50) and Eq. (3.51) indicated an even bigger difference

* This chapter is based on the publication Ref. [A2].

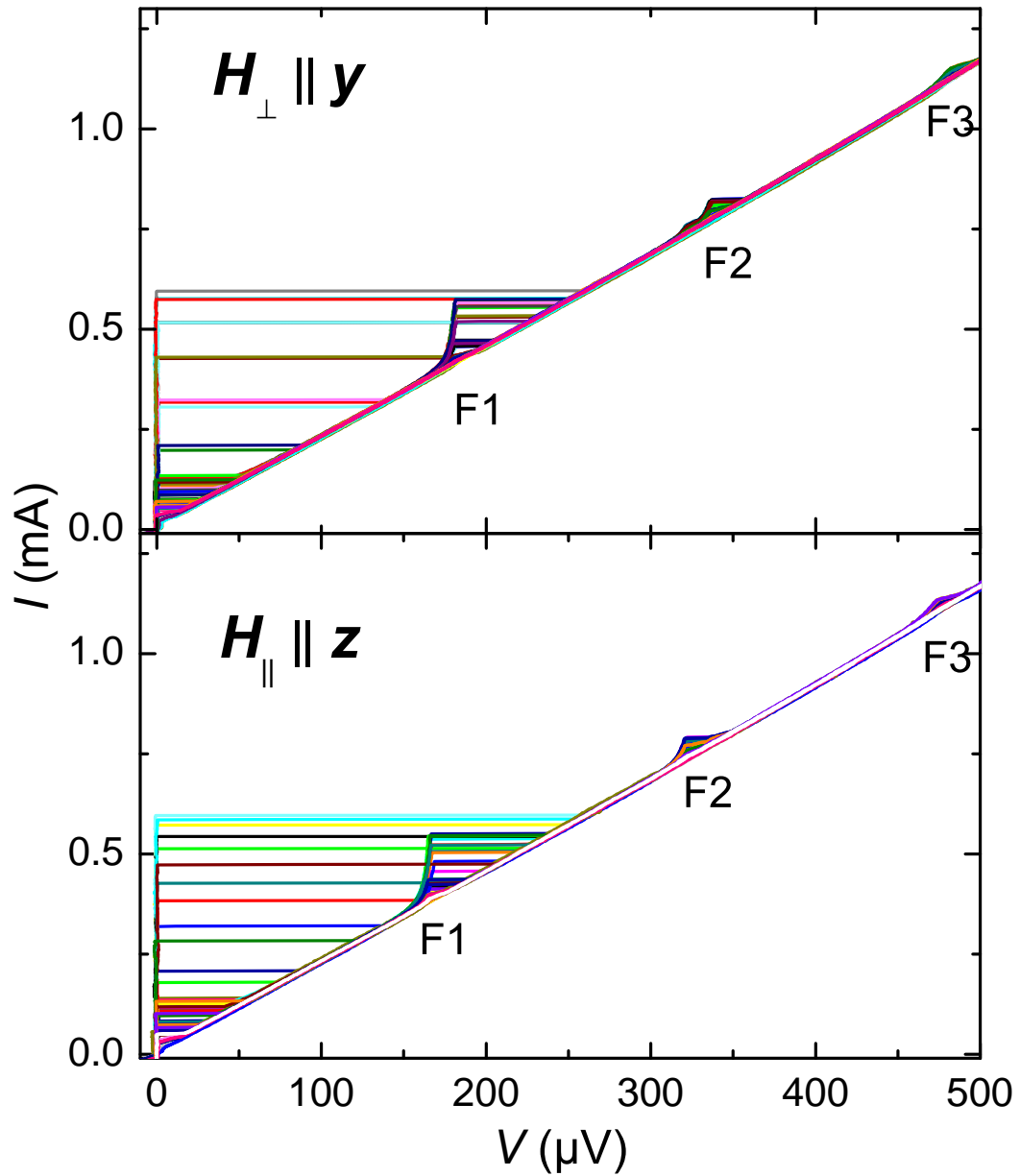


Fig. 7.1: Current-voltage characteristics (IVCs) of the $50 \times 50 \mu\text{m}^2$ junction of the sample GInsitu-203b measured at 500 mK for different magnetic fields applied parallel (bottom) and perpendicular (top) to the bottom electrode. The first three Fiske resonances are clearly seen and labeled F1, F2, and F3.

number n of Fiske step	1/2	1	2	3	4	5
$H \parallel$ bottom electrode (z -direction):						
$\Delta I_{n,\parallel}^{\max}$ (μA)		140	48	27	13	6
$Q_{n,\parallel}$		22	27	35	30	22
$V_{n,\parallel}$ (μV)	83.5	167	322	475	630	772
$H \perp$ bottom electrode (y -direction):						
$\Delta I_{n,\perp}^{\max}$ (μA)		130	46	24	13	5
$Q_{n,\perp}$		19	26	31	30	18
$V_{n,\perp}$ (μV)	90.5	181	336	483	636	780

Tab. 7.1: Voltage position $V_{n,\parallel}$ ($V_{n,\perp}$) and step height $\Delta I_{n,\parallel}^{\max}$ ($\Delta I_{n,\perp}^{\max}$) of the n -th Fiske steps obtained for the magnetic field applied parallel (perpendicular) to the bottom electrode. The data were derived from the IVCs of the $50 \times 50 \mu\text{m}^2$ junction of the sample GInsitu-203b measured at 500 mK (cf. Figs. 7.1 and 7.2). Also listed are the quality factors $Q_{n,\parallel}$ and $Q_{n,\perp}$ of the n -th Fiske resonance, which are obtained by fitting the measured $\Delta I_{n,\parallel}(V, \Phi)$ and $\Delta I_{n,\perp}(V, \Phi)$ dependencies by Kulik's theory.^{256, 257}

between the lateral and longitudinal mode. However, the quantitative evaluation of this difference depends on the details of the junction geometry and properties of the involved materials (e.g. dielectric constants) and therefore needs a more elaborate effort.^{261, 262} Qualitatively, we can say that the effect of the idle region is reduced on going to higher frequencies (smaller wavelengths) due to a stronger confinement of the modes in the junction area. That is, the difference of the resonance voltages of the lateral and longitudinal mode is decreasing on going to higher harmonics. This nicely agrees with our observation and reports in literature.²⁶¹

The Fiske steps $\Delta I_n(V, \Phi)$ are obtained from the measured IVCs (cf. Fig. 7.1) by subtracting an ohmic background, which is determined by the about constant subgap resistance. Equivalently, $\Delta I_n(V, \Phi)$ can be obtained by integration of the dV/dI curves shown in Fig. 7.2, again after subtraction of the subgap resistance. The latter method yields better results for the higher modes; both methods agree very well in the intermediate range. Fitting the current steps $\Delta I_n(V)$ measured at fixed applied flux to Eq. (3.42) allows us to determine the voltage positions $V_{n,\parallel}$ ($V_{n,\perp}$) and the maximum step heights $\Delta I_{n,\parallel}^{\max}$ ($\Delta I_{n,\perp}^{\max}$) for the magnetic field applied parallel (perpendicular) to the base electrode. For low $n \leq 2$, the quality factors determined by Eq. (3.44) are not within the validity of Kulik's theory applicable only for low Q . Therefore, the quality factors $Q_{n,\parallel}$ ($Q_{n,\perp}$) listed in Table 7.1 have been calculated via the theory introduced by Eqs. (3.45) and (3.46).

As discussed in section 3.2.4, for short Josephson junctions the excitation of the cavity resonances is most effective if the spatial period of the Josephson current distribution along the junction is about matching the spatial period of the n -th resonant

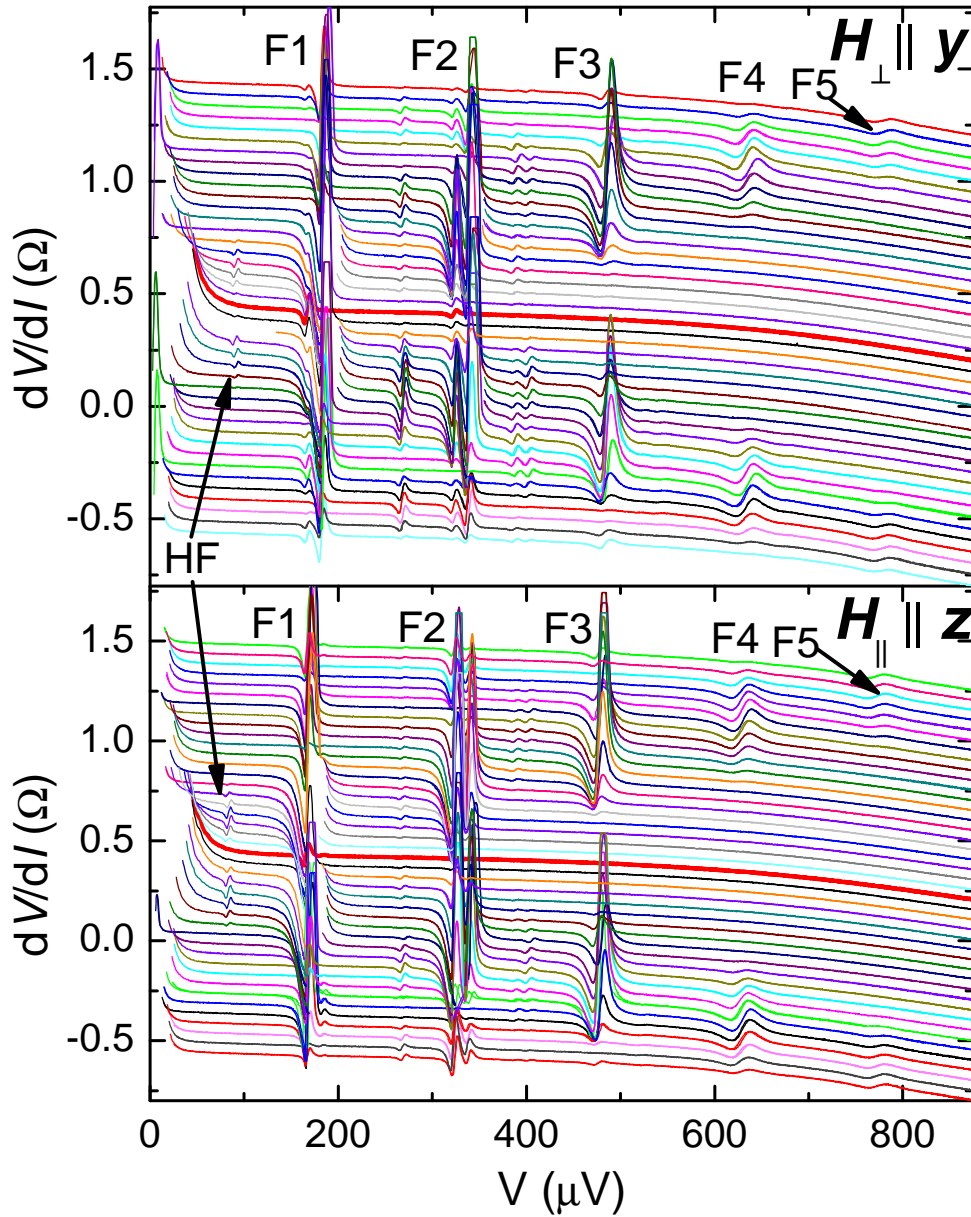


Fig. 7.2: The differential resistance dV/dI versus the applied voltage V measured with a lock-in technique at 500 mK for different magnetic fields applied parallel (bottom) and perpendicular (top) to the bottom electrode. The data are taken for the $50 \times 50 \mu\text{m}^2$ junction of GInsitu-203b simultaneously to those shown in Fig. 7.1. Fiske resonances are observed up to almost $800 \mu\text{V}$ corresponding to a frequency of about 400 GHz. The origin of the resonance labeled HF at half the first Fiske voltage is discussed in the text. The thick red lines mark the measurements taken at zero applied magnetic field. These curves are not shifted vertically, whereas all other curves are subsequently shifted by 0.1Ω for clarity.

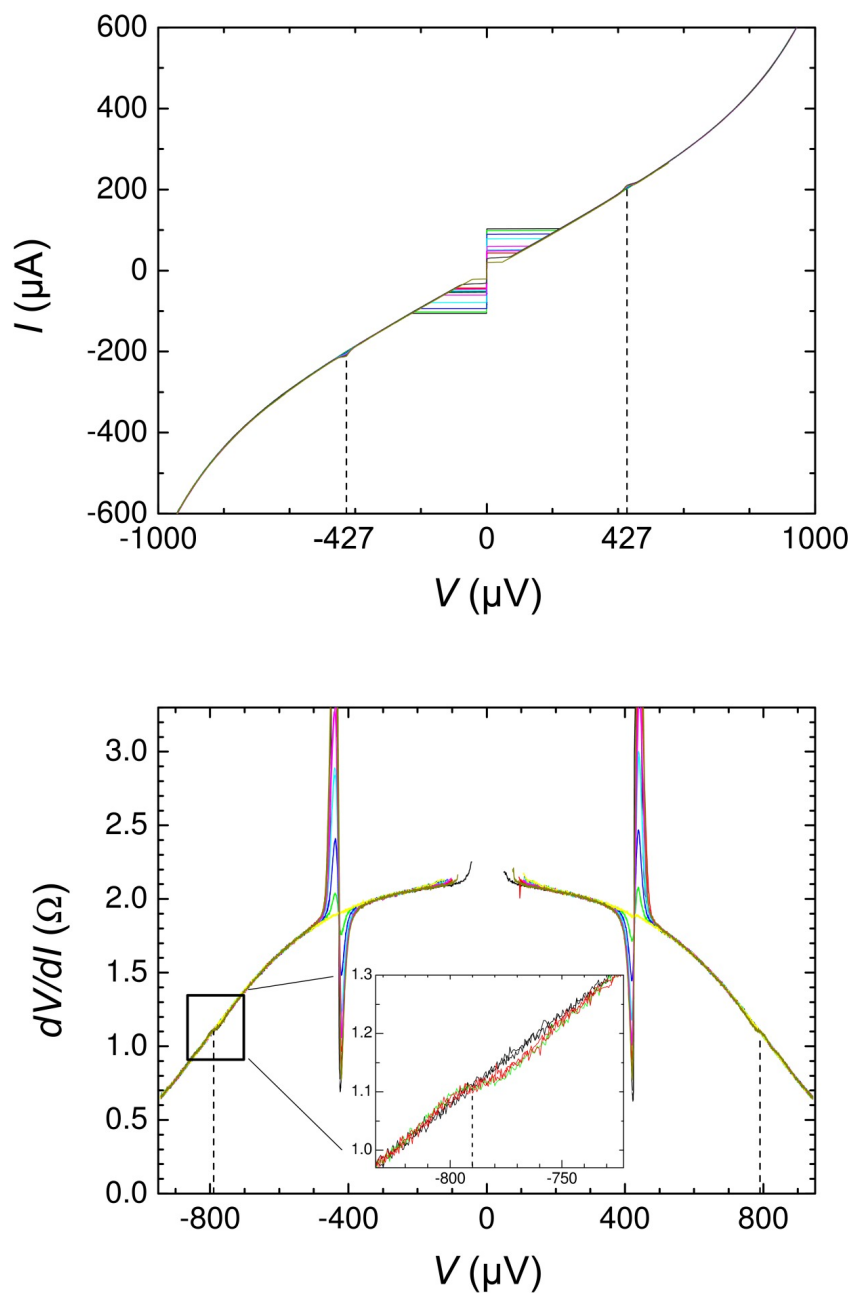


Fig. 7.3: Current-voltage characteristics (top) and the differential resistance dV/dI versus the applied voltage V (bottom) for the $20\mu\text{m}$ junction of the sample GInsitu-203b measured in different applied in-plane magnetic fields at 2K. In the bottom diagram, the inset shows a zoom into the second Fiske step position. The voltage positions of the first and the second Fiske resonance are determined to $427\mu\text{V}$ and $790\mu\text{V}$, respectively.

electromagnetic mode of the junction. Therefore, the height of the Fiske steps strongly depends on the applied magnetic field and has a pronounced maximum at a particular field value. This is shown in Fig. 7.4 where we have plotted the height ΔI_n^{\max} of the n -th Fiske step together with the critical current I_c of a $50 \times 50 \mu\text{m}^2$ junction versus the applied magnetic flux. For large n , the Fiske step has a maximum height at $\Phi \simeq n\Phi_0/2$ where the Josephson current shows about the same spatial modulation along the junction as the cavity mode.

The voltage positions V_n of the Fiske resonances allow us to derive several interesting junction parameters such as the Swihart velocity, the specific capacitance, or the junction plasma frequency. To avoid any ambiguities related to the overlap effect discussed above, we use the Fiske voltages found for $H \parallel z$ to derive these parameters. Obviously, the values $V_n = n \frac{\Phi_0 \bar{c}}{2L}$ directly give the Swihart velocity \bar{c} . From the position $V_1 = 165 \mu\text{V}$ of the first Fiske step, we obtain \bar{c} to $0.027 \cdot c$ where c is the speed of light in vacuum. We note that the derived Swihart velocity may slightly vary with increasing step number, e.g. due to a non vanishing dispersion of the dielectric constant of the barrier material.^{262, 361} Using the Josephson penetration depth $\lambda_J \simeq 70 \mu\text{m}$ determined in section 6.3, the plasma frequency $\omega_p/2\pi = \bar{c}/2\pi\lambda_J$ is obtained to 17.8 GHz. Since $\omega_p = \sqrt{2e j_c / \hbar C_s}$, we can derive the specific capacitance C_s of the junction to $C_s = 54 \text{fF}/\mu\text{m}^2$. This value is about two times larger than typical values reported in literature for Nb/AlO_x/Nb Josephson junctions.³⁶² With these values the quality factor $Q_{\text{Swihart}} = \omega_p R_p A C_s$ can be estimated, which directly follows from the Swihart velocity derived from the position of the first Fiske resonance. Here, R_p is the resistance of the junction measured at a voltage $V_p = \frac{\omega_p \Phi_0}{2\pi} \simeq 35 \mu\text{V}$ corresponding to the plasma frequency. R_p agrees well with the subgap resistance $R_{\text{sg}} = 0.44 \Omega$. Using this value, we obtain the quality factor $Q_{\text{Swihart}} = 6.6$, which corresponds to the quality factor Q_{IVC} determined from the retrapping current of the IVCs of the same junction using the RCSJ-model. The fact that Q_{Swihart} is slightly larger than the value $Q_{\text{IVC}} = 5.7$ is not astonishing keeping in mind effects of premature switching/retrapping due to noise in the IVCs measurement. For the $20 \times 20 \mu\text{m}^2$ junction, we observed Fiske resonances at $V_1 = 427 \mu\text{V}$ and $V_2 = 790 \mu\text{V}$ (see Fig. 7.3). Taking into account a slight increase of the first Fiske step voltage due to the overlap effect and a decrease of the second Fiske step voltage due to dispersion effects, we can estimate a Fiske step distance of about $415 \mu\text{V}$. This value leads to $C_s = 53 \text{fF}/\mu\text{m}^2$ in nice agreement with the value obtained for the large junction. The derived plasma frequency is $\omega_p/2\pi = 21.7 \text{GHz}$ and the quality factor is $Q_{\text{Swihart}} = 6.2$.

We next use the quality factors derived from the Fiske steps to analyze damping effects. In the theoretical description of the Fiske resonances, a finite damping is assumed. However, the origin of this damping is usually not specified. It turns out that the experimental values of Q_n derived from the Fiske resonances can be both larger and smaller than the quality factor Q_{IVC} derived from the resistively and capacitively shunted junction (RCSJ) model. The reason is that, on the one hand, the RCSJ model overestimates the losses due to quasiparticle tunneling since a voltage independent resistance is assumed in this model. On the other hand, the RCSJ model does not take

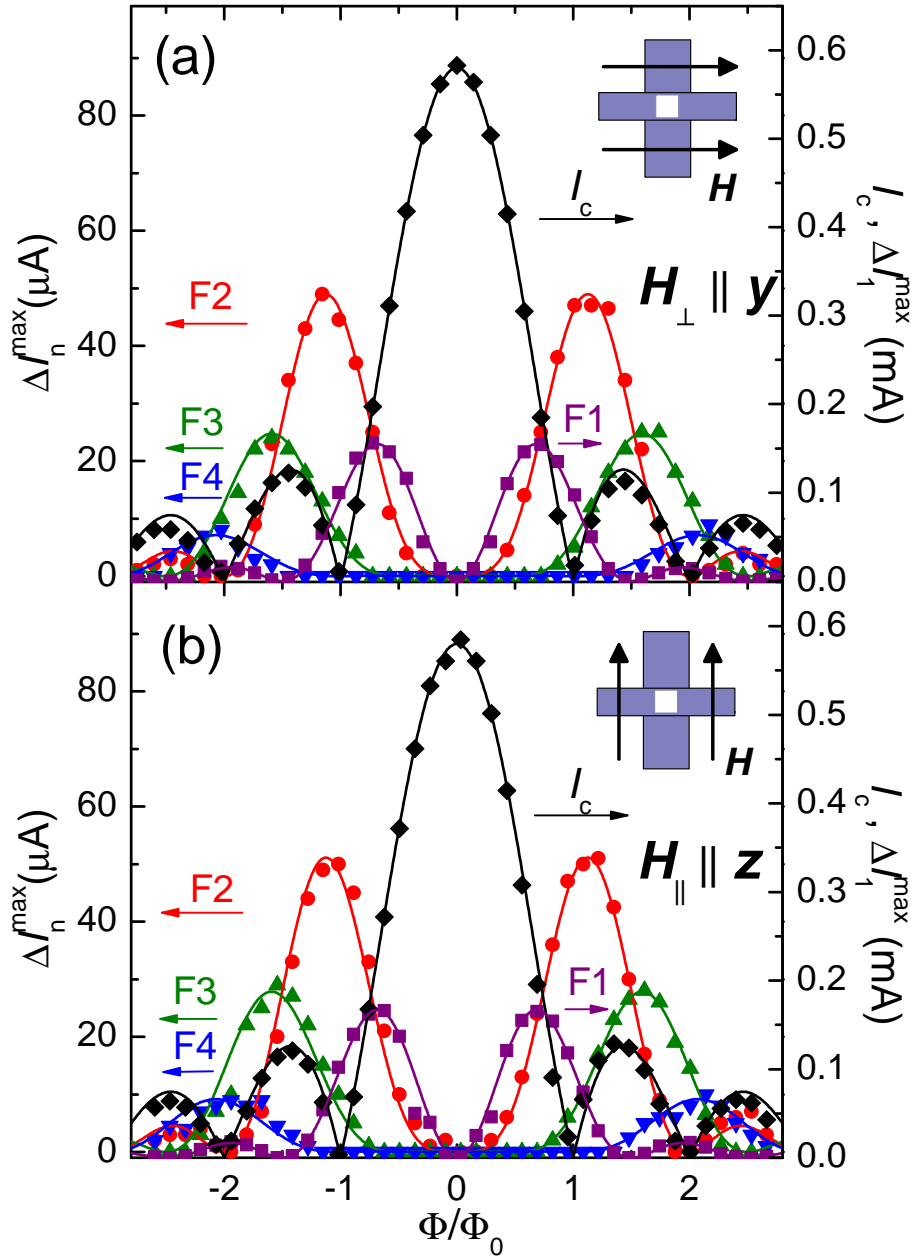


Fig. 7.4: Dependence of the critical current I_c and the height ΔI_n^{\max} of the Fiske steps on the magnetic flux generated by a magnetic field applied perpendicular (a) and parallel (b) to the bottom electrode. The data are obtained for the $50 \times 50 \mu\text{m}^2$ SIFS π Josephson junction of the sample GInsitu-203b at 500 mK. For clarity, the magnetic field dependence of I_c and the height of the first Fiske step (F1) are linked to the right axis. The data are fitted to a Fraunhofer pattern and Kulik's theory.^{256, 257}

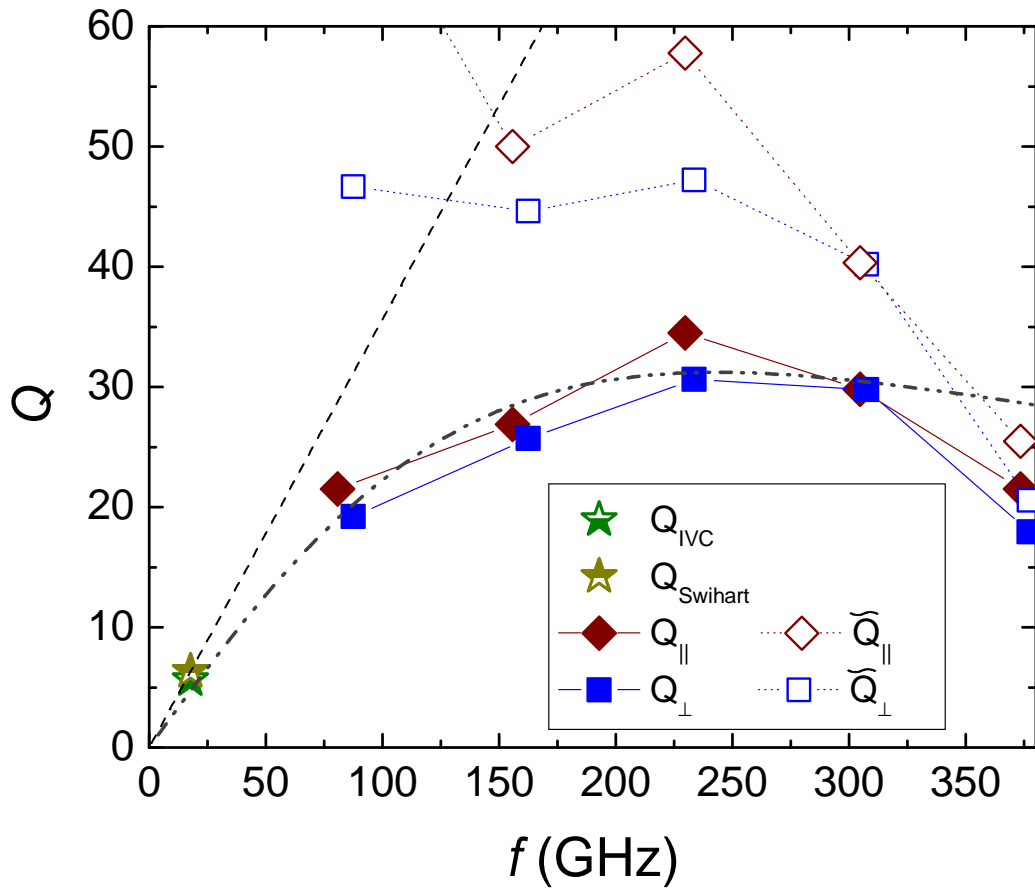


Fig. 7.5: Quality factors Q_{IVC} and $Q_{Swihart}$ derived from the IVCs and the Swihart velocity by assuming only quasiparticle damping. The broken straight line gives an extrapolation of these values to higher frequencies. Also shown are the quality factors Q_{\parallel} and Q_{\perp} derived from the Fiske resonances (full symbols). The open symbols represent the quality factors \tilde{Q}_{\parallel} and \tilde{Q}_{\perp} derived from the Fiske resonances after subtraction of the extrapolated quasiparticle damping. The dash-dotted line is obtained by fitting the data using Eq. (7.8).

into account other loss mechanisms, e.g. due to a finite surface resistance. Assuming that there are various loss mechanisms, the total quality factor of the Fiske resonances can be written as

$$Q_n = \left(\frac{1}{Q_{n,\text{qp}}} + \underbrace{\frac{1}{Q_{n,\text{rad}}} + \frac{1}{Q_{n,\varepsilon}} + \frac{1}{Q_{n,R_s}} + \frac{1}{Q_{n,L}}}_{1/\tilde{Q}_n} \right)^{-1}. \quad (7.1)$$

Here, the different contributions represent losses due to quasiparticle tunneling ($Q_{n,\text{qp}}$) and a finite surface resistance (Q_{n,R_s}) as well as radiation losses ($Q_{n,\text{rad}}$), and dielectric losses ($Q_{n,\varepsilon}$).³⁶³ Furthermore, variations ΔL^j in the junction length L^j lead to a broadening of the resonances, which can be expressed by a frequency independent quality factor $Q_{n,L} = L^j/\Delta L^j$.

If quasiparticle tunneling is the only damping mechanism, we would expect $Q_{n,\text{qp}} = \omega_n RC$. Here, R is the junction normal resistance at the voltage $V_n = \hbar\omega_n/2e$, which is given by the about constant subgap resistance R_{sg} in the relevant regime. Therefore, $Q_{n,\text{qp}}$ is expected to increase about linearly with increasing resonant mode frequency. Above, we have determined $Q_{\text{Swihart}} = \omega_p RC = 6.6$. Extrapolating the value to larger frequency, we would expect $Q_{n,\text{qp}} = 0.37 \cdot (\omega/2\pi) \text{GHz}^{-1}$. This dependence is shown in Fig. 7.5 by the broken straight line. Obviously, the quality factors determined from the Fiske resonances do not follow this line. From this, we conclude that there are additional damping mechanisms beside quasiparticle tunneling. In order to get some insight into the frequency dependence of these additional mechanisms, we have used Eq. (7.1) to determine the part in the quality factor due to the additional damping mechanisms by subtracting the quasiparticle damping. The resulting values \tilde{Q}_n are shown as open symbols in Fig. 7.5. It is evident that \tilde{Q}_n decreases significantly with increasing frequency.

As discussed above there are several possible mechanisms leading to additional damping in Josephson junctions. However, radiation and dielectric losses can be usually neglected due to the large impedance mismatch at the junction boundaries and the small volume of the dielectric, respectively. Furthermore, in our fabrication process, $L^j/\Delta L^j \simeq 100$ for $L^j = 50 \mu\text{m}$ resulting in $Q_{n,L} \simeq 100$. That is, the geometric inhomogeneities set an upper limit for the quality factor of the junctions, which is above the measured values. The remaining mechanism is damping due to the finite surface resistance of the junction electrodes. Expressing the complex surface impedance of a superconductor as $Z_s = R_s + iX_s$, the contribution of the junction electrodes to the quality factor is given by the ratio³⁶⁴

$$Q_{n,R_s} = \frac{X_s}{R_s}. \quad (7.2)$$

For a rough estimate of Q_{n,R_s} , we can use a simple two-fluid model. Expressing the conductivity of the superconductor as the sum $\sigma = \sigma_s + \sigma_n$ of the superconducting and

normal conducting carriers and using the simple relations¹¹¹

$$\sigma_s = \frac{1}{i\omega\mu_0\lambda_L^2} \quad (7.3)$$

$$\sigma_n = \frac{n_n e^2}{m_n} \frac{\tau}{1 + i\omega\tau}, \quad (7.4)$$

we can derive the following expression for the real and imaginary part of the complex surface impedance:

$$R_s = \frac{1}{2}\omega^2\mu_0^2\lambda_L^3\sigma_N\left(\frac{n_n}{n}\right) \quad (7.5)$$

$$X_s = \omega\mu_0\lambda_L. \quad (7.6)$$

Here, n_n/n is the temperature dependent fraction of normal electrons, m_n the mass of the normal electrons, and σ_N is the conductivity of the superconductor in the normal state where $n_n = n$. With these expressions we obtain

$$Q_{n,R_s} = \frac{2}{\omega\mu_0\lambda_L^2\sigma_N(n_n/n)}. \quad (7.7)$$

We see that Q_{n,R_s} strongly increases with decreasing temperature due to the freeze out of the normal electrons. However, due to the uncertainties in n_n/n , σ_N in the PdNi/Nb bilayer, and the simplicity of our approach, Eq. (7.7) certainly cannot be used to estimate the absolute value of Q_{n,R_s} . However, according to Eq. (7.7) we expect $Q_{n,R_s} \propto 1/\omega$. This explains the observed decrease of \tilde{Q}_n with increasing frequency shown in Fig. 7.5.

With the quasiparticle tunneling, the finite surface resistance, and the geometric inhomogeneities as the three main contributions to the measured quality factor, we expect

$$\frac{1}{Q_n} = \frac{1}{Q_{n,qp}^0\omega} + \frac{\omega}{Q_{n,R_s}^0} + \frac{1}{Q_{n,L}}. \quad (7.8)$$

As shown in Fig. 7.5, this expression well fits the measured data with $Q_{n,qp}^0 = 0.046 \times 10^{-9}\text{s}$, $Q_{n,R_s}^0 = 2500 \times 10^9\text{s}^{-1}$, and $Q_{n,L} = 100$. From this, we learn that the quality factor of our SIFS junctions is limited by quasiparticle tunneling at low frequencies and the finite surface resistance at high frequencies. In the intermediate regime, there may be an effect of geometric inhomogeneities when going to small area junctions.

The quality factors measured for our SIFS Josephson junctions are slightly lower than the values reported for Nb/AlO_x/Nb tunnel junctions.³⁶⁵ This is not astonishing because there is the additional F layer in our SIFS junctions. First, this layer reduces the $I_c R_n$ product of the SIFS junction compared to an SIS junction and thereby increases the effect of quasiparticle damping characterized by $Q_{IVC} \simeq Q_{Swihart} = \omega_p R_n C = \sqrt{2eI_c R_n^2 C / \hbar}$. Furthermore, the F layer results in an increased surface resistance since

the PdNi/Nb bilayer has increased σ_N and an increased fraction n_n/n of the normal electrons. The increased n_n/n value is a result of the inverse proximity effect, increasing the quasiparticle density in the superconducting electrodes.³⁶⁶ Finally, effects originating from magnetic impurity scattering on Ni atoms diffused into the niobium top layer may play a role.³⁶⁷

Comparing SIFS to SFS junctions, it is immediately evident that the quality factors of SFS junctions will be very small. Due to the much smaller normal resistance and vanishing capacitance, SFS junctions are overdamped ($Q_0 < 1$). The larger quality factors of the SIFS junctions are obtained by the additional tunneling barrier, which causes large R_n and C . Increasing the thickness t^j of the tunneling barrier is expected to result in an exponential increase of R_n , while $I_c R_n$ should stay constant and C should decrease as $1/t^j$. Therefore, increasing t^j in principle can be used to further increase the quality factors of SIFS junctions. However, this is obtained at the cost of lower j_c and ω_p what may be a problem for some applications. The quality factors between about 5 and 30 in the frequency regime between about 10 and 400 GHz achieved in our experiments are already sufficient for applications in quantum information circuits or for the studies of macroscopic quantum tunneling in section 8.4.

We conclude the discussion of the Fiske resonances by paying attention to the small resonances labeled HF in Fig. 7.2, which occur at exactly half of the voltage of the first Fiske step. This observation reminds us of the appearance of half-integer Shapiro steps at the $0-\pi$ transition of SFS junctions due to a second harmonic component in the current-phase relation.³⁶⁸ However, since the F layer thickness of the SIFS junctions studied in our work is about three half the thickness of the $0-\pi$ transition, this scenario would require a significant F layer thickness variation of a few nanometers.³⁶⁹ This is in contradiction to the small rms roughness of our F layers. Furthermore, the presence of a double-sinusoidal current-phase relation as the origin of the HF resonance is in contradiction with the measured magnetic flux dependence of its height. Clearly, the measured HF step height dependence on the applied in-plane magnetic field in Fig. 7.6 cannot be mapped on the one of the first Fiske step with half the applied field.³⁷⁰ Nonequilibrium effects may be a possible explanation for the observed HF resonance.³⁷¹ However, further experiments are required to clarify this point.

7.1 Concluding Remarks

We have carefully studied the Fiske current steps present in the IVCs of the two SIFS π Josephson junctions, whose IVCs and $I_c(H)$ dependencies we have already examined in sections 6.3 and 6.4. These steps are generated by a nonlinear interaction between the Josephson oscillation and the eigenmodes of the cavity formed by the junction geometry; the associated resonances are referred to as Fiske resonances. The Fiske current steps appear in the IVCs of the junctions in an applied in-plane magnetic field where their detailed shape reveals the resonance qualities of the associated Fiske resonances.

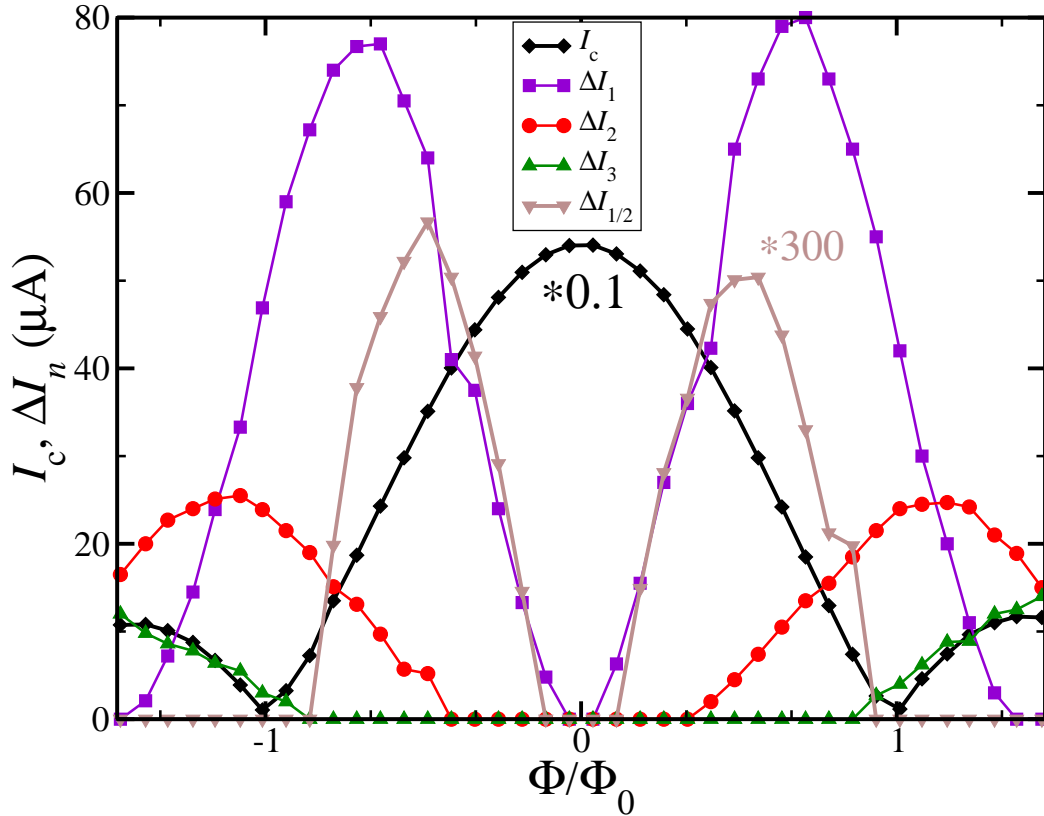


Fig. 7.6: Dependence of the critical current I_c and the height ΔI_n of the first three Fiske steps and the HF resonance ($n = 1/2$) on the magnetic flux Φ generated by an applied in-plane magnetic field. The data are obtained for the SIFS Josephson junction with $A = 50 \times 50 \mu m^2$ on the sample GInsitu-187 ($d_F = 8.4 \text{ nm}$; oxidation time: 3 h) at 500 mK. For clarity, I_c is scaled down by 0.1, while the height of the HF resonance is determined from the lock-in measurement and enlarged by a factor of 300. It is clearly observable that the dependence of the height of the HF resonance on the applied magnetic field cannot be mapped on the one of the first Fiske resonance with half the applied field, which one expects for resonances generated by a non-vanishing double-sinusoidal contribution to the current-phase relation of the junction.

In our junctions, we observe resonances up to a few hundred GHz. We extract from the voltage positions of the resonances the specific junction capacitance $C_s \sim 54 \text{ fF}/\mu\text{m}^2$ and the plasma frequency $\omega_p/2\pi \sim 20 \text{ GHz}$. We note that these values are already sufficient for the application of the junctions in quantum information processing and to test their macroscopic quantum behavior in section 8.4.

Furthermore, we determine the Fiske resonance qualities from the shape of the steps present in the IVCs. These values provide valuable new information on the damping mechanisms up to 400 GHz present in SIFS Josephson junctions. Here, it turns out that damping due to quasiparticle tunneling dominates at low frequencies, whereas at high frequencies the surface impedance plays the dominant role. In the latter case, we detect slightly reduced resonance qualities compared to SIS tunnel junctions reported in literature and attribute this increased damping to an increased quasiparticle density in the superconducting electrodes due to the inverse proximity effect.

To conclude, we find in our SIFS junctions damping analogously to tunnel junctions, that is, the dynamic properties of SIFS junctions are dominated by the tunneling barrier. Hence, SIFS junctions are in contrast to SFS junctions underdamped. The small damping exposes SIFS junctions as ideal π -shift elements for superconducting electronics.

Chapter 8

SWITCHING EXPERIMENTS AND MACROSCOPIC QUANTUM TUNNELING

This chapter discusses secondary quantum effects in a Josephson junction with a ferromagnetic interlayer. These effects can be illustrated as follows: We treat the metastable potential minima in the tilted washboard potential (cf. Fig. 3.2) quantum mechanically and locally confine the phase particle in a potential well, that is, we look at a JJ in the zero-voltage state. Hence, the phase particle can only occupy discrete eigenstates. These eigenstates define the Josephson dynamics at very low temperatures T when the thermal energy $k_B T$ is of the order of the level spacing $\hbar\omega_a$ between the discrete states. We note that these low temperatures are commonly only achieved in dilution refrigerators, which we introduce in section 8.1. There, one usually uses switching experiments, which we explain in section 8.2, to evaluate the switching rate* $\Gamma(i_b)$ from the zero-voltage state into the voltage state of a JJ. The information extracted out of these measurements is twofold. On the one hand, one can determine the switching rate for a JJ under microwave irradiation, which gives accurate information on the plasma frequency ω_p of the junction as we see in section 8.3. On the other hand, the switching rate can be analyzed at different temperatures. This allows in section 8.4 to experimentally observe the crossover between thermally activated (TA) switching and switching due to a tunneling process at the crossover temperature T^* , that is in the picture of the phase particle the crossover between TA escape over and quantum tunneling through the potential barrier. By comparing the experimentally determined crossover temperature of a $20 \times 20 \mu\text{m}^2$ SIFS π -junction with the theoretical prediction, we conclude that we indeed observe for the first time macroscopic quantum tunneling (MQT) in a Josephson junction with a ferromagnetic interlayer. The observation of macroscopic quantum properties gives strong evidence that noise induced by the ferromagnetic interlayer does not render SIFS junctions unusable for quantum information processing.^{264, 265} Moreover, critical current fluctuations induced by a dynamic reorientation of the magnetic domain structure of the interlayer are excluded.

We remind the reader that we strictly distinguish in this section between the plasma

* The expression “switching rate” has the same meaning as “escape rate” within this work. In general, the first expression relates to the switching of a JJ from the zero-voltage into the voltage state, while the latter expression goes back to the escape of the phase particle from a metastable state.

frequency ω_p and the intrinsic junction quality Q_0 for a junction in the absence of a bias current and the attempt frequency $\omega_a = (1 - i_b^2)^{1/4} \omega_p$ and the resonance quality $Q = (1 - i_b^2)^{1/4} Q_0$ for a junction with the normalized bias current $i_b = I_b/I_c$ (see section 3.1).

8.1 The Experimental Setup[†]

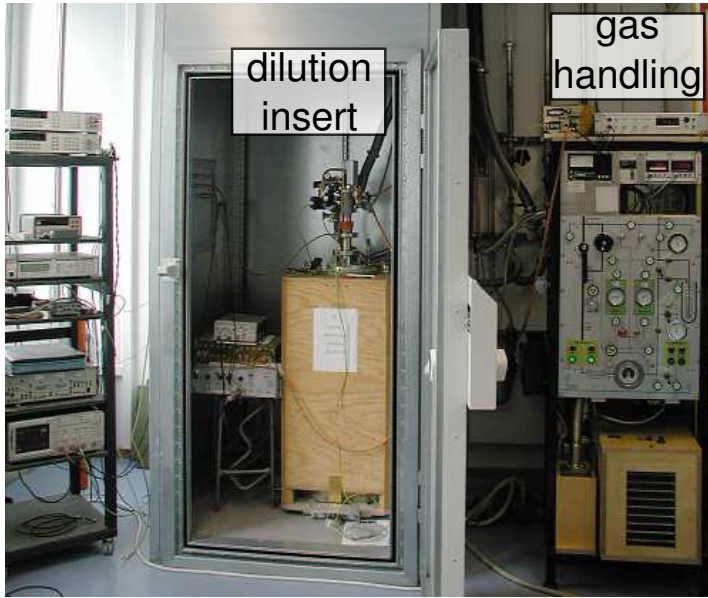


Fig. 8.1: Photograph of the dilution refrigerator setup. One observes in the shielded cabinet the dilution insert in the cryostat, the battery powered current source and the preamplifier. On the left hand side, the measurement devices are installed, while on the right hand side the gas handling system provides a continuous ^3He circulation. (similar to Ref. [227])

We evaluate secondary quantum effects in our Josephson junctions with a ferromagnetic interlayer in the following experiments. As we know from chapter 7, the plasma frequency ω_p of our junctions is of the order of $\omega_p/2\pi \sim 20$ GHz, which typically results in an attempt frequency $\omega_a/2\pi \sim 10$ GHz when the switching from the zero-voltage into the voltage state takes place at the switching current I_{sw} . That is, a metastable potential well in the tilted washboard potential is well approximated by a harmonic potential with the eigenfrequency $\omega_a/2\pi \sim 10$ GHz of the phase particle. Because of this, one expects quantum levels with an energy level spacing of $\hbar\omega_a \approx 40 \mu\text{eV}$ there, so that the cooling of a junction into the quantum mechanical ground state requires a temperature $\hbar\omega_a/2\pi k_B < 100$ mK (cf. Eq. (4.16)). This is not achievable in evaporation cryostats as the one used in section 6.1 where the lowest possible temperature is limited to about 250 mK due to residual heat leaks.³⁷² Hence, the examination of secondary quantum effects is for our SIFS Josephson junctions only possible in a ^3He - ^4He dilution refrigerator where the cooling process is essentially based on dissolving ^3He in ^4He .^{373, 374} Because of this, we perform the following experiments in a dilution

[†] This section is partially based on my work Ref. [227].

refrigerator setup constructed at the WMI. It provides a minimal base temperature of about 30 mK at a circulation rate of $25 - 30 \mu\text{mol/s}$ of ^3He .²²⁷

The setup is shown in Fig. 8.1. It consists of the dilution insert and a rack-mounted gas handling system. The latter one contains on the left side of the rack (front to the shielded room) the vacuum control equipment (mechanical and diffusion pump) and on the front side the helium gas handling system including the ^3He circulation pump and a nitrogen cold trap to withhold water and other contaminants. Two 15 liter tanks for the storage of the helium mixture and pressure control sensors for the vacuum and the helium lines are also mounted there. The gas handling system is connected to the dilution insert in the shielded cabinet by supply lines, which are fed through the cabinet wall with commercially available feedthroughs to sustain the hermetic rf sealing of the shielded cabinet. Plastic sealing rings in the lines galvanically disconnect the gas handling system from the shielded room, which was the main grounding point.²²⁷

The ^4He reservoir for the dilution unit in the shielded cabinet is provided by a glass fiber reinforced (GFK) cryostat, which is mounted on a vibration damping base. We note that the magnetic shielding is there provided by two concentric mumetal³⁴² shields around the dewar.

Since the mechanical built-up and the electrical filtering (cf. Fig. 8.3) of the dilution unit have already been intensively discussed in Refs. [227], [375] and [376], we refer the interested reader for details to these sources. Here, we concentrate on the sample holder. It is mounted below the mixing chamber of the dilution unit as shown in Fig. 8.5. There, the electrical connections are filtered via a stainless steel powder filter^{351, 352}; the microwave line (coaxial cable) is directly guided to the sample where an antenna is used to irradiate the device under test with microwaves. The superconducting coil shown in Fig. 8.5 is used for the measurement in Fig. 9.2 to

apply a tiny magnetic field. The sample is mounted on the silver sample plate, which is shown in the bonding fixture device in Fig. 8.2. The junctions are bonded using aluminum-sputtered gold bonding wires. Since in contrast to aluminum gold does not get superconducting, this promises high electronic thermal conductivity down to lowest temperatures.³⁷⁷ Moreover, the problem of bad mechanical stability of gold bonds is solved by the sputtered aluminum layer. The sample is glued to the silver plate, which is thermally connected to the sample holder, to thermalize the sample.

The dilution insert is equipped with multiple temperature sensors at different temperature stages. The temperatures reported within this work are acquired by the temperature sensor shown in Fig. 8.5 (a 1 k Ω Dale resistor), which was calibrated by K. Neumaier and thermally anchored directly on the sample stage (for a description of the prepa-

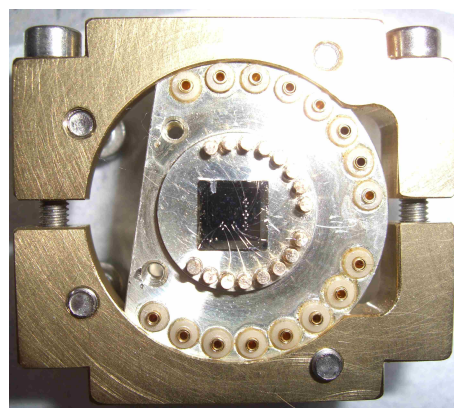


Fig. 8.2: A bonded sample on the silver sample plate (mounted in the bonding tool).

ration details see for example Ref. [378] and the references therein). It is read out via a Picowatt AVS-47 resistance measurement bridge. To evaluate the temperature dependence of the junction properties, a heater is mounted on the sample stage. Since a PID temperature control with a heater control unit Picowatt TDS-530 was found vulnerable to crosstalk between the current supply lines and the temperature readout, in the measurements reported in section 8.4 the heating is provided by a low noise current source (Knick J-152) with constant currents up to $400\ \mu\text{A}$ whereby the average temperature was acquired during the measurement. Here, it was essential to constantly monitor the pressures of the circulating ^3He and the sample holder temperature and to automatically turn off the measurement when the dilution unit suffered from unstable operating conditions, especially when microwaves with a high power additionally heated the fridge.

Switching rate measurements are very sensitive to current noise originating from the current source, the wiring, and the *LCR* and *RC* filters. Hence, one uses in such type of measurements several low-pass filters at different temperature stages to subsequently suppress the Jonson-Nyquist noise^{379, 380} generated at room temperature and by the filtering itself. As sketched in Fig. 8.3, we have installed a low-pass *LCR* filter at room temperature followed by a two-stage *RC* filter at liquid helium temperature. A stainless steel powder filter blocks high frequency noise at the sample stage. For the filter details, we refer the reader to Ref. [227]. The dilution insert is equipped with an additional coaxial line to irradiate the device under test with microwaves. The thermalization of the inner conductor of the microwave line is provided by a 20 dB and a 10 dB attenuator thermally anchored to the helium bath and to the Joule-Thompson stage. The line is guided near to the sample where a $\lambda/4$ -antenna couples microwaves into the device under test. The details of the microwave setup are discussed in Refs. [375] and [376]. We use a Rohde&Schwarz SMP 04 microwave generator, which reliably provides microwaves with frequencies between 10 MHz and 40 GHz with an output power up to +20 dbm; however, the coupling between the antenna and the device under test strongly depends on frequency as characterized in Fig. 8.6.

During the present work, the setup has been extensively improved. When this work was started, the assembly was capable to identify macroscopic quantum tunneling in SIS Josephson tunnel junctions at about 100 mK.²²⁷ It was thereafter equipped with a microwave line, so that spectroscopic experiments (cf. section 4.4) were possible.^{375, 376} A superconducting coil (cf. Fig. 8.4) was installed to allow magnetizing the ferromagnetic layer of the SIFS junctions in a large out-of-plane magnetic field. Moreover, the measurement setup inside the shielded room was upgraded. Today, the current source and the preamplifier are powered by large lead-acid batteries ($\pm 12\ \text{V}\ 100\ \text{Ah}$, $\pm 24\ \text{V}\ 30\ \text{Ah}$), which provide enough power to run the whole setup for about 1 week. To achieve this, an external power input was installed in the current source. Moreover, the trigger unit of the current source was optimized to prevent triggering on false signals generated by the preamplifier electronics and mutual inductive and capacitive couplings between the current supply and the voltage sense lines. The noise properties of the whole setup have been intensively investigated to understand the measurements in

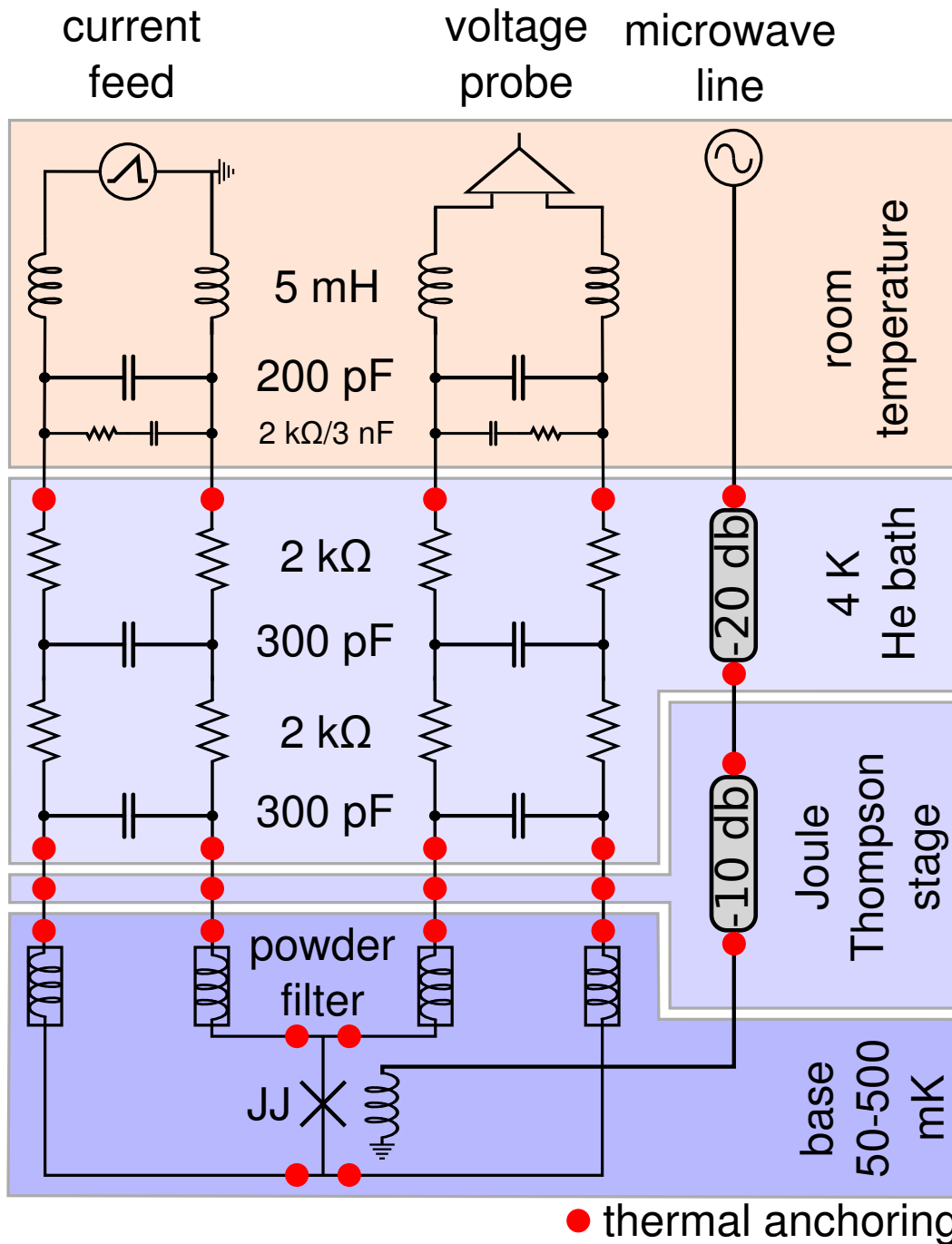


Fig. 8.3: Schematic diagram of the current feed, voltage probe and microwave wiring. The current feed and voltage probe lines are filtered by LCR and RC filters and by a stainless steel powder filter; for thermalization, they are anchored at different temperatures as indicated in the drawing. In contrast, the microwave line is only thermally connected above the mixing chamber by commercial attenuators, that is at the Joule-Thompson stage and at the ^4He bath. We note that the device under test is attached to a silicon wafer, which is glued to a thermalized silver plate.



Fig. 8.4: A superconducting coil mounted in the dilution unit dewar setup. For the out-of-plane magnetization of the ferromagnetic interlayer of a SIFS π -junction in chapter 9, a commercially available superconducting coil is mounted in the dilution unit dewar setup.

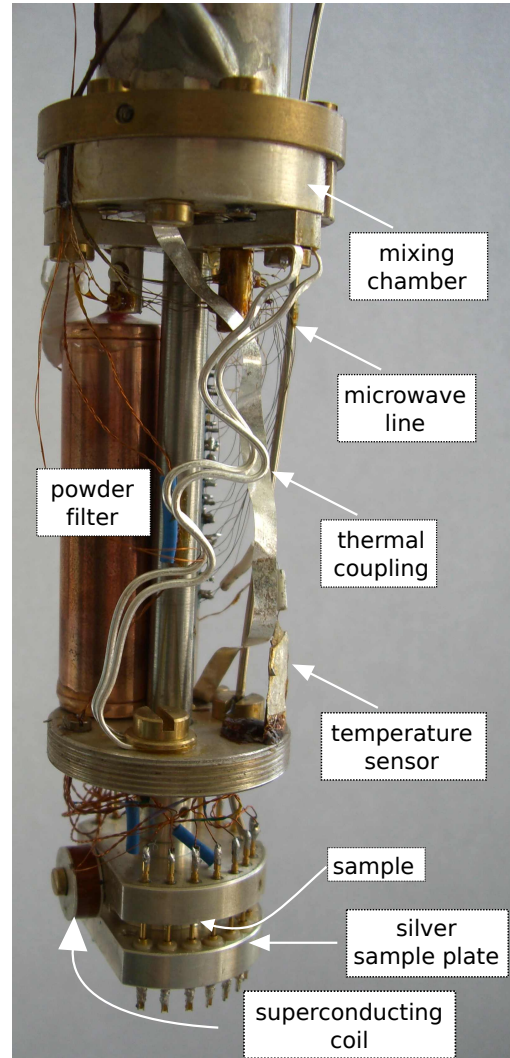


Fig. 8.5: Sample holder fixed at the mixing chamber of the dilution unit. One observes the microwave line guided near to the sample, the stainless steel powder filter, the thermal coupling and the Dale temperature sensor. The small superconducting coil was used in the measurement in Fig. 9.2 to provide a tiny magnetic field.

section 8.4 in detail. The data acquisition is fully automated today, which allows to run computer-controlled sequences such as the temperature sweeps in section 8.4 or the study of the escape behavior under microwave irradiation of different frequencies and powers in section 8.3. Of course, it was this way also possible to characterize the dependence of the coupling between the antenna and the JJs on the microwave frequency $\omega_{\text{mw}}/2\pi$ in Fig. 8.6.

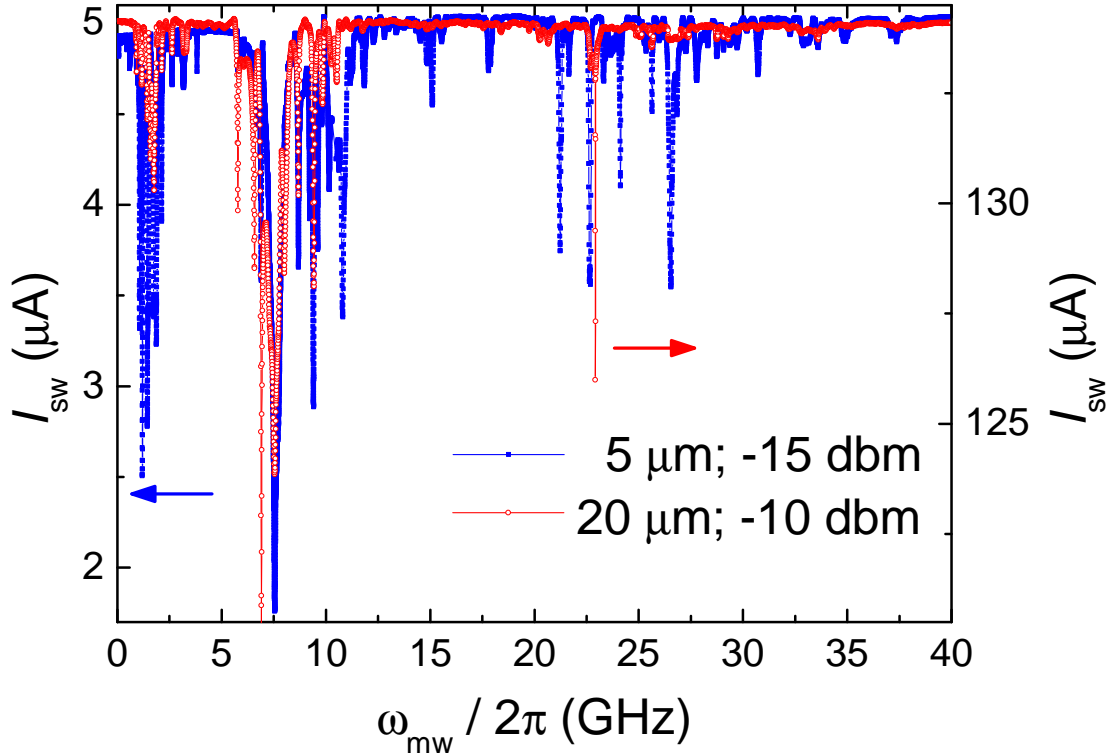


Fig. 8.6: The switching current I_{sw} versus the microwave frequency $\omega_{\text{mw}}/2\pi$ for the 5 μm (20 μm) SIFS Josephson junction of the sample GInsitu-203b irradiated with microwaves of the frequency $\omega_{\text{mw}}/2\pi$ and the power -15 dbm (-10 dbm). One observes at specific microwave frequencies a strong suppression of the critical current of the JJs. Most likely, this is mainly not connected to the Josephson dynamics, but predominantly reflects the different coupling coefficients between the antenna and the JJs. For clarity, the switching current of the 5 μm (20 μm) junction is linked to the left (right) axis.

8.2 Switching Experiments[‡]

In switching experiments, one investigates the switching probability of a Josephson junction from the zero-voltage state into the voltage state, which depends on the junction

[‡] This section is partially based on my work Ref. [227].

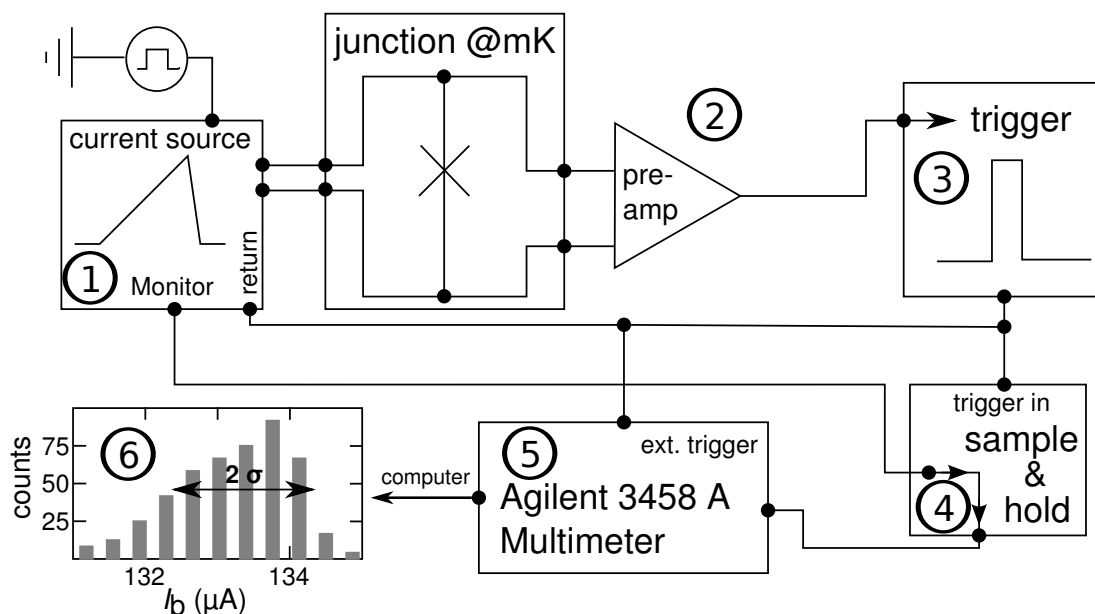


Fig. 8.7: Schematic diagram of a switching experiment. An external voltage pulse starts a current ramp in the home-made current source ①. It is sent over various filter stages into the JJ mounted on the cold finger of a dilution refrigerator. The voltage across the junction is detected by voltage sense lines, which couple to the input port of the voltage preamplifier ②. The preamplifier output port controls the trigger ③ built into the current source ①. The latter is now able to detect the switching of the JJ from the zero-voltage into the voltage state and to trigger the sample-and-hold stage ④, which saves the current amplitude at the switching event. Additionally, the trigger pulse initiates the current source to fast ramp down the current to prevent dissipative heating in the junction. Subsequent to a short trigger stabilize time, the sample-and-hold unit and hence the switching current is read out by the multimeter ⑤. After repeating this measurement a few hundred times, one is able to determine the histogram ⑥, that is the number of switching events versus the bias current I_b , using a digital computer. (similar to Ref. [227])

bias current I_b . For measurement setups with heavily filtered supply lines, T. Fulton and L. Dunkleberger introduced a current ramp technique and developed its data evaluation.¹⁵³ Below, we introduce this technique shortly based on our measurement setup, which is schematically illustrated in Fig. 8.7. For a more detailed introduction see e.g. Ref. [227].

To measure the switching probability of a junction at different bias currents I_b , one ramps up a current across the JJ for typically a few thousand times and records the switching currents, that are the currents where the junction switches from the zero-voltage into the voltage state. In contrast to SIS Josephson junctions where the switching into the voltage state results in about twice the gap voltage across the junction, that is for niobium 3 mV, in SIFS junctions we observe due to the strongly suppressed critical current I_c approximately $I_c R_{sg} \sim 200 \mu\text{V}$ (cf. Fig. 6.7a). To detect such small

voltages, we use a four-probe setup with two pairs of twisted wires for current feed and voltage probe. In our case, the current ramp is provided by a home-made, analog current source (① in Fig. 8.7), which feeds a low-noise sawtooth current signal into the junction. The lower limit of the ramp is set below zero to assure that the junction has switched back from the voltage state to the superconducting state³⁸¹; the upper limit is dynamically given by the switching of the junction. In the measurements reported in this work, ramp rates about $I_c/5$ ms have been chosen for technical reasons. A waiting cycle of typically 500 ms before ramping up allows the junction to thermalize. The voltage across the junction -amplified using the Stanford Research SR 560 low-noise voltage preamplifier ② by a factor of typically 10 000- is used to detect the switching of the junction in the trigger unit ③. Once the switching is detected, the current source changes the ramping direction, feeds the current magnitude into the sample&hold module ④ and triggers the multimeter Agilent 3458A ⑤ to read out this value with a typical integration time of about 200 ms. The value is stored in the internal memory of the multimeter and, after accumulating a certain number of events, the data are transferred to a digital computer and stored in an ASCII file for later evaluation. In the computer, a histogram ⑥ of the switching currents is generated. We note that the theoretically expected probability of switching into the voltage state

$$P(I_b) = \Gamma(I_b) \left(\frac{dI}{dt} \right)^{-1} \left(1 - \int_0^{I_b} P(u) du \right) \quad (8.1)$$

can be calculated at the bias current I_b from the escape rate $\Gamma(I_b)$, the inverse ramping velocity $(dI/dt)^{-1}$, and the probability that the junction has not switched into the voltage state at the bias current I_b .¹⁵³

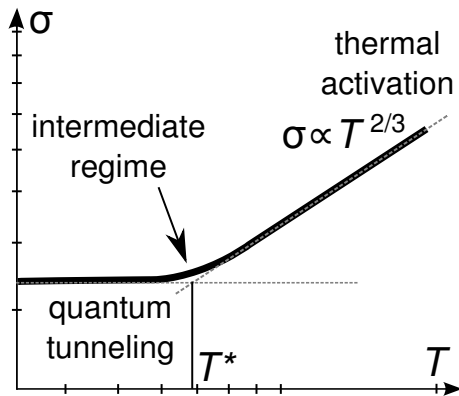


Fig. 8.8: Typical standard deviation σ of the switching currents I_{sw} versus the junction temperature T . We observe thermally activated escape above the crossover temperature T^* , while below T^* switching from the zero-voltage into the voltage state is dominated by macroscopic quantum tunneling.

For the evaluation of the switching rates regarding the transition from thermal escape to macroscopic quantum tunneling (MQT), one typically evaluates the standard deviation σ determined from switching current histograms (cf. ⑥ in Fig. 8.7) at different junction temperatures T . Here, the escape probability is defined by MQT below the crossover temperature T^* (see section 4.2) and hence does not depend on temperature there, that means that σ saturates into a constant value at low temperatures.

In contrast, the switching is governed by thermal activation above T^* (see section 4.1.3). There, σ scales approximately proportional to $T^{2/3}$.^{382, 383} The transition between both limits is characterized by the crossover temperature T^* , which lies in the center of the intermediate regime (see section 4.3). The different behaviors are illustrated in Fig. 8.8.

8.3 The Irradiation of a Josephson Junction with Microwaves

Conveniently, the plasma frequency ω_p of a JJ is best determined by microwave spectroscopy where one probes the quantized level structure of a potential well in the tilted washboard potential by the resonant absorption of photons (see section 4.4.1). However, for our junctions this interpretation is according to Eq. (4.19) only valid for $\omega_{mw} \lesssim 0.2 \omega_p$. Hence, we have to interpret the dynamics of our JJs under microwave irradiation by an effective suppression of the potential barrier, which is particularly strong in the resonant case as discussed in section 4.4.2. However, it gets quite clear by looking at the dynamics of the phase particle in the metastable potential well (cf. Eq. (4.26)) that we do not expect sharp excitations for our junctions with the typical quality factors $Q = \alpha Q_0 \sim 3$. This results in a switching dynamics different to what has ever been reported before.

For this reason, we first get an overview of the different resonances observed in the 20 μm junction of the sample GInsitu-203b under microwave irradiation. Therefore, we look in Fig. 8.9 into the standard deviation σ of the switching currents of the junction under microwave irradiation of different frequencies $\omega_{mw}/2\pi$. Here, stepwise increasing the incident microwave power P_{mw} from typically -40 dbm to +10 dbm[§] suppresses the critical current of the JJ and allows to measure σ at different switching currents I_{sw} .[¶]^{384, 385} In the experiment, we observe at particular switching currents and frequencies a large standard deviation σ of the switching currents. We first clarify the question whether the enlarged half-width^{||} σ has to be explained quantum mechanically or is of semi-classical nature. Therefore, we analyze in Fig. 8.10 σ versus the normalized attempt frequency $\alpha = \omega_a/\omega_p$ for a junction under microwave irradiation of the frequency $\omega_{mw}/2\pi = 7580\text{MHz}$, that is a single trace of Fig. 8.9, at different temperatures. If the dynamics of the switching process has to be described in this

[§] The given microwave power corresponds to the output of the microwave source. One can estimate a loss of 30 db in the attenuators and 10 db in the wiring. However, to estimate the microwave power coupled into the junction requires detailed knowledge about the coupling coefficient between the antenna and the junction. Hence, the values above give only an upper limit for the microwave power which is coupled into the junction.

[¶] The parameter I_{sw} represents the average value of the switching currents under study within this section.

^{||} The expression half-width is used as synonym for standard deviation within this work.

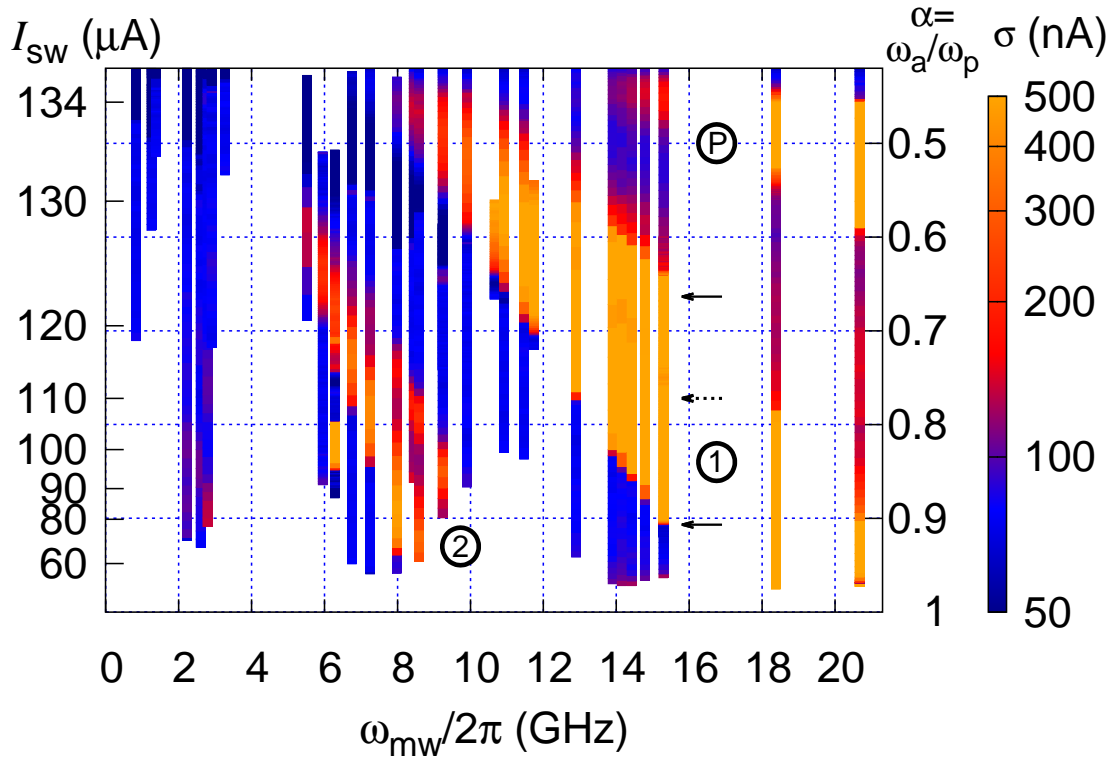


Fig. 8.9: The standard deviation σ of the switching currents in color versus the microwave frequency $\omega_{\text{mw}}/2\pi$ and the mean switching current I_{sw} measured at 40 mK for the 20 μm JJ of the sample GInsitu-203b. The JJ is irradiated with microwaves of the frequency $\omega_{\text{mw}}/2\pi$. The switching current I_{sw} of the junction is suppressed with increasing microwave power. This allows to study the half-width σ of the switching current histograms for different switching currents I_{sw} , which equals different attempt frequencies $\omega_a = \alpha\omega_p = \sqrt[4]{1 - i_{\text{sw}}^2} \omega_p$ due to the different potential tilts. The reduced plasma frequency α determined by the bias current $i_{\text{sw}} = I_{\text{sw}}/I_c$ on the right axis defines the y-axis scaling. An increased histogram width σ indicates a suppression of the potential barrier due to resonance effects. The arrows link to the special positions in Fig. 8.12. We note that for technical reasons (sample&hold unit) there is a slight offset of I_{sw} .

measurement by the escape process of a phase particle excited to a higher quantum mechanical discrete energy state, we would expect that analogously to Fig. 8.8 σ increases with T since we are at least for $T \geq 100\text{mK}$ in the thermal regime. In contrast, we observe in Fig. 8.10 that σ is nearly temperature independent. From that we learn that we have to explain our data by the classical dynamics of a resonantly driven phase particle in a nonlinear potential.

We follow Yu *et al.*³⁸⁶ for the semi-classical explanation and identify a decreased potential barrier height due to the resonant absorption of microwaves by an increased width of the switching current histogram. Here, the phase particle is excited inside

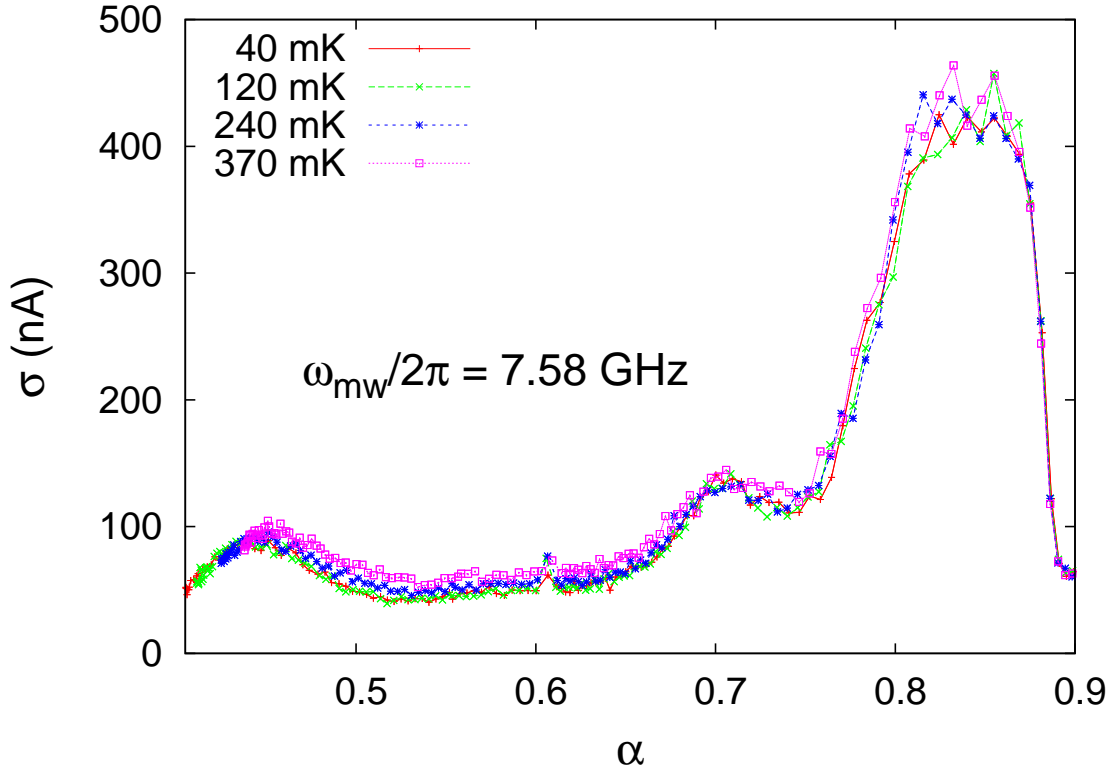


Fig. 8.10: The standard deviation σ of the switching currents versus the reduced attempt frequency $\alpha = (1 - I_{\text{sw}}^2/I_C^2)^{1/4}$ acquired at different temperatures for the same junction as in Fig. 8.9. The junction is irradiated with microwaves of the frequency 7580 MHz and different powers. We identify a reduction of the switching current with increasing temperature without microwave irradiation (smallest α values). There, the escape may be dominated by MQT. Under microwave driving the switching histograms are temperature independent.

the potential well and partly climbs up the wall before it tunnels through the barrier.** This excitation is not only possible due to the absorption of microwaves at the attempt frequency, but also at sub- (Ⓢ) and superharmonic (Ⓣ) frequencies (cf. section 4.4.2). As the y-axis in Fig. 8.9 scales with the reduced plasma frequency $\alpha = \omega_a/\omega_p = (1 - I_{\text{sw}}^2/I_C^2)^{1/4}$, it is obvious that the measurement resembles the junction dynamics where e.g. the plasma resonance shifts from ≈ 20 GHz in the junction without bias current ($\alpha = 1$) to ≈ 10 GHz when the bias current reduces the plasma frequency by $\alpha = 50\%$. However, from the data we are not able to understand clearly, at which position of the resonance we have to identify the plasma frequency. Therefore, we look in Fig. 8.12 in detail into the switching current histograms acquired under microwave irradiation with the frequency $\omega_{\text{mw}}/2\pi = 15.295$ GHz and different powers P_{mw} .

However, we first prove the validity of the semi-classical interpretation by a sim-

** The large oscillation in the resonant case can be seen from Eq. (4.24) where in the resonant case the square root gets very small and hence the oscillation amplitude gets huge.

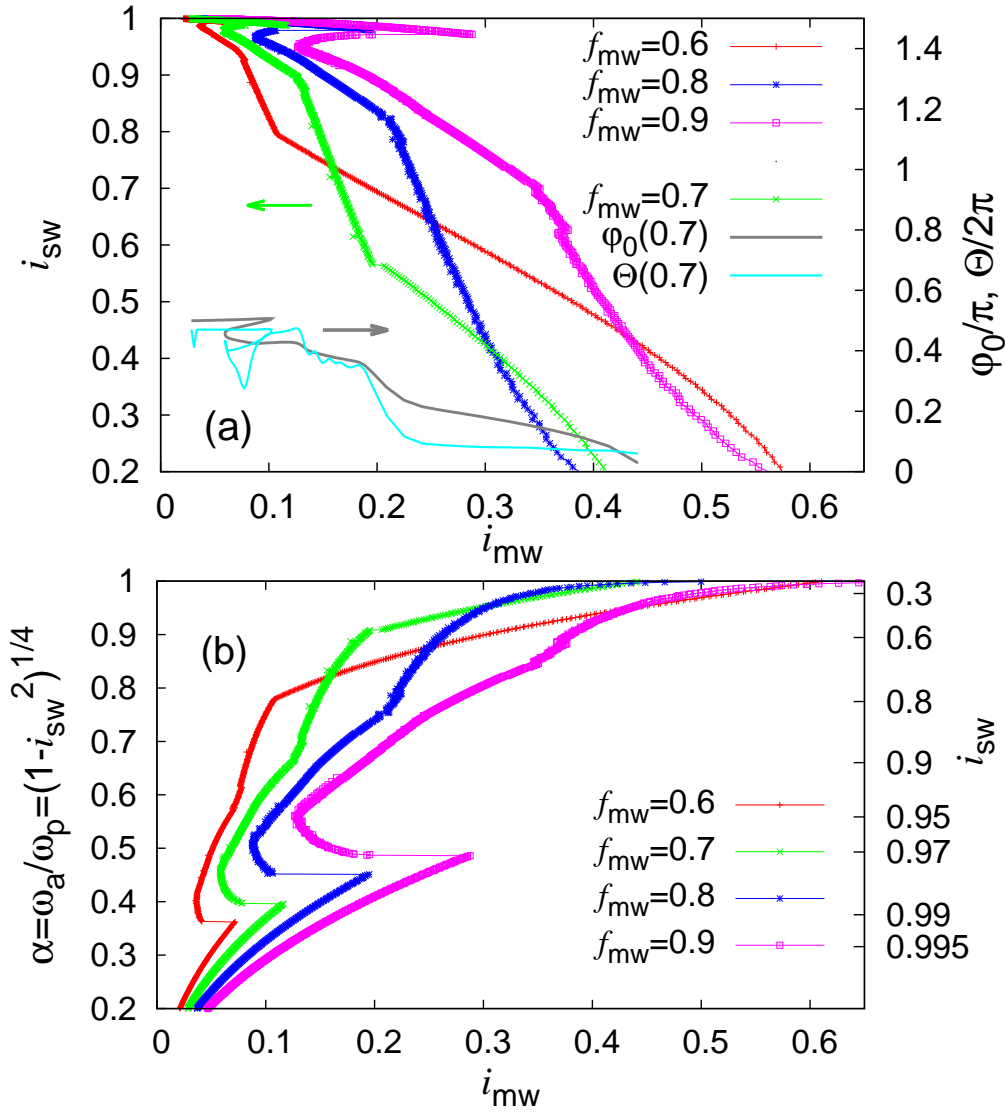


Fig. 8.11: Semi-classical simulation of the switching current i_{sw} (a) and the corresponding reduced attempt frequency α (b) versus the magnitude of the microwave current i_{mw} for a JJ with the intrinsic quality factor $Q_0 = 6$ under strong microwave irradiation with the frequency $f_{mw} = \omega_{mw}/\omega_p$. The simulation algorithm is introduced in Appendix B. One observes in the upper diagram a kink analogously to the experiment in Fig. 8.12. The frequency of the kink can be easily extracted from the bottom diagram (b) where directly α is analyzed. We learn from this analysis that the kink is found at the attempt frequency of the JJ for the microwave frequencies $f_{mw} = \omega_{mw}/\omega_p = 0.6, 0.7, 0.8$, and 0.9 . For $f_{mw} = 0.7$, the time averaged phase position $\varphi_0(0.7)$ and the phase difference $\Theta(0.7)$ between the driving and the oscillation are given in (a) for the last stable oscillation smoothed by a Bézier curve. For clarity, in (a) the switching current i_{sw} is linked to the left axis while for the phase differences the right axis is used; the right axis in (b) links the values on the left axis to the appropriate switching currents i_{sw} .

ulation based on classical dynamics before we interpret our experiment on the basis of nonlinear physics. We use dimensionless units for this theoretical study and model our JJ by superimposing a microwave current $i_{\text{mw}} \cos(\omega_{\text{mw}}t)$ on its bias current i_{b} . This allows to look at the phase evolution across the junction and to increase at a given bias current i_{b} the microwave current until the phase escapes as we discuss in detail in Appendix B. The applied microwave current i_{mw} at which the phase particle starts to run down the potential is extracted from the simulations and given in Fig. 8.11a on the x -axis versus the applied bias current i_{b} on the y -axis for the applied microwaves with the frequencies $f_{\text{mw}} = \omega_{\text{mw}}/\omega_{\text{p}} = 0.6, 0.7, 0.8,$ and 0.9 . We name the bias current i_{b} in this particular case switching current i_{sw} since it defines the current at which the JJ switches into the voltage state under a specified microwave driving. Figure 8.11b plots the data of Fig. 8.11a with the reduced plasma frequency $\alpha = (1 - i_{\text{sw}}^2)^{1/4}$ on the left y -axis. We now focus on $f_{\text{mw}} = 0.7$ for a detailed study where we also plot the time average of the phase φ_0 and the phase difference Θ between the driving and the particle oscillation^{††} for the last stable orbit in Fig. 8.11a. We identify three regions with different behaviors. First, we clearly observe for small microwave drivings only a moderate suppression of the critical current $i_{\text{sw}} \approx 1$ as predicted by Eq. (4.28). Here, the position of the phase particle agrees very well with the expected $\varphi_0 = \pi/2$, and the particle position and the driving are inversely phased ($\Theta \approx \pi$). In literature, this escape is associated with the primary peak (cf. Fig. 8.12).^{302, 386} Second, the region $1 \gtrsim i_{\text{sw}} > 0.5$ is defined by a strong influence of resonant phenomena. They are described by the additional oscillations $\delta\varphi$ in Eq. (4.22). We approximate these oscillations following Eq. (4.26) by a simple harmonic oscillator model with the quality factor $Q = \alpha Q_0 \sim 0.7 \cdot 6 \sim 4$ (cf. Fig. 8.9), that is, we expect the resonant activation of an oscillation in the potential well within a bandwidth $\Delta\omega_{\text{a}} = 2\omega_{\text{a}}/Q \sim 0.5 \omega_{\text{a}}$, which quite well fits to what we observe in the simulation Fig. 8.11 (cf. Eq. (4.26)).³⁸⁷ Here, we note that a more detailed treatment is possible using the Mathieu equation³⁸⁸ according to Ref. [300]. We observe in Fig. 8.11a at the center of the resonance, which is at the attempt frequency, a kink in the $i_{\text{sw}}(i_{\text{mw}})$ dependence indicating a change in the absorption properties below and above the attempt frequency. We note that the kink position matches the attempt frequency for all drivings (cf. Fig. 8.11b). Third, after the resonance region ($i_{\text{sw}} < 0.5$), the switching current is again explained by Eq. (4.28) and the driving is in phase with the particle position. In literature, this region corresponds to the resonance peak.^{302, 386}

Now, we come back to the measurement in Fig. 8.12, which shows the switching probability color-coded versus the bias current I_{b} and the power P_{mw} of the microwaves with the frequency $\omega_{\text{mw}}/2\pi = 15.295 \text{ GHz}$ irradiated onto the JJ. We clarify that in this measurement we do not sweep the microwave power as in the simulation, but for experimental reasons use switching experiments, that is, we ramp up the bias current as explained in section 8.2. We expect in these experiments that our junction switches into the voltage state at a well defined bias current I_{b} for a given microwave power and call

^{††} Technically, this value is extracted from the simulation as the phase difference between the maxima of both quantities.

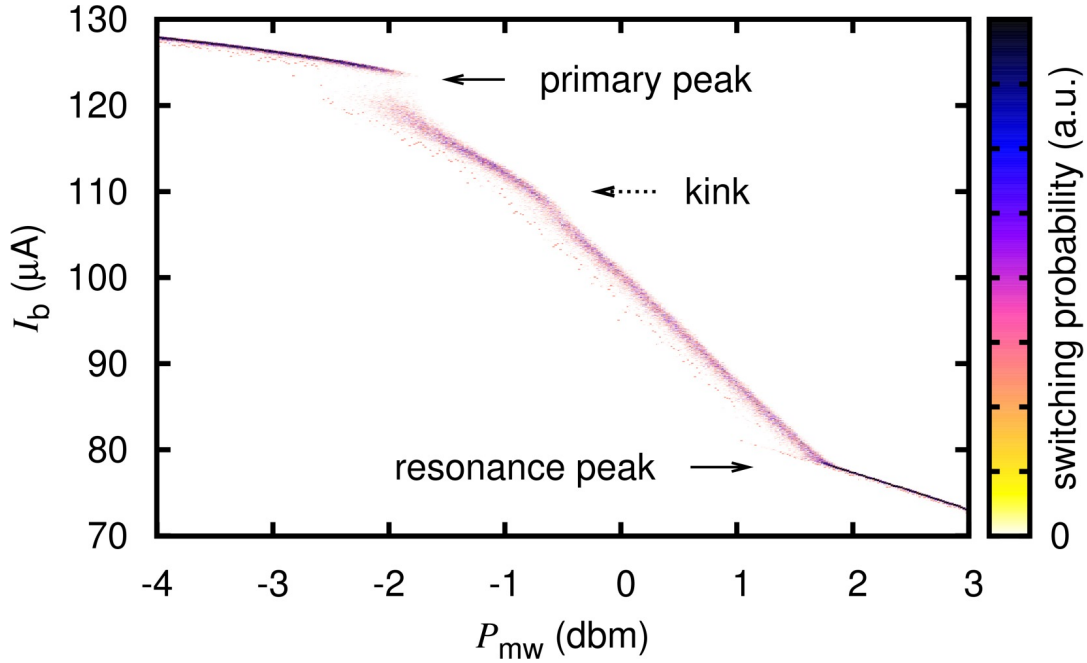


Fig. 8.12: Switching current histograms versus the applied microwave power P_{mw} . The $20\ \mu\text{m}$ junction of GInsitu-203b is irradiated with microwaves of the frequency $15\ 295\ \text{MHz}$ and different powers P_{mw} . For each microwave power P_{mw} , 400 times the switching current of the junction is measured. The color-coding shows for each microwave power a histogram of the switching currents. Comparing these histograms with Fig. 8.9, one observes multi-valued switching probabilities at $123\ \mu\text{A}$ and $78\ \mu\text{A}$ (solid black arrows) correlating to $\alpha \approx 0.66$ and $\alpha \approx 0.91$, respectively. The kink position $110\ \mu\text{A}$ (dotted black arrow) corresponds to $\alpha \approx 0.77$.

this bias current again switching current I_{sw} . We note that compared to the simulation, where we sweep i_{mw} , we are this way only able to detect the lowest switching current, or in some rare situations the two lowest currents. In Fig. 8.12 we clearly identify in the limit of weak microwave driving the nearly power-independent primary peak, which reflects the reduction of the critical current due to the incident microwaves. With increasing microwave power, this peak splits and gives rise to a double-peaked histogram, whose origin can be explained by nonlinear phenomena as we have seen this feature also in the simulation.^{114–117} We, moreover, observe the resonance peak at $P_{mw} \gtrsim 2\ \text{dbm}$. Between the primary peak and the resonance peak the switching behavior is defined by the oscillations described by $\delta\varphi$ in section 4.4.2; due to the resonant activation (cf. Eq. (4.24)), the barrier height is there reduced, which explains according to Yu *et al.*³⁸⁶ the broadening of the switching histograms. This region extends according to Fig. 8.9 between $\alpha \sim 0.66$ and $\alpha \sim 0.91$. Despite the simplicity of the harmonic oscillator model and the neglect of thermal and quantum noise, this is in good agreement with the bandwidth $2\omega_a/Q \sim 0.5\ \omega_a$ of the resonance estimated above. We also identify in the middle of the resonance the kink in the switching current I_{sw}

dependence on the applied microwave power P_{mw} , which defines the plasma frequency. Its position $I_b \approx 110 \mu\text{A}$ allows to estimate the plasma frequency

$$\omega_p/2\pi \approx 20 \text{ GHz} \quad (8.2)$$

of our junction in the absence of a bias current. This value slightly underestimates the plasma frequency $\omega_p/2\pi \approx 21.7 \text{ GHz}$, which we have determined in the Fiske resonance study. This is not astonishing keeping in mind the reduction of the attempt frequency in our non-harmonic potential for large oscillation amplitudes κ (cf. Eq. (4.29)), which we also identify in the simulation Fig. 8.11b.

We conclude the discussion of the dynamics of SIFS Josephson junctions under microwave irradiation with a study of the temperature dependence of the resonance marked © in Fig. 8.9. Therefore, we examine in Fig. 8.13 switching current histograms of the JJ irradiated with microwaves of the frequency $\omega_{\text{mw}}/2\pi = 18.38 \text{ GHz}$ and different powers P_{mw} at the junction temperatures $T = 54 \text{ mK}$, 219 mK , 267 mK , 342 mK , 385 mK , and 424 mK , respectively. At low temperatures, we clearly observe double-peaked histograms, which obviously depend on temperature this time. However, it is quite unlikely that they originate from a resonant excitation of higher quantized energy levels although we observe the resonance at $I_b \sim I_c$, that is at a very low microwave driving power. In this case, we would expect switching due to thermal activation above the crossover temperature T^* , which we determine in section 8.4 to $T^* \sim 60 \text{ mK}$. In contrast, we observe the vanishing of the double-peaked histograms above approximately 400 mK . Thus, we again identify the dynamics of a driven phase particle in a nonlinear potential. From this measurement we learn that thermal noise can also significantly disturb the dynamics of a junction under strong microwave driving when the junction follows semi-classical physics. This particularly explains why we do not detect discrete excitations in Fig. 8.13, but only broader histograms. The latter reflect the non-quantized thermal noise, which influences the phase particle in our nonlinear potential.

8.4 The Observation of Macroscopic Quantum Tunneling

In this section, we discuss the switching process of a SIFS Josephson junction from the zero-voltage state into the voltage state, which we have modeled in section 3.1 by the escape of a phase particle out of a potential well. As we have discussed in chapter 4, this escape is explained at high temperatures by thermal activation over the barrier (see section 4.1) or by quantum tunneling through the barrier at low temperatures (see section 4.2). Experimentally, the transition between these regimes can be examined by switching experiments, which we have introduced in section 8.2. Typical switching current histograms acquired by this technique are shown in Fig. 8.14 for the $20 \mu\text{m}$ junction of the sample GInsitu-203b for different temperatures of the heat bath where the junction is anchored to; we note that the dynamics of this junction has already

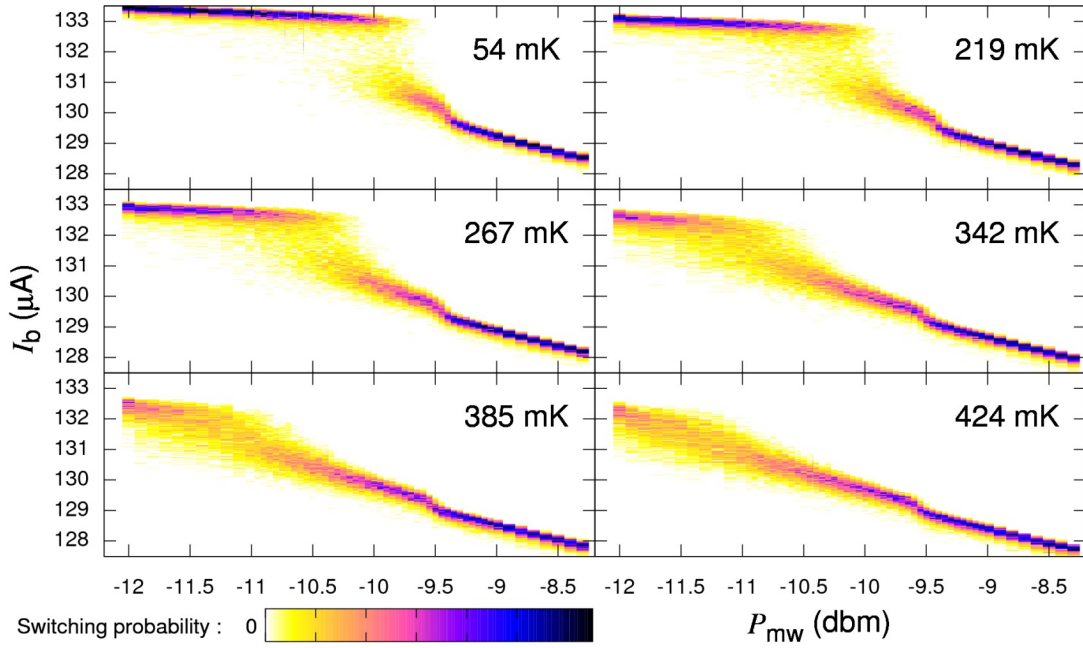


Fig. 8.13: Switching current histograms versus the applied microwave powers P_{mw} measured for the $20\ \mu\text{m}$ junction of the sample GInsitu-203b irradiated with microwaves of the frequency $18\,380\ \text{MHz}$ and different powers P_{mw} at different junction temperatures. For each microwave driving power P_{mw} , 400 times the switching current of the junction is measured. The color-coding shows for each microwave power a histogram of the switching currents. We note that there is a slight offset in I_b for technical reasons (sample&hold unit). We use a ramp rate of $I_c/15.1\ \text{ms}$.

been characterized by the study of the Fiske resonances in chapter 7 and by microwave driving experiments in section 8.3. We clearly identify thermally activated escape at elevated temperatures with broad, temperature dependent switching histograms, while we reach at low temperatures a quantum limited situation with temperature independent histograms. In this section, we experimentally determine the crossover temperature T_{exp}^* between these regimes and compare it to the theoretically expected crossover temperature T_{th}^* . This way, we clarify the questions whether the escape process really follows macroscopic quantum behavior and whether critical current fluctuations generated e.g. by a dynamic reorientation of the magnetic domain structure of the ferromagnetic interlayer play a role.

However, we have not yet characterized the noise present in the switching current histograms in Fig. 8.14, so that we cannot be sure that the observed saturation is not due to noise sources in the wiring or the detection electronics. Hence, current ramp experiments require a careful examination and thorough understanding of possible noise sources present in the experimental arrangement. This includes the noise originating from the bias current supply, but also extends to the detection electronics. In our experience, the current source is usually heavily filtered by RC and stainless steel powder

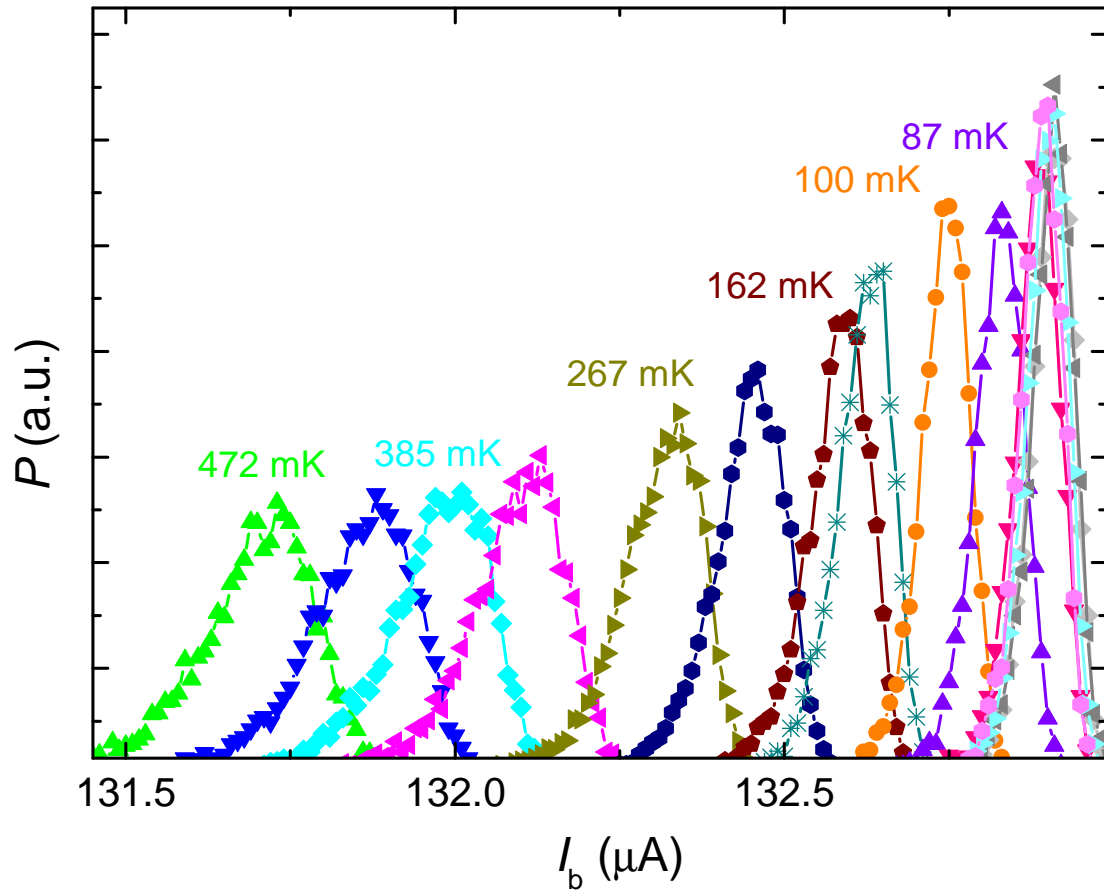


Fig. 8.14: Switching current histograms acquired for the $20\ \mu\text{m}$ junction of the sample GInsitu-203b at different bath temperatures T . Each histogram is based on 6 000 switching events. The strong temperature dependence observed for $T > T^* \approx 70\ \text{mK}$ proves thermally activated escape as the switching mechanism there, while the saturation at low temperatures indicates a quantum limit. We note that in these data considerable noise background is present, so that we refer the reader for the exact determination of the crossover temperature T^* to Fig. 8.15 where we analyze the half-width of histograms after a detailed noise background optimization and characterization. We note that for technical reasons there is a slight offset in I_b (sample&hold unit). We use a ramp rate of $I_c/15.1\ \text{ms}$.

filters^{351, 352}, which leaves the detection electronics as the main noise source. This is in line with our measurement where we found charging the monolithic sample-and-hold circuit LF398³⁸⁹ on our sample&hold unit defining our noise limit.^{‡‡} Another important question is the junction temperature. Here, one usually uses the sample holder temperature (bath temperature) and assumes a good thermalization of the junction. However, Josephson junctions with a ferromagnetic interlayer have a crossover temperature <100 mK, so that dissipative heat generated after the junction has switched into the voltage state is hardly dissipated; that means the junction temperature may saturate above the temperature of the heat bath. In this case, we observe temperature independent histograms mimicking macroscopic quantum tunneling. This may particularly explain why literature reports that the quantum limit could not be reached in NiCu SINFS junctions^{150, 151} since there one possibly detects not the crossover temperature, but the minimal junction temperature. To circumvent this problem, we have used a waiting cycle of at least ≈ 500 ms before each ramp cycle in our measurements to give the junction a chance to thermalize. This is obviously sufficient since typically the junction thermalization was experimentally observed after $\approx 100 - 200$ ms by a waiting time independent switching current of the junction at lowest temperatures.

We point out that the careful and thorough analysis of the switching current histograms Fig. 8.14 revealed a noise floor with a standard deviation $\sigma_n \approx 35$ nA, which originates from our sample&hold circuitry^{‡‡}; we circumvent this inconvenience by adding a current divider into the current supply lines, so that the voltage recorded in the sample&hold unit is increased, and hence the relative error is diminished. This allows to investigate in Fig. 8.15 the escape probability with increased sensitivity. In this study, we acquire measurements at much more temperature values than in Fig. 8.14 to determine the crossover temperature more accurately; however, we have to pay a price for the acquisition of so many values with long waiting cycle between every switching detection: Acquiring the data for Fig. 8.15 took approximately 24 h. Although this seems unimportant since the whole measurement process was automated during this work, it is not negligible: A long term temperature drift of the current source hides the absolute value of the critical current, that is our switching current histograms slightly shift with time. Anyhow, for detecting the crossover from TA escape to quantum escape only the histogram width is important, that is we can neglect this drawback and only examine the half-width σ of our switching current histograms. This quantity is shown in Fig. 8.15 versus the temperature T of the heat bath where the junction is anchored to. One observes at high temperatures the expected thermal $\sigma \propto T^{2/3}$ behavior as indicated by the dashed black line.^{382, 390} At low temperatures, the histogram width saturates

^{‡‡} The noise introduced by the sample&hold unit is quantified by performing a measurement where we trigger instead of the junction voltage on a comparator comparing the monitor output of our current source to an externally given value. From this experiment, we conclude that the uncertainty of the value stored in our sample&hold unit is 0.53 mV. This results for the measurement in Fig. 8.14, where 10 V equals 10 mA sent over a current divider 1:17.5 into the junction, in a noise $\sigma_n \sim 30$ nA; in Fig. 8.15, where 10 V equals 1 mA sent over a current divider 1:6.5, we expect a noise $\sigma_n \sim 8$ nA.

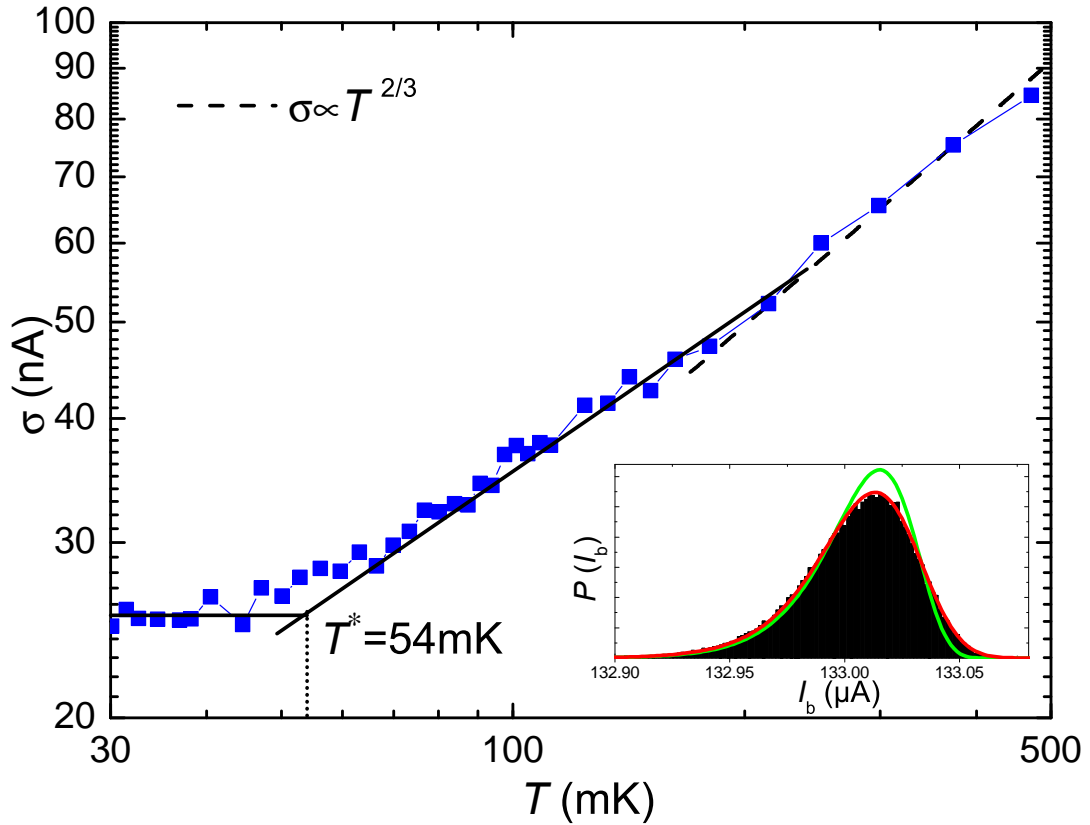


Fig. 8.15: The standard deviation σ of the switching currents versus the bath temperature T acquired for the $20\ \mu\text{m}$ junction of the sample GInsitu-203b. The statistics is based each time on 2500 switching events. The dashed line denotes the theoretically expected $\sigma \propto T^{2/3}$ dependence at high temperature. One observes a crossover from thermally activated escape (TA) to quantum tunneling (MQT) at $T_{\text{exp}}^* = 54$ mK. The inset shows a switching current histogram acquired at base temperature for 62 500 escape events ($\sigma \approx 26$ nA) and the theoretical expectation for $T^* = 54$ mK (green line). The red line superposes $\sigma_n = 10$ nA Gaussian noise, which takes into account the fluctuations due to the detection electronics. The agreement between the measured and the expected histogram proves that we are indeed limited by the Josephson dynamics and not by the measurement setup. All data is acquired with a duty-cycle of 0.5 s to let the JJ thermalize. We note that there is a slight offset in I_b for technical reasons (sample&hold unit). We use a ramp rate of $I_c/20.1$ ms.

indicating the crossover to the quantum limit. The experimental crossover temperature

$$T_{\text{exp}}^* = 54 \text{ mK} \quad (8.3)$$

is here determined as the intersection point between the saturation width and a power law dependence ($\sigma \propto T^{2/3}$ is only valid for $T \gg T^*$).³⁹¹

In the inset of Fig. 8.15, we compare an experimentally determined switching current histogram measured at lowest temperature with the theoretically expected escape distribution (green line) in the presence of $\sigma_n = 10 \text{ nA}$ Gaussian noise originating from our measurement setup (red line). 8 nA here originate from the sample&hold unit of the analog electronics^{‡‡}; the remaining 2 nA can be attributed to small fluctuations due to a temperature drift of the analog electronics and to Johnson-Nyquist noise^{379, 380} from the RC filters and the preamplifier. The excellent agreement between the experimentally determined switching histogram and the theoretical expectation proves that the saturation of the histogram width follows the Josephson dynamics and is not given by the measurement setup or fluctuations of the critical current of our junction.

The theoretically expected escape temperature T_{th}^* of the junction examined in Fig. 8.15 can be calculated using Eq. (4.16). We assume the plasma frequency $\omega_p/2\pi \approx 21 \text{ GHz}$ (as a compromise between the 21.7 GHz calculated from the Fiske study in chapter 7 and the $\approx 20 \text{ GHz}$ from the strong driving analysis in section 8.3). It is suppressed by the potential tilt to $\alpha \approx 40\%$ at the quantum escape, so that we end in an attempt frequency $\omega_a/2\pi = 8.4 \text{ GHz}$ for the phase particle. This results in a theoretically expected crossover temperature $T_{\infty}^* = 64 \text{ mK}$ when we neglect dissipation. For our junction with $Q = \alpha Q_0 \simeq 3$, we end in the theoretically expected crossover temperature

$$T_{\text{th}}^* = \frac{\hbar\omega_a}{2\pi k_B} \left(\sqrt{1 + \left(\frac{1}{2Q}\right)^2} - \frac{1}{2Q} \right) \approx 53 \text{ mK}. \quad (8.4)$$

This value is in excellent agreement with the experimental observation Eq. (8.3). From this result we learn that the critical current of our junction does not fluctuate due to a dynamic reorientation of the magnetic domain structure of the interlayer, that is that SIFS junctions do have a well defined critical current I_c . Moreover, our result experimentally verifies that the lowest eigenstates in the well of the tilted washboard potential coincide with their theoretical prediction. This clearly proves macroscopic quantum behavior in our π -coupled SIFS Josephson junctions, which gives strong evidence that these devices are well suited for applications in quantum information processing.

8.5 Concluding Remarks

We have studied the dynamics of a SIFS π Josephson junction at mK temperatures in the preceding sections. In particular, we have examined the switching probability from

the zero-voltage into the voltage state with and without microwave irradiation. We have clearly seen resonant activation by microwaves in the Josephson dynamics and explained it within semi-classical models and numerical simulations. In contrast, the switching dynamics without applied microwaves clearly shows secondary quantum effects at lowest temperatures. Here, we could observe for the first time macroscopic quantum tunneling in a Josephson junction with a ferromagnetic interlayer. This observation excludes, first, fluctuations of the critical current in SIFS junctions as a consequence of an unstable magnetic domain structure of the ferromagnetic interlayer and, second, a coupling between low-energy excitations in the ferromagnetic interlayer and the Josephson dynamics. Hence, SIFS Josephson junctions are well suited as active and passive π -shift elements for quantum information processing.

Chapter 9

EXCITATIONS IN THE FERROMAGNETIC INTERLAYER

As we have seen in chapter 3, the dynamics of small Josephson junctions can be described within the Stewart-McCumber model, which is modified by a spatial modulation of the supercurrent across the junction in an applied in-plane magnetic field. The latter modification gives rise to the Fiske resonances, which we have extensively studied in chapter 7. Within this chapter, we discuss the question whether additional resonances are observed due to an interaction between the Josephson dynamics and ferromagnetic excitations. Therefore, we first discuss the available literature and compare it to our experimental observations.

A traditional access to excitations in solids is to analyze spontaneous symmetry breaking. As we have already seen in section 5.3.3, the magnetization of our ferromagnetic interlayer does not align isotropically; when we cool down a ferromagnet from above to below its Curie temperature, its magnetization orients spontaneously along the easy axis, that is in our case perpendicular to the film plane. We know from theory that such spontaneous symmetry breaking generates a spinless and massless elementary excitation, a so-called Nambu-Goldstone boson.^{195, 392, 393} For magnetism the associated Nambu-Goldstone boson is named a magnon. We note that a magnon can be understood as a quantized spin wave^{394, 395} and hence follows the dynamics described by the Landau-Lifshitz-Gilbert equation³⁹⁶⁻³⁹⁹. Today, spin waves and spin dynamics are studied by ferromagnetic resonance (FMR), that is by the resonant absorption of a high-frequency magnetic field in ferromagnetic substances.⁴⁰⁰ In traditional FMR, the sample under test with a macroscopic and uniform magnetization M is mounted in a microwave cavity where a bias field H leads to a precessional motion of M . When the magnetic precession frequency $\omega_s/2\pi$ matches the cavity frequency, a strong increase in microwave absorption can be detected. We note that while nowadays traditional FMR is well understood and serves for the characterization of the anisotropy of magnetic materials and magnetic damping, the excitation of spin-waves in solids with an inhomogeneous static magnetization, so-called multi-domain ferromagnets, is not well understood and has recently attracted scientific interest.⁴⁰¹⁻⁴⁰⁴ However, conventional FMR requires a macroscopic sample, so that experiments with very thin and small structures are not possible. This limitation can be circumvented by growing the ferromagnetic layer into a Josephson junction and using the Josephson dynamics to excite

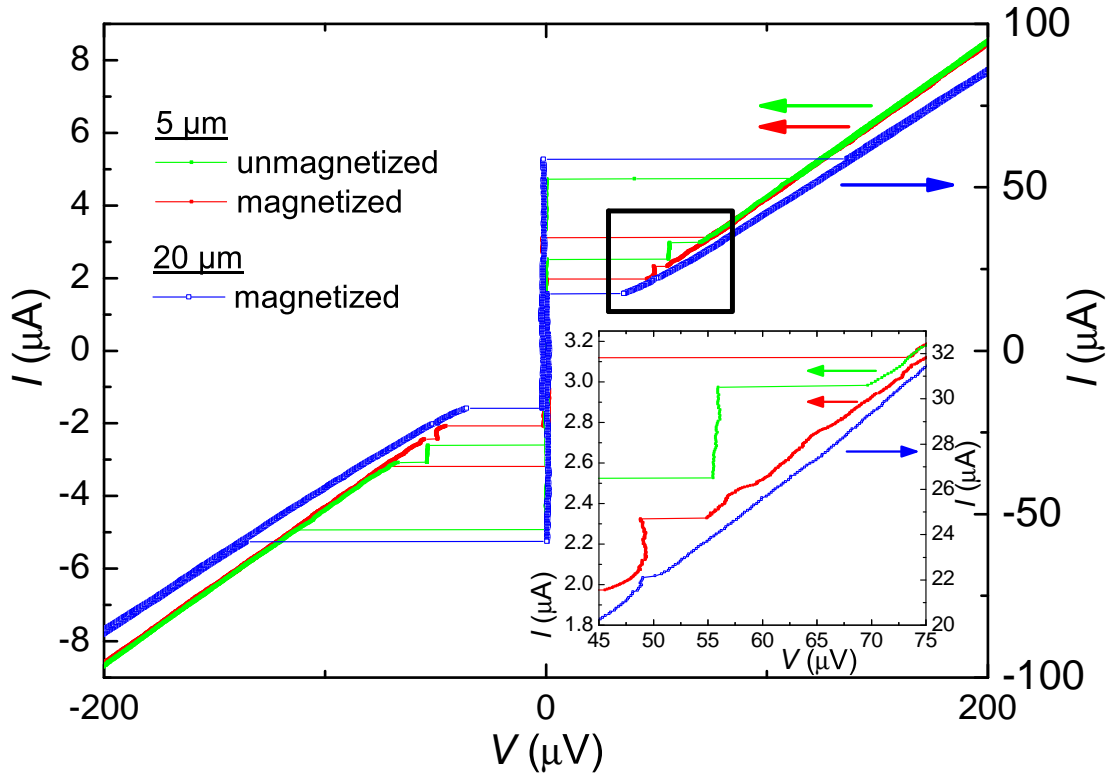


Fig. 9.1: Current-voltage characteristics of a $5 \times 5 \mu\text{m}^2$ and a $20 \times 20 \mu\text{m}^2$ SIFS π Josephson junction (GInsitu-203b; $d_F = 8.4 \text{ nm}$; oxidation time: 4 h) with and without a magnetized ferromagnetic interlayer measured without applied magnetic field at 40 mK. In the resistive state at $\sim 50 \mu\text{V}$, one observes enlarged currents (black box), which are shown in detail in the inset. The green lines depict the IVCs of the $5 \times 5 \mu\text{m}^2$ Josephson junction cooled down in zero magnetic field, while the red and blue lines are acquired for the same junction and the $20 \times 20 \mu\text{m}^2$ junction on the same sample magnetized in an out-of-plane magnetic field of 210 mT. Before acquiring the latter measurement, the junctions have been thermally cycled above T_c of the niobium electrodes. The current of the $5 \times 5 \mu\text{m}^2$ ($20 \times 20 \mu\text{m}^2$) junction is linked to the left (right) axis. We note that the voltage position $\approx 55 \mu\text{V}$ of the zero differential resistance region was reproduced for the sample with the unmagnetized interlayer in a separate cool-down two weeks after the first measurement.

and detect FMR. We note that since the micromagnetic structure of the F layers in SFS junctions typically consists of multiple domains, classical FMR can be only observed in a magnetized sample.

The first discussion of FMR in the ferromagnetic interlayer of an SFS junction goes back to Petković *et al.*^{112, 113} who examined an SFS Josephson junction with a 20 nm $\text{Pd}_{0.9}\text{Ni}_{0.1}$ ferromagnetic layer. They used the internal current oscillations of SFS Josephson junctions to resonantly excite FMR in the F interlayer and detected the absorption by the reduced dc component of the current I across the JJ at an applied

voltage $V = \hbar\omega_s/2e$. Here, they affirmed the spin wave frequency ω_s by conventional FMR. This way, they were able to observe FMR in only 10^7 Ni atoms. We note that we did not observe the effect of a decreased current due to power absorption within this work.

In contrast to the results reported in literature for SFS junctions, we observe in our SIFS junctions a current step above the subgap resistance at the voltage V_f , e.g. at $V_f \simeq 56 \mu\text{V}$ for a zero-field cooled $5 \times 5 \mu\text{m}^2$ SIFS Josephson junction (green line in Fig. 9.1). Most probable, the difference of the observed resonances in the IVCs of SFS and SIFS junctions relates to the junction coupling; while an SFS junction represents a weak link, a SIFS one is best described as a real tunnel junction, that is, the resistance R and the capacitance C of SFS junctions are defined by the F layer, while in SIFS junctions R and C are predominantly given by the insulating barrier and only the Josephson coupling depends on the I and F layer. We characterize below the current step observed in the IVCs of our junctions by applying, first, a magnetic field and, second, microwaves of different power. Finally, we prove that the excitation does not influence macroscopic quantum behavior.

Figure 9.1 shows the current-voltage characteristics of a $5 \times 5 \mu\text{m}^2$ SIFS Josephson junction (GInsitu-203b; $d_F = 8.4 \text{ nm}$; oxidation time: 4 h) with an unmagnetized and a magnetized ferromagnetic interlayer (green and red line) and of a $20 \times 20 \mu\text{m}^2$ junction with a magnetized F layer (blue line). To magnetize the interlayer, a magnetic field of 210 mT is applied out-of-plane, and the sample is thermally cycled above T_c of the niobium electrodes to remove Abrikosov vortices. In the inset of Fig. 9.1, we clearly observe in all three measurements regions with negligible differential resistance reminding us of the Fiske resonances or the Shapiro steps. We find the current steps, which were reproducible in various cool-downs, at different voltage positions for the same sample with and without a magnetized interlayer; however, for the magnetized $5 \mu\text{m}$ and $20 \mu\text{m}$ junction the voltage positions coincide. From that we learn that the current step is not caused by a spatial modulation of the current across the JJ in agreement with the small diameter of the junctions ($5, 20 \mu\text{m} \ll \lambda_J \simeq 95, 70 \mu\text{m}$). Moreover, we conclude that an excitation in the ferromagnetic layer is most probable the reason for the current step. However, in contrast to a decrease of the current, which was observed by Petković *et al.*^{112, 113} for SFS junctions, the observed increase can only be explained by an interaction between the ferromagnetic layer and the Josephson dynamics. For a possible explanation, we follow the theory of Shapiro steps^{167, 247, 254, 405, 406} and evaluate the time t dependent Josephson current²⁵⁴

$$I(t) = I_c \sin \left(\omega_{dc} t + \frac{\omega_{dc} V_{ac}}{\omega_{ac} V_{dc}} \sin(\omega_{ac} t + \Theta) + \varphi_0 \right) \quad (9.1)$$

across an ac voltage V_{ac} and dc voltage V_{dc} biased Josephson junction where $V_{dc} = \hbar\omega_{dc}/2e$, and ω_{ac} denotes the ac frequency. Here, Θ is the phase difference between the Josephson oscillation and the ac bias and φ_0 is an arbitrary phase. Equation (9.1) can be expanded using the Bessel functions J_n of the first kind and order n . Although usually in the voltage state no net supercurrent flows, in the case $\omega_{ac} = n\omega_{dc}$ an additional dc

component²⁵⁴

$$\overline{I(t)} = I_c (-1)^n J_n \left(\frac{nV_{ac}}{V_{dc}} \right) \sin(\varphi_0 - n\Theta) \quad (9.2)$$

is observed across a Josephson junction. Depending on the phase difference $\varphi_0 - n\Theta$, its value $\overline{I(t)}$ may be positive or negative; a positive current corresponds to the tunneling of a Cooper-pair with induced n -quantum emission and a negative current corresponds to an n -quantum absorption process.²⁵⁴ Hence, albeit the microscopic details are not known, we can interpret our enhanced current with Shapiro's theory in mind as an emission of photons, which are absorbed in the ferromagnetic interlayer. We note that the voltage step at $56 \mu\text{V}$ can be hardly interpreted by simple FMR since, on the one hand, the ferromagnetic sample is not magnetized in this case and, on the other hand, the voltage V_f requires an internal magnetic field

$$B_{\text{int}} = \frac{hV_f/\Phi_0}{g\mu_B} \simeq 1 \text{ T} \quad (9.3)$$

with the spectroscopic splitting factor g and the Bohr magneton μ_B ²⁰⁴, which is above all relevant fields determined by SQUID magnetometry in section 5.3.3. Here, for a detailed understanding one needs detailed information on the magnetic anisotropy of the interlayer and its magnetic domain structure. However, we doubt that a micromagnetic simulation is possible with the standard tools⁴⁰⁷ since here we do not only have to take into account the magnetization dynamics, but also quantum effects related to the Josephson dynamics may play a role.

We further discuss the observed current step in Fig. 9.2 and apply an in-plane magnetic field to the $5 \times 5 \mu\text{m}^2$ junction. In this case, we clearly detect a reduction of the current step height. We compare the reduction of the critical current $I_c \simeq 4.8 \mu\text{A}$ by $\approx 70 \text{ nA}$ with the reduction of the step maximum at $\approx 3 \mu\text{A}$ by $\approx 55 \text{ nA}$, that is a reduction of 1.5 % compared to 1.8 %. Since both values coincide within the experimental resolution, we can explain the decrease of the step height by a reduction of I_c due to an applied magnetic field. However, the reduced step height opens the view on a second current step at $64 \mu\text{V}$, which was hidden behind the bigger step. Here, for a detailed understanding additional experiments are necessary, e.g. an angle resolved magneto-resistance characterization going to higher magnetic fields.

In Fig. 9.3, we study the IVCs of the unmagnetized $5 \times 5 \mu\text{m}^2$ JJ irradiated with microwaves of different powers, but with the fixed frequency 26570 MHz , which approximately translates to the voltage of the current step position via the ac Josephson equation (2.11). We observe at high applied microwave powers Shapiro steps at $56 \mu\text{V}$ and $112 \mu\text{V}$ as expected.^{167, 405} Their power-dependent height allows to relate the irradiated microwave power* to the induced voltage across the junction²⁴⁷; an irradiation

* The given microwave power corresponds to the output of the microwave source. One can estimate a loss of 30 db in the attenuators and 10 db in the wiring. However, to estimate the microwave power coupled into the junction requires detailed knowledge about the coupling coefficient between the antenna and the junction. Hence, the values above give only an upper limit of the microwave power which is coupled into the junction.

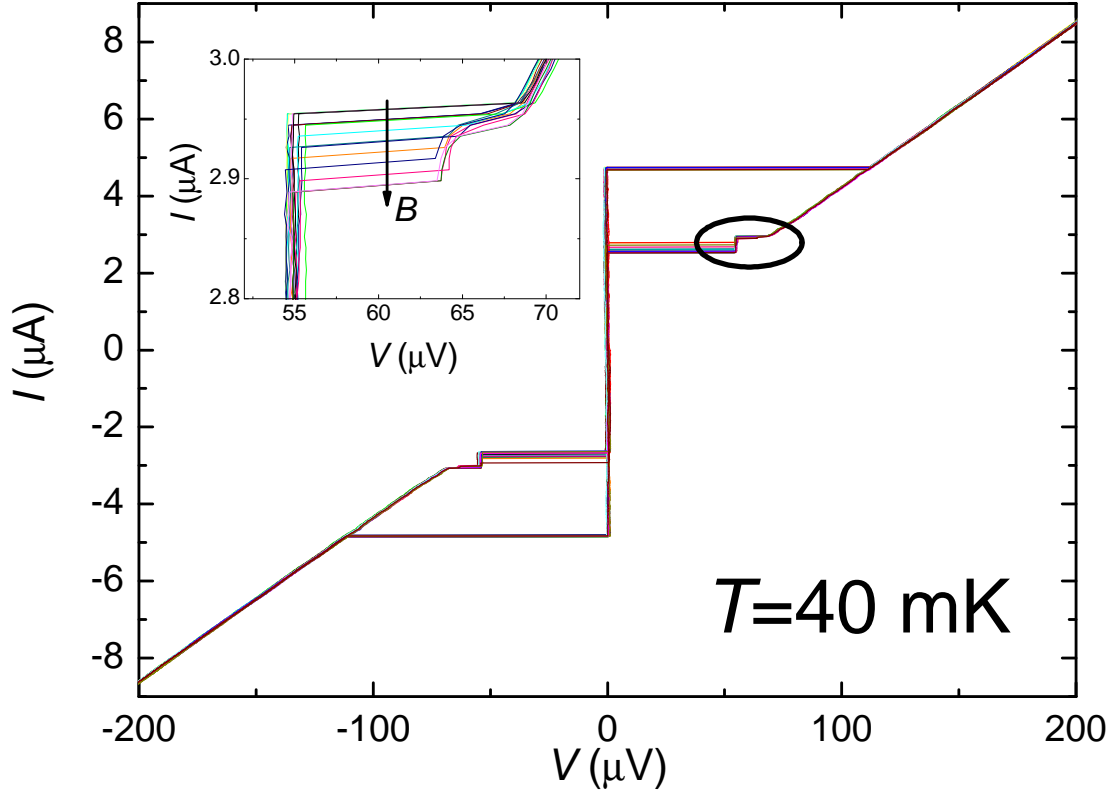


Fig. 9.2: Current-voltage characteristics of a $5 \times 5 \mu\text{m}^2$ SIFS π Josephson junction (GInsitu-203b; $d_F = 8.4\text{nm}$; oxidation time: 4 h) in different applied in-plane magnetic fields. One clearly observes an enhancement of the current above the ohmic subgap resistance at $V_f \simeq 56 \mu\text{V}$; the inset shows a zoom into this region. With increasing magnetic field, the enhancement diminishes giving rise to a second plateau at $64 \mu\text{V}$.

power of +5 dbm equals an induced ac voltage of $210 \mu\text{V}$. We note that we do not observe half-integer Shapiro steps in our measurement, which are sometimes observed in SFS junctions and are attributed to a double-sinusoidal current-phase relation or an alternating Josephson coupling.^{368, 408} Additionally, we observe -as expected- the resonance introduced above. A detailed analysis of the resonance region (see the inset of Fig. 9.3) reveals that the first Shapiro step influences our resonance for an applied microwave power $P_{\text{mw}} \gtrsim -34\text{dbm}$.⁴⁰⁹ From this measurement we can quantify our resonance by stating that it is modified by an applied ac voltage of $\approx 2 \mu\text{V}$.

Finally, here at the end of this short review of magnetic excitations observed in the IVCs, we discuss the influence of the observed current step and its possible effects on the lowest states in a potential well of the tilted washboard potential. As we have seen in chapter 8, the plasma frequency of our JJs is about 8 GHz during an escape process and hence clearly falls behind the frequency $\frac{56 \mu\text{V}}{\Phi_0} \simeq 26\text{GHz}$ associated with the observed resonance phenomenon. Hence, we expect the escape process in our Josephson junctions only defined by the Josephson dynamics, which is clearly affirmed

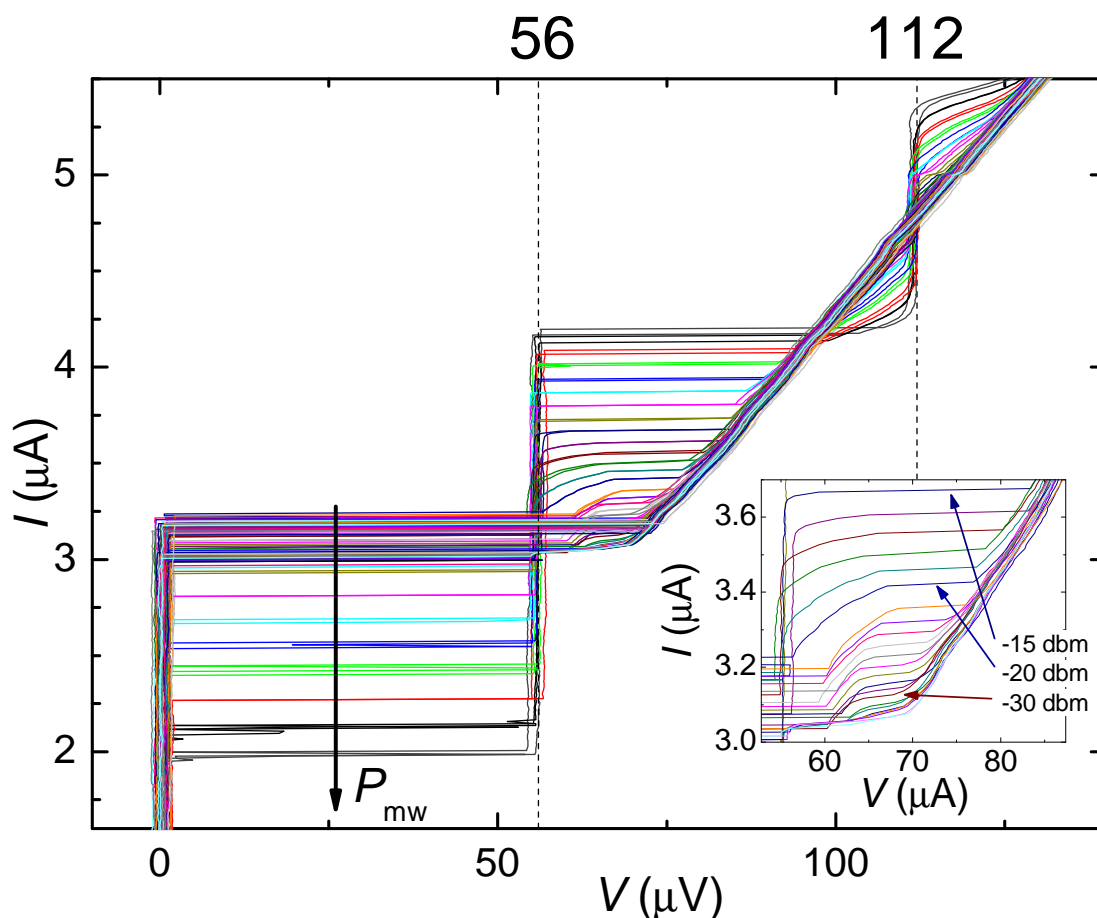


Fig. 9.3: Current-voltage characteristics of a $5 \times 5 \mu\text{m}^2$ SIFS π Josephson junction (GInsitu-203b; $d_F = 8.4 \text{ nm}$; oxidation time: 4 h) under microwave irradiation of the frequency $\omega_{\text{mw}}/2\pi = 26570 \text{ MHz}$ and different powers P_{mw} measured at 40 mK. One clearly observes Shapiro steps at $56 \mu\text{V}$ and $112 \mu\text{V}$. The inset shows a zoom into the first Shapiro step; the microwave power values in the inset are linked to the output of the microwave generator at room temperature. The first minimum in the dependence of the Shapiro step height on the applied microwave power is found at +5 dbm. Hence, a microwave power of +5 dbm creates an ac voltage $V_{\text{ac}} \simeq 210 \mu\text{V}$ across the junction. We note that the data are acquired in steps of 1 dbm. For experimental reasons, the measurement with an irradiation power of -21 dbm is missing; here, helium refill may have slightly changed the experimental parameters. We note that the roundings of the second step are related to thermal effects.⁴¹⁰

by the measurement of the width of the switching current histograms versus the bath temperature T in Fig. 9.4. Here, the crossover temperature $T_{\text{exp},5\mu\text{m}}^* \simeq 56 \text{ mK}$ for the $5 \mu\text{m}$ junction under study is close to the $T_{\text{exp}}^* \simeq 54 \text{ mK}$, which we have determined for the $20 \mu\text{m}$ junction on the same sample in section 8.4. Hence, we do not observe any influence of the detected resonance on the macroscopic quantum behavior of our SIFS junctions.

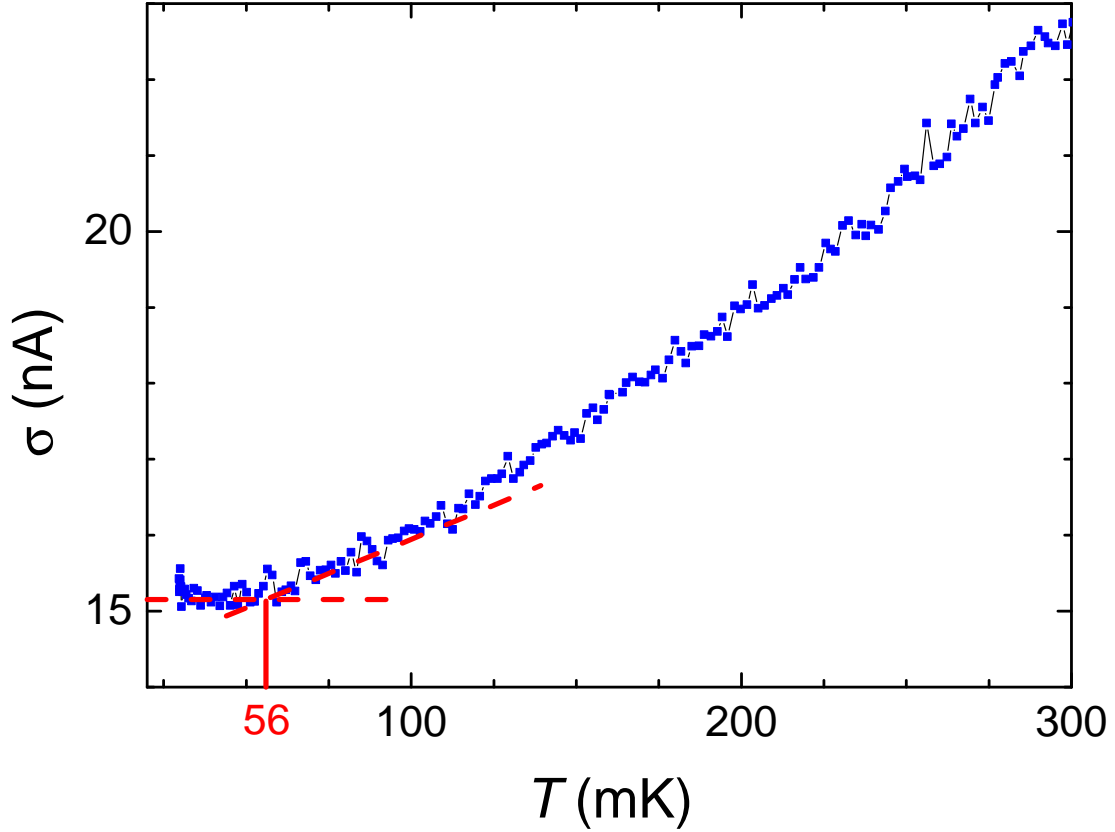


Fig. 9.4: The standard deviation $\sigma = \sqrt{\sigma_{\text{exp}}^2 + \sigma_{\text{n}}^2}$ of the switching currents versus the bath temperature T for a $5 \times 5 \mu\text{m}^2$ SIFS π Josephson junction (GInsitu-203b; $d_{\text{F}} = 8.4 \text{ nm}$; oxidation time: 4 h). The histogram half-width σ_{exp} defined by the Josephson dynamics is enlarged by the noise half-width σ_{n} originating from the measurement setup. The crossover between thermally activated escape and quantum tunneling is observed at $T_{5\mu\text{m}}^* \approx 56 \text{ mK}$, which well coincides with the 54 mK determined for the $20 \times 20 \mu\text{m}^2$ junction of the same sample discussed in Fig. 8.15. The statistics of each point is based on $\approx 11\,000$ switching events, which have been acquired without an additional waiting time between the measurements.

As illustrated within this chapter, SIFS Josephson junctions are an ideal tool to study the coupling between the Josephson effect and excitations in the ferromagnetic interlayer. We have already observed a resonance in the IVCs and attribute it to the ferromagnetic interlayer. This resonance manifests itself by an increased current at a defined voltage V_f , which is in contrast to the observation of FMR in SFS junctions in previous works. This suggests that we observe the phase dynamics across the Josephson junction and not energy absorption by FMR. Hence, it would be quite interesting to further study this resonance, not only on the one hand to understand the coupling between the Josephson effect and FMR, but also on the other hand to evaluate possible applications of this effect for sensor applications.

Part IV

CONCLUSION AND OUTLOOK

Chapter 10

CONCLUSION AND FUTURE PROSPECTS

10.1 Implications of This Work

The purpose of this work was to establish a fabrication process for Josephson junctions with a ferromagnetic interlayer and to evaluate the macroscopic quantum properties of SIFS Josephson junctions with a particular focus on their application in quantum electronics. These goals have been completely achieved, especially by observing macroscopic quantum tunneling in a SIFS π -junction. We give below a short summary of the scientific results achieved within this work.

In chapter 5, we describe the development of a self-align multilayer growth process for Nb/AlO_x/Pd_{0.82}Ni_{0.18}/Nb superconductor/insulator/ferromagnetic metal/superconductor (SIFS) Josephson junctions with controllable and reproducible properties. High critical current densities up to more than 30 A/cm² and $R_n \cdot A$ values above 130 $\Omega \mu\text{m}^2$ have been achieved. The $I_c(\Phi/\Phi_0)$ dependencies are close to an ideal Fraunhofer diffraction pattern clearly demonstrating good spatial homogeneity of the junction barrier and the ferromagnetic interlayer. Hence, our junctions compete very well with SIFS π -junctions reported in literature^{14, 54, 66} and are apparently well suited for applications in quantum information processing and to study their macroscopic quantum behavior.

In chapter 6, we examine the crossover between 0- and π -coupling with an increasing F layer thickness. We clearly observe a transition from 0- to π -coupled junctions for the thickness $d_F \simeq 6$ nm of the Pd_{0.82}Ni_{0.18} layer. The Pd_{0.82}Ni_{0.18} layers show an out-of-plane anisotropy. They have a Curie temperature of 150 K, an exchange energy $E_{\text{ex}} \simeq 20$ meV, and a saturation magnetization of about $1\mu_B$ per Ni atom, indicating that there are negligible magnetic dead layers at the interfaces. The $I_c R_n(d_F)$ dependence of the SIFS junctions can be well described by the dirty limit theory of Buzdin *et al.*³³ yielding the single characteristic length scale $\xi_F = 3.88$ nm for the decay and the oscillation of the critical current. Hence, in chapter 6 we prove that we can reproducibly grow individual junctions with a defined zero- or π -coupling and that we understand the underlying physics.

With this profound knowledge in technology, junction composition, and Josephson coupling, we now pay attention to the static, dynamic, and quantum properties of SIFS junctions. To do so, we concentrate on a single sample (GInsitu-203b) containing

π -coupled SIFS junctions, which we introduce in section 6.3. The concentration on a single sample allows the reader to compare the parameters and results obtained from the different types of experiments. For their comparison, we remind the reader that all extracted parameters are compiled in Table D.1.

In our first experiment, we analyze the damping present in SIFS junctions in chapter 7 to understand the dissipation mechanisms in quantum electronic circuits containing SIFS π -junctions. Here, not only low frequencies are important, but also the dynamics up to a few hundred GHz plays a role, e.g. for clocked rapid single flux quantum circuits. Obviously, this frequency range is not accessible with today's microwave technology, so that dissipation mechanisms can be only explored by investigating junction eigen resonances, which are illustrated as standing electromagnetic waves in the cavity formed by the junction geometry. Since these Fiske resonances nonlinearly couple to the Josephson dynamics, they appear at finite applied magnetic flux in the IVCs of the junctions where their shape reveals their resonance quality. This gives access to dissipation mechanisms in a wide frequency range up to 400 GHz. In this analysis, the quality factor increases about linearly with the frequency ω at low frequencies due to the about frequency independent damping related to quasiparticle tunneling, whereas it decreases proportional to $1/\omega$ at high frequencies due to the increasing surface resistance of the junction electrodes. The achieved quality factors range between about 5 at the junction plasma frequency and 30 at about 200 GHz. From this valuable new information, we conclude that, first, the ferromagnetic layer in SIFS junctions does not significantly contribute to the damping when we neglect its influence on I_c and R_n ; at most, it may slightly enhance the quasiparticle density in the superconducting electrodes due to the inverse proximity effect, which increases the surface impedance. Second, we affirm that the quality factor of our junctions is sufficient for their application in superconducting quantum circuits or for experiments to examine macroscopic quantum tunneling.

Inspired by the detailed study of the junction resonances above, we further investigate the properties of our Josephson junction under microwave driving in section 8.3. Here, it is often conversely discussed in literature whether these properties are related to secondary quantum effects or simply reflect a driven nonlinear oscillator. For our case, we answer this question by a classical simulation of a phase particle in a metastable state, which clearly reproduces our experimental findings. This proves that, first, the excitations found in a microwave driven SIFS junction are governed by semi-classical physics and, second, affirms the value of the plasma frequency, which we have determined by the analysis of the Fiske resonances. We note that already the existence of well-defined excitations indicates that the Josephson dynamics is not influenced by the F layer.

With the previous achievements, we can now tackle the main question we answer within this work, that is whether Josephson junctions with a ferromagnetic interlayer are suitable for quantum information processing or not. We note that this question recently got a lot of attention when it was reported not possible to cool a Josephson junction with a ferromagnetic NiCu interlayer into its quantum mechanical ground state^{150, 151}, possibly due to low-lying excitations in the ferromagnetic layer or because of critical

current fluctuations due to a dynamic reorientation of the ferromagnetic microstructure of the junctions. We note that these experiments are extremely noise sensitive and rely on transport measurements at very low temperatures. Excited by these puzzling results, we have performed an analogue study for our junctions. A challenging task in this type of research is the exact determination of the plasma frequency which we have already extracted from the measurements mentioned above. This allows for the calculation of the theoretically expected crossover temperature, below which the JJ is cooled into its quantum mechanical ground state. It compares very well with the crossover temperature extracted from the switching experiments in section 8.4. This agreement proves, first, that we have indeed observed for the first time macroscopic quantum behavior in Josephson junctions with a ferromagnetic interlayer. Second, it affirms that critical current fluctuations caused by the ferromagnetic interlayer are small compared to the thermal and quantum fluctuations. And third, it gives strong evidence that the junction under study is well suited for applications in quantum information processing.

10.2 Outlook

We have intensively studied the dynamic and quantum properties of SIFS Josephson junctions in this work, that is, we have explained the different dissipation mechanisms in these junctions and verified the macroscopic quantum behavior. Consequently, this work clarifies that SIFS π Josephson junctions are well suited for applications in quantum electronics. This includes the application for classical computation in rapid single flux quantum circuits, but the proof of macroscopic quantum behavior recommends our junctions first of all for quantum information processing. Hence, we identify SIFS π -junctions as a new element in the toolbox of quantum electronics, providing quantum circuit engineers a further degree of freedom.

However, there are still fundamentally important questions to be examined in Josephson junctions with a ferromagnetic interlayer: The coupling between ferromagnetic excitations and the Josephson dynamics on the one hand and, on the other hand, the incorporation of ferromagnetic layers with a high permeability. For the first topic, we refer the reader to chapter 9 where we have introduced excitations observed in a $5 \times 5 \mu\text{m}^2$ SIFS π Josephson junction. Here, we suggest to examine the IVCs in higher magnetic fields and at different temperatures, which would e.g. allow to relate the Fraunhofer diffraction pattern expected for the critical current dependence on an applied magnetic field to the unknown dependence of the newly discovered current step. Together with an angle-resolved magneto-transport characterization, this would prove whether the observed resonances really originate from the ferromagnetic interlayer or not.

Another interesting topic is the incorporation of ferromagnetic layers with a high relative permeability μ as the F layer. Although it is at the moment not clear which material

to choose, an interlayer with a high permeability would concentrate the magnetic field in the ferromagnetic layer and hence completely change the underlying physics. We particularly stress the point that analogously to an electromagnetic wave in matter the characteristic wave impedance Z of such a Josephson transmission line scales with $\sqrt{\mu}$ (cf. Eq. (3.32)), which would allow to increase Z . This way, the wave impedance of a Josephson transmission line might be matched to the wave impedance of free space and hence exposes Josephson junctions as microwave receivers and detectors.^{254, 384, 411, 412}

10.3 Conclusion

The present work intensively discusses technological aspects and quantum properties of SIFS Josephson junctions. From the technological point of view, it has established niobium thin film technology at the WMI, whose extensive study during this work was not only necessary to grow SIFS junctions, but was also widely used to define superconducting resonators. Moreover, the growth of niobium Josephson junctions, of course, requires a mesa etch process, which was implemented during this work in a self-align manor. Naturally, this process was also well suited to grow SIFS junctions on the leading edge of today's technology.

From the physical point of view, one of the highlights of this work is a thorough analysis of the damping mechanisms present in SIFS Josephson junctions in the frequency range from the plasma frequency at 20 GHz up to 400 GHz. Here, dissipation due to quasiparticle tunneling dominates at low frequencies, while at high frequencies surface impedance plays the dominant role. However, the main achievement during the presented study is the observation of macroscopic quantum tunneling in a Josephson junction with a ferromagnetic interlayer. We note that there has been an intensive debate whether the demonstration of macroscopic quantum behavior is really possible since it has not been seen in junctions with a NiCu interlayer.^{150, 151} This question is now positively answered during this work. To conclude, the approval of macroscopic quantum behavior in switching experiments excludes low-lying excitations in the junctions and rules out a fluctuating critical current due to a dynamic reorientation of the magnetic domain structure in the F layer. This qualifies SIFS π -junctions as π -phase shift elements in superconducting qubits.

Since now, at the end of this work, the questions concerning the application of SIFS π -junctions in quantum electronics have been conclusively answered, let us think of future applications of SIFS junctions. As we have seen in chapter 9, excitations most likely originating from the ferromagnetic interlayer of our junctions have been observed during this work. Their understanding is interesting, on the one hand, from the theoretical point of view, but also for sensor or microwave emitter applications.^{254, 384, 411, 412} This way, the study of quantum systems is potentially relevant for applications beside fundamental research.

Part V

APPENDIX

Appendix A

JUNCTION GROWTH RECIPE

1. Clean Si (001) substrate (oxide thickness 50 nm) in acetone/isopropanol
2. Multilayer deposition
 - (a) Resist stencil
 - i. Spin coat MicroChemicals AZ 5214E using program 2 (4 000 rpm)
 - ii. Bake 70 s at 111°C
 - iii. Edge bead removal (edge exposure 10 s with the mask aligner (MA); development with MicroChemicals AZ Developer:H₂O 1:1 for 120 s)
 - iv. Flood exposure with the MA for 0.7 s
 - v. Bake 120 s at 130°C
 - vi. Exposure structure with the MA for 5.5 s (red mask in Fig. 5.5)
 - vii. Develop with MicroChemicals AZ Developer:H₂O 1:1 for 14 min
 - (b) Sputter with the parameters in Table 5.2
 - (c) Lift-off with acetone/isopropanol
3. Mesa definition
 - (a) Spin coat MicroChemicals AZ 6212 using program 2 (4 000 rpm)
 - (b) Bake 70 s at 111°C
 - (c) Edge bead removal (edge exposure 30 s with the MA; development with MicroChemicals AZ Developer:H₂O 1:1 for 120 s)
 - (d) Exposure structure with the MA for 4.5 s (hatched mask in Fig. 5.5)
 - (e) Develop with MicroChemicals AZ Developer:H₂O 1:1 for 30 s
4. Etching with the parameters in Table 5.1
5. Sputter deposition of SiO₂ with the parameters in Table 5.2
6. Lift-off with acetone/isopropanol
7. Wiring layer deposition

- (a) Resist stencil
 - i. Spin coat MicroChemicals AZ 6212 using program 2 (4 000 rpm)
 - ii. Bake 70 s at 111°C
 - iii. Edge bead removal (edge exposure 10 s with the MA; development with MicroChemicals AZ Developer:H₂O 1:1 for 120 s)
 - iv. Exposure structure with the MA for 4.5 s (magenta mask in Fig. 5.5)
 - v. Develop with MicroChemicals AZ Developer:H₂O 1:1 for 30 s
- (b) Sputter Nb with the parameters in Table 5.2
- (c) Lift-off with acetone/isopropanol

Appendix B

THE SEMI-CLASSICAL SIMULATION OF THE JOSEPHSON JUNCTION DYNAMICS

In this appendix, we shortly discuss the semi-classical simulation of a Josephson junction under microwave irradiation based on a first order Runge-Kutta method.^{413, 414} We essentially simulate the evolution of the phase difference φ across the JJ, which depends on the velocity $\tilde{v} = \frac{\partial \varphi}{\partial \tau}$ and the reduced time $\tau = \omega_p t$. The algorithm for the simulation in Fig. 8.11 essentially consists for each driving frequency f_{mw} of the following steps:

1. Start with $i_b \approx 1$.
2. Set a small driving current i_{mw} and the phase difference $\varphi = \arcsin(i_b)$ at zero velocity $\tilde{v} = 0$.
3. Let the phase particle oscillate for typically 100 oscillations using the method introduced in section B.1; remember the last phase difference φ and velocity \tilde{v} . If the particle does not escape, increase the driving current i_{mw} and repeat this step starting with the perceived φ and \tilde{v} .
4. Note down, at which driving the particle escaped.
5. Slightly decrease the bias current i_b and reduce the driving until a stable oscillation exists.
6. Go back to item 3.

B.1 The Time Evolution of the Phase Difference

To find a system of equations which is suitable to simulate the junction dynamics, we start with Eq. (3.2) and transform it to

$$\frac{1}{\omega_p^2} \ddot{\varphi} + \underbrace{\frac{1}{\omega_p RC}}_{Q_0^{-1}} \frac{1}{\omega_p} \dot{\varphi} + \left(\sin \varphi - \frac{I_b}{I_c} \right) = 0.$$

In the case of external driving, the bias current I_b has to be replaced by $I_b + I_{mw} \cos(\omega_{mw}t)$, which results in

$$\ddot{\varphi} + Q_0^{-1} \omega_p \dot{\varphi} + \omega_p^2 \left(\sin \varphi - \frac{I_b}{I_c} - \frac{I_{mw}}{I_c} \cos(\omega_{mw}t) \right) = 0.$$

This yields

$$\Delta\dot{\varphi} = \left(-Q_0^{-1} \dot{\varphi} - \omega_p \left(\sin \varphi - \frac{I_b}{I_c} - \frac{I_{mw}}{I_c} \cos(\omega_{mw}t) \right) \right) \omega_p \Delta t,$$

and after introducing the abbreviations $\tau = \omega_p t$ and $\tilde{v} = \frac{\partial \varphi}{\partial \tau}$, we arrive at

$$\Delta\tilde{v} = \left(-\frac{1}{Q_0} \tilde{v} - \sin \varphi + \frac{I_b}{I_c} + \frac{I_{mw}}{I_c} \cos\left(\frac{\omega_{mw}}{\omega_p} \tau\right) \right) \Delta\tau.$$

Hence, we obtain the set of equations

$$\begin{aligned} \tau' &= \tau + \Delta\tau \\ \varphi' &= \varphi + \tilde{v} \Delta\tau \\ \tilde{v}' &= \tilde{v} + \left(-\frac{\tilde{v}}{Q_0} - \sin \varphi + \frac{I_b}{I_c} + \frac{I_{mw}}{I_c} \cos\left(\frac{\omega_{mw}}{\omega_p} \tau\right) \right) \Delta\tau, \end{aligned} \quad (\text{B.1})$$

which describes the change of the phase difference φ and the velocity \tilde{v} in a short time interval $\Delta\tau$. It allows to simulate the dynamics of the phase difference by dividing an oscillation period in typically 100 time segments.

Appendix C

MATERIAL CONSTANTS

niobium			
		value	source
T_c	critical temperature	9.26 K	Ref. [415]
Δ_0	energy gap	1.45 meV	Figure 5.9
	melting point	2468 K	Ref. [316]
λ_L	London penetration depth (sputtered thin film)	90 nm	Ref. [259]

$\text{Pd}_{0.82}\text{Ni}_{0.18}$			
		value	source
T_C	Curie temperature	150 K	Section 5.3.3
D	Diffusion coefficient	$5 \cdot 10^{-3} \text{ m}^2/\text{s}$	Section 6.2
E_{ex}	exchange energy	20 meV	Section 6.2
v_F	Fermi velocity Pd	$2 \cdot 10^5 \text{ m/s}$	Ref. [416]
		$5 \cdot 10^5 \text{ m/s}$	Ref. [348]
	spec. resistance	$\approx 19 \mu\Omega \text{ cm}$	this work
	spec. resistance $\text{Ni}_{0.90}\text{Pd}_{0.10}$	$24 \mu\Omega \text{ cm}$	Ref. [324]
$\mu_0 M_s$	saturation magnetization (interlayer of the thickness 8.4 nm; out-of-plane)	0.2 T	Section 5.3.3

Appendix D

THE PARAMETERS OF THE SAMPLE GINSITU-203B

An essential point for the proof of macroscopic quantum behavior in Josephson junctions is the observation of the transition from thermal escape to macroscopic quantum tunneling at the theoretically expected temperature, which is calculated from the plasma frequency of the junction. To unambiguously prove this important quantity, this work has reexamined all important measurements for one and the same sample GInsitu-203b, which contains π -coupled SIFS Josephson junctions (oxidation time: 4 h, $d_F = 8.4$ nm). We sum up the parameters extracted from the IVCs, the study of the Fiske resonances, and the microwave driving analysis in Table D.1. The clear and distinct agreement of these values clearly affirms the determined plasma frequency.

length l area A	50 μm 2500 μm^2	20 μm 400 μm^2	Figure 5.5 Figure 5.5			
critical current I_c retrapping current I_r normal resistance R_n subgap resistance R_{sg}	555 μA 125 μA 51 $\text{m}\Omega$ 439 $\text{m}\Omega$	131 μA 27 μA 333 $\text{m}\Omega$ 2140 $\text{m}\Omega$	Chapter 6 Chapter 6 Chapter 6 Chapter 6	IVCs		
critical current density j_c $I_c R_n$ $R_n \cdot A$ $I_c R_{sg}$ λ_J $Q_0 = 4I_c / \pi I_r$	22 A/cm^2 28 μV 128 $\Omega\mu\text{m}^2$ 244 μV 71 μm 5.65	33 A/cm^2 44 μV 133 $\Omega\mu\text{m}^2$ 280 μV 59 μm 6.18	Chapter 6 Chapter 6 Chapter 6 Chapter 6 Chapter 6 Chapter 6			
Fiske step spacing	$\approx 165 \mu\text{V}$	$\approx 415 \mu\text{V}$	Chapter 7		Fiske	
Swihart velocity \bar{c} plasma frequency ω_p plasma frequency $\omega_p/2\pi$ capacitance C specific capacitance $C_s = C/A$ $Q_0 = \omega_p RC$	7.98 $\cdot 10^6 \text{m/s}$ 112 GHz 17.8 GHz 135 pF 54 $\text{fF}/\mu\text{m}^2$ 6.64	8.03 $\cdot 10^6 \text{m/s}$ 136 GHz 21.7 GHz 21 pF 53 $\text{fF}/\mu\text{m}^2$ 6.24	Chapter 7 Chapter 7 Chapter 7 Chapter 7 Chapter 7 Chapter 7			
plasma frequency $\omega_p/2\pi$		$\approx 20 \text{GHz}$	Section 8.3			Microwaves
crossover temperature: measured T_{exp}^* calculated T_{th}^*		54 mK 53 mK	Section 8.4 Section 8.4			

Tab. D.1: Summary of the parameters determined for the sample GInsitu-203b.

Appendix E

NOMENCLATURE

A	junction area	
$\alpha = \frac{\omega_a}{\omega_p}$	reduced plasma frequency	Equation (4.9)
a_q	correction factor to quantum escape	Equation (4.14)
a_t	correction factor to thermal escape	Equation (4.11)
$\beta_c = Q_0^2$	McCumber parameter	Section 3.1
C	capacitance between the JJ electrodes	Section 3.1
\mathcal{C}	capacitance per length	Equation (3.27)
$\bar{c} = \sqrt{\frac{t^j}{\mu_0 \epsilon_r \epsilon_0 t_B}}$	Swihart velocity	Equation (3.23)
d	barrier or interlayer thickness	
d_F	ferromagnetic interlayer thickness	
Δ, Δ_0	energy gap of a superconductor	
e	elementary charge	$1.602176 \cdot 10^{-19} \text{ C}$
$\epsilon_0 = 1/\mu_0 c^2$	electric constant	$8.854 \cdot 10^{-12} \text{ As/Vm}$
ϵ_r	relative dielectric constant in a solid	
$\epsilon^{i,j}$	relative dielectric constant in an idle region or junction	
ϵ	potential energy above E_F	
\vec{E}	electric field vector	
E_{ex}	exchange energy of a ferromagnet	Section 2.3
E_F	Fermi energy	
$E_J = \frac{\Phi_0 I_c}{2\pi}$	Josephson energy	Equation (3.4)
E_{Th}	Thouless energy	
$E_{\text{Th}} = \hbar v_F / t^j$	(ballistic SNS junction)	Equation (2.18)
$E_{\text{Th}} = \hbar D / t^{j^2}$	(diffusive SNS junction)	Equation (2.25)
$F_n^2(\Phi)$	dependence of the Fiske resonance height on the applied magnetic flux	Equation (3.43)
φ	gauge-invariant macroscopic phase difference between superconducting electrodes	
$\delta\varphi$	additional small oscillation	Section 4.4.2
$\Phi_0 = \frac{h}{2e}$	magnetic flux quantum	$2.067833 \cdot 10^{-15} \text{ Wb}$

Φ_H	flux due to an externally applied magnetic field	Section 6.4
Φ_M	flux due to the magnetization of an F layer	Section 6.4
$\phi = \frac{\Phi}{\Phi_0}$	reduced flux	Section 3.2.4
Γ	escape/switching rate	
\vec{H}	magnetic field vector	
h	Planck constant	$6.62606 \cdot 10^{-34}$ Js
\hbar	$h/2\pi$	$1.054571 \cdot 10^{-34}$ Js
$\iota = \sqrt{-1}$	imaginary unit	
$\Im(x)$	imaginary part of x	
I_b	bias current	
$i_b = \frac{I_b}{I_c}$	normalized bias current	
I_c	critical current of a JJ	
I_{mw}	microwave current	
$i_{mw} = \frac{I_{mw}}{I_c}$	normalized microwave current	
ΔI_n	current height of the n -th Fiske step	Equation (3.42)
I_r	retrapping current	
I_s	supercurrent	
j	current density	
$j_c = \frac{I_c}{A}$	critical current density	
J_m	Bessel function of the first kind and order m	
κ	small oscillation amplitude	Section 4.4.2
k_B	Boltzmann constant	$1.38065 \cdot 10^{-23}$ J/K
K_J	Josephson constant	483.5978 GHz/mV
\mathcal{L}	capacitance per length	Equation (3.30)
λ_J	Josephson penetration depth	Equation (3.12)
λ_L	London penetration depth	
L^i	length of an idle region	Figure 3.6
L^j	length of a JJ	
$m^* = 2m_e$	Cooper-pair mass	
m_e	electron mass	$9.10938 \cdot 10^{-31}$ kg
n	arbitrary integer variable	
n_n^*	Cooper-pair density in the superconductor	
n		
μ	relative permeability of a solid	
μ_0	vacuum permeability	$4\pi \cdot 10^{-7}$ Vs/Am
$\mu_B = \frac{e\hbar}{2m_e}$	Bohr magneton	$9.274009 \cdot 10^{-24}$ J/T
p_F	Fermi momentum	
Ψ	macroscopic wave function of a superconductor	

$Q_0 = \omega_p RC$	intrinsic quality factor of a JJ in the absence of a bias current	Section 3.1
$Q = \alpha Q_0$	intrinsic quality factor of a JJ under a bias current	Section 3.1
Q_{IVC}	Q_0 determined from the IVCs and the RCSJ model	Chapter 7
Q_{Swihart}	Q_0 determined from the Swihart velocity	Chapter 7
\tilde{Q}	quality factor of the n -th Fiske resonance after subtraction of quasiparticle damping	Chapter 7
Q_n	quality factor of the n -th Fiske resonance	Equation (3.41)
$P(I_b)$	probability of switching into voltage state at bias current I_b	Equation (8.1)
R_K	von Klitzing constant	25 812.8074 Ω
R_n	normal resistance of a Josephson junction (resistance measured at an applied voltage much higher than the gap sum voltage)	
$\Re(x)$	real part of x	
R_{sg}	subgap resistance of a Josephson junction	
Θ	macroscopic phase of a superconductor	
\ominus	phase difference between the driving and the particle position	Section 4.4.2
t	time	
$\tau = \omega_p t$	reduced time	Equation (3.7)
T	temperature	
T_{esc}	escape temperature	Section 4.3
T^*	crossover temperature	Equation (4.16)
$t_B = 2\lambda_L + \mu d_F + t^j$	magnetic junction thickness	Section 3.2
t_B^j	effective magnetic thickness for junction resonances	Equation (3.48)
\tilde{t}_B^j	effective magnetic thickness for $I_c(H)$	Equation (3.49)
$t^{i,j}$	insulator thickness in the idle region or junction	
$U(\varphi, i_b)$	tilted washboard potential	Equation (3.3)
v_F	Fermi velocity	
V_n	voltage position of the n -th Fiske step	Equation (3.34)
$V_c = I_c R_n$	characteristic voltage	Section 6.2
$V_g = \frac{2\Delta_0}{e}$	gap sum voltage	
V_f	resonance position	Chapter 9
$\omega_a = \alpha \omega_p$	attempt frequency of the phase particle	Equation (4.9)
$\omega_p = \sqrt{\frac{2eI_c}{\hbar C}}$	plasma frequency of a JJ without bias current	Equation (3.6)
v_{ph}	wave velocity	Section 3.2.6

W	barrier height in the tilted washboard potential	Equation (4.8)
W^j	width of a JJ	
ξ_N	decay length at an SN interface	Equation (2.22)
ξ_F	decay constant at an SF interface	Equation (2.28)
ξ_{F1}	decay length at an SF interface	Equation (2.29)
$2\pi\xi_{F2}$	oscillation length at an SF interface	Equation (2.30)
Z	characteristic wave impedance	Equation (3.32)
$Z_0 = \mu_0 c$	characteristic wave impedance of the vacuum	376.73 Ω
Z_n	parameter for the n -th high- Q Fiske resonance	Equation (3.46)

All explicitly given values of natural constants follow Ref. [417].

Bibliography

- [1] J. Needham. *Science and Civilisation in China*, volume 4, Physics and Physical Technology. Cambridge University Press, 1962.
- [2] M. N. Baibich, J. M. Broto, A. Fert, F. Nguyen Van Dau, F. Petroff, P. Etienne, G. Creuzet, A. Friederich, and J. Chazelas. Giant magnetoresistance of (001)Fe/(001)Cr magnetic superlattices. *Phys. Rev. Lett.*, 61(21):2472–2475, 1988.
- [3] G. Binasch, P. Grünberg, F. Saurenbach, and W. Zinn. Enhanced magnetoresistance in layered magnetic structures with antiferromagnetic interlayer exchange. *Phys. Rev. B*, 39(7):4828–4830, 1989.
- [4] S. S. P. Parkin, N. More, and K. P. Roche. Oscillations in exchange coupling and magnetoresistance in metallic superlattice structures: Co/Ru, Co/Cr, and Fe/Cr. *Phys. Rev. Lett.*, 64(19):2304–2307, 1990.
- [5] S. S. P. Parkin, R. Bhadra, and K. P. Roche. Oscillatory magnetic exchange coupling through thin copper layers. *Phys. Rev. Lett.*, 66(16):2152–2155, 1991.
- [6] S. M. Thompson. The discovery, development and future of GMR: The Nobel Prize 2007. *J. Phys. D*, 41(9):093001, 2008.
- [7] M. Julliere. Tunneling between ferromagnetic films. *Phys. Lett. A*, 54(3):225–226, 1975.
- [8] Y. Aharonov and D. Bohm. Significance of electromagnetic potentials in the quantum theory. *Phys. Rev.*, 115(3):485–491, 1959.
- [9] Y. Aharonov and D. Bohm. Further considerations on electromagnetic potentials in the quantum theory. *Phys. Rev.*, 123(4):1511–1524, 1961.
- [10] B. D. Josephson. Possible new effects in superconductive tunnelling. *Phys. Lett.*, 1(7):251–253, 1962.
- [11] B. D. Josephson. Coupled superconductors. *Rev. Mod. Phys.*, 36(1):216–220, 1964.
- [12] B. D. Josephson. Supercurrents through barriers. *Adv. Phys.*, 14(56):419–451, 1965.
- [13] H. Meissner. Superconductivity of contacts with interposed barriers. *Phys. Rev.*, 117(3):672–680, 1960.
- [14] V. V. Ryazanov, V. A. Oboznov, A. Yu. Rusanov, A. V. Veretennikov, A. A. Golubov, and J. Aarts. Coupling of two superconductors through a ferromagnet: Evidence for a π junction. *Phys. Rev. Lett.*, 86(11):2427–2430, 2001.
- [15] L. N. Bulaevskii, V. V. Kuzii, and A. A. Sobyenin. Superconducting system with weak coupling to the current in the ground state. *JETP Lett.*, 25:290–294, 1977.
- [16] E. A. Demler, G. B. Arnold, and M. R. Beasley. Superconducting proximity effects in magnetic metals. *Phys. Rev. B*, 55(22):15174–15182, 1997.
- [17] A. A. Golubov, M. Yu. Kupriyanov, and E. Il’ichev. The current-phase relation in Josephson junctions. *Rev. Mod. Phys.*, 76(2):411–469, 2004.
- [18] J. J. A. Baselmans, B. J. van Wees, and T. M. Klapwijk. Direct demonstration of circulating

- currents in a controllable π -SQUID generated by a 0 to π transition of the weak links. *Phys. Rev. B*, 65(22):224513, 2002.
- [19] J. J. A. Baselmans, T. T. Heikkilä, B. J. van Wees, and T. M. Klapwijk. Direct observation of the transition from the conventional superconducting state to the pi state in a controllable Josephson junction. *Phys. Rev. Lett.*, 89(20):207002, 2002.
- [20] J.-P. Cleuziou, W. Wernsdorfer, V. Bouchiat, T. Ondarçuhu, and M. Monthieux. Carbon nanotube superconducting quantum interference device. *Nature Nanotechnology*, 1(1):53–59, 2006.
- [21] V. B. Geshkenbein, A. I. Larkin, and A. Barone. Vortices with half magnetic flux quanta in “heavy-fermion” superconductors. *Phys. Rev. B*, 36(1):235–238, 1987.
- [22] D. A. Wollman, D. J. Van Harlingen, W. C. Lee, D. M. Ginsberg, and A. J. Leggett. Experimental determination of the superconducting pairing state in YBCO from the phase coherence of YBCO-Pb dc SQUIDS. *Phys. Rev. Lett.*, 71(13):2134–2137, 1993.
- [23] D. J. Van Harlingen. Phase-sensitive tests of the symmetry of the pairing state in the high-temperature superconductors; evidence for $d_{x^2-y^2}$ symmetry. *Rev. Mod. Phys.*, 67(2):515–535, 1995.
- [24] L. B. Ioffe, V. B. Geshkenbein, M. V. Feigel’man, A. L. Fauchère, and G. Blatter. Environmentally decoupled SDS-wave Josephson junctions for quantum computing. *Nature*, 398(6729):679–681, 1999.
- [25] C. C. Tsuei and J. R. Kirtley. Pairing symmetry in cuprate superconductors. *Rev. Mod. Phys.*, 72(4):969–1016, 2000.
- [26] C. C. Tsuei and J. R. Kirtley. d-wave pairing symmetry in cuprate superconductors—fundamental implications and potential applications. *Physica C*, 367(1-4):1–8, 2002.
- [27] H. J. H. Smilde, Ariando, D. H. A. Blank, G. J. Gerritsma, H. Hilgenkamp, and H. Rogalla. d-wave-induced Josephson current counterflow in $\text{YBa}_2\text{Cu}_3\text{O}_{7-\delta}/\text{Nb}$ zigzag junctions. *Phys. Rev. Lett.*, 88(5):057004, 2002.
- [28] F. Lombardi, F. Tafuri, F. Ricci, F. Miletto Granozio, A. Barone, G. Testa, E. Sarnelli, J. R. Kirtley, and C. C. Tsuei. Intrinsic d-wave effects in $\text{YBa}_2\text{Cu}_3\text{O}_{7-\delta}$ grain boundary Josephson junctions. *Phys. Rev. Lett.*, 89(20):207001, 2002.
- [29] H. Hilgenkamp, Ariando, H. H. Smilde, D. H. A. Blank, G. Rijnders, H. Rogalla, J. R. Kirtley, and C. C. Tsuei. Ordering and manipulation of the magnetic moments in large-scale superconducting π -loop arrays. *Nature*, 422(6927):50–53, 2003.
- [30] Ariando, D. Darminto, H. J. H. Smilde, V. Leca, D. H. A. Blank, H. Rogalla, and H. Hilgenkamp. Phase-sensitive order parameter symmetry test experiments utilizing $\text{Nd}_{2-x}\text{Ce}_x\text{CuO}_{4-y}/\text{Nb}$ zigzag junctions. *Phys. Rev. Lett.*, 94(16):167001, 2005.
- [31] Wikipedia English. *Pi Josephson junction*. Accessed online on April 13th, 2011.
- [32] D. J. Van Harlingen, T. L. Robertson, B. L. T. Plourde, P. A. Reichardt, T. A. Crane, and John Clarke. Decoherence in Josephson-junction qubits due to critical-current fluctuations. *Phys. Rev. B*, 70(6):064517, 2004.
- [33] A. Buzdin and I. Baladié. Theoretical description of ferromagnetic π junctions near the critical temperature. *Phys. Rev. B*, 67(18):184519, 2003.
- [34] T. Kato, A. A. Golubov, and Y. Nakamura. Decoherence in a superconducting flux qubit with a π -junction. *Phys. Rev. B*, 76(17):172502, 2007.
- [35] Y. Tanaka and S. Kashiwaya. Theory of Josephson effect in superconductor-ferromagnetic-insulator-superconductor junction. *Physica C*, 274(3-4):357–363, 1997.
- [36] O. Vávra, S. Gaži, D. S. Golubović, I. Vávra, J. Dérer, J. Verbeeck, G. Van Tendeloo, and V. V.

- Moshchalkov. 0 and π phase Josephson coupling through an insulating barrier with magnetic impurities. *Phys. Rev. B*, 74(2):020502, 2006.
- [37] S. Kawabata, S. Kashiwaya, Y. Asano, Y. Tanaka, and A. A. Golubov. Macroscopic quantum dynamics of π junctions with ferromagnetic insulators. *Phys. Rev. B*, 74(18):180502, 2006.
- [38] S. Kawabata, Y. Asano, Y. Tanaka, A. A. Golubov, and S. Kashiwaya. Josephson π state in a ferromagnetic insulator. *Phys. Rev. Lett.*, 104(11):117002, 2010.
- [39] S. Kawabata and Y. Asano. Theory of quantum transport in Josephson junctions with a ferromagnetic insulator. *Low Temp. Phys.*, 36(10):915–919, 2010.
- [40] P. Fulde and R. A. Ferrell. Superconductivity in a strong spin-exchange field. *Phys. Rev.*, 135(3A):A550–A563, 1964.
- [41] A. I. Larkin and Yu. N. Ovchinnikov. Inhomogeneous state of superconductors. *Sov. Phys.-JETP*, 20(3):762–769, 1965.
- [42] A.I. Buzdin, L.N. Bulaevskii, and S.V. Panyukov. Critical-current oscillations as a function of the exchange field and thickness of the ferromagnetic metal (F) in an S-F-S Josephson junction. *JETP Lett.*, 35(4):178–180, 1982.
- [43] A.I. Buzdin. Proximity effects in superconductor-ferromagnet heterostructures. *Rev. Mod. Phys.*, 77(3):935–976, 2005.
- [44] A. I. Buzdin, B. Vujcic, and M. Yu. Kupriyanov. Superconductor-ferromagnet structures. *Sov. Phys. JETP*, 74:124–129, 1992.
- [45] Z. Radović, M. Ledvij, L. Dobrosavljević-Grujić, A. I. Buzdin, and J. R. Clem. Transition temperatures of superconductor-ferromagnet superlattices. *Phys. Rev. B*, 44(2):759–764, 1991.
- [46] J. S. Jiang, D. Davidović, Daniel H. Reich, and C. L. Chien. Oscillatory superconducting transition temperature in Nb/Gd multilayers. *Phys. Rev. Lett.*, 74(2):314–317, 1995.
- [47] J. Y. Gu, C.-Y. You, J. S. Jiang, J. Pearson, Ya. B. Bazaliy, and S. D. Bader. Magnetization-orientation dependence of the superconducting transition temperature in the ferromagnet-superconductor-ferromagnet system: CuNi/Nb/CuNi. *Phys. Rev. Lett.*, 89(26):267001, 2002.
- [48] Th. Mühge, N. N. Garif'yanov, Yu. V. Goryunov, G. G. Khaliullin, L. R. Tagirov, K. Westerholt, I. A. Garifullin, and H. Zabel. Possible origin for oscillatory superconducting transition temperature in superconductor/ferromagnet multilayers. *Phys. Rev. Lett.*, 77(9):1857–1860, 1996.
- [49] J. Aarts, J. M. E. Geers, E. Brück, A. A. Golubov, and R. Coehoorn. Interface transparency of superconductor/ferromagnetic multilayers. *Phys. Rev. B*, 56(5):2779–2787, 1997.
- [50] L. Lazar, K. Westerholt, H. Zabel, L. R. Tagirov, Yu. V. Goryunov, N. N. Garif'yanov, and I. A. Garifullin. Superconductor/ferromagnet proximity effect in Fe/Pb/Fe trilayers. *Phys. Rev. B*, 61(5):3711–3722, 2000.
- [51] A. V. Veretennikov, V. V. Ryazanov, V. A. Oboznov, A. Yu. Rusanov, V. A. Larkin, and J. Aarts. Supercurrents through the superconductor-ferromagnet-superconductor (SFS) junctions. *Physica B*, 284-288(1):495–496, 2000.
- [52] V. V. Ryazanov, V. A. Oboznov, A. S. Prokofiev, V. V. Bolginov, and A. K. Feofanov. Superconductor-Ferromagnet-Superconductor π -junctions. *J. Low Temp. Phys.*, 136(5):385–400, 2004.
- [53] V. A. Oboznov, V. V. Bol'ginov, A. K. Feofanov, V. V. Ryazanov, and A. I. Buzdin. Thickness dependence of the Josephson ground states of superconductor-ferromagnet-superconductor junctions. *Phys. Rev. Lett.*, 96(19):197003, 2006.
- [54] T. Kontos, M. Aprili, J. Lesueur, F. Genêt, B. Stephanidis, and R. Boursier. Josephson junction through a thin ferromagnetic layer: Negative coupling. *Phys. Rev. Lett.*, 89(13):137007, 2002.

- [55] H. Sellier, C. Baraduc, F. Lefloch, and R. Calemczuk. Temperature-induced crossover between 0 and π states in S/F/S junctions. *Phys. Rev. B*, 68(5):054531, 2003.
- [56] M. Aprili, T. Kontos, W. Guichard, J. Lesueur, and P. Gandit. Ferromagnetic π -junctions. *Physica C*, 408-410:606–609, 2004.
- [57] V. M. Krasnov, O. Ericsson, S. Intiso, P. Delsing, V. A. Oboznov, A. S. Prokofiev, and V. V. Ryazanov. Planar S-F-S Josephson junctions made by focused ion beam etching. *Physica C*, 418(1-2):16–22, 2005.
- [58] J. W. A. Robinson, S. Piano, G. Burnell, C. Bell, and M.G. Blamire. Critical current oscillations in strong ferromagnetic π junctions. *Phys. Rev. Lett.*, 97(17):177003, 2006.
- [59] J. W. A. Robinson, S. Piano, G. Burnell, C. Bell, and M. G. Blamire. Zero to π transition in superconductor-ferromagnet-superconductor junctions. *Phys. Rev. B*, 76(9):094522, 2007.
- [60] S. M. Frolov, M. J. A. Stoumoules, T. A. Crane, D. J. Van Harlingen, V. A. Oboznov, V. V. Ryazanov, A. Ruosi, C. Granata, and M. Russo. Imaging spontaneous currents in superconducting arrays of π -junctions. *Nature Physics*, 4(1):32–36, 2008.
- [61] A. A. Bannykh, J. Pfeiffer, V. S. Stolyarov, I. E. Batov, V. V. Ryazanov, and M. Weides. Josephson tunnel junctions with a strong ferromagnetic interlayer. *Phys. Rev. B*, 79(5):054501, 2009.
- [62] D. Sprungmann, K. Westerholt, H. Zabel, M. Weides, and H. Kohlstedt. Josephson tunnel junctions with ferromagnetic $\text{Fe}_{0.75}\text{Co}_{0.25}$ barriers. *J. Phys. D*, 42(7):075005, 2009.
- [63] T. S. Khaire, W. P. Pratt, and N. O. Birge. Critical current behavior in Josephson junctions with the weak ferromagnet PdNi. *Phys. Rev. B*, 79(9):094523, 2009.
- [64] M. Zareyan, W. Belzig, and Yu. V. Nazarov. Oscillations of Andreev states in clean ferromagnetic films. *Phys. Rev. Lett.*, 86(2):308–311, 2001.
- [65] M. Zareyan, W. Belzig, and Yu. V. Nazarov. Superconducting proximity effect in clean ferromagnetic layers. *Phys. Rev. B*, 65(18):184505, 2002.
- [66] F. Born, M. Siegel, E. K. Hollmann, H. Braak, A. A. Golubov, D. Yu. Gusakova, and M. Yu. Kupriyanov. Multiple 0- π transitions in SIFS Josephson tunnel junctions. *Phys. Rev. B*, 74(14):140501, 2006.
- [67] P. Carelli and G. Paternò. *Principles and Applications of Superconducting Quantum Interference Devices*, chapter Macroscopic quantum interference: DC-SQUID, pages 1–75. World Scientific Publishing Co. Pte. Ltd., 1992.
- [68] R. C. Jaklevic, J. Lambe, A. H. Silver, and J. E. Mercereau. Quantum interference effects in Josephson tunneling. *Phys. Rev. Lett.*, 12(7):159–160, 1964.
- [69] R. C. Jaklevic, J. Lambe, J. E. Mercereau, and A. H. Silver. Macroscopic quantum interference in superconductors. *Phys. Rev.*, 140(5A):A1628–A1637, 1965.
- [70] V. V. Ryazanov, V. A. Oboznov, A. V. Veretennikov, and A. Yu. Rusanov. Intrinsically frustrated superconducting array of superconductor-ferromagnet-superconductor π junctions. *Phys. Rev. B*, 65(2):020501, 2001.
- [71] W. Guichard, M. Aprili, O. Bourgeois, T. Kontos, J. Lesueur, and P. Gandit. Phase sensitive experiments in ferromagnetic-based Josephson junctions. *Phys. Rev. Lett.*, 90(16):167001, 2003.
- [72] S. M. Frolov, D. J. Van Harlingen, V. A. Oboznov, V. V. Bolginov, and V. V. Ryazanov. Measurement of the current-phase relation of superconductor/ferromagnet/superconductor π Josephson junctions. *Phys. Rev. B*, 70(14):144505, 2004.
- [73] M. Weides, M. Kemmler, E. Goldobin, D. Koelle, R. Kleiner, H. Kohlstedt, and A. Buzdin. High quality ferromagnetic 0 and π Josephson tunnel junctions. *Appl. Phys. Lett.*, 89(12):122511, 2006.
- [74] M. Weides. *Josephson tunnel junctions with ferromagnetic interlayer*. PhD thesis, Universität zu

- Köln, 2006.
- [75] A. Buzdin and A. Koshelev. Periodic alternating 0- and π -junction structures as realization of φ -Josephson junctions. *Phys. Rev. B*, 67(22):220504, 2003.
- [76] M. Weides, M. Kemmler, H. Kohlstedt, R. Waser, D. Koelle, R. Kleiner, and E. Goldobin. 0 – π Josephson tunnel junctions with ferromagnetic barrier. *Phys. Rev. Lett.*, 97(24):247001, 2006.
- [77] M. Weides, C. Schindler, and H. Kohlstedt. Low- T_c Josephson junctions with tailored barrier. *J. Appl. Phys.*, 101(6):063902, 2007.
- [78] H. Hilgenkamp. Pi-phase shift Josephson structures. *Sup. Sci. Tech.*, 21(3):034011, 2008.
- [79] J. B. Majer, J. R. Butcher, and J. E. Mooij. Simple phase bias for superconducting circuits. *Appl. Phys. Lett.*, 80(19):3638–3640, 2002.
- [80] D. S. Golubović, W. V. Pogosov, M. Morelle, and V. V. Moshchalkov. Magnetic phase shifter for superconducting qubits. *Phys. Rev. Lett.*, 92(17):177904, 2004.
- [81] C. E. Shannon. *A symbolic analysis of relay and switching circuits*. PhD thesis, Massachusetts Institute of Technology, Dept. of Electrical Engineering, 1940.
- [82] National Security Agency Office of Corporate Assessments. Superconducting technology assessment. <http://www.nitrd.gov/pubs/nsa/sta.pdf>, 2005.
- [83] D. K. Brock. RSFQ Technology: Circuits and systems. *Int. J. High Speed Electron. Syst.*, 11:307–362, 2001.
- [84] W. Anacker. Josephson computer technology: an IBM research project. *IBM J. Res. Dev.*, 24:107–112, 1980.
- [85] H. Kroger. Josephson devices and technology. In *Japanese Assessment*, pages 250–306. Noyes Data Corporation, Park Ridge, NJ, 1980.
- [86] K. K. Likharev and V. K. Semenov. RSFQ logic/memory family: a new Josephson-junction technology for sub-terahertz-clock-frequency digital systems. *IEEE Trans. Appl. Sup.*, 1(1):3–28, 1991.
- [87] K. Likharev. Ultrafast superconductor digital electronics: RSFQ technology roadmap. *Czechoslovak J. Phys.*, 46(Suppl. S6):3331–3338, 1996.
- [88] K. Likharev. Recent progress and prospects of superconductor digital technology. Technical report, FED Report, 1997.
- [89] J. Ren and V. K. Semenov. Progress with physically and logically reversible superconducting digital circuits. *IEEE/CSC & ESAS European Superconductivity News Forum (ESNF)*, 15:ST241, 2011.
- [90] Wikipedia English. *Rapid single flux quantum*. Accessed online on April 18th, 2011.
- [91] F. Wanlass and C. Sah. Nanowatt logic using field-effect metal-oxide semiconductor triodes. In *1963 IEEE International Solid-State Circuits Conference, Digest of Technical Papers*, volume 6, 1963.
- [92] A. V. Ustinov and V. K. Kaplunenko. Rapid single-flux quantum logic using π -shifters. *J. Appl. Phys.*, 94(8):5405–5407, 2003.
- [93] T. Ortlev, A. O. Mielke, C. J. M. Verwijs, K. F. K. Foo, A. Andreski, H. Rogalla, F. H. Uhlmann, and H. Hilgenkamp. RSFQ circuitry using intrinsic π -phase shifts. *IEEE Trans. Appl. Sup.*, 17(2):659–663, 2007.
- [94] E. Terzioglu and M. R. Beasley. Complementary Josephson junction devices and circuits: a possible new approach to superconducting electronics. *IEEE Trans. Appl. Sup.*, 8(2):48–53, 1998.
- [95] A. K. Feofanov, V. A. Oboznov, V. V. Bol’ginov, J. Lisenfeld, S. Poletto, V. V. Ryazanov,

- A. N. Rossolenko, M. Khabipov, D. Balashov, A. B. Zorin, P. N. Dmitriev, V. P. Koshelets, and A. V. Ustinov. Implementation of superconductor/ferromagnet/superconductor π -shifters in superconducting digital and quantum circuits. *Nature Physics*, 6:593–597, 2010.
- [96] M. Nielsen and I. Chuang. *Quantum Computation and Quantum Information*. Cambridge University Press, 2000.
- [97] D. Estève. *Quantum Entanglement and Information Processing*. Elsevier, Amsterdam, 2004.
- [98] T. P. Orlando, J. E. Mooij, Lin Tian, C. H. van der Wal, L. S. Levitov, S. Lloyd, and J. J. Mazo. Superconducting persistent-current qubit. *Phys. Rev. B*, 60(22):15398–15413, 1999.
- [99] I. Chiorescu, Y. Nakamura, C. Harmans, and J. Mooij. Coherent quantum dynamics of a superconducting flux qubit. *Science*, 299:1869–1871, 2003.
- [100] F. Deppe, M. Mariantoni, E. P. Menzel, S. Saito, K. Kakuyanagi, H. Tanaka, T. Meno, K. Semba, H. Takayanagi, and R. Gross. Phase coherent dynamics of a superconducting flux qubit with capacitive bias readout. *Phys. Rev. B*, 76(21):214503, 2007.
- [101] F. Deppe, M. Mariantoni, E. P. Menzel, A. Marx, S. Saito, K. Kakuyanagi, T. Meno, K. Semba, H. Takayanagi, E. Solano, and R. Gross. Two-photon probe of the Jaynes-Cummings model and controlled symmetry breaking in circuit QED. *Nature Physics*, 4:686–691, 2008.
- [102] T. Niemczyk, F. Deppe, M. Mariantoni, E. P. Menzel, E. Hoffmann, G. Wild, L. Eggenstein, A. Marx, and R. Gross. Fabrication technology of and symmetry breaking in superconducting quantum circuits. *Sup. Sci. Tech.*, 22(3):034009, 2009.
- [103] T. Niemczyk, F. Deppe, H. Huebl, E. P. Menzel, F. Hocke, M. J. Schwarz, J. J. Garcia-Ripoll, D. Zueco, T. Hümmer, E. Solano, A. Marx, and R. Gross. Circuit quantum electrodynamics in the ultrastrong-coupling regime. *Nature Physics*, 6:772–776, 2010.
- [104] G. Blatter, V.B. Geshkenbein, and L.B. Ioffe. Design aspects of superconducting-phase quantum bits. *Phys. Rev. B*, 63(17):174511, 2001.
- [105] T. Yamashita, K. Tanikawa, S. Takahashi, and S. Maekawa. Superconducting π qubit with a ferromagnetic Josephson junction. *Phys. Rev. Lett.*, 95(9):097001, 2005.
- [106] T. Yamashita, S. Takahashi, and S. Maekawa. Superconducting π qubit with three Josephson junctions. *Appl. Phys. Lett.*, 88(13):132501, 2006.
- [107] J. Pfeiffer, M. Kemmler, D. Koelle, R. Kleiner, E. Goldobin, M. Weides, A. K. Feofanov, J. Lisenfeld, and A. V. Ustinov. Static and dynamic properties of 0, π , and 0- π ferromagnetic Josephson tunnel junctions. *Phys. Rev. B*, 77(21):214506, 2008.
- [108] I. Petković and M. Aprili. Phase dynamics of ferromagnetic Josephson junctions. *Phys. Rev. Lett.*, 102(15):157003, 2009.
- [109] I. Petković. *Dynamique de la phase dans des jonctions Josephson ferromagnétiques*. PhD thesis, Université Paris-Sud 11, 2009.
- [110] R. W. Simmonds, K. M. Lang, D. A. Hite, S. Nam, D. P. Pappas, and J. M. Martinis. Decoherence in Josephson phase qubits from junction resonators. *Phys. Rev. Lett.*, 93(7):077003, 2004.
- [111] Tinkham. *Introduction to superconductivity*. McGraw-Hill, New York, 1975.
- [112] I. Petković, M. Aprili, S. E. Barnes, F. Beuneu, and S. Maekawa. Direct dynamical coupling of spin modes and singlet Josephson supercurrent in ferromagnetic Josephson junctions. *Phys. Rev. B*, 80(22):220502, 2009.
- [113] S. E. Barnes, M. Aprili, I. Petković, and S. Maekawa. Ferromagnetic resonance with a magnetic Josephson junction. 2010.
- [114] M. V. Fistul, A. Wallraff, and A. V. Ustinov. Quantum escape of the phase in a strongly driven Josephson junction. *Phys. Rev. B*, 68(6):060504, 2003.

-
- [115] N. Grønblech-Jensen, M. G. Castellano, F. Chiarello, M. Cirillo, C. Cosmelli, L. V. Filippenko, R. Russo, and G. Torrioli. Microwave-induced thermal escape in Josephson junctions. *Phys. Rev. Lett.*, 93(10):107002, 2004.
- [116] N. Grønbech-Jensen and M. Cirillo. Rabi-type oscillations in a classical Josephson junction. *Phys. Rev. Lett.*, 95(6):067001, 2005.
- [117] N. Grønbech-Jensen, M.G. Castellano, F. Chiarello, M. Cirillo, C. Cosmelli, V. Merlo, R. Russo, and G. Torrioli. Anomalous thermal escape in Josephson systems perturbed by microwaves, 2006.
- [118] G. Rotoli, T. Bauch, T. Lindstrom, D. Stornaiuolo, F. Tafuri, and F. Lombardi. Classical resonant activation of a Josephson junction embedded in an LC circuit. *Phys. Rev. B*, 75(14):144501, 2007.
- [119] D. Esteve, M. Devoret, and J. Martinis. Effect of an arbitrary dissipative circuit on the quantum energy levels and tunneling of a Josephson junction. *Phys. Rev. B*, 34(1):158–163, 1986.
- [120] J. M. Martinis, M. H. Devoret, and J. Clarke. Energy-level quantization in the zero-voltage state of a current-biased Josephson junction. *Phys. Rev. Lett.*, 55(15):1543–1546, 1985.
- [121] J. M. Martinis, M. H. Devoret, and J. Clarke. Experimental tests for the quantum behavior of a macroscopic degree of freedom: The phase difference across a Josephson junction. *Phys. Rev. B*, 35(10):4682–4698, 1987.
- [122] J. E. Marchese, M. Cirillo, and N. Grønbech-Jensen. Classical analysis of phase-locking transients and Rabi-type oscillations in microwave-driven Josephson junctions. *Phys. Rev. B*, 73(17):174507, 2006.
- [123] R. F. Voss and R. A. Webb. Macroscopic quantum tunneling in 1- μm Nb Josephson junctions. *Phys. Rev. Lett.*, 47(4):265–268, 1981.
- [124] L. D. Jackel, J. P. Gordon, E. L. Hu, R. E. Howard, L. A. Fetter, D. M. Tennant, R. W. Epworth, and J. Kurkijärvi. Decay of the zero-voltage state in small-area, high-current-density Josephson junctions. *Phys. Rev. Lett.*, 47(9):697–700, 1981.
- [125] U. Weiss. *Quantum Dissipative Systems*, volume 10. World Scientific Publishing, 1999.
- [126] S. Takagi. *Macroscopic Quantum Tunneling*. Cambridge University Press, 2002.
- [127] J. R. Friedman, V. Patel, W. Chen, S. K. Tolpygo, and J. E. Lukens. Quantum superposition of distinct macroscopic states. *Nature*, 406(6791):43–46, 2000.
- [128] C. H. van der Wal, A. C. J. ter Haar, F. K. Wilhelm, R. N. Schouten, C. J. P. M. Harmans, T. P. Orlando, S. Lloyd, and J. E. Mooij. Quantum superposition of macroscopic persistent-current states. *Science*, 290(5492):773–777, 2000.
- [129] J. M. Martinis, S. Nam, J. Aumentado, and C. Urbina. Rabi oscillations in a large Josephson-junction qubit. *Phys. Rev. Lett.*, 89(11):117901, 2002.
- [130] Y. Yu, S. Han, Xi Chu, S. Chu, and Z. Wang. Coherent temporal oscillations of macroscopic quantum states in a Josephson junction. *Science*, 296(5569):889–892, 2002.
- [131] J. E. Mooij, T. P. Orlando, L. Levitov, Lin Tian, C. H. van der Wal, and S. Lloyd. Josephson persistent-current qubit. *Science*, 285(5430):1036–1039, 1999.
- [132] Y. Nakamura, Yu. A. Pashkin, and J. S. Tsai. Coherent control of macroscopic quantum states in a single-Cooper-pair box. *Nature*, 398(6730):786–788, 1999.
- [133] D. Vion, A. Aassime, A. Cottet, P. Joyez, H. Pothier, C. Urbina, D. Esteve, and M. H. Devoret. Manipulating the quantum state of an electrical circuit. *Science*, 296(5569):886–889, 2002.
- [134] N. Giordano. Evidence for macroscopic quantum tunneling in one-dimensional superconductors. *Phys. Rev. Lett.*, 61(18):2137–2140, 1988.
- [135] N. Giordano and E. R. Schuler. Macroscopic quantum tunneling and related effects in a one-dimensional superconductor. *Phys. Rev. Lett.*, 63(21):2417–2420, 1989.

- [136] A. Bezryadin, C. N. Lau, and M. Tinkham. Quantum suppression of superconductivity in ultrathin nanowires. *Nature*, 404(6781):971–974, 2000.
- [137] C. N. Lau, N. Markovic, M. Bockrath, A. Bezryadin, and M. Tinkham. Quantum phase slips in superconducting nanowires. *Phys. Rev. Lett.*, 87(21):217003, 2001.
- [138] F. Altomare, A. M. Chang, M. R. Melloch, Y. Hong, and C. W. Tu. Evidence for macroscopic quantum tunneling of phase slips in long one-dimensional superconducting Al wires. *Phys. Rev. Lett.*, 97(1):017001, 2006.
- [139] M. Sahu, M. Bae, A. Rogachev, D. Pekker, T. Wei, N. Shah, P. M. Goldbart, and A. Bezryadin. Individual topological tunnelling events of a quantum field probed through their macroscopic consequences. *Nature Physics*, 5(7):503–508, 2009.
- [140] G. Sonne and L. Y. Gorelik. Ground-state cooling of a suspended nanowire through inelastic macroscopic quantum tunneling in a current-biased Josephson junction. *Phys. Rev. Lett.*, 106(16):167205, 2011.
- [141] F. Sharifi, J. L. Gavilano, and D. J. Van Harlingen. Macroscopic quantum tunneling and thermal activation from metastable states in a dc SQUID. *Phys. Rev. Lett.*, 61(6):742–745, 1988.
- [142] S. Li, Y. Yu, Yu Zhang, Wei Qiu, S. Han, and Z. Wang. Quantitative study of macroscopic quantum tunneling in a dc SQUID: A system with two degrees of freedom. *Phys. Rev. Lett.*, 89(9):098301, 2002.
- [143] K. Inomata, S. Sato, K. Nakajima, A. Tanaka, Y. Takano, H. B. Wang, M. Nagao, H. Hatano, and S. Kawabata. Macroscopic quantum tunneling in a d-wave high- T_C $\text{Bi}_2\text{Sr}_2\text{CaCu}_2\text{O}_{8+\delta}$ superconductor. *Phys. Rev. Lett.*, 95(10):107005, 2005.
- [144] X. Y. Jin, J. Lisenfeld, Y. Koval, A. Lukashenko, A. V. Ustinov, and P. Müller. Enhanced macroscopic quantum tunneling in $\text{Bi}_2\text{Sr}_2\text{CaCu}_2\text{O}_{8+\delta}$ intrinsic Josephson-junction stacks. *Phys. Rev. Lett.*, 96(17):177003, 2006.
- [145] Y. Kubo, Y. Takahide, S. Ueda, Y. Takano, and Y. Ootuka. Macroscopic quantum tunneling in a $\text{Bi}_2\text{Sr}_2\text{CaCu}_2\text{O}_{8+\delta}$ single crystalline whisker. *Applied Physics Express*, 3(6):063104, 2010.
- [146] T. Bauch, F. Lombardi, F. Tafuri, A. Barone, G. Rotoli, P. Delsing, and T. Claeson. Macroscopic quantum tunneling in d-wave $\text{YBa}_2\text{Cu}_3\text{O}_{7-\delta}$ Josephson junctions. *Phys. Rev. Lett.*, 94(8):087003, 2005.
- [147] T. Bauch, T. Lindstrom, F. Tafuri, G. Rotoli, P. Delsing, T. Claeson, and F. Lombardi. Quantum dynamics of a d-wave Josephson junction. *Science*, 311(5757):57–60, 2006.
- [148] A. Barone, F. Lombardi, G. Rotoli, and F. Tafuri. Macroscopic quantum phenomena in Josephson structures. *Low Temp. Phys.*, 36(10):876–883, 2010.
- [149] R. Stolle. Makroskopisches Quantenverhalten von Josephson Kontakten aus Hochtemperatur-Supraleitern, diploma thesis, TUM, 2006.
- [150] J. Pfeiffer, T. Gaber, D. Koelle, R. Kleiner, E. Goldobin, M. Weides, H. Kohlstedt, J. Lisenfeld, A. K. Feofanov, and A. V. Ustinov. Escape rate measurements and microwave spectroscopy of 0, π , and 0- π ferromagnetic Josephson tunnel junctions, 2009. arXiv-condmat/0903.1046.
- [151] K. Madek, S. Beutner, G. Wild, Ch. Probst, M. Weides, H. Kohlstedt, A. Marx, and R. Gross. Observation of macroscopic quantum behavior in Josephson junctions with ferromagnetic interlayer. Unpublished, 2006.
- [152] V. M. Krasnov, T. Golod, T. Bauch, and P. Delsing. Anticorrelation between temperature and fluctuations of the switching current in moderately damped Josephson junctions. *Phys. Rev. B*, 76(22):224517, 2007.
- [153] T.A. Fulton and L.N. Dunkleberger. Lifetime of the zero-voltage state in Josephson tunnel junctions. *Phys. Rev. B*, 9(11):4760–4768, 1974.

- [154] H. Grabert and U. Weiss. Crossover from thermal hopping to quantum tunneling. *Phys. Rev. Lett.*, 53(19):1787–1790, 1984.
- [155] T. A. Ohki, J. L. Habif, M. J. Feldman, and M. F. Bocko. Thermal design of superconducting digital circuits for millikelvin operation. *IEEE Trans. Appl. Sup.*, 13(2):978–981, 2003.
- [156] J. Bardeen, L. N. Cooper, and J. R. Schrieffer. Theory of superconductivity. *Phys. Rev.*, 108(5):1175–1204, 1957.
- [157] K. Fosshem and A. Sudbø. *Superconductivity - Physics and Applications*. John Wiley & Sons Ltd., 2004.
- [158] H. Kammerlingh-Onnes. The resistance of pure mercury at helium temperatures. *Leiden Comm.*, 120b, 1911.
- [159] H. Kammerlingh-Onnes. The disappearance of the resistivity of mercury. *Leiden Comm.*, 122b, 1911.
- [160] H. Kammerlingh-Onnes. On the sudden change in the rate at which the resistance of mercury disappears. *Leiden Comm.*, 124c, 1911.
- [161] R. Doll and M. Näbauer. Experimental proof of magnetic flux quantization in a superconducting ring. *Phys. Rev. Lett.*, 7(2):51–52, 1961.
- [162] B. S. Deaver and W. M. Fairbank. Experimental evidence for quantized flux in superconducting cylinders. *Phys. Rev. Lett.*, 7(2):43–46, 1961.
- [163] K. K. Likharev. *Dynamics of Josephson Junctions and Circuits*. Gordon and Breach Science Publishers, 1986.
- [164] T. P. Orlando. *Foundations of Applied Superconductivity*. Addison Wesley, 1990.
- [165] P. W. Anderson and J. M. Rowell. Probable observation of the Josephson superconducting tunneling effect. *Phys. Rev. Lett.*, 10(6):230–232, 1963.
- [166] V. Ambegaokar and A. Baratoff. Tunneling between superconductors. *Phys. Rev. Lett.*, 10(11):486–489, 1963. (erratum: *Phys. Rev. Lett.* 11(2):104, July 1963).
- [167] S. Shapiro. Josephson currents in superconducting tunneling: The effect of microwaves and other observations. *Phys. Rev. Lett.*, 11(2):80–82, 1963.
- [168] J. Clarke. Experimental comparison of the Josephson voltage-frequency relation in different superconductors. *Phys. Rev. Lett.*, 21(23):1566–1569, 1968.
- [169] K. Likharev and A. Zorin. Theory of the Bloch-wave oscillations in small Josephson junctions. *J. Low Temp. Phys.*, 59(3):347–382, 1985.
- [170] R. L. Kautz and F. L. Lloyd. Precision of series-array Josephson voltage standards. *Appl. Phys. Lett.*, 51(24):2043–2045, 1987.
- [171] C. A. Hamilton. Josephson voltage standards. *Rev. Sci. Instr.*, 71(10):3611–3623, 2000.
- [172] K. H. J. Buschow, editor. *Concise encyclopedia of magnetic and superconducting materials*. Elsevier Science, 2005.
- [173] Bureau International des Poids et Mesures. The international system of units. 8th edition, 2006.
- [174] K. v. Klitzing, G. Dorda, and M. Pepper. New method for high-accuracy determination of the fine-structure constant based on quantized hall resistance. *Phys. Rev. Lett.*, 45(6):494–497, 1980.
- [175] D. R. Yennie. Integral quantum Hall effect for nonspecialists. *Rev. Mod. Phys.*, 59(3):781–824, 1987.
- [176] R. Fazio and G. Schoen. Mesoscopic effects in superconductors. In L.L. Sohn, editor, *Mesoscopic electron transport*, volume Mesoscopic electron transport of *NATO ASI series E*, Dordrecht, 1997.
- [177] P. G. de Gennes. Boundary effects in superconductors. *Rev. Mod. Phys.*, 36(1):225–237, 1964.

- [178] H. Fröhlich. Theory of the superconducting state. I. The ground state at the absolute zero of temperature. *Phys. Rev.*, 79(5):845–856, 1950.
- [179] A. F. Andreev. Theoretical thermal conductivity of the intermediate state in superconductors. *Sov. Phys.-JETP*, 19:1228–1231, 1964.
- [180] B. Pannetier and H. Courtois. Andreev reflection and proximity effect. *J. Low Temp. Phys.*, 118(5):599–615, 2000.
- [181] I. O. Kulik. Macroscopic quantization and the proximity effect in S-N-S junctions. *Sov. Phys.-JETP*, 30(5):944–950, 1970.
- [182] T. M. Klapwijk, G. E. Blonder, and M. Tinkham. Explanation of subharmonic energy gap structure in superconducting contacts. *Physica B+C*, 109-110(3):1657–1664, 1982.
- [183] G. E. Blonder, M. Tinkham, and T. M. Klapwijk. Transition from metallic to tunneling regimes in superconducting microconstrictions: Excess current, charge imbalance, and supercurrent conversion. *Phys. Rev. B*, 25(7):4515–4532, 1982.
- [184] M. Octavio, M. Tinkham, G. E. Blonder, and T. M. Klapwijk. Subharmonic energy-gap structure in superconducting constrictions. *Phys. Rev. B*, 27(11):6739–6746, 1983.
- [185] R. Kümmel and W. Senftinger. Andreev-reflected wave packets in voltage-biased superconducting quantum wells. *Z. Phys. B*, 59:275–281, 1985.
- [186] G. B. Arnold. Superconducting tunneling without the tunneling Hamiltonian. II. Subgap harmonic structure. *J. Low Temp. Phys.*, 68(1):1–27, 1987.
- [187] K. Flensberg, J. B. Hansen, and M. Octavio. Subharmonic energy-gap structure in superconducting weak links. *Phys. Rev. B*, 38(13):8707–8711, 1988.
- [188] H. Courtois, P. Charlat, Ph. Gandit, D. Mailly, and B. Pannetier. The spectral conductance of a proximity superconductor and the reentrance effect. *J. Low Temp. Phys.*, 116(3):187–213, 1999.
- [189] A.A. Abrikosov. *Fundamentals of the Theory of Metals*. North-Holland, Amsterdam, 1988.
- [190] C. W. J. Beenakker. Why does a metal-superconductor junction have a resistance? In I.O. Kulik and R. Ellialtiogam, editors, *Quantum Mesoscopic Phenomena and Mesoscopic Devices in Microelectronics*, volume 559 of *NATO Science Series C*, pages 51–60. Springer, 1999. arXiv:condmat/9909293.
- [191] C. W. J. Beenakker. Random-matrix theory of quantum transport. *Rev. Mod. Phys.*, 69(3):731–808, 1997.
- [192] Wikipedia English. *Andreev Reflection*. Accessed online on April 18th, 2011.
- [193] M. J. M. de Jong and C. W. J. Beenakker. Andreev reflection in ferromagnet-superconductor junctions. *Phys. Rev. Lett.*, 74(9):1657–1660, 1995.
- [194] P. G. de Gennes. *Superconductivity of Metals and Alloys*. Benjamin, New York, 1966.
- [195] Y. Nambu. Quasi-particles and gauge invariance in the theory of superconductivity. *Phys. Rev.*, 117(3):648–663, 1960.
- [196] J. B. Ketterson and S. B. Song. *Superconductivity*. Cambridge University Press, 1999.
- [197] A. C. Richie-Halford. Numerical modeling of the singlet proximity effect in a superconductor-ferromagnet trilayer. Master’s thesis, California State University, Long Beach, 2010.
- [198] N. N. Bogoliubov. Principle of compensation and the method of the self-consistent field. *Sov. Phys.-Usp.*, 2:236, 1959.
- [199] M. G. Vavilov and A. I. Larkin. Quantum disorder and quantum chaos in Andreev billiards. *Phys. Rev. B*, 67(11):115335, 2003.
- [200] C. Ishii. Thermodynamical properties of Josephson junction with normal metal barrier. *Prog.*

Theor. Phys., 47(5):1464–1481, 1972.

- [201] J. Bardeen and J. L. Johnson. Josephson current flow in pure superconducting-normal-superconducting junctions. *Phys. Rev. B*, 5(1):72–78, 1972.
- [202] A. M. Zagoskin. *Quantum theory of many-body systems: Techniques and applications*. Springer, Berlin, 1998.
- [203] C. Gerthsen. *Physik*. Springer, 1958.
- [204] C. Kittel. *Introduction to solid state physics*. John Wiley and Sons, Inc., 1996.
- [205] S. Guéron, H. Pothier, N. O. Birge, D. Esteve, and M. H. Devoret. Superconducting proximity effect probed on a mesoscopic length scale. *Phys. Rev. Lett.*, 77(14):3025–3028, 1996.
- [206] J. Bentner. *Zur Strom-Phasen-Relation diffusiver Supraleiter/Normalleiter/Supraleiter Josephson-Kontakte*. PhD thesis, Naturwissenschaftliche Fakultät II - Physik der Universität Regensburg, 2004.
- [207] K.-H. Bennemann and J. B. Ketterson, editors. *Superconductivity: Conventional and Unconventional Superconductors*, volume 1. Springer-Verlag New York, LLC, 2008.
- [208] M. G. Flokstra. *Proximity effects in superconducting spin-valve structures*. PhD thesis, Universiteit Leiden, 2010.
- [209] L. P. Gorkov. Microscopic derivation of the Ginzburg-Landau equations in the theory of superconductivity. *Sov. Phys. JETP*, 9:1364–1367, 1959.
- [210] K. D. Usadel. Generalized diffusion equation for superconducting alloys. *Phys. Rev. Lett.*, 25(8):507–509, 1970.
- [211] W. Belzig, F. K. Wilhelm, C. Bruder, G. Schön, and A. D. Zaikin. Quasiclassical Green’s function approach to mesoscopic superconductivity. *Superlattices and Microstructures*, 25(5-6):1251–1288, 1999.
- [212] F. K. Wilhelm, G. Schön, and A. D. Zaikin. Mesoscopic superconducting-normal metal-superconducting transistor. *Phys. Rev. Lett.*, 81(8):1682–1685, 1998.
- [213] S.-K. Yip. Energy-resolved supercurrent between two superconductors. *Phys. Rev. B*, 58(9):5803–5807, 1998.
- [214] P. Anderson. Absence of diffusion in certain random lattices. *Phys. Rev.*, 109(5):1492–1505, 1958.
- [215] D. J. Thouless. Electrons in disordered systems and the theory of localization. *Phys. Rep.*, 13(3):93–142, 1974.
- [216] T. T. Heikkilä, J. Särkkä, and F. K. Wilhelm. Supercurrent-carrying density of states in diffusive mesoscopic Josephson weak links. *Phys. Rev. B*, 66(18):184513, 2002.
- [217] A. M. Clogston. Upper limit for the critical field in hard superconductors. *Phys. Rev. Lett.*, 9(6):266–267, 1962.
- [218] B. S. Chandrasekhar. A note on the maximum critical field of high-field superconductors. *Appl. Phys. Lett.*, 1(1):7–8, 1962.
- [219] I. Bloch, J. Dalibard, and W. Zwerger. Many-body physics with ultracold gases. *Rev. Mod. Phys.*, 80(3):885–964, 2008.
- [220] Wikipedia English. *Fulde-Ferrell-Larkin-Ovchinnikov phase*. Kiwix ZIM file, version 0.8, 2010.
- [221] H. A. Radovan, N. A. Fortune, T. P. Murphy, S. T. Hannahs, E. C. Palm, S. W. Tozer, and D. Hall. Magnetic enhancement of superconductivity from electron spin domains. *Nature*, 425(6953):51–55, 2003.
- [222] C. F. Miclea. *Investigation of superconducting order parameters in heavy-fermion and low-*

- dimensional metallic systems under pressure*. PhD thesis, Technische Universität Dresden, 2005.
- [223] L. N. Bulaevskii, A. I. Buzdin, M. L. Kulić, and S. V. Panjukov. Coexistence of superconductivity and magnetism — Theoretical predictions and experimental results. *Adv. Phys.*, 34(2):175–261, 1985.
- [224] A. V. Andreev, A. I. Buzdin, and R. M. Osgood. π phase in magnetic-layered superconductors. *Phys. Rev. B*, 43(13):10124–10131, 1991.
- [225] L. N. Cooper. Bound electron pairs in a degenerate Fermi gas. *Phys. Rev.*, 104(4):1189–1190, 1956.
- [226] P. Zeeman. The effect of magnetisation on the nature of light emitted by a substance. *Nature*, 55:347, 1897.
- [227] G. Wild. Macroscopic quantum tunneling in Josephson junctions - a method to characterize a well-shielded low temperature setup, diploma thesis, TUM, 2004.
- [228] M. I. Khabipov, D. V. Balashov, F. Maibaum, V. A. Zorin, A. B. Oboznov, V. V. Bolginov, A. N. Rossolenko, and V. V. Ryazanov. A single flux quantum circuit with a ferromagnet-based Josephson π -junction. *Sup. Sci. Tech.*, 23(4):045032, 2010.
- [229] G. E. Moore. Cramming more components onto integrated circuits. *Electronics Magazine*, 38(8):114–117, 1965. <ftp://download.intel.com/research/silicon/moorespaper.pdf>.
- [230] R. Jozsa and N. Linden. On the role of entanglement in quantum-computational speed-up. *Proc. Roy. Soc. Lond. A*, 459(2036):2011–2032, 2003.
- [231] Wikipedia English. *Qubit*. Kiwix ZIM file, version 0.8, 2010.
- [232] Wikipedia English. *Quantum entanglement*. Kiwix ZIM file, version 0.8, 2010.
- [233] R. Gross and A. Marx. Applied superconductivity: Josephson effect and superconducting electronics.
- [234] P. W. Shor. *Algorithms for quantum computation: discrete logarithms and factoring*, pages 124–134. Proceedings of the 35th Annual Symposium on the Foundations of Computer Science. S. Goldwasser, 1994.
- [235] L. Grover. *A fast quantum mechanical algorithm for database search*, pages 212–219. Proceedings of the 28th ACM Symposium on Theory of Computing. Association for Computing Machinery Press, New York, 1999.
- [236] L. M. K. Vandersypen, M. Steffen, G. Breyta, C. S. Yannoni, M. H. Sherwood, and I. L. Chuang. Experimental realization of Shor’s quantum factoring algorithm using nuclear magnetic resonance. *Nature*, 414:883–886, 2001.
- [237] T. P. Spiller. Superconducting circuits for quantum computing. *Fortschritte der Physik*, 48(9-11):1075–1094, 2000.
- [238] D. V. Averin. Quantum computing and quantum measurement with mesoscopic Josephson junctions. *Fortschritte der Physik*, 48(9-11):1055–1074, 2000.
- [239] Y. Makhlin, G. Schön, and A. Shnirman. Quantum-state engineering with Josephson-junction devices. *Rev. Mod. Phys.*, 73(2):357–400, 2001.
- [240] S. L. Braunstein, H.-K. Lo, and P. Kok, editors. *Scalable Quantum Computers - Paving the Way to Realization*. WILEY-VCH Verlag Berlin GmbH, 1st edition, 2001.
- [241] G. Wendin and V. S. Shumeiko. Quantum bits with Josephson junctions. *Low Temp. Phys.*, 33(9):724–744, 2007.
- [242] W. C. Stewart. Current-voltage characteristics of Josephson junctions. *Appl. Phys. Lett.*, 12(8):277–280, 1968.

- [243] D. E. McCumber. Effect of ac impedance on dc voltage-current characteristics of superconductor weak-link junctions. *J. Appl. Phys.*, 39(7):3113–3118, 1968.
- [244] F. London. *Superfluids*, volume 1. John Wiley & Sons, Inc., 1950.
- [245] D. H. Towne. *Wave phenomena*. General Publishing Company, Ltd., 1988.
- [246] D. M. Siegel. *Innovation in Maxwell's Electromagnetic Theory*. Cambridge University Press, 2002.
- [247] A. Barone and G. Paterno. *Physics and applications of the Josephson effect*. John Wiley & Sons, Inc., 1982.
- [248] J. D. Jackson. *Classical Electrodynamics*. John Wiley & Sons, Inc.
- [249] R. E. Eck, D. J. Scalapino, and B. N. Taylor. Self-detection of the ac Josephson current. *Phys. Rev. Lett.*, 13(1):15–18, 1964.
- [250] J. C. Swihart. Field solution for a thin-film superconducting strip transmission line. *J. Appl. Phys.*, 32(3):461–469, 1961.
- [251] J. C. A. Wevers. Physics formulary. <http://www.xs4all.nl/~johanw/physics-hyperref.pdf>, 2001.
- [252] D. D. Coon and M. D. Fiske. Josephson ac and step structure in the supercurrent tunneling characteristic. *Phys. Rev.*, 138(3A):A744–A746, 1965.
- [253] M. D. Fiske. Temperature and magnetic field dependences of the Josephson tunneling current. *Rev. Mod. Phys.*, 36(1):221–222, 1964.
- [254] D. N. Langenberg, D. J. Scalapino, and B. N. Taylor. Josephson-type superconducting tunnel junctions as generators of microwave and submillimeter wave radiation. *Proc. IEEE*, 54(4):560–575, 1966.
- [255] Y. S. Gou and R. I. Gayley. Self-resonant modes in high- Q Josephson tunnel junctions. *Phys. Rev. B*, 10(11):4584–4592, 1974.
- [256] I. O. Kulik. Theory of “steps” of voltage-current characteristic of the Josephson tunnel current. *JETP Lett.*, 2:84–87, 1965.
- [257] I. O. Kulik. Theory of resonance phenomena in superconducting tunneling. *Sov. Phys. Tech. Phys.*, 12(1):111–116, 1967.
- [258] G. Paterno and J. Nordman. Self-resonant modes in Nb-NbO_x-Pb Josephson junctions. *J. Appl. Phys.*, 49(4):2456–2460, 1978.
- [259] H. Kohlstedt, A. V. Ustinov, and F. Peter. Double barrier long Josephson junctions with a contact to the intermediate superconducting layer. *IEEE Trans. Appl. Sup.*, 5(2):2939–2942, 1995.
- [260] M. Weihnacht. Influence of film thickness on d. c. Josephson current. *phys. stat. sol.*, 32(2):K169–K172, 1969.
- [261] G. S. Lee. Analysis of linear resonances in modern Josephson geometries. *IEEE Trans. Appl. Sup.*, 1(3):121–125, 1991.
- [262] G. S. Lee and A. T. Barfknecht. Geometric and material dispersion in Josephson transmission lines. *IEEE Trans. Appl. Sup.*, 2(2):67–73, 1992.
- [263] R. Monaco, G. Costabile, and N. Martucciello. Influence of the idle region on the dynamic properties of window Josephson tunnel junctions. *J. Appl. Phys.*, 77(5):2073–2080, 1995.
- [264] J. Ankerhold and P. Pechukas. Quantum fluctuating barriers. *Europhys. Lett.*, 52(3):264–270, 2000.
- [265] M. Duckheim and J. Ankerhold. Influence of low-frequency noise on macroscopic quantum tunneling in superconducting circuits. *Phys. Rev. B*, 71(13):134501, 2005.
- [266] P. Hänggi, P. Talkner, and M. Borkovec. Reaction-rate theory: Fifty years after Kramers. *Rev.*

- Mod. Phys.*, 62(2):251–341, 1990.
- [267] N. G. van Kampen. *Stochastic processes in physics and chemistry*. Elsevier Science publishers B. V., 1992.
- [268] P. E. Blöchl. *Statistical physics*, 2004.
- [269] H. A. Kramers. Brownian motion in a field of force and the diffusion model of chemical reactions. *Physica*, 7(4):284–304, 1940.
- [270] M. Büttiker, E. P. Harris, and R. Landauer. Thermal activation in extremely underdamped Josephson-junction circuits. *Phys. Rev. B*, 28(3):1268–1275, 1983.
- [271] Yu. M. Ivanchenko and L. A. Zil’berman. Destruction of Josephson current by fluctuations. *JETP Lett.*, 8(4):113–115, 1968.
- [272] V. Ambegaokar and B. I. Halperin. Voltage due to thermal noise in the dc Josephson effect. *Phys. Rev. Lett.*, 22(25):1364–1366, 1969.
- [273] P. Kopietz and S. Chakravarty. Lifetime of metastable voltage states of superconducting tunnel junctions. *Phys. Rev. B*, 38(1):97–110, 1988.
- [274] G. Gamow. Zur Quantentheorie des Atomkernes. *Z. Physik*, 51(3–4):204–212, 1928.
- [275] R. W. Gurney and E. U. Condon. Wave mechanics and radioactive disintegration. *Nature*, 122:439, 1928.
- [276] R. W. Gurney and E. U. Condon. Quantum mechanics and radioactive disintegration. *Phys. Rev.*, 33(2):127–140, 1929.
- [277] F. Schwabl. *Quantenmechanik*. Springer, 6. edition, 2002.
- [278] Wikipedia English. *Quantum tunneling*. Kiwix ZIM file, version 0.8, 2010.
- [279] H. Jeffreys. On certain approximate solutions of linear differential equations of the second order. *Proc. Math. Soc. London*, 23:428–436, 1924.
- [280] G. Wentzel. Eine Verallgemeinerung der Quantenbedingungen für die Zwecke der Wellenmechanik. *Zeitschrift für Physik A*, 38(6):518–529, 1926.
- [281] H. A. Kramers. Wellenmechanik und halbzahlige Quantisierung. *Zeitschrift für Physik A*, 39(10):828–840, 1926.
- [282] L. Brillouin. La mécanique ondulatoire de Schrödinger: une méthode générale de résolution par approximations successives. *Comptes Rendus de l’Academie des Sciences*, 183:24–26, 1926.
- [283] Wikipedia English. *WKB approximation*. Kiwix ZIM file, version 0.8, 2010.
- [284] A. O. Caldeira and A. J. Leggett. Influence of dissipation on quantum tunneling in macroscopic systems. *Phys. Rev. Lett.*, 46:211–214, 1981.
- [285] A. O. Caldeira and A. J. Leggett. Quantum tunnelling in a dissipative system. *Ann. Phys. (NY)*, 149:374–456, 1983.
- [286] A. I. Larkin and Yu. N. Ovchinnikov. The crossover from classical to quantum regime in the problem of the decay of the metastable state. *J. Stat. Phys.*, 41(3):425–443, 1985.
- [287] E. Freidkin, P. S. Riseborough, and P. Hänggi. Quantum tunneling at low temperatures: Results for weak damping. *Z. Phys. B*, 64:237–246, 1986. (see also addendum, *Z. Phys. B*, 67:271, 1987).
- [288] C. G. Callan and S. Coleman. Fate of the false vacuum. II. First quantum corrections. *Phys. Rev. D*, 16(6):1762–1768, 1977.
- [289] S. Coleman. Fate of the false vacuum: Semiclassical theory. *Phys. Rev. D*, 15(10):2929–2936, 1977.
- [290] S. Coleman. Erratum: Fate of the false vacuum: Semiclassical theory. *Phys. Rev. D*, 16(4):1248,

1977.

- [291] A. Wallraff, A. Lukashenko, C. Coqui, A. Kemp, T. Duty, and A. V. Ustinov. Switching current measurements of large area Josephson tunnel junctions. *Rev. Sci. Instr.*, 74(8):3740–3748, 2003.
- [292] S. Washburn, R. A. Webb, R. F. Voss, and S. M. Faris. Effects of dissipation and temperature on macroscopic quantum tunneling. *Phys. Rev. Lett.*, 54(25):2712–2715, 1985.
- [293] A. Wallraff, T. Duty, A. Lukashenko, and A. V. Ustinov. Multiphoton transitions between energy levels in a current-biased Josephson tunnel junction. *Phys. Rev. Lett.*, 90(3):037003, 2003.
- [294] A. I. Larkin and Yu. N. Ovchinnikov. Resonance reduction of the lifetime of the metastable state of tunnel junctions. *J. Low Temp. Phys.*, 63(3):317–329, 1986.
- [295] P. Silvestrini, V. G. Palmieri, B. Ruggiero, and M. Russo. Observation of energy levels quantization in underdamped Josephson junctions above the classical-quantum regime crossover temperature. *Phys. Rev. Lett.*, 79(16):3046–3049, 1997.
- [296] J. Lisenfeld. Probing quantum states of Josephson junctions by microwaves, diploma thesis, Physikalisches Institut III, Friedrich-Alexander-Universität Erlangen-Nürnberg, 2003.
- [297] C. Cohen-Tannoudji, B. Diu, and F. Laloe. *Quantum Mechanics*. Wiley, New York, 1977.
- [298] R. L. Kautz and R. Monaco. Survey of chaos in the rf-biased Josephson junction. *J. Appl. Phys.*, 57(3):875–889, 1985.
- [299] R. L. Kautz. Noise, chaos, and the Josephson voltage standard. *Rep. Prog. Phys.*, 59(8):935–992, 1996.
- [300] N. F. Pedersen, M. R. Samuelsen, and K. Saermark. Parametric excitation of plasma oscillations in Josephson junctions. *J. Appl. Phys.*, 44(11):5120–5124, 1973.
- [301] M. V. Fistul and A. V. Ustinov. Libration states of a nonlinear oscillator: Resonant escape of a pinned magnetic fluxon. *Phys. Rev. B*, 63(2):024508, 2000.
- [302] S. Guozhu, W. Yiwen, C. Junyu, C. Jian, Ji Zhengming, K. Lin, Xu Weiwei, Yu Yang, Han Siyuan, and Wu Peiheng. Microwave-induced phase escape in a Josephson tunnel junction. *Phys. Rev. B*, 77(10):104531, 2008.
- [303] G. J. Dolan. Offset masks for lift-off photoprocessing. *Appl. Phys. Lett.*, 31(5):337–339, 1977.
- [304] T. A. Fulton and G. J. Dolan. Observation of single-electron charging effects in small tunnel junctions. *Phys. Rev. Lett.*, 59(1):109–112, 1987.
- [305] B. Cord, C. Dames, K. K. Berggren, and J. Aumentado. Robust shadow-mask evaporation via lithographically controlled undercut. *J. Vac. Sci. Tech. B*, 24(6):3139–3143, 2006.
- [306] M. Grundner and J. Halbritter. XPS and AES studies on oxide growth and oxide coatings on niobium. *J. Appl. Phys.*, 51(1):397–405, 1980.
- [307] M. Gurvitch, M. Washington, H. Huggins, and J. Rowell. Preparation and properties of Nb Josephson junctions with thin Al layers. *IEEE Trans. Mag.*, 19(3):791–794, 1983.
- [308] J. M. Rowell, M. Gurvitch, and J. Geerk. Modification of tunneling barriers on Nb by a few monolayers of Al. *Phys. Rev. B*, 24(4):2278–2281, 1981.
- [309] B. T. Matthias, H. Suhl, and E. Corenzwit. Spin exchange in superconductors. *Phys. Rev. Lett.*, 1(3):92–94, 1958.
- [310] A. W. Lichtenberger, D. M. Lea, and F. L. Lloyd. Investigation of etching techniques for superconductive Nb/Al-Al₂O₃/Nb fabrication processes. *IEEE Trans. Appl. Sup.*, 3(1):2191–2196, 1993.
- [311] T. Serikawa and S. Seiiti. Deposition characteristics and properties of SiO₂ films prepared by reactive sputtering in hydrogen-, oxygen- and nitrogen-argon mixtures. *Jpn. J. Appl. Phys.*,

- 33(7B):4465–4468, 1994.
- [312] Clariant GmbH. *Datasheet AZ 5214E Image Reversal Photoresist*.
- [313] B. Huber. Herstellung von π -Josephson-Kontakten mit Supraleiter/Ferromagnet/Supraleiter Schichtsystemen, diploma thesis, TUM, 2006.
- [314] F. Family and T. Vicsek. Scaling of the active zone in the Eden process on percolation networks and the ballistic deposition model. *J. Phys. A*, 18(2):L75–L81, 1985.
- [315] J. A. Thornton. High rate thick film growth. *Ann. Rev. Mater. Sci.*, 7(1):239–260, 1977.
- [316] C. K. Gupta and A. K. Suri. *Extractive Metallurgy of Niobium*. CRC Press, 1994.
- [317] S. Rössner. Projektbericht. Technical report, Walther-Meißner-Institut, Garching, 2004.
- [318] C. Wu. Intrinsic stress of magnetron-sputtered niobium films. *Thin Solid Films*, 64(1):103–110, 1979.
- [319] T. Imamura, T. Shiota, and S. Hasuo. Fabrication of high quality Nb/AlO_x-Al/Nb Josephson junctions. I. Sputtered Nb films for junction electrodes. *IEEE Trans. Appl. Sup.*, 2(1):1–14, 1992.
- [320] N. R. Werthamer. Nonlinear self-coupling of Josephson radiation in superconducting tunnel junctions. *Phys. Rev.*, 147(1):255–263, 1966.
- [321] T. Noguchi, T. Suzuki, A. Endo, and T. Tamura. Contribution of the imaginary part of the superconducting gap energy on the SIS tunneling current. *Physica C*, 469(15-20):1585–1588, 2009.
- [322] J. C. Ododo and B. R. Coles. The critical concentration for the onset of ferromagnetism in CuNi alloys. *J. Phys. F*, 7(11):2393–2400, 1977.
- [323] J. W. Cable. Local environment effects in disordered alloys. *J. Appl. Phys.*, 49(3):1527–1531, 1978.
- [324] C. Cirillo, S. L. Prischepa, M. Salvato, and C. Attanasio. Transport properties of Nb/PdNi bilayers. *J. Phys. Chem. Sol.*, 67(1-3):412–415, 2006.
- [325] C. Cirillo, S. L. Prischepa, M. Salvato, and C. Attanasio. Interface transparency of Nb/Pd layered systems. *Eur. Phys. J. B*, 38(1):59–64, 2004.
- [326] P. Bruno and J.-P. Renard. Magnetic surface anisotropy of transition metal ultrathin films. *Appl. Phys. A*, 49(5):499–506, 1989.
- [327] C. A. F. Vaz, J. A. C. Bland, and G. Lauhoff. Magnetism in ultrathin film structures. *Rep. Prog. Phys.*, 71:056501, 2008.
- [328] E. C. Stoner and E. P. Wohlfarth. A mechanism of magnetic hysteresis in heterogeneous alloys. *Phil. Trans. R. Soc. Lond. A*, 240(826):599–642, 1948.
- [329] A. Hubert and R. Schäfer. *Magnetic domains: The analysis of magnetic microstructures*. Springer Verlag, 2008.
- [330] J. Stöhr and H. C. Siegmann. *Magnetism: From Fundamentals to Nanoscale Dynamics*. Springer Verlag, 2006.
- [331] A. Ruotolo, C. Bell, C. W. Leung, and M. G. Blamire. Perpendicular magnetic anisotropy and structural properties of NiCu/Cu multilayers. *J. App. Phys.*, 96(1):512–518, 2004.
- [332] J. W. Cable and H. R. Child. Magnetic moment distribution in Ni-Pd alloys. *Phys. Rev. B*, 1(9):3809–3814, 1970.
- [333] K. Ikeda. Electrical resistivity and ferromagnetism in Ni-Pd alloys. *J. Appl. Phys.*, 62(11):4499–4503, 1987.
- [334] S. Franssila. *Introduction to Microfabrication*. John Wiley & Sons Ltd., 2010.

- [335] K. R. Williams and R. S. Muller. Etch rates for micromachining processing. *J. Micromech. Syst.*, 5(4):256–269, 1996.
- [336] K. R. Williams, K. Gupta, and M. Wasilik. Etch rates for micromachining processing—part II. *J. Micromech. Syst.*, 12(6):761–778, 2003.
- [337] C.-K. Hu, N. Mazzeo, S. J. Wind, D. J. Pearson, and M. B. Ketchen. Reactive ion etching of Nb/AlO_x/Nb for Josephson technology. *Thin Solid Films*, 206(1-2):151–155, 1991.
- [338] D. J. Adelerhof, M. E. Bijlsma, P. B. M. Fransen, T. Weiman, J. Flokstra, and H. Rogalla. Fabrication of Nb/Al,AlO_x/Al/Nb Josephson tunnel junctions using reactive ion etching in SF₆. *Physica C*, 209:477–485, 1993.
- [339] T. Imamura and S. Hasuo. Effects of intrinsic stress on submicrometer Nb/AlO_x/Nb Josephson junctions. *IEEE Trans. Mag.*, 25(2):1119–1122, 1989.
- [340] E. R. Grilly and R. L. Mills. Melting properties of He³ and He⁴ up to 3500 kg/cm². *Ann. Phys.*, 8(1):1–23, 1959.
- [341] F. Pobell. *Matter and Methods at Low Temperatures*. Springer-Verlag New York, LLC, 2006.
- [342] W. F. Randall. Nickel-iron alloys of high permeability, with special reference to mumetal. *Journal of the Institution of Electrical Engineers*, 80(486):647–658, 1937.
- [343] National Instruments Corporation. *LabView 2010*, 2010. <http://www.ni.com/labview>.
- [344] F. S. Bergeret, A. F. Volkov, and K. B. Efetov. Manifestation of triplet superconductivity in superconductor-ferromagnet structures. *Phys. Rev. B*, 68(6):064513, 2003.
- [345] F. S. Bergeret, A. F. Volkov, and K. B. Efetov. Scattering by magnetic and spin-orbit impurities and the Josephson current in superconductor-ferromagnet-superconductor junctions. *Phys. Rev. B*, 75(18):184510, 2007.
- [346] M. Fauré, A. I. Buzdin, A. A. Golubov, and M. Yu. Kuprianov. Properties of superconductor/ferromagnet structures with spin-dependent scattering. *Phys. Rev. B*, 73(6):064505, 2006.
- [347] T. Kontos, M. Aprili, J. Lesueur, and X. Grison. Inhomogeneous superconductivity induced in a ferromagnet by proximity effect. *Phys. Rev. Lett.*, 86(2):304–307, 2001.
- [348] D. H. Dye, S. A. Campbell, G. W. Crabtree, J. B. Ketterson, N. B. Sandesara, and J. J. Vuillemin. Fermi surface and many-body enhancement in Pd. *Phys. Rev. B*, 23(2):462–473, 1981.
- [349] A. Bauer, J. Bentner, M. Aprili, M. L. Della Rocca, M. Reinwald, W. Wegscheider, and C. Strunk. Spontaneous supercurrent induced by ferromagnetic π junctions. *Phys. Rev. Lett.*, 92(21):217001, 2004.
- [350] C. Cirillo, S. L. Prischepa, M. Salvato, C. Attanasio, M. Hesselberth, and J. Aarts. Superconducting proximity effect and interface transparency in Nb-PdNi bilayers. *Phys. Rev. B*, 72(14):144511, 2005.
- [351] D. Vion, P. F. Orfila, P. Joyez, D. Esteve, and M. H. Devoret. Miniature electrical filters for single electron devices. *J. Appl. Phys.*, 77(6):2519–2524, 1995.
- [352] A. Fukushima, A. Sato, A. Iwasa, Y. Nakamura, T. Komatsuzaki, and Y. Sakamoto. Attenuation of microwave filters for single-electron tunneling experiments. *IEEE Trans. Instrum. Meas.*, 46(2):289–293, 1997.
- [353] R. Gross and D. Koelle. Low temperature scanning electron microscopy of superconducting thin films and Josephson junctions. *Rep. Prog. Phys.*, 57(7):651–741, 1994.
- [354] J. Bosch, R. Gross, M. Koyanagi, and R. P. Huebener. Direct probing of the spatial distribution of the maximum Josephson current in a superconducting tunnel junction. *Phys. Rev. Lett.*, 54(13):1448–1451, 1985.
- [355] G. M. Fischer, B. Mayer, R. Gross, T. Nissel, K.-D. Husemann, R. P. Huebener, T. Freltoft, Y. Shen,

- and P. Vase. Spatially resolved observation of static magnetic flux states in $\text{YBa}_2\text{Cu}_3\text{O}_{7-\delta}$ grain boundary Josephson junctions. *Science*, 263(5150):1112–1114, 1994.
- [356] R. Gerdemann, K.-D. Husemann, R. Gross, L. Alff, A. Beck, B. Elia, W. Reuter, and M. Siegel. Spatially resolved analysis of high- T_c grain boundary Josephson junctions and arrays. *J. Appl. Phys.*, 76(12):8005–8015, 1994.
- [357] B. Crouzy, S. Tollis, and D. A. Ivanov. Josephson current in a superconductor-ferromagnet-superconductor junction with in-plane ferromagnetic domains. *Phys. Rev. B*, 76(13):134502, 2007.
- [358] A. I. Buzdin, A. S. Mel'nikov, and N. G. Pugach. Domain walls and long-range triplet correlations in SFS Josephson junctions. *Phys. Rev. B*, 83(14):144515, 2011.
- [359] M. Weides. Magnetic anisotropy in ferromagnetic Josephson junctions. *Appl. Phys. Lett.*, 93:052502, 2008.
- [360] A. A. Golubov and M. Yu. Kupriyanov. Theoretical investigation of Josephson tunnel junctions with spatially inhomogeneous superconducting electrodes. *J. Low Temp. Phys.*, 70(1):83–130, 1988.
- [361] Z. Hermon, A. Stern, and E. Ben-Jacob. Quantum dynamics of a fluxon in a long circular Josephson junction. *Phys. Rev. B*, 49(14):9757–9762, 1994.
- [362] H. S. J. van der Zant, R. A. M. Reecer, T. P. Orlando, and A. W. Kleinsasser. One-dimensional parallel Josephson-junction arrays as a tool for diagnostics. *Appl. Phys. Lett.*, 65(16):2102–2104, 1994.
- [363] H. J. T. Smith. Q of self-resonances in Josephson proximity junctions. *Phys. Rev. B*, 24(1):190–196, 1981.
- [364] R. F. Broom and P. Wolf. Q factor and resonance amplitude of Josephson tunnel junctions. *Phys. Rev. B*, 16(7):3100–3107, 1977.
- [365] J. G. Gijsbertsen, E. P. Houwman, J. Flokstra, H. Rogalla, J. B. le Grand, and P. A. J. de Korte. Field dependence of Fiske resonances in Nb-AlOx based Josephson junctions. *IEEE Trans. Appl. Sup.*, 3(1):2100–2103, 1993.
- [366] F. S. Bergeret, A. Levy Yeyati, and A. Martín-Rodero. Inverse proximity effect in superconductor-ferromagnet structures: From the ballistic to the diffusive limit. *Phys. Rev. B*, 72(6):064524, 2005.
- [367] S. Nam. Theory of electromagnetic properties of strong-coupling and impure superconductors. *Phys. Rev.*, 156(2):487–493, 1967.
- [368] H. Sellier, C. Baraduc, F. Lefloch, and R. Calemczuk. Half-integer Shapiro steps at the $0 - \pi$ crossover of a ferromagnetic Josephson junction. *Phys. Rev. Lett.*, 92(25):257005, 2004.
- [369] E. Goldobin, D. Koelle, R. Kleiner, and A. Buzdin. Josephson junctions with second harmonic in the current-phase relation: Properties of ϕ junctions. *Phys. Rev. B*, 76(22):224523, 2007.
- [370] K. Biedermann, A. Chrestin, T. Matsuyama, and U. Merkt. Magnetic-field dependence of Fiske resonances in Nb/p-type InAs/Nb weak links. *Appl. Sup.*, 5:255–260, 1997.
- [371] N. Argaman. Nonequilibrium Josephson-like effects in wide mesoscopic SNS junctions. *Superlattices and Microstructures*, 25(5-6):861–875, 1999.
- [372] C. Enss and S. Hunklinger. *Low-temperature physics*. Springer Verlag, 2005.
- [373] P. Das, R. de Bruyn Ouboter, and K. W. Taconis. *A Realization of a London-Clarke-Mendoza Type Refrigerator*, pages 1253–1255. Proc. 9th Internat. Conf. on Low Temp. Physics. Plenum Press, 1965.
- [374] G. Frossati. Obtaining ultralow temperatures by dilution of ^3He into ^4He . *J. Phys. Colloques*,

- 39:C6–1578–C6–1589, 1978.
- [375] K. Madek. Untersuchung der Zustandsquantisierung in Josephson-Kontakten, diploma thesis, TUM, 2005.
- [376] S. Beutner. Probing quantum states of Josephson junctions with ferromagnetic barriers by microwaves, diploma thesis, TUM, 2006.
- [377] E. W. Collings. *Applied Superconductivity, Metallurgy, and Physics of Titanium Alloys*, volume 1: Fundamentals. Plenum Press, 1985.
- [378] K. Uhlig. Magnetoresistance of thick film chip resistors at millikelvin temperatures. *Cryogenics*, 35:525–528, 1995.
- [379] H. Nyquist. Thermal agitation of electric charge in conductors. *Phys. Rev.*, 32(1):110–113, 1928.
- [380] J. B. Johnson. Thermal agitation of electricity in conductors. *Phys. Rev.*, 32(1):97–109, 1928.
- [381] T. A. Fulton and R. C. Dynes. Switching to zero voltage in Josephson tunnel junctions. *Solid State Comm.*, 9:1069–1073, 1971.
- [382] J. Kurkijärvi. Intrinsic fluctuations in a superconducting ring closed with a Josephson junction. *Phys. Rev. B*, 6(3):832–835, 1972.
- [383] A. Garg. Escape-field distribution for escape from a metastable potential well subject to a steadily increasing bias field. *Phys. Rev. B*, 51(21):15592–15595, 1995.
- [384] C. C. Grimes and S. Shapiro. Millimeter-wave mixing with Josephson junctions. *Phys. Rev.*, 169(2):397–406, 1968.
- [385] P. K. Tien and J. P. Gordon. Multiphoton process observed in the interaction of microwave fields with the tunneling between superconductor films. *Phys. Rev.*, 129(2):647–651, 1963.
- [386] H. F. Yu, X. B. Zhu, Z. H. Peng, W. H. Cao, D. J. Cui, Ye Tian, G. H. Chen, D. N. Zheng, X. N. Jing, Li Lu, S. P. Zhao, and S. Han. Quantum and classical resonant escapes of a strongly driven Josephson junction. *Phys. Rev. B*, 81(14):144518, 2010.
- [387] V. Krishnan. *Probability and Random Processes*. Wiley, John & Sons, Inc., 2006.
- [388] M. Abramowitz and I. A. Stegun, editors. *Handbook of Mathematical Functions With Formulas, Graphs, and Mathematical Tables*. National bureau of standards, 1964.
- [389] National Semiconductor Corporation. *LF198/LF298/LF398, LF198A/LF398A Monolithic Sample-and-Hold Circuits*, 2000.
- [390] L. D. Jackel, W. W. Webb, J. E. Lukens, and S. S. Pei. Measurement of the probability distribution of thermally excited fluxoid quantum transitions in a superconducting ring closed by a Josephson junction. *Phys. Rev. B*, 9(1):115–118, 1974.
- [391] A. Kemp. *Quantum and Thermal Phase Escape in Extended Josephson Systems*. PhD thesis, Naturwissenschaftliche Fakultäten der Friedrich-Alexander-Universität Erlangen-Nürnberg, 2006.
- [392] J. Goldstone. Field theories with superconductor solutions. *Nuovo Cimento*, 19(1):154–164, 1961.
- [393] J. Goldstone, A. Salam, and S. Weinberg. Broken symmetries. *Phys. Rev.*, 127(3):965–970, 1962.
- [394] T. Holstein and H. Primakoff. Field dependence of the intrinsic domain magnetization of a ferromagnet. *Phys. Rev.*, 58(12):1098–1113, 1940.
- [395] F. J. Dyson. General theory of spin-wave interactions. *Phys. Rev.*, 102(5):1217–1230, 1956.
- [396] L.D. Landau and E.M. Lifshitz. On the theory of the dispersion of magnetic permeability in ferromagnetic bodies. *Phys. Zeitsch. der Sow.*, 8:153–169, 1935.
- [397] T. L. Gilbert. Lagrangian formulation of the gyromagnetic equation of the magnetization field. *Phys. Rev.*, 100:1243, 1955.

- [398] T. L. Gilbert. A phenomenological theory of damping in ferromagnetic materials. *IEEE Trans. Mag.*, 40(6):3443–3449, 2004.
- [399] G. V. Skrotskiĭ. The Landau-Lifshitz equation revisited. *Sov. Phys. Usp.*, 27:977–979, 1984.
- [400] S. V. Vonsovskii. *Ferromagnetic Resonance: The Phenomenon of Resonant Absorption of a High-Frequency Magnetic Field in Ferromagnetic Substances*. Pergamon press Inc., 1966.
- [401] R. Hertel, W. Wulfhekel, and J. Kirschner. Domain-wall induced phase shifts in spin waves. *Phys. Rev. Lett.*, 93(25):257202, 2004.
- [402] C. Bayer, H. Schultheiss, B. Hillebrands, and R. L. Stamps. Phase shift of spin waves traveling through a 180° Bloch-domain wall. *IEEE Trans. Magn.*, 41(10):3094–3096, 2005.
- [403] K. Perzlmaier, M. Buess, C. H. Back, V. E. Demidov, B. Hillebrands, and S. O. Demokritov. Spin-wave eigenmodes of permalloy squares with a closure domain structure. *Phys. Rev. Lett.*, 94(5):057202, 2005.
- [404] S. J. Hermsdörfer. *Untersuchungen zur Wechselwirkung von Spinwellen und Domänenwänden in dünnen magnetischen Strukturen*. PhD thesis, Technischen Universität Kaiserslautern, 2009.
- [405] S. Shapiro, A. R. Janus, and S. Holly. Effect of microwaves on Josephson currents in superconducting tunneling. *Rev. Mod. Phys.*, 36(1):223–225, 1964.
- [406] C. A. Hamilton and S. Shapiro. rf-induced effects in superconducting tunnel junctions. *Phys. Rev. B*, 2(11):4494–4503, 1970.
- [407] M. J. Donahue and D. G. Porter. *OOMMF User's Guide, Version 1.0, Interagency Report NISTIR 6376*. National Institute of Standards and Technology, Gaithersburg, MD, 1999.
- [408] M. Moshe and R. G. Mints. Shapiro steps in Josephson junctions with alternating critical current density. *Phys. Rev. B*, 76(5):054518, 2007.
- [409] V. E. Kose and D. B. Sullivan. Influence of external noise on microwave-induced Josephson steps. *J. Appl. Phys.*, 41(1):169–174, 1970.
- [410] W. H. Henkels and W. W. Webb. Intrinsic fluctuations in the driven Josephson oscillator. *Phys. Rev. Lett.*, 26(19):1164–1167, 1971.
- [411] I. Giaever. Detection of the ac Josephson effect. *Phys. Rev. Lett.*, 14(22):904–906, 1965.
- [412] C. C. Grimes, P. L. Richards, and S. Shapiro. Josephson-effect far-infrared detector. *J. App. Phys.*, 39(8):3905–3912, 1968.
- [413] C. D. T. Runge. Über die numerische Auflösung von Differentialgleichungen. *Math. Ann.*, 46:167–178, 1895.
- [414] W. M. Kutta. Beitrag zur näherungsweise Integration totaler Differentialgleichungen. *Z. Math. Phys.*, 46:435–453, 1901.
- [415] V. Novotny and P. P. M. Meincke. Single superconducting energy gap in pure niobium. *J. Low Temp. Phys.*, 18(1):147–157, 1975.
- [416] L. Dumoulin, P. Nedellec, and P. M. Chaikin. Proximity-effect tunneling in Pd-Pb sandwiches. *Phys. Rev. Lett.*, 47(3):208–211, 1981.
- [417] P. J. Mohr and B. N. Taylor. CODATA recommended values of the fundamental physical constants: 2002. *Rev. Mod. Phys.*, 77(1):1–107, 2005.
- [418] J. W. Eaton. *GNU Octave Manual*. Network Theory Limited, 2002.
- [419] R. M. Stallman and GCC Developer Community. *Using The GNU Compiler Collection: A GNU Manual For GCC*. CreateSpace, Paramount, CA, 2009.
- [420] *The GNU C Library*. Free Software Foundation, Inc., 2010.

LIST OF PUBLICATIONS

- [A1] T. Niemczyk, F. Deppe, M. Mariani, E. P. Menzel, E. Hoffmann, G. Wild, L. Eggenstein, A. Marx, and R. Gross. Fabrication Technology of and Symmetry Breaking in Superconducting Quantum Circuits. *Sup. Sci. Tech.* 22:034009, 2009

- [A2] G. Wild, C. Probst, A. Marx, and R. Gross. Josephson coupling and Fiske dynamics in ferromagnetic tunnel junctions. *Eur. Phys. J. B* 78:509-523, 2010
arXiv-condmat:1008.3341, doi:10.1140/epjb/e2010-10636-4

- [A3] E. Hoffmann, F. Deppe, T. Niemczyk, T. Wirth, E. P. Menzel, G. Wild, H. Huebl, M. Mariani, T. Weißl, A. Lukashenko, A. P. Zhuravel, A. V. Ustinov, A. Marx, and R. Gross. A Superconducting 180° Hybrid Ring Coupler for circuit Quantum Electrodynamics. *Appl. Phys. Lett.* 97:222508, 2010

ACKNOWLEDGMENTS

The persons initiating the research on Josephson junctions with a ferromagnetic interlayer at the WMI are Prof. Dr. Rudolf Gross and Dr. Achim Marx. I thankfully acknowledge their effort in interpreting the experiments, publishing the results and the careful review of this manuscript.

The lowest temperature experiments highly profit from the expertise available at the WMI, especially from the profound knowledge of dilution refrigerators and sample thermalization of Dr. C. Probst. I thankfully acknowledge the upgrading and maintenance of the dilution fridge by K. Madek, S. Beutner, and T. Niemczyk and the calibration of the Dale temperature sensors by K. Neumaier. Furthermore, I have to thank Dr. J. Schuler for introducing me in lithography techniques, Dr. M. Opel for teaching me the basics of magnetism and his patience in the maintenance of the SQUID magnetometer, and Dr. A. Erb for the EDX analysis of the PdNi. I, moreover, greatly respect the work of my diploma student B. Huber, who optimized the thin film deposition of the multilayer process, and thank E. Menzel, T. Heimbeck, and Dr. F. Deppe for their experimental help and useful discussions. Moreover, I value all my colleges for the friendly environment I found in the last years at the WMI.

But not only scientists are essential to get excellent results. So, I exceptionally highlight the technicians helping to realize this work. The engineer T. Brenninger took care of the thin-film instruments and together with J. Höß engineered many low temperature setups. The mechanical workshops headed by R. Müller and H. Thies manufactured excellent cryostats and the helium liquefaction team always provided enough helium for the experiments. The engineer W. Hehn engineered the ^3He pumping cryostat. The electrical engineers D. Guratzsch and U. Guggenberger always tried hard to implement electronic circuits and to have the measurement devices running.

The data evaluation in this work greatly profits from the high-level interactive language octave⁴¹⁸. Simulations are performed using the GNU Compiler Collection.^{419, 420}

This work was funded by the DFG (German science foundation) via the cooperative research center 631 for solid state based quantum information processing, by the German excellence initiative via NIM, and by the Bavarian academy of sciences and humanities.

INDEX

- AFM microscopy, 75, 76
 - rms roughness, 77
- Aharonov-Bohm effect, 3
- algorithm
 - Grover, 33
 - Shor, 33
- Ambegaokar-Baratoff relation, 17
- Andreev
 - bound state, 20
 - discrete energy levels, 22, 28
 - pair, 20
 - reflection, 19
- Andreev pair, 24
- anisotropy
 - Fermi surface, 24
 - magnetic, 79, 96, 135, 138, 145
- BCS theory, 15
- bonding, 68, 72
 - gold, 115
- BTK theory, 23
- cleaning
 - in-situ, 69
- coherent tunneling, 17
- constants
 - material constants, 155
 - nomenclature, 159
- Cooper pair, 15
- crossover
 - temperature, 59, 133, 141, 142
 - thermal/quantum escape, 58, 128, 141, 142
- Curie temperature, 78, 80, 98, 135, 145, 155
- current-phase relation, 3
 - second harmonic, 109, 139
- SFS, 28
- SNS, 23
- diffusive transport
 - SFS, 28
 - SNS, 23
- easy axis, 79
- EDX, 79
- escape
 - crossover thermal/quantum, 58, 128
 - experiment, 128, 140
 - quantum, 57
 - thermal, 54
- etching, 74, 80
 - RIE, 68
 - parameters, 70
- exchange energy, 4, 88, 92, 145, 155
- exchange length, 90
- excitation
 - ferromagnetic interlayer, 135, 147
 - microwave, 59, 122
- experimental setup
 - 500 mK setup, 85
 - bonding, 72
 - dilution refrigerator, 114
 - filtering, 117
 - microwave setup, 116
 - ramping experiments, 119
 - UHV system, 74
 - wiring, 117
- external driving, 59
 - classical interpretation, 61

- experiment, 122
 - quantum mechanical interpretation, 60
- ferromagnetic layer, 79
 - high permeability, 148
- FFLO state, 4, 30
- Fiske resonance, 44, 99
 - height, 105
 - quality, 46, 106, 146
- Fiske step, *see* Fiske resonance
- fluxoid
 - quantization, 15
- Fröhlich interaction, 19
- Fraunhofer pattern, 43, 97
- Fulde-Ferrel-Larkin-Ovchinnikov state, *see* FFLO state
- GInsitu-203b, 157
- growth, 67
 - etching, 68
 - lift-off, 74
 - recipe, 151
 - sputtering, 74
- $I_c(H)$, 96
- $I_c R_n$
 - SIS, 17
 - SNS, 23
- $I_c R_n(d_F)$, 90
- idle region, 51
- interlayer
 - ferromagnetic, 79
 - magnetized, 98, 137
- ion-gun, 69
- IVCs, 100
 - RCSJ model, 38
 - resonances, 19, 44, 99, 135
 - Shapiro step, 137
 - SIS, 76
 - without applied field, 92
- Josephson
 - energy, 35
 - equations, 17
 - transmission line, 46
- Josephson junction, 15
 - applications
 - QIP, 32
 - dynamics, 8, 35
 - extended, 40
 - external driving, 59, 122
 - classical interpretation, 61
 - quantum mechanical interpretation, 60
 - growth, 67
 - magnetic field, 40
 - π -junction, *see* π -junction
 - S-FI-S, 4
 - SFS, 27
 - clean limit, 5, 27
 - diffusive transport, 28
 - dirty limit, 5, 28
 - historical, 30
 - NiCu, 5, 9, 31, 79, 97, 131
 - PdNi, 5, 31, 68, 88
 - SIFS, 4
 - SIS, 15
 - SNS, 18
 - clean limit, 20
 - diffusive transport, 23
 - dirty limit, 23
- Kramers' theory, 55
 - underdamped Josephson junction, 56
- Kulik's theory, 46, 101
 - high Q , 48
- Landau-Lifshitz-Gilbert equation, 135
- lift-off, 74
- lithography
 - mask, 71
- London
 - equations, 40
 - penetration depth, 42, 49
- macroscopic
 - quantum behavior, 8

- quantum tunneling, 9, 57, 113, 128, 133
 - wave function, 15
- magnetic thickness, 41
 - effective, 49
- magnetization, 78
 - saturation, 79, 145
- magnetoresistance, 3
- material
 - constants, 155
 - dispersion, 51, 101
- McCumber parameter, 37
- mean free path, 5, 90
- measurement
 - 500 mK setup, 85
 - dilution refrigerator, 114
 - IVCs, 88
- mesa, 69, 70, 72
 - definition, 80, 151
- metastable state, 53
- microwave driving, 8, 146
 - experiment, 122
 - experiments, 59
 - simulation equations, 153
 - strong, 61
- MQT, *see* macroscopic quantum tunneling
- multilayer
 - deposition, 151
 - etching, 80
 - growth, 74
 - niobium, 77
 - oxidation, 74
 - patterning, 68
 - PdNi, 79
 - sputtering, 74
- niobium, 77
- nomenclature, 159
- nonlinear phenomena, 48, 61
- order parameter, 20, 24
 - oscillation, 4
- overgrowth
 - SiO₂-Nb, 70
 - oxidation, 74
- π -junction, 3, 6
 - active, 7, 34
 - dynamics, 36
 - I_c sign change, 88
 - passive, 8, 34
 - realization, 4
 - theory, 27
- PdNi, 79
- plasma frequency, 36
- proximity effect, 19
- QIP, *see* quantum information processing
- quality factor, 109
 - Fiske resonance, 46, 99, 101, 104, 106–108
 - hysteresis IVCs, 37, 39, 92, 95, 104, 106
- quantum
 - effects
 - secondary, 113, 114
 - electronics, 6, 32
 - information processing, 32
- qubit, 32
 - persistent current, 7, 34
 - phase, 7
 - quiet, 6, 34
- Rabi oscillation, 9
- ramping experiment, 119
- rapid single flux quantum, *see* RSFQ
- RCSJ model, 35, 104
 - current-voltage characteristics, 38
- resonance
 - ferromagnetic, 136
 - HF, 102, 109, 110
- retrapping current, 39, 92
- RSFQ, 6, 32
- setup, *see* experimental setup
- Shapiro step, 137
 - half integer, 139

- Sine-Gordon-Equation, 43
- SiO₂, 69, 96
- spin wave, 136
- sputtering, 74
 - parameters, 70, 74
- SQUID magnetometry, 78, 79
- Stewart-McCumber model, *see* RCSJ model
- superconducting coherence length, 90
- supercurrent density, 23, 26
- surface resistance, 107
- Swihart velocity, 43, 51
- switching current
 - histogram, 120, 130
 - histogram width, 122, 128, 131–133
- Thouless energy
 - ballistic, 22
 - diffusive, 26
- tilted washboard potential, 37
 - metastable state, 53, 113
- transition state theory, 54
- two-fluid model, 107
- Usadel equation, 24, 29
- wiring
 - deposition, 151